Instrumentation and Control of Unmanned Air Vehicles

Nissen, Henrik Ditlev; Jannerup, Ole Erik; Sørensen, Paul Haase

Publication date:
2003

Document Version
Early version, also known as pre-print

Citation (APA):
Nissen, H. D., Jannerup, O. E., & Sørensen, P. H. (2003). Instrumentation and Control of Unmanned Air Vehicles.

HENRIK DITLEV NISSEN

Instrumentation and Control of Unmanned Air Vehicles

PhD thesis

AUTOMATION

Ørsted•DTU

SEPTEMBER 2002

ØRSTED•DTU, Automation

DTU, Bld. 326

DK-2800 Kgs. Lyngby

Denmark

Phone +45 4525 3550

Printed in Denmark at DTU, Kgs. Lyngby

03-A-923

ISBN 87-91184-15-0

Technical University of Denmark

September 2002

Henrik D. Nissen

Preface

This thesis is submitted as partial fulfilment of the requirements for the Ph.D.degree in electrical engineering at Ørsted-DTU. Associate professor Ph.D. Ole Jannerup and associate professor Ph.D. Paul Haase Sørensen of the department acted as supervisors on this project.

I would like to thank both my supervisors for helpful discussions and guidance throughout the project period. The support and patience of especially Ole Jannerup and Louise Buhelt during particularly the last months of this project was crucial in getting this thesis finished. During the project I have received invaluable support from the entire staff at the department, in particular the technical staff has provided great assistance in fabrication of many mechanical and electronic parts and subsystems. Also I would like to thank David Christensen for programming the microcontroller and PC interfaces to the GPS receiver boards which where used in the DGPS experiments. Finally I would like to thank my parents for starting my interest in all things aeronautcal.

Abstract

This thesis treats a number of instrumentation and control problems related to autonomous Unmanned Aerial Vehicles (UAV’s). Autonomous Micro Air Vehicles (MAV’s) are of special interest to the Author. These are characterised by their small size, typically below 10kg takeoff weight. Due to their small size, normal avionics are not suited for MAV’s. Instead it is more appropriate to use standard model airplane components and actuators. This has the added benefit of reducing the vehicle cost. However this also means that the vehicle designer has to characterise and design many of the instruments and actuators used for MAV’s.

The first part of this thesis concentrates on obtaining an aerodynamic model for a canard configuration fixed wing UAV. Particular emphasis is placed on treatment of uncertainties in the model and the resulting influence on the UAV dynamics. A model of an electric propulsion system is also proposed, based partly on propeller characteristics obtained by comparing the geometry of the propeller with that of a propeller with known characteristics.

Model airplane actuators are a logical choice for MAV’s because of there availability, price and performance. It is however difficult to obtain published data concerning the dynamics of these actuators. For these reasons a part of this thesis treats the procedure used in experimentally identifying a dynamic model of model airplane actuators. It is shown that a particular make of actuators employ a proportional-derivative bang-bang controller scheme. As a result of this observation, a feedback linearization scheme is proposed and simulated for this type of actuator.

Different lateral guidance strategies are discussed based on the assumption that the desired flight path of the UAV is defined by a number of “waypoints”. It is shown that a “moving point” guidance strategy has certain advantages with respect to autopilot implementation and smooth transition from one heading to another in the vicinity of a waypoint.

The most critical flight phase with respect to guidance and navigation accuracy is the approach and landing. In order to accomplish an autonomous landing it is important to be able to determine the position of the UAV with great accuracy and reliability. The only practical system for accurate navigation at the present, which does not require expensive ground based equipment, is the satellite based Global Positioning System, commonly known as GPS. However this alone does not have sufficient accuracy for the task. By using a differential positioning approach involving a ground based GPS receiver at a known location, it is possible to construct a Differential GPS (DGPS). Such a system has been implemented and studied in detail using a pair of commercially available receivers. It is shown through analysis of experimental data that the most significant error source in DGPS systems is multipath, caused by reflections of the signal from objects in the vicinity of the receiver antennas. Furthermore it is shown that these errors can be correlated with the receiver Signal to Noise Ratio (SNR). Using this information a kinematic Kalman filter is proposed for filtering the raw measurement data. “Simulation” of this filter using actual measurement data shows that a significant improvement in positioning accuracy is obtained.

Finally some issues relating to the design of an Inertial Navigation System (INS) and realtime synchronized instruments are discussed.

Resume

Denne afhandling behandler en række instrumenterings og styringsproblemer med relation til ubemandede fly. Små selvstyrende ubemandede fly udgør et specielt interesseområde for forfatteren. Disse fly har typisk en startvægt på under 10kg. På grund af deres lille størrelse er normale fly instrumenter og aktuatorer uegnet til brug i små ubemandede fly. Istedet er det mere fordelagtigt at bruge modelfly komponenter og aktuatorer. Det har den ekstra fordel at det reducerer fartøjets pris drastisk. Desværre medfører det også at konstruktøren skal tage et større ansvar for at karakteriserer og designe flere af instrumenterne og aktuatorerne til små udemandede fly.

I den første del af denne afhandling opstilles en aerodynamisk model for et ubemandet fly af ente typen. Modellen omfatter et begrundet skøn over usikkerheden af kritiske aerodynamiske egenskaber og belyser deres indflydelse på flyets opførelse. En model af et elektrisk fremdrivningssystem er også opstillet. Den inkluderer en semiemperisk model af en propel med fast stigning.

Modelfly aktuatorer er et logisk valg til små ubemandede fly på grund af deres tilgængelighed, pris og gode ydeevne. Desværre er det svært at skaffe tilgængelige data for deres dynamiske respons. Derfor omhandler en del af afhandlingen en eksperimentiel metode til at bestem en dynamisk aktuator model. Brug af denne metode har vist at den undersøgte aktuator bruger en bang-bang styring. Som resultat af denne observation er der foreslået en general metode til at lineariserer aktuatoren ved hjælp af tilbagekoblingslinearisering.

Forskellige laterale styringsstrategier bliver diskuteret med hensyn til deres evne til at styre et ubemandet fly langs en rute defineret ved et antal ‘waypoints’. Det vises at en styringsstrategi baseret på at styre imod et punkt som løber langs den ‘ideelle’ rute har et antal praktiske fordele.

Landningen er den mest kritiske fase for et ubemandet selvstyrende fly med hensyn til præcis styring og navigation. Det satellitbaserede GPS system er det eneste tilgængelige system til præcis navigation uden dyrt og kompliseret jordudstyr. Desværre er selv præcisionen af GPS ikke tilstrækkeligt til sikker og præcis autonom landing. Ved at bruge et Differentielt GPS system baseret på en ekstra GPS modtager på en kendt position, kan nøjagtigheden øges betragteligt. Et sådant system er blevet konstrueret baseret på to kommercielt tilgængelige modtagerer. Ved forsøg med dette system har det vist sig at den største fejlkilde består i refleksion af signalet fra bygninger og andre genstande i nærheden af modtager antennen. Det er har dog vist sig at disse fejl kan korreleres med signal-støj forholdet som bestemmes af modtageren. Udfra dette er det lykkedes at konstruerer et kinematisk Kalman filter baseret DGPS system med forbedret nøjagtigheden.

Tilsidst omtales nogle betragtninger vedrørende konstruktionen af en inertial ‘platform’ og synkroniserede realtids instrumenter.

Table of contents

Chapter 1 Introduction to UAV systems

Chapter 2 Aerodynamic Model

Chapter 3 UAV actuators

Table of contents

Chapter 4 Lateral Guidance

Chapter 5 DGPS Instrument: Theory and Performance

Table of contents

Chapter 6 Inertial Navigation System

Chapter 7 General Instrument Program Structure

Chapter 1

Introduction to UAV systems

1.1 UAV definitions and categories:

The term Unmanned Aerial Vehicle (UAV) is a generic term for unmanned aircraft. In practice the term UAV is reserved for vehicles which contain an active payload and some kind of “intelligence” or guidance. This means that even though a radio controlled model plane is unmanned, it is usually not considered as belonging to the UAV category. Also military target “drones” are usually not considered as belonging to the UAV category since they usually do not contain an active payload or perform a “self contained” mission.

The broad UAV category is further subdivided into subcategories:

- Remotely Piloted Vehicles (RPV’s): A class of UAV’s which are piloted by an remote operator (pilot) using a telecommand system. The primary feedback mechanism is usually a vehicle mounted forward looking vision system. The operator flies the vehicle by directly manipulating the control surfaces through the telecommand system.
- Micro Air Vehicle (MAV): A small UAV usually limited to less then about 10 kg takeoff mass. Since such a small vehicle is obviously incapable of carrying a human payload, it is unnecessary to specify that it is unmanned.
- Autonomous Unmanned Aerial Vehicle: An UAV which is capable of flight without constant human control. This is in itself a broad category; the simplest system consists of some kind of onboard autopilot and navigation system which enables autonomous flight between operator defined waypoints. More advanced systems enable autonomous takeoff and landing, thus completely eliminating the need for operator piloting skills. At an even higher level are systems which are able to make autonomous mission decisions. This might entail changing the mission plan in response to onboard sensor readings. This could be useful in cases where tracking of some kind of “target” is required or in responds to failure of the telecommand system or vehicle critical systems.

1.2 Past and future UAV applications:

The concept of an unmanned aircraft is almost as old as flight itself. The main UAV application in the past has been military reconnaissance. This is motivated by the desire to reduce the risk of pilot death or capture during often dangerous combat reconnaissance missions. Significant early examples of this includes the use by the US airforce of converted airlaunched target drones for post strike damage assessment in Vietnam. Incidentally these missions where so secret that the mere existence of these units where only acknowledged several years after the Vietnam war. Separately, the Israeli airforce developed a range of simple small slow flying reconnaissance RPVs. Early versions where apparently used in Lebanon from the late 1970’s.

While military applications of UAV’s will undoubtedly continue and escalate in the future, the primary interest of this author lies in the civilian field. The civilian applications of UAV’s roughly fall into two categories.

- Law enforcement and search and rescue: This basically uses the UAV in a reconnaissance mode to search for suspects or survivors. An advanced application would be autonomous search and tracking using electro-optical payloads with onboard pattern recognition.
- Environment monitoring and mapping: This type of mission uses the UAV as an instrument platform to scan a geographical region using one or more environmental sensors. The type of sensors can roughly be divided into two types; remote sensing and in-situ sensors. Remote sensing sensors would in most cases be some kind of electro-optical camera system. The primary advantages of using airborne electro-optical sensors instead of satellite systems, are that airborne systems can avoid cloud cover by flying below the cloud base, in addition an airborne system can be used on demand and provide near real time data of high resolution. Another group of measurements which can be extremely useful are in-situ measurements of air borne pollution. For this latter application, the most interesting region is close to ground level. This means that an UAV capable of flying close to the ground would be a particularly valuable asset for these missions.

Military applications of UAV’s have been primarily concerned with eliminating the need for an onboard pilot and crew, of course this lowers the cost of the vehicle, as well as fuel costs, because a smaller vehicle is needed for a given payload. However for many potential civilian applications this would not provide a major mission cost reduction since a pilot would still be needed even though he or she is located on the ground. A more drastic mission price reduction could be achieved if the pilot was replaced by a “mission manager” which could be responsible for overall mission planning, payload supervision and overall operations, but would not be required to manually pilot the UAV. This of course requires that the UAV should be capable of both autonomous navigation, control and guidance during all phases of flight.

Another important issue for civilian UAV applications is the complexity of launch and recovery operations. Many early and some contemporary military UAV’s use special launch and recovery systems such as catapults, parachutes and airbags (to cushion ground impact). These systems may be well suited to military operations in places without adequate prepared takeoff and landing fields. However most of these systems are costly in terms of operations and maintenance. Even in the best of circumstances they need workers to prepare and load catapults, retrieve vehicles and repack parachutes and airbags. In addition there is a high degree of uncertainty involved in parachute assisted landing because it may be difficult to predict the exact point of impact. This gives a relatively high risk of ground impact damage due to ground obstacles.

We can thus assume that a successful civilian UAV should be able to perform a controlled landing in a small predefined area regardless of wind and weather. This can either be achieved using conventional landing procedures on a small prepared surface or alternatively a vertical takeoff and landing capability can be used to land in a very small area.

1.3 Autonomous UAV systems:

From the preceding discussion it is clear that a successful civilian UAV should be capable of autonomous control, navigation, guidance and takeoff and landing. To accomplish this the following systems are necessary:

- A reliable aerial vehicle with suitable control surfaces, actuators and propulsion system.
- A mathematical model of the vehicle and actuator response of sufficient accuracy to simulate the behaviour of the vehicle and allow for control system design.
- A low level control system capable of following a prescribed flight path, with sufficient robustness to allow for model uncertainties and nonlinearities in a reliable manner.
- A guidance system to generate the reference flight path from a user defined mission description.
- An accurate navigation system capable of determining the 3 dimensional position of the UAV in real time with sufficient accuracy to achieve autonomous approach and landing capabilities.
- An Inertial Navigation System (INS) capable of determining the orientation of the vehicle relative to the ground.
- An “airdata” system capable of determining the flightspeed relative to the atmosphere.

1.4 Scope of this thesis:

Due to the diverse range of subjects involved in instrumentation and control of UAV’s, it has not been possible for the author to cover all these in this thesis. The author has concentrated on doing some of the basic “groundwork” necessary for actually designing and building an autonomous Micro Air Vehicle.

Chapter 2

Aerodynamic Model

2.1 Aeroplane aerodynamics

An aeroplane can be defined as a heavier then air vehicle that predominately uses aerodynamic forces to generate lift. In traditional fixed wing configurations, the aerodynamic lift is predominately generated by air flowing around dedicated lifting surfaces. Depending on the type of configuration, the lifting surfaces have names such as; wings, main wing (typically the largest wing on a vehicle), canard, horizontal tail and so on. It can be shown that in order to minimize the drag due to lift (so called induced drag) for a subsonic aeroplane, it is an advantage to have long wings (a large "wing span) (see (Ref. 8, chapter 4) for details). This typically leads to wings with a large span and small chord (the longitudinal dimension of the wing), as shown for the conceptual design below:

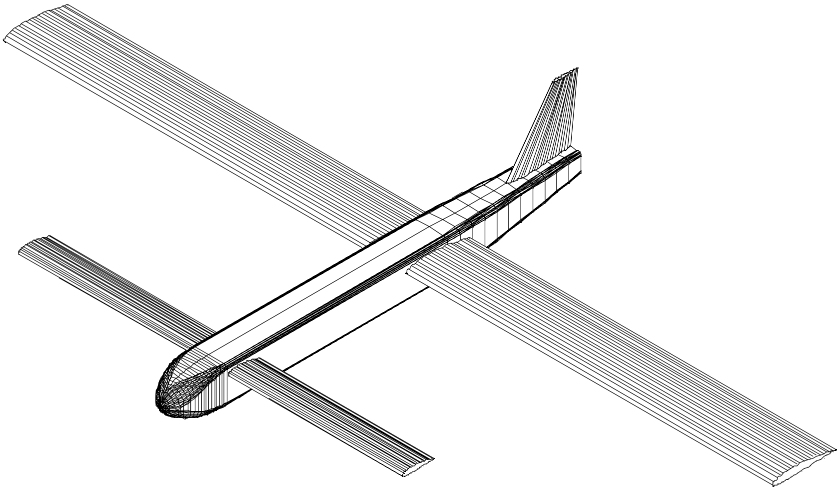

FIGURE 2.1 3D view of conceptual canard configuration UAV design

Since the wings have a much larger across stream then streamwise dimension (a large *aspect ratio*), the flow around the wings will be predominately two dimensional. It is difficult to give a comprehensive and at the same time simple explanation of the lift generation process. The airflow around a two dimensional wing is characterized by predominately frictionless (inviscid) flow which can be described by Laplace equation. However at the same time it can be shown that lift can only be generated if the so called "Kutta" condition is imposed at the trailing edge (the rear) of the airfoil (see (Ref. 3) section 9.3 for details). The Kutta condition basically states that real air cannot flow at infinite speeds around a sharp corner. This is due to the nonzero air viscosity. Combining the predominately inviscid flow with the Kutta condition at the trailing edge gives a flow that everywhere follows Laplace equation, except in the wake of the airfoil (the streamline that originates at the airfoil trailing edge).

It can then be shown that in subsonic two dimensional airfoil flow, lift is generated by two airfoil properties; “camber” and “angle of attack”. Camber is commonly seen as the airfoil geometry where the top of the wing is more curved then the bottom. However lift can just as well be generated by a symmetrical wing set at an *angle of attack* to the freestream. For a well designed airfoil at low angles of attack, the lift is proportional to both the airfoil camber and the airfoil angle of attack (see (Ref. 8, chapter 4) for details). The lift of any real airfoil or wing is limited by flow separation, which simply stated is the inability of the air to follow the contours of the top wing surface at large angles of attack. The resulting loss in lift is commonly called stall. As we shall see later, stall limits, among other things, the minimum flight speed of the aeroplane, which is of great significance in determining the minimum takeoff and landing distances.

2.2 6-DOF kinematic model

In order to treat longitudinal and lateral dynamics and kinematics in a unified approach, it is appropriate to introduce a 6 degree of freedom (6-DOF) model of UAV motion relative to the earth. To this end, we will use the following orthogonal cartesian coordinate systems:

- *Earth fixed* coordinate system with unit vectors $\mathbf{e}_{xe}$, $\mathbf{e}_{ye}$ and $\mathbf{e}_{ze}$: This coordinate system approximates the local geoid with a “flat earth” approximation. By convention $\mathbf{e}_{ze}$ points in the local vertical downwards direction, $\mathbf{e}_{xe}$ points in the local true north direction and $\mathbf{e}_{ye}$ points in the local east direction.
- *Vehicle* coordinate system with unit vectors $\mathbf{e}_{xv}$, $\mathbf{e}_{yv}$ and $\mathbf{e}_{zv}$: This coordinate system has the same orientation as the *Earth fixed* coordinate system, but moves with the vehicle (UAV) center of gravity (CG).
- *Body* fixed coordinate system with unit vectors $\mathbf{e}_{xb}$, $\mathbf{e}_{yb}$ and $\mathbf{e}_{zb}$: This coordinate system is fixed to the body of the UAV. By convention $\mathbf{e}_{xb}$ comprises the longitudinal axis of the UAV, pointing forward. $\mathbf{e}_{yb}$ points out through the right side of the vehicle, and $\mathbf{e}_{zb}$ points out through the bottom of the UAV.

All these coordinate systems are “right hand oriented”, i.e. they follow the “right hand convention”. This means that they can be made to coincide, purely by rotations and translations.

The relations between these three coordinate systems can be shown schematically below:

FIGURE 2.2 Coordinate system transformations

Where **P** is the coordinate of the CG of the UAV in earth coordinates and $\mathbf{M}_{vb}$ is the transformation matrix describing the rotations that brings the *vehicle* coordinate system into alignment with the *body* (fixed) coordinate system.

The following figure shows how the body coordinate system is fixed to the body UAV:

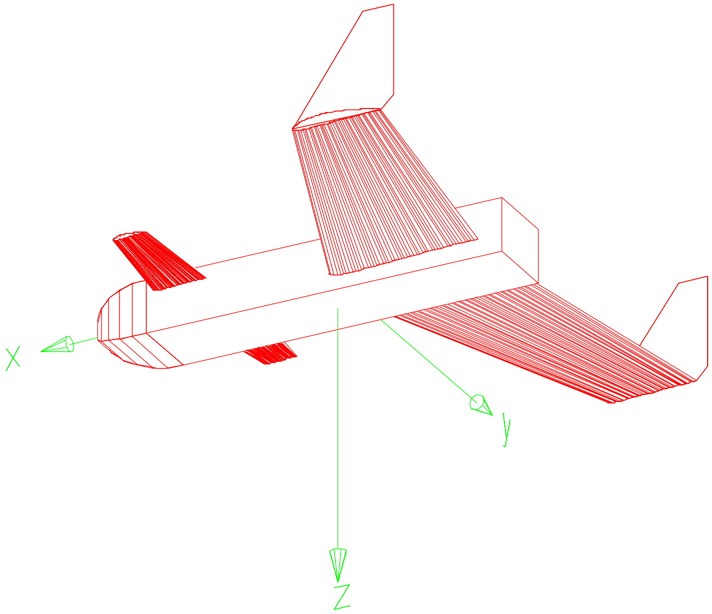

FIGURE 2.3 Body fixed coordinate system.

We will later return to the problem of how to determine the transformation matrix $\mathbf{M}_{vb}$ between vehicle and body coordinates.

2.3 Aerodynamic forces

When considering an aerodynamic model for a UAV, we must decide what purpose such a model must serve:

- The aerodynamic model of the UAV must enable the calculation of aerodynamic forces and moments on the UAV, with sufficient accuracy for design and simulation of open and closed loop response of the UAV in the design flight envelope of the UAV.
- The framework of the model must make it possible to examine robustness to modelling errors by identifying and varying stochastic parameters that have a large influence on the response and stability of the vehicle.
- In addition the aerodynamic model should be able to predict the quantitative behaviour of the UAV in all practical deviations from the design conditions. I.e. the model should predict if a certain abnormal flight condition converges towards or diverges from the “normal” flight envelope.

2.3.1 A framework for aerodynamic forces

As a first step in deciding the framework of the model, we can determine which aerodynamic variables that influence the aerodynamic forces and moments. These aerodynamic variables can be divided into the following categories:

1. The steady motion of the UAV through the atmosphere, in a straight flight path.
2. The curvature of the flight path relative to the atmosphere.
3. Rotation of the UAV relative to the flight path.
4. Unsteady motion of the atmosphere (gusts and turbulence).
5. Activation of control devices (elevator, ailerons, rudder, flaps, speed brake, etc.).
6. “Power” setting of propulsion system(s).

Before going into detail, a few assumptions about the aerodynamic forces are in order:

1. The aerodynamic forces do not depend on the orientation of the UAV relative to the earth.
2. Aside from control deflections, the UAV is symmetrical about the $(\mathbf{e}_{xb}, \mathbf{e}_{zb})$ plane.
3. The aerodynamic forces are deterministic functions of the motion of the UAV relative to the (moving) atmosphere and of the control deflections.

2.3.1.1 Steady motion of the nonrotating UAV relative to the stationary atmosphere

It is apparent that three independent variables are sufficient to describe this motion:

The airspeed U, the angle of attack α and the sideslip angle β.

Definition:

The $\mathbf{e}_{xb}$ vector (UAV longitudinal axis) can be made to point in the same direction as the airspeed vector $\mathbf{v}$, by the following rotations of the body fixed coordinate system:

1. A rotation of $-\beta$ around the $\mathbf{e}_{zb}$ vector.
2. A rotation of $-\alpha$ around the new $\mathbf{e}_y$ vector.

The airspeed U is the length of the airspeed vector $\mathbf{v}$.

The resulting coordinate system $\mathbf{e}_{xf}$, $\mathbf{e}_{yf}$, $\mathbf{e}_{zf}$ is denoted the *flight* path coordinate system.

The relation between the flight path coordinate system and the body coordinate system is shown below:

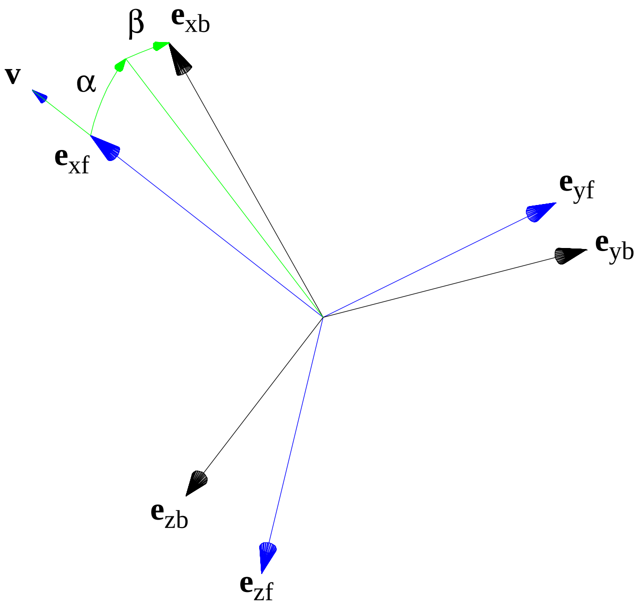

FIGURE 2.4 Flight path coordinate system.

2.3.1.2 Flight path curvature

The curvature of the flight path is by definition the partial derivative of the change in flight path direction, per unit distance travelled. We will represent the flight path curvature as two independent curvatures κ_a and κ_b. The longitudinal curvature κ_a will defined as the curvature of the flight path in the negative $\mathbf{e}_{zf}$ direction, while the lateral curvature κ_b will be defined as the curvature in the positive $\mathbf{e}_{yf}$ direction. This implies that κ_a has the same sense as α, and κ_b has the same sense as β.

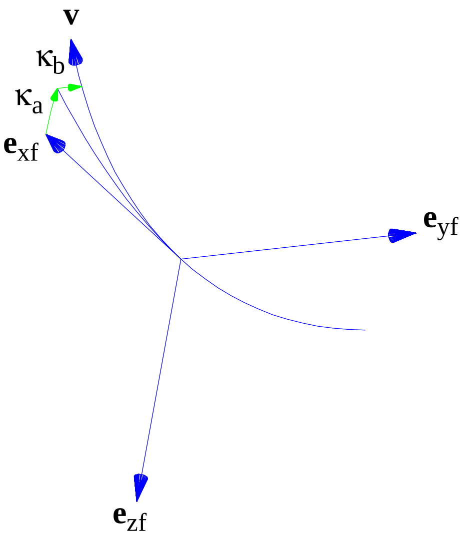

FIGURE 2.5 Flight path curvature.

With this definition of κ_a and κ_b, the curvatures may be computed as:

- κ_a is equal to the rate of rotation of the flight coordinate system around the $\mathbf{e}_{yf}$ axis, divided by the flight speed U.
- κ_b is equal to the rate of rotation of the flight coordinate system around the $\mathbf{e}_{zf}$ axis, divided by the flight speed U.

2.3.1.3 Rotation relative to the flight path

We have already introduced the angle of attack α and the sideslip angle β, as angles describing the stationary difference between the longitudinal axis of the body coordinate system and the velocity vector. In a dynamic sense, we must however also account for the aerodynamic forces due to rotation around the velocity vector. For this purpose we will introduce the *flight coordinate system* roll rate ω_{rf}.

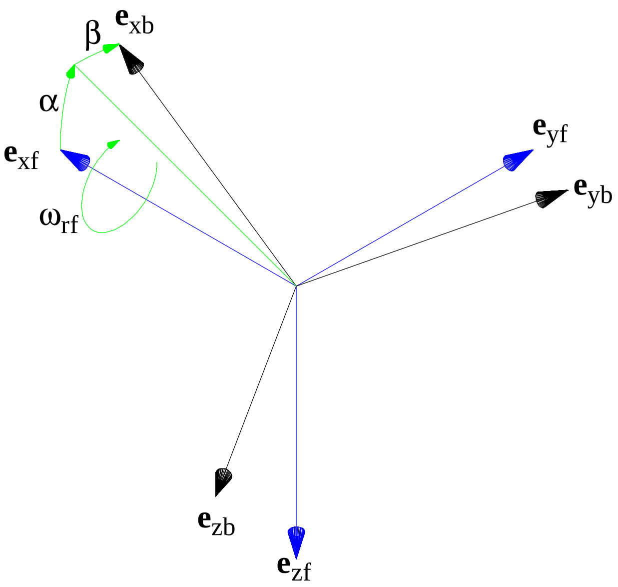

FIGURE 2.6 Rotation around the flight path.

Thus, we will characterize rotation relative to the flight path by $\dot{\alpha}(t)$, $\dot{\beta}(t)$ and ω_{rf}.

2.3.1.4 Atmospheric motion

In general the atmospheric motion consists of several phenomenon; steady wind, stochastic turbulence and gusts and wind shear. In reality these are often interrelated. For the purpose of calculating the aerodynamic forces due to these natural motions of the atmosphere, it is desirable to obtain a simple description with the following properties:

- Unified treatment of longitudinal and lateral response.
- Same method for stochastic and deterministic atmospheric motion.
- Quantitative correct treatment of some nonlinear gust related phenomenon (i.e. gust induced flow separation).

The first requirement, entails a 3 dimensional description. The second requirement can be fulfilled by considering the atmospheric motion *input* to the aerodynamic model, as a general temporal and spatial function. The third requirement implies that the total flow field due to aircraft and atmosphere motion, must be determined before calculating the total aerodynamic forces (instead of summing the forces from each contribution afterwards).

What is really desired is a description, that allows the three main “modes” of the aircraft to be excited by gusts: Pitch, yaw and roll. This can be ensured by the following atmospheric motion variables.

- Wind vector $\mathbf{w}_{gf}(s)$ at the vehicle CG, where the subscript “f” denotes flight coordinates and the parameter “s” is distance along the flight path.
- Wind roll rate $\omega_w(s)$ about the flight path direction.

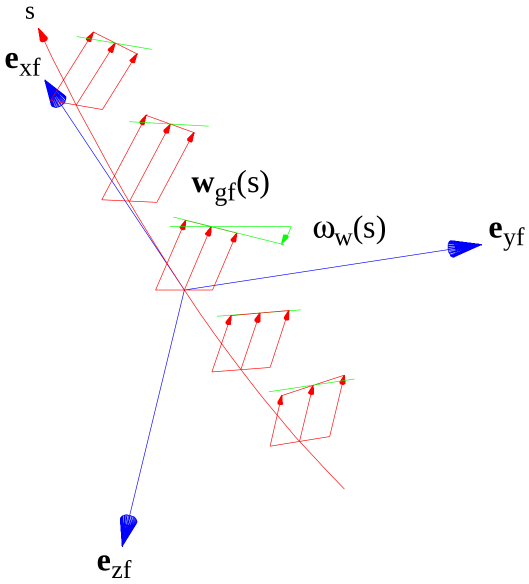

FIGURE 2.7 Atmospheric wind components.

This description implicitly assumes the “frozen gust assumption”. Where the time variation of the atmospheric wind is assumed negligible in the timespan the vehicle uses to travel through a gust. This simplifies calculation of the aerodynamic forces on the vehicle, because the individual components of the vehicle are influenced by the same gust delayed by a timespan, equal to the longitudinal position of the aerodynamic component, divided by the flightspeed of the vehicle.

2.3.1.5 Control surfaces

Control surfaces, are defined as any individually controllable variable geometry of the aeroplane, used to control the orientation and/or the trajectory of the vehicle. The control deflections are given by the control vector η_j:

- The aerodynamic forces due to control deflections, are assumed instantaneous so that the aerodynamic forces only depend on the instantaneous value of η_j.

In general, any modification of the aerodynamic shape of the vehicle will result in a new flow pattern around the entire aeroplane. Thus in principle, all aerodynamic coefficients should be re-evaluated for each possible control deflection and control deflection combinations. This is of course a practical impossibility, especially when considering multiple controls.

2.3.1.6 Propulsion system(s)

We will assume that the main propulsion system is one or more propellers, driven by an electric motor using onboard electric power stored in some sort of high performance rechargable battery system.

2.3.2 Force and moment systems

In general the dynamics of a rigid body can be determined from the force vector **F**(t) and torque vector **M**(t), acting through the CG of the body. For practical purposes it is appropriate to split the force and moment vectors into scalar components, referenced to an ortogonal cartesian coordinate system. This gives three force components and three torque components:

- F_x, F_y and F_z in the positive $\mathbf{e}_x$, $\mathbf{e}_y$ and $\mathbf{e}_z$ directions respectively.
- M_{xx}, M_{yy} and M_{zz} in the positive $\mathbf{e}_x$, $\mathbf{e}_y$ and $\mathbf{e}_z$ directions according to the “right hand” rule.

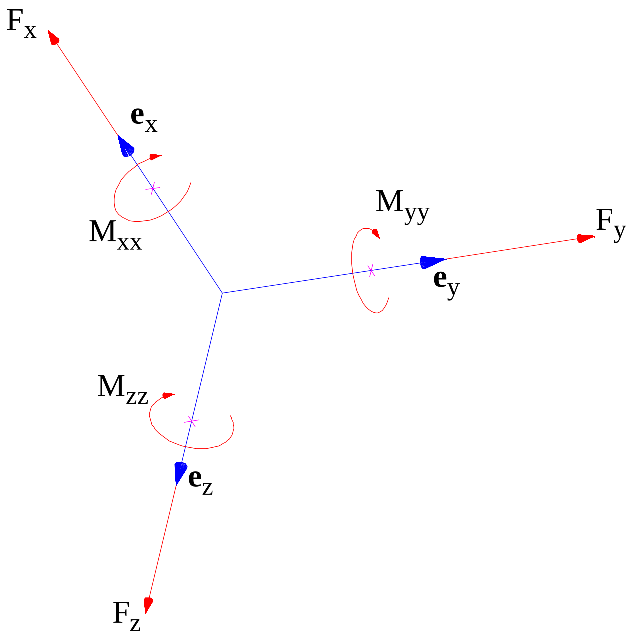

FIGURE 2.8 Force and moment components.

There is no clear cut “best” coordinate system for the forces and moments. In general different coordinate systems each have favourable properties:

- The *Earth fixed* coordinate system with unit vectors $\mathbf{e}_{xe}$, $\mathbf{e}_{ye}$ and $\mathbf{e}_{ze}$ is best suited for integrating the forces to obtain the trajectory (Newtons second law), assuming that the *Earth fixed* coordinate system is an inertial system.
- The *Body fixed* coordinate system with unit vectors $\mathbf{e}_{xb}$, $\mathbf{e}_{yb}$ and $\mathbf{e}_{zb}$ is best suited for integrating the moments to obtain the angular velocity relative to the Earth fixed coordinate system.
- The *Flight path* coordinate system $\mathbf{e}_{xf}$, $\mathbf{e}_{yf}$ and $\mathbf{e}_{zf}$ is best suited for determining the aerodynamic forces and moments.

It is possible to use all of the above coordinate systems in the same model, by applying the appropriate transformation matrices.

2.3.3 Aerodynamic coefficients

The atmosphere is composed of a mixture of gases, normally called “air”. The physical properties of air that are important from an aerodynamic point of view are:

- The density ρ; together with the airspeed determines the aerodynamic forces on a vehicle.
- The viscosity μ; determines the type of flow and skin friction.
- The speed of sound c; determines the effect of compressibility.

Without going into details, we can use the flight speed U_{TAS} and characteristic length “d” to obtain the following nondimensional parameters:

- The Reynolds number (Re): $Re_d \equiv \frac{\rho U_{TAS} d}{\mu}$
- The Mach number (M): $M \equiv \frac{U_{TAS}}{c}$

It can be shown experimentally that for Mach numbers less than 0.3, the effects of compressibility is negligible. If the Re is higher than approximately 10^5, the air flow will be mostly turbulent and most aerodynamic forces will be the result of inertial forces, rather then viscous forces. However the Re still plays a role in determining the flow field. Especially the onset of flow separation and stall is governed by the Re up to above Re = 10^7.

It can be shown through dimensional analysis that the effects of the air speed and density can be combined into a single parameter “q” called the *dynamic pressure*, that directly determines the aerodynamic forces:

$$q \equiv \frac{1}{2}\rho U_{TAS}^2 \tag{2.3.1}$$

Which is in fact the pressure, relative to the atmosphere at rest, measured by an open ended forward pointing tube, closed at the other end.

We are now ready to define the general form of the nondimensional aerodynamic coefficients used to determine the forces and moments on the vehicle:

Aerodynamic force:

$$F = qS_{ref}C \tag{2.3.2}$$

Aerodynamic moment:

$$M = qS_{ref}l_{ref}C \tag{2.3.3}$$

Where F and M represent an arbitrary force and moment, S_{ref} is a reference aerodynamic area (wing area, body crossection...), l_{ref} is a reference aerodynamic distance (wing chord) and C is a nondimensional aerodynamic coefficient.

In the following, it is implied that the aerodynamic coefficients are expressed in the *flight* coordinate system, if nothing else is mentioned.

The nondimensional coefficients for the *complete* UAV, are defined below:

Lift:

$$F_L \equiv qS_wC_L \tag{2.3.4}$$

Drag:

$$F_D \equiv qS_wC_D \tag{2.3.5}$$

Side force:

$$F_Y \equiv qS_wC_Y \tag{2.3.6}$$

Pitching moment:

$$M_{yy} \equiv qS_wc_wC_m \tag{2.3.7}$$

Rolling moment:

$$M_{xx} \equiv qS_wb_{wb}C_l \tag{2.3.8}$$

Yawing moment:

$$M_{zz} \equiv qS_wc_wC_n \tag{2.3.9}$$

Where S_w is the *exposed* main wing area, c_w is the mean chord of the main wing and b_{wb} is the total main wing-body span.

It is important to note that *capital letter* subscripts “L”, “D” and “Y”, relate to forces, while the subscripts “m”, “l” and “n” relate to aerodynamic moments (torques).

The reference point for the aerodynamic moments is the vehicle CG, unless otherwise noted.

While the aerodynamic moments, are directly related to the coordinate system axis as defined in Figure 2.8, the lift and drag forces are defined as:

$$F_L \equiv -F_{zf} \qquad F_D \equiv -F_{xf} \tag{2.3.10}$$

It is apparent that the lift and drag are directly related to the primary forces in the flight coordinate system.

2.3.4 Aerodynamic modelling assumptions

In Section 2.3, the following aerodynamic variables where defined:

- The angle of attack α and the sideslip angle β.
- The longitudinal curvature flight path κ_a and the lateral curvature κ_b.
- The derivatives of the angle of attack $\dot{\alpha}$ and of the sideslip angle $\dot{\beta}$.
- The roll rate ω_{rf}.
- The aerodynamic wind vector $\mathbf{w}_{gf}(s)$ and the wind roll rate $\omega_w(s)$.
- The control deflection vector δ_j.
- The propulsion system rotational speed N_p.

Neglecting wind, control surface deflections and the propulsion system, there are 7 independent variables describing the aerodynamic state. Even assuming linearity, the number of coefficients needed to describe the aerodynamics, would still be large. For this reason, some assumptions regarding the structure of the aerodynamic model are very useful.

Definition:

- The *longitudinal* aerodynamic system consists of the forces F_L and F_D and the pitching moment M_{yy}.
- The *lateral* aerodynamic system consists of the force F_Y and the moments M_{xx} and M_{zz}.

Assumptions:

1. The *longitudinal* aerodynamic forces and pitching moment only depend on the *longitudinal aerodynamic variables* α, $\dot{\alpha}$, κ_a, w_{gfx}, w_{gfz}, δ_{aj} and N_p.
2. The *lateral* aerodynamic force and moments only depend on *lateral aerodynamic variables* β, $\dot{\beta}$, κ_b, ω_{rf}, w_{gfy}, ω_w and δ_{bj}, and on the longitudinal angle of attack α.

Where δ_{aj} refers to longitudinal control surfaces and δ_{bj} refers to lateral control surfaces. Some control surfaces may belong to both types, in which case the same physical control surface is treated as one longitudinal *and* one lateral control surface.

The primary motivation for the above assumptions, is the geometrical assumption that the vehicle is symmetrical about the $(\mathbf{e}_{xb},\mathbf{e}_{zb})$ plane.

2.3.5 Longitudinal aerodynamic coefficients

A general but deterministic model of the longitudinal aerodynamic forces and moments for small dynamic disturbances can then be expressed in nondimensional form as:

Lift force:

$$C_L \cong C_L(\alpha, \delta_{aj}) + C_{L\dot{\alpha}}\frac{\dot{\alpha}c_w}{2U} + C_{L\kappa_a}\frac{\kappa_a c_w}{2} + C_{L\dot{w}_{gfz}}\frac{\dot{w}_{gfz}c_w}{2U^2} \tag{2.3.11}$$

It must be remembered that according to the definition of the flight path coordinate system, the static effects of the atmospheric wind modifies the orientation of the flight path coordinate system in such a way that the static effects of w_{gfz} are included in α. In the same way, the “static” effects of w_{gfx} are implicitly included in the model via the airspeed U. The direct effect of $\dot{w}_{gfx}$ upon the lift has been ignored since it is probably small compared to the “static” effect obtained through changes in U.

Drag force:

$$C_D \cong C_D(\alpha, \delta_{aj}) \tag{2.3.12}$$

All dynamic drag derivatives are ignored because rapid drag fluctuations usually only have a small influence on the flight dynamics.

Pitching moment:

$$C_m \cong C_m(\alpha, \delta_{aj}) + C_{m\dot{\alpha}}\frac{\dot{\alpha}c_w}{2U} + C_{m\kappa_a}\frac{\kappa_a c_w}{2} + C_{m\dot{w}_{gfz}}\frac{\dot{w}_{gfz}c_w}{2U^2} + C_{m\dot{U}}\frac{\dot{U}c_w}{2U^2} \tag{2.3.13}$$

2.3.6 A simple longitudinal aerodynamic model

There are many sources of information on determining the aerodynamic coefficients of a fixed wing flying vehicle. A complete aerodynamic discussion with (relatively) simple approximations for the aerodynamic coefficients can be found in (Ref. 1). The USAF Datcom (Ref. 4) is a comprehensive multiple volume collection of semiemperical and analytical methods for determining the aerodynamic coefficients of most fixed wing vehicles. The most significant aerodynamic coefficients are discussed in (Ref. 8), in a framework suitable for conceptual and preliminary aircraft design. This reference is highly recommended for getting a “feel” of aircraft design. The aerodynamic coefficients can at least in principle be determined using Computational Fluid Dynamics (CFD). Finally, wind tunnel tests can be used to determine at least the static aerodynamic coefficients. Since neither the CFD route nor a wind tunnel was available to the author of this thesis, it was necessary to use semiemperical and simple computational methods for this task. While the author acknowledges that the above references and numerous others are excellent in their one right, it was also felt that for the purpose of this thesis it was necessary to provide an aerodynamic model with special emphasis on:

- Dynamic stability and control aspects.

- Aerodynamic coefficients in flight path axes.
- Unified treatment of the dynamic effects of atmospheric wind gusts.
- Explicit treatment of aerodynamic model uncertainties and their effects on stability and control.
- Subsonic canard configurations.
- A self contained step by step derivation from simple aerodynamic concepts.

It is hoped that the following model will meet these objectives. It is however noted that readers with prior aerodynamic modelling experience can skip lightly through much of the following derivation, which may seem basic to specialists in the field.

Having introduced the longitudinal aerodynamic coefficients, the next step is to determine their numerical value for a particular airframe geometry. In this chapter we will determine the longitudinal aerodynamic coefficients for a canard type UAV using a very simple aerodynamic model. Using this model as a starting point we will later discuss the effects of uncertain aerodynamic forces on the dynamics and stability of the UAV.

For the simple model we will make the following six assumptions:

1. The longitudinal aerodynamics are entirely determined by the lift and drag forces on the wing and canard, plus the propeller thrust.
2. The lift is a linear function of the local angle of attack of the lifting surfaces.
3. The canard flap acts as a linear aerodynamic control.
4. No aerodynamic interference between the canard and wing.
5. The propeller efficiency is constant.
6. The airframe is a rigid body with rigid control surfaces.

The first step in deriving the model is to determine the local angle of attack of the canard and the wing. The local angle of attack will be defined as the effective angle of attack at the quarter chord “point” of the mean aerodynamic chord of a lifting surface, including the effects of dynamic motion of the UAV and dynamic wind effects.

The angle of attack α as used in Eq. 2.3.11 to Eq. 2.3.13 is the effective angle of attack of the UAV Center of Gravity (CG)[1]. The effect of UAV dynamic motion and dynamic wind effects will now be discussed.

As a first step, the effects of dynamic angle of attack changes ($\dot{\alpha}$) on the effective angle of attack of a lifting surface will be derived. A nonzero angle of attack rate, will induce

---

[1] More correctly but seldom used: Center of Mass (CM).

an extra effective angle of attack contribution which is a function of the distance between the lifting surface aerodynamic center and the CG of the UAV.

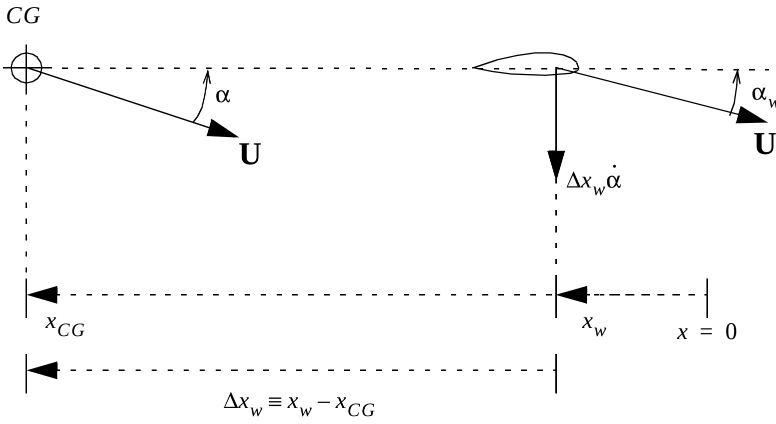

FIGURE 2.9 Effective angle of attack of lifting surface due to angle of attack rate.

Figure 2.9 shows the situation for a single lifting surface affected by angle of attack rate $\dot{\alpha}$. It is assumed that the angle of attack at the CG of the vehicle is denoted by α. Assuming a moderate angle of attack α gives the following expression for the derivative of the effective angle of attack with respect to the angle of attack rate:

$$\frac{\partial\alpha_w}{\partial\dot{\alpha}} = \frac{\Delta x_w}{U} \tag{2.3.14}$$

Next we will consider the effects of the flight path curvature alone, with the angle of attack α held constant.

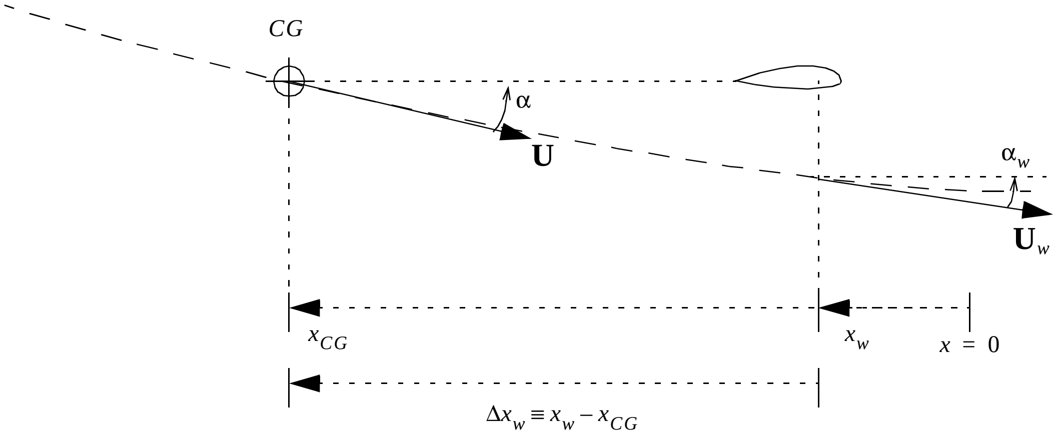

FIGURE 2.10 Effective angle of attack of lifting surface due to flight path curvature.

Since the flight path curvature is by definition the change in flight path angle per unit flight path distance, it follows that difference between the effective angle of attack at the lifting surface and at the CG is equal to Δx_w:

$$\frac{\partial \alpha_w}{\partial \kappa_a} = \Delta x_w \tag{2.3.15}$$

The final step is to determine the effects of the atmospheric wind. Since the flight coordinate system is defined according to the relative motion between the vehicle and the atmosphere, the effects of constant atmospheric wind is already included in the model using the equations above. In most real situations the wind is not steady but in fact quite turbulent due to weather and Atmospheric Boundary Layer (ABL) phenomenon. Thus it is necessary to ensure that a qualitatively correct treatment of atmospheric turbulence is included in the model. As a start we will look at the case where the vehicle flight path is straight relative to the earth and the attitude of the vehicle is constant relative to the earth.

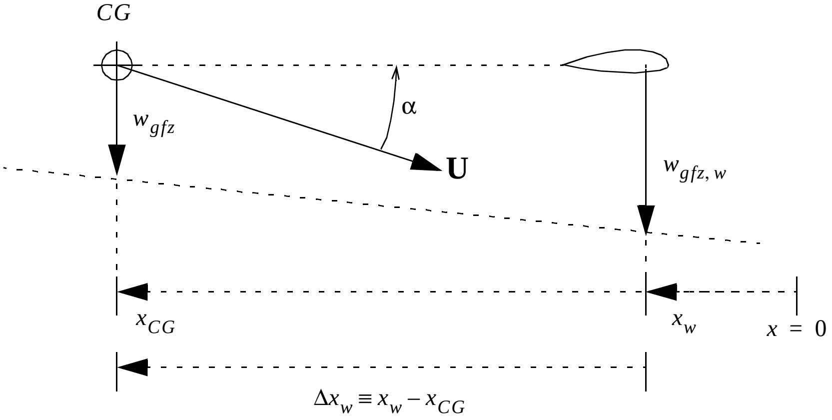

FIGURE 2.11 Effective angle of attack of lifting surface due to atmospheric turbulence.

From Figure 2.11 it follows that the angle of attack α will decrease for $\dot{w}_{gfz} > 0$ because the airspeed vector $\mathbf{U}$ will turn upwards into the resulting downwash:

$$\frac{\partial \dot{\alpha}}{\partial \dot{w}_{gfz}} = -\frac{1}{U} \tag{2.3.16}$$

The turning of the airspeed vector caused by $\dot{w}_{gfz} \neq 0$ will by definition also result in an apparent flight path curvature.

$$\frac{\partial \kappa_a}{\partial \dot{w}_{gfz}} = \frac{1}{U^2} \tag{2.3.17}$$

However we can deduce from Figure 2.11 that the net effect of $\dot{w}_{gfz} \neq 0$ should be:

$$\frac{d\alpha_w}{d\dot{w}_{gfz}} = \frac{\Delta x_w}{U^2} \tag{2.3.18}$$

The net effect of $\dot{w}_{gfz} \neq 0$ can also be expressed as the sum of the contributions due to each of the above effects:

$$\frac{d\alpha_w}{d\dot{w}_{gfz}} = \frac{\partial\alpha_w}{\partial\dot{\alpha}}\frac{\partial\dot{\alpha}}{\partial\dot{w}_{gfz}} + \frac{\partial\alpha_w}{\partial\kappa_a}\frac{\partial\kappa_a}{\partial\dot{w}_{gfz}} + \frac{\partial\alpha_w}{\partial\dot{w}_{gfz}} \tag{2.3.19}$$

We can now solve for the derivative $\partial\alpha_w/\partial\dot{w}_{gfz}$:

$$\frac{\partial\alpha_w}{\partial\dot{w}_{gfz}} = \frac{d\alpha_w}{d\dot{w}_{gfz}} - \frac{\partial\alpha_w}{\partial\dot{\alpha}}\frac{\partial\dot{\alpha}}{\partial\dot{w}_{gfz}} - \frac{\partial\alpha_w}{\partial\kappa_a}\frac{\partial\kappa_a}{\partial\dot{w}_{gfz}} = \frac{\Delta x_w}{U^2} - \frac{\partial\alpha_w}{\partial\dot{\alpha}}\left(-\frac{1}{U}\right) - \frac{\partial\alpha_w}{\partial\kappa_a}\left(\frac{1}{U^2}\right) \tag{2.3.20}$$

Using Eq. 2.3.14 and Eq. 2.3.15 gives an explicit expression for the derivative $\partial\alpha_w/\partial\dot{w}_{gfz}$:

$$\frac{\partial\alpha_w}{\partial\dot{w}_{gfz}} = \frac{\Delta x_w}{U^2} - \frac{\partial\alpha_w}{\partial\dot{\alpha}}\left(-\frac{1}{U}\right) - \frac{\partial\alpha_w}{\partial\kappa_a}\left(\frac{1}{U^2}\right) = \frac{\Delta x_w}{U^2} - \frac{\Delta x_w}{U}\left(-\frac{1}{U}\right) - (\Delta x_w)\left(\frac{1}{U^2}\right) = \frac{\Delta x_w}{U^2} \tag{2.3.21}$$

Comparing to Eq. 2.3.18 leads to the conclusion that the contributions from varying α and κ_a, due to $\dot{w}_{gfz}$, exactly cancels each other out.

We can now write the complete expression for the effective angle of attack at a lifting surface located $\Delta x_w \equiv x_w - x_{CG}$ behind the CG of the UAV:

$$\alpha_w = \alpha + \frac{\partial\alpha_w}{\partial\dot{\alpha}}\dot{\alpha} + \frac{\partial\alpha_w}{\partial\kappa_a}\kappa_a + \frac{\partial\alpha_w}{\partial\dot{w}_{gfz}}\dot{w}_{gfz} = \alpha + \frac{\Delta x_w}{U}\dot{\alpha} + \Delta x_w\kappa_a + \frac{\Delta x_w}{U^2}\dot{w}_{gfz} \tag{2.3.22}$$

Now that we have an expression for the effective angle of attack at a lifting surface, we need to obtain a relationship between the angle of attack of a lifting surface (wing) and its lift. According to the assumptions outlined in the beginning of this chapter, the aerodynamic model of the lift of a lifting surface should be linear in both angle of attack and control surface deflection. A model for the lift coefficient of the canard and wing satisfying these assumptions is given by:

Canard:

$$C_{Lw1} = C_{L\alpha 1}\left(\alpha_{w1} + i_{w1} - \left(\alpha_{0L1} + \frac{\partial\alpha_{0L1}}{\partial\delta_e}\delta_e\right)\right) \tag{2.3.23}$$

Wing:

$$C_{Lw2} = C_{L\alpha 2}(\alpha_{w2} + i_{w2} - \alpha_{0L2}) \tag{2.3.24}$$

Where $C_{L\alpha}$ is the wing (or canard) lift curve slope based on the wing (or canard) planform area, α_w is the effective angle of attack (as given by Eq. 2.3.22), i_w is the constant wing incidence angle, α_{0L} is the wing zero lift angle of attack and $\partial\alpha_{0L1}/\partial\delta_e$ is the derivative of α_{0L} with respect to the elevator control surface deflection δ_e.

For the moment being we will not discuss how $C_{L\alpha}$ is actually related to the wing or canard geometry. We will only mention that for an ideal wing with infinite aspect ratio (wingspan to wing chord ratio), the value of $C_{L\alpha}$ approaches the two dimensional ideal flow value of 2π. For real wings, the value of $C_{L\alpha}$ will be somewhat smaller then this.

Before we proceed we also need a model for the drag coefficient of the lifting surfaces. In general it can be assumed within a moderate Reynoulds number range, the drag coefficient of a 3 dimensional lifting surface is composed of a fixed part due to surface friction and flow separation and a variable part due to lift. One convenient model for lifting surfaces of large aspect ratio and moderate profile camber is discussed in (Ref. 8, p. 321):

$$C_{Dw} = C_{D0w} + K_w C_{Lw}^2 \tag{2.3.25}$$

Where C_{D0w} is the zero lift drag coefficient of the wing and $K_w C_{Lw}^2$ is the drag due to lift. The coefficient K_w is mainly determined by the planform of the wing.

This model will be used for both the canard and main wing, even though it neglects the direct effect of elevator deflection on the canard drag.

It is now possible to determine most of the aerodynamic coefficients defined by Eq. 2.3.11 to Eq. 2.3.13. First we need to look at the general geometry of a vehicle with canard platform:

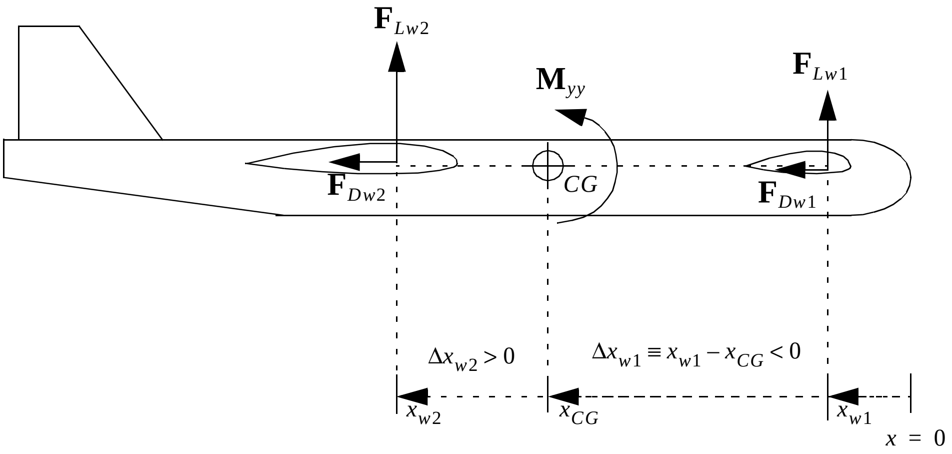

FIGURE 2.12 Longitudinal UAV aerodynamic forces and resulting pitching moment.

Figure 2.12 shows the UAV aerodynamic forces on the canard and wings. In addition the net aerodynamic pitching moment $\mathbf{M}_{yy}$ around the CG is shown. Note that $\mathbf{M}_{yy}$ is not a separate moment, but rather the net moment from all other aerodynamic forces and moments. It is assumed that the angle of attack is so small that the lift acts perpendicular to the vehicle centerline and the drag acts parallel to the centerline. The difference in “vertical” spacing between the wing, canard and CG is also neglected in the following analysis.

From the definition of the lift coefficient, we are able to write the following expressions for the lift on the canard and wings:

$$F_{Lw1} = qC_{Lw1}S_{w1} \qquad F_{Lw2} = qC_{Lw2}S_{w2} \tag{2.3.26}$$

The total lift can be expressed as:

$$F_L = qC_LS_w = qC_LS_{w2} \tag{2.3.27}$$

Notice that we have defined the UAV vehicle reference area as the planform area of the main wing, which is wing #2 for a canard configuration.

Combining Eq. 2.3.26 and Eq. 2.3.27 gives an expression for the UAV lift coefficient:

$$C_L = \frac{S_{w1}}{S_w}C_{Lw1} + C_{Lw2} \qquad (2.3.28)$$

Using the wing and canard lift models given by Eq. 2.3.23 and Eq. 2.3.24 gives an explicit expression for the UAV lift coefficient as a function of the effective angles of attack:

$$C_L = \frac{S_{w1}}{S_w}C_{L\alpha 1}\left(\alpha_{w1} + i_{w1} - \left(\alpha_{0L1} + \frac{\partial\alpha_{0L1}}{\partial\delta_e}\delta_e\right)\right) + C_{L\alpha 2}(\alpha_{w2} + i_{w2} - \alpha_{0L2}) \qquad (2.3.29)$$

Since $\alpha_{w1} = \alpha_{w2} = \alpha$ in the “static” case, we are now able to determine an explicit expression for $C_L(\alpha, \delta_{aj})$ in Eq. 2.3.11:

$$C_L(\alpha, \delta_{aj}) = \frac{S_{w1}}{S_w}C_{L\alpha 1}\left(\alpha + i_{w1} - \left(\alpha_{0L1} + \frac{\partial\alpha_{0L1}}{\partial\delta_e}\delta_e\right)\right) + C_{L\alpha 2}(\alpha + i_{w2} - \alpha_{0L2}) \qquad (2.3.30)$$

Similarly the derivative $C_{L\dot{\alpha}}$ can be determined as:

$$\frac{\partial C_L}{\partial\dot{\alpha}} = \frac{S_{w1}}{S_w}C_{L\alpha 1}\frac{\partial\alpha_{w1}}{\partial\dot{\alpha}} + C_{L\alpha 2}\frac{\partial\alpha_{w2}}{\partial\dot{\alpha}} = \frac{S_{w1}}{S_w}C_{L\alpha 1}\frac{\Delta x_{w1}}{U} + C_{L\alpha 2}\frac{\Delta x_{w2}}{U} \qquad (2.3.31)$$

According to Eq. 2.3.11, we can write $\frac{\partial C_L}{\partial\dot{\alpha}} = C_{L\dot{\alpha}}\frac{c_w}{2U}$, thus giving:

$$C_{L\dot{\alpha}} = \frac{2U}{c_w}\frac{\partial C_L}{\partial\dot{\alpha}} = 2\left(\frac{S_{w1}}{S_w}C_{L\alpha 1}\frac{\Delta x_{w1}}{c_w} + C_{L\alpha 2}\frac{\Delta x_{w2}}{c_w}\right) \qquad (2.3.32)$$

The derivative $C_{L\kappa_a}$ is determined as:

$$\frac{\partial C_L}{\partial\kappa_a} = \frac{S_{w1}}{S_w}C_{L\alpha 1}\frac{\partial\alpha_{w1}}{\partial\kappa_a} + C_{L\alpha 2}\frac{\partial\alpha_{w2}}{\partial\kappa_a} = \frac{S_{w1}}{S_w}C_{L\alpha 1}\Delta x_{w1} + C_{L\alpha 2}\Delta x_{w2} \qquad (2.3.33)$$

According to Eq. 2.3.11, we can write $\frac{\partial C_L}{\partial\kappa_a} = C_{L\kappa_a}\frac{c_w}{2}$, thus giving:

$$C_{L\kappa_a} = \frac{2}{c_w}\frac{\partial C_L}{\partial\kappa_a} = 2\left(\frac{S_{w1}}{S_w}C_{L\alpha 1}\frac{\Delta x_{w1}}{c_w} + C_{L\alpha 2}\frac{\Delta x_{w2}}{c_w}\right) \qquad (2.3.34)$$

Notice that for this simple aerodynamic model we have $C_{L\kappa_a} = C_{L\dot{\alpha}}$.

The derivative $C_{L\dot{w}_{gfz}}$ is determined as:

$$\frac{\partial C_L}{\partial\dot{w}_{gfz}} = \frac{S_{w1}}{S_w}C_{L\alpha 1}\frac{\partial\alpha_{w1}}{\partial\dot{w}_{gfz}} + C_{L\alpha 2}\frac{\partial\alpha_{w2}}{\partial\dot{w}_{gfz}} = \frac{S_{w1}}{S_w}C_{L\alpha 1}\frac{\Delta x_{w1}}{U^2} + C_{L\alpha 2}\frac{\Delta x_{w2}}{U^2} \qquad (2.3.35)$$

According to Eq. 2.3.11, we can write $\frac{\partial C_L}{\partial\dot{w}_{gfz}} = C_{L\dot{w}_{gfz}}\frac{c_w}{2U^2}$, thus giving:

$$C_{L\dot{w}_{gfz}} = \frac{2U^2}{c_w}\frac{\partial C_L}{\partial\dot{w}_{gfz}} = 2\left(\frac{S_{w1}}{S_w}C_{L\alpha 1}\frac{\Delta x_{w1}}{c_w} + C_{L\alpha 2}\frac{\Delta x_{w2}}{c_w}\right) \qquad (2.3.36)$$

Here again we have that $C_{L\dot{w}_{gfz}} = C_{L\dot{\alpha}}$ for this aerodynamic model.

The drag coefficient as expressed by Eq. 2.3.12 is readily determined as:

$$C_D \cong C_D(\alpha, \delta_{aj}) = \frac{S_{w1}}{S_w}(C_{D0w1} + K_{w1}C_{Lw1}^2) + (C_{D0w2} + K_{w2}C_{Lw2}^2) \qquad (2.3.37)$$

Expressed as functions of the wing and canard lift coefficients.

Using Figure 2.12 we can determine the net aerodynamic pitching moment around the CG as (pitch up positive):

$$M_{yy} = -(\Delta x_{w1}F_{Lw1} + \Delta x_{w2}F_{Lw2}) \qquad (2.3.38)$$

Like above we have neglected the influence of the drag forces and assumed that the lift forces are close to ortogonal with the vehicle longitudinal axis. Notice that in most cases the two terms in Eq. 2.3.38 are of opposite sign.

In analogy with the treatment of the total vehicle lift, we can nondimensionalize Eq. 2.3.38 as:

$$C_m = -\left(\frac{S_{w1}}{S_w}\frac{\Delta x_{w1}}{c_w}C_{Lw1} + \frac{\Delta x_{w2}}{c_w}C_{Lw2}\right) \qquad (2.3.39)$$

By using the wing and canard lift models given by Eq. 2.3.23 and Eq. 2.3.24, an explicit expression for the UAV pitching moment coefficient as a function of the effective angles of attack can be determined:

$$C_m = -\left(\frac{S_{w1}}{S_w}\frac{\Delta x_{w1}}{c_w}C_{L\alpha 1}\left(\alpha_{w1} + i_{w1} - \left(\alpha_{0L1} + \frac{\partial \alpha_{0L1}}{\partial \delta_e}\delta_e\right)\right) + \frac{\Delta x_{w2}}{c_w}C_{L\alpha 2}(\alpha_{w2} + i_{w2} - \alpha_{0L2})\right) \qquad (2.3.40)$$

Using the static case $\alpha_{w1} = \alpha_{w2} = \alpha$, gives an expression for the term $C_m(\alpha, \delta_{aj})$ in Eq. 2.3.13:

$$C_m(\alpha, \delta_{aj}) = -\left(\frac{S_{w1}}{S_w}\frac{\Delta x_{w1}}{c_w}C_{L\alpha 1}\left(\alpha + i_{w1} - \left(\alpha_{0L1} + \frac{\partial \alpha_{0L1}}{\partial \delta_e}\delta_e\right)\right) + \frac{\Delta x_{w2}}{c_w}C_{L\alpha 2}(\alpha + i_{w2} - \alpha_{0L2})\right) \qquad (2.3.41)$$

The derivative $C_{m\dot{\alpha}}$ can be determined using Eq. 2.3.22:

$$\frac{\partial C_m}{\partial \dot{\alpha}} = -\left(\frac{S_{w1}}{S_w}\frac{\Delta x_{w1}}{c_w}C_{L\alpha 1}\frac{\partial \alpha_{w1}}{\partial \dot{\alpha}} + \frac{\Delta x_{w2}}{c_w}C_{L\alpha 2}\frac{\partial \alpha_{w2}}{\partial \dot{\alpha}}\right) = -\left(\frac{S_{w1}}{S_w}\frac{\Delta x_{w1}}{c_w}C_{L\alpha 1}\frac{\Delta x_{w1}}{U} + \frac{\Delta x_{w2}}{c_w}C_{L\alpha 2}\frac{\Delta x_{w2}}{U}\right) \qquad (2.3.42)$$

From Eq. 2.3.13 we have that $\frac{\partial C_m}{\partial \dot{\alpha}} = C_{m\dot{\alpha}}\frac{c_w}{2U}$, thus giving:

$$C_{m\dot{\alpha}} = -\frac{2U}{c_w}\left(\frac{S_{w1}}{S_w}\frac{(\Delta x_{w1})^2}{c_w U}C_{L\alpha 1} + \frac{(\Delta x_{w2})^2}{c_w U}C_{L\alpha 2}\right) = -2\left(\frac{S_{w1}}{S_w}\left(\frac{\Delta x_{w1}}{c_w}\right)^2 C_{L\alpha 1} + \left(\frac{\Delta x_{w2}}{c_w}\right)^2 C_{L\alpha 2}\right) \qquad (2.3.43)$$

As we shall see later this derivative is very important for pitch damping.

The derivative $C_{m\kappa_a}$ is determined in a similar fashion:

$$\frac{\partial C_m}{\partial \kappa_a} = -\left(\frac{S_{w1}}{S_w}\frac{\Delta x_{w1}}{c_w}C_{L\alpha 1}\frac{\partial \alpha_{w1}}{\partial \kappa_a} + \frac{\Delta x_{w2}}{c_w}C_{L\alpha 2}\frac{\partial \alpha_{w2}}{\partial \kappa_a}\right) = -\left(\frac{S_{w1}}{S_w}\frac{\Delta x_{w1}}{c_w}C_{L\alpha 1}\Delta x_{w1} + \frac{\Delta x_{w2}}{c_w}C_{L\alpha 2}\Delta x_{w2}\right) \qquad (2.3.44)$$

According to Eq. 2.3.13, we can write $\frac{\partial C_m}{\partial \kappa_a} = C_{m\kappa_a}\frac{c_w}{2}$, thus giving:

$$C_{m\kappa_a} = \frac{2}{c_w}\frac{\partial C_m}{\partial \kappa_a} = -2\left(\frac{S_{w1}}{S_w}\left(\frac{\Delta x_{w1}}{c_w}\right)^2 C_{L\alpha 1} + \left(\frac{\Delta x_{w2}}{c_w}\right)^2 C_{L\alpha 2}\right) \tag{2.3.45}$$

Which is the same as $C_{m\dot{\alpha}}$ for this aerodynamic model.

The derivative $C_{m\dot{w}_{gfz}}$ is determined in a similar fashion:

$$\frac{\partial C_m}{\partial \dot{w}_{gfz}} = -\left(\frac{S_{w1}}{S_w}\frac{\Delta x_{w1}}{c_w}C_{L\alpha 1}\frac{\partial \alpha_{w1}}{\partial \dot{w}_{gfz}} + \frac{\Delta x_{w2}}{c_w}C_{L\alpha 2}\frac{\partial \alpha_{w2}}{\partial \dot{w}_{gfz}}\right) = -\left(\frac{S_{w1}}{S_w}\frac{\Delta x_{w1}}{c_w}C_{L\alpha 1}\frac{\Delta x_{w1}}{U^2} + \frac{\Delta x_{w2}}{c_w}C_{L\alpha 2}\frac{\Delta x_{w2}}{U^2}\right) \tag{2.3.46}$$

According to Eq. 2.3.13, we can write $\frac{\partial C_m}{\partial \dot{w}_{gfz}} = C_{m\dot{w}_{gfz}}\frac{c_w}{2U^2}$, thus giving:

$$C_{m\dot{w}_{gfz}} = \frac{2U^2}{c_w}\frac{\partial C_m}{\partial \dot{w}_{gfz}} = -2\left(\frac{S_{w1}}{S_w}\left(\frac{\Delta x_{w1}}{c_w}\right)^2 C_{L\alpha 1} + \left(\frac{\Delta x_{w2}}{c_w}\right)^2 C_{L\alpha 2}\right) \tag{2.3.47}$$

Again we get the same result as $C_{m\dot{\alpha}}$.

The derivative $C_{m\dot{U}}$ is determined by taking into account the differences in dynamic pressure due to differences in the axial wind component along the flight path:

$$\frac{\partial C_m}{\partial \dot{U}} = -\left(\frac{S_{w1}}{S_w}\frac{\Delta x_{w1}}{c_w}C_{Lw1}\frac{\left(\frac{\partial q_{w1}}{\partial \dot{U}}\right)}{q} + \frac{\Delta x_{w2}}{c_w}C_{Lw2}\frac{\left(\frac{\partial q_{w2}}{\partial \dot{U}}\right)}{q}\right) \tag{2.3.48}$$

In order to determine the derivatives $\partial q_w / \partial \dot{U}$ for the canard and wing, we can first look at the definition of the dynamic pressure q:

$$q \equiv \frac{1}{2}\rho U^2 \quad \Rightarrow \quad \frac{\partial q}{\partial U} = \rho U \tag{2.3.49}$$

The next step is to determine the relationship between the local airspeed at the lifting surface and the airspeed derivative at the vehicle CG. For constant airspeed derivative we obtain:

$$U_w \cong U + \Delta x_w\frac{\partial U}{\partial x} = U + \Delta x_w\dot{U}\frac{\partial t}{\partial x} = U - \Delta x_w\frac{\dot{U}}{U} \quad \Rightarrow \quad \frac{\partial U_w}{\partial \dot{U}} = -\frac{\Delta x_w}{U} \tag{2.3.50}$$

The chain rule is then used to obtain the desired derivative:

$$\frac{\partial q_w}{\partial \dot{U}} = \frac{\partial q_w}{\partial U_w}\frac{\partial U_w}{\partial \dot{U}} = \rho U\left(-\frac{\Delta x_w}{U}\right) = -\rho\Delta x_w \tag{2.3.51}$$

We can now proceed with Eq. 2.3.48:

$$\frac{\partial C_m}{\partial \dot{U}} = -\left(\frac{S_{w1}}{S_w}\frac{\Delta x_{w1}}{c_w}C_{Lw1}\frac{\left(\frac{\partial q_{w1}}{\partial \dot{U}}\right)}{q} + \frac{\Delta x_{w2}}{c_w}C_{Lw2}\frac{\left(\frac{\partial q_{w2}}{\partial \dot{U}}\right)}{q}\right) = \frac{S_{w1}}{S_w}\frac{\Delta x_{w1}}{c_w}C_{Lw1}\left(\frac{\rho\Delta x_{w1}}{q}\right) + \frac{\Delta x_{w2}}{c_w}C_{Lw2}\left(\frac{\rho\Delta x_{w2}}{q}\right)$$

(2.3.52)

According to Eq. 2.3.13, we can write $\frac{\partial C_m}{\partial \dot{U}} = C_{m\dot{U}}\frac{c_w}{2U^2}$, thus giving:

$$C_{m\dot{U}} = \frac{2U^2}{c_w}\frac{\partial C_m}{\partial \dot{U}} = 4\left(\frac{S_{w1}}{S_w}\left(\frac{\Delta x_{w1}}{c_w}\right)^2 C_{Lw1} + \left(\frac{\Delta x_{w2}}{c_w}\right)^2 C_{Lw2}\right) \tag{2.3.53}$$

Notice that $C_{m\dot{U}}$ is a function of the lift coefficients C_{Lw1} and C_{Lw2}, this means that even though the aerodynamic model of the lift is linear, this derivative is not constant.

In summary we have the following linear aerodynamic model of the vehicle:

Static lift:

$$C_L(\alpha, \delta_{aj}) = \frac{S_{w1}}{S_w}C_{L\alpha1}\left(\alpha + i_{w1} - \left(\alpha_{0L1} + \frac{\partial\alpha_{0L1}}{\partial\delta_e}\delta_e\right)\right) + C_{L\alpha2}(\alpha + i_{w2} - \alpha_{0L2})$$

$$C_L(\alpha, \delta_{aj}) = C_{L\alpha}\left(\alpha + \frac{\partial\alpha_{0L}}{\partial\delta_e}\delta_e - \alpha_{0L}\right)$$

$$C_{L\alpha} = \frac{S_{w1}}{S_w}C_{L\alpha1} + C_{L\alpha2} \qquad \frac{\partial\alpha_{0L}}{\partial\delta_e} = \frac{S_{w1}C_{L\alpha1}}{S_wC_{L\alpha}}\frac{\partial\alpha_{0L1}}{\partial\delta_e} \qquad \alpha_{0L} = \frac{S_{w1}C_{L\alpha1}}{S_wC_{L\alpha}}(\alpha_{0L1} - i_{w1}) + \frac{C_{L\alpha2}}{C_{L\alpha}}(\alpha_{0L2} - i_{w2})$$

(2.3.54)

Dynamic lift:

$$C_{L\dot{\alpha}} = C_{L\kappa_a} = C_{L\dot{w}_{gfz}} = 2\left(\frac{S_{w1}}{S_w}C_{L\alpha1}\frac{\Delta x_{w1}}{c_w} + C_{L\alpha2}\frac{\Delta x_{w2}}{c_w}\right) \tag{2.3.55}$$

Drag:

$$C_D \cong C_D(\alpha, \delta_{aj}) = \frac{S_{w1}}{S_w}(C_{D0w1} + K_{w1}C_{Lw1}^2) + (C_{D0w2} + K_{w2}C_{Lw2}^2) \tag{2.3.56}$$

Static pitching moment:

$$C_m(\alpha, \delta_{aj}) = -\left(\frac{S_{w1}}{S_w}\frac{\Delta x_{w1}}{c_w}C_{L\alpha1}\left(\alpha + i_{w1} - \left(\alpha_{0L1} + \frac{\partial\alpha_{0L1}}{\partial\delta_e}\delta_e\right)\right) + \frac{\Delta x_{w2}}{c_w}C_{L\alpha2}(\alpha + i_{w2} - \alpha_{0L2})\right)$$

$$C_m(\alpha, \delta_{aj}) = C_{m\alpha}\alpha + C_{m\delta_e}\delta_e + C_{m0}$$

$$C_{m\alpha} = -\left(\frac{S_{w1}}{S_w}\frac{\Delta x_{w1}}{c_w}C_{L\alpha1} + \frac{\Delta x_{w2}}{c_w}C_{L\alpha2}\right) \qquad C_{m\delta_e} = \frac{S_{w1}}{S_w}\frac{\Delta x_{w1}}{c_w}C_{L\alpha1}\frac{\partial\alpha_{0L1}}{\partial\delta_e} \tag{2.3.57}$$

$$C_{m0} = \frac{S_{w1}}{S_w}\frac{\Delta x_{w1}}{c_w}C_{L\alpha1}(\alpha_{0L1} - i_{w1}) + \frac{\Delta x_{w2}}{c_w}C_{L\alpha2}(\alpha_{0L2} - i_{w2})$$

Dynamic pitching moment:

$$C_{m\dot{\alpha}} = C_{m\kappa_a} = C_{m\dot{w}_{gfz}} = -2\left(\frac{S_{w1}}{S_w}\left(\frac{\Delta x_{w1}}{c_w}\right)^2 C_{L\alpha1} + \left(\frac{\Delta x_{w2}}{c_w}\right)^2 C_{L\alpha2}\right) \tag{2.3.58}$$

Dynamic pitching moment (axial wind derivative):

$$C_{m\dot{U}} = \frac{2U^2}{c_w}\frac{\partial C_m}{\partial \dot{U}} = 4\left(\frac{S_{w1}}{S_w}\left(\frac{\Delta x_{w1}}{c_w}\right)^2 C_{Lw1} + \left(\frac{\Delta x_{w2}}{c_w}\right)^2 C_{Lw2}\right) \tag{2.3.59}$$

In addition to the aerodynamic forces on the airframe, a propulsive force is also required to maintain normal flight. For the moment we will assume that the propulsive force is supplied by a propeller driven by a suitable DC electric motor through appropriate gears. We can define the propulsive efficiency η_p of a propeller as:

$$\eta_p \equiv \frac{F_{th}U}{W_p} \tag{2.3.60}$$

Where F_{th} is the propeller thrust and W_p is the mechanical power applied to the propeller shaft (by the motor).

2.3.7 Approximate dynamic analysis

An approximate dynamic analysis of the vehicle motion can be used to get an idea of the vehicle dynamics caused by the aerodynamic forces on the lifting surfaces. For this analysis we will use a longitudinal kinematic system described by three degrees of freedom, the vehicle body pitch angle θ_e (elevation angle), the flight path angle γ_e and the airspeed U. The definitions of the angles are shown below for the special case of zero windspeed:

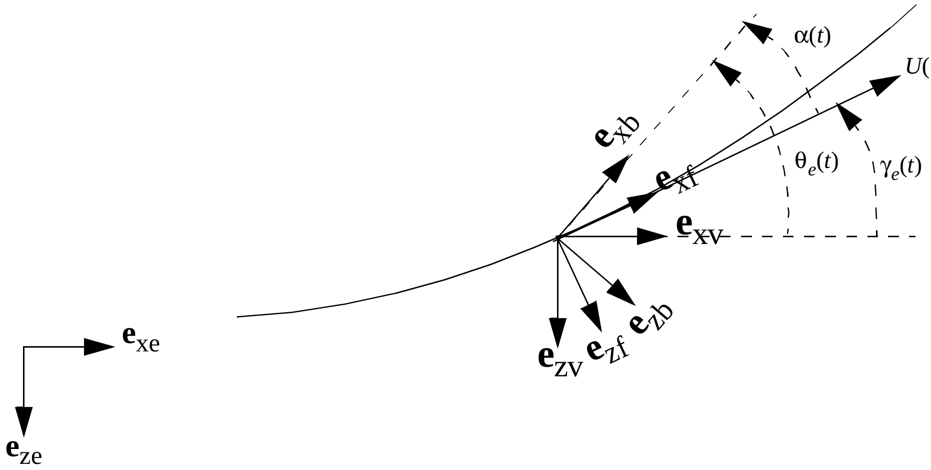

FIGURE 2.13 Longitudinal UAV kinematics.

To simplify this analysis we will postulate that under certain conditions the open loop longitudinal motion is dominated by two distinct modes. The *short period* mode and the *phugoid* mode.

2.3.7.1 Short period mode

The short period mode is determined by assuming that the vehicle velocity vector is constant (speed and direction) while the vehicle pitch attitude is perturbed from equilibrium. In order to describe this motion we need only one degree of freedom; the vehicle body pitch angle (elevation angle) θ_e.

Since θ_e is fixed to the body, the rigid body dynamic equations of motion for the vehicle is given symbolically by (Ref. 21, page 7-10):

$$J_{yy}\ddot{\theta}_e = M_{yy} \tag{2.3.61}$$

Where M_{yy} is the aerodynamic pitching moment (positive pitch up) referenced to the CG of the vehicle.

Using the aerodynamic model above, the aerodynamic pitching moment for a straight flight path is given by:

$$M_{yy} = qS_w c_w C_m = qS_w c_w \left(C_{m\alpha}\alpha + C_{m\delta_e}\delta_e + C_{m0} + C_{m\dot{\alpha}}\frac{\dot{\alpha} c_w}{2U} \right) \tag{2.3.62}$$

From Figure 2.13 we have the following expression for the angle of attack:

$$\alpha(t) = \theta_e(t) - \gamma_e(t) \tag{2.3.63}$$

Using the above relationships it is possible to obtain a second order differential equation describing the short period mode:

$$J_{yy}\ddot{\theta}_e = \left(\frac{1}{2}\rho U^2\right) S_w c_w \left(C_{m\alpha}(\theta_e - \gamma_e) + C_{m\delta_e}\delta_e + C_{m0} + C_{m\dot{\alpha}}\frac{\dot{\theta}_e c_w}{2U} \right) \tag{2.3.64}$$

Since we have assumed that γ_e is constant for the short period mode, the homogenous part of the short period differential equation is given by:

$$\begin{gathered} J_{yy}\ddot{\theta}_e = \left(\frac{1}{2}\rho U^2\right) S_w c_w \left(C_{m\alpha}\theta_e + C_{m\dot{\alpha}}\frac{\dot{\theta}_e c_w}{2U} \right) = \frac{1}{2}\rho S_w c_w \left(C_{m\alpha} U^2 \theta_e + C_{m\dot{\alpha}} U \frac{\dot{\theta}_e c_w}{2} \right) \\ \ddot{\theta}_e - \frac{\rho S_w c_w^2 C_{m\dot{\alpha}} U}{4 J_{yy}}\dot{\theta}_e - \frac{\rho S_w c_w C_{m\alpha} U^2}{2 J_{yy}}\theta_e = 0 \end{gathered} \tag{2.3.65}$$

From this it is immediately apparent that the *pitch stiffness* k_{yy} is given by:

$$k_{yy} = -\frac{1}{2}\rho S_w c_w C_{m\alpha} U^2 \tag{2.3.66}$$

The solution thus depends critically on the sign of k_{yy}. If the pitch stiffness is negative, the short period mode is unstable. This is in general unsatisfactory for most flying vehicles because it usually demands a very fast active control system to maintain closed loop stability.

For the moment we will assume that the pitch stiffness is positive, this is usually called positive “static (pitch) stability” in aeronautical terms. Since $\frac{1}{2}\rho S_w c_w U^2$ is always positive it follows that static stability is the same as $C_{m\alpha} < 0$!.

The characteristic equation of the ODE given by Eq. 2.3.65 can be determined as:

$$s^2 - \frac{\rho S_w c_w^2 C_{m\dot{\alpha}} U}{4 J_{yy}} s - \frac{\rho S_w c_w C_{m\alpha} U^2}{2 J_{yy}} = 0 \tag{2.3.67}$$

Where s is the Laplace operator.

The undamped natural frequency and damping ratio can immediately be determined as (Ref. 9, chapter 4-4):

$$\omega_{n,yy} = \sqrt{\frac{k_{yy}}{J_{yy}}} = \sqrt{\frac{\rho S_w c_w (-C_{m\alpha}) U^2}{2 J_{yy}}} = \sqrt{\frac{S_w c_w (-C_{m\alpha}) q}{J_{yy}}} \qquad C_{m\alpha} \le 0 \tag{2.3.68}$$

$$\zeta_{yy} = \frac{1}{2\omega_{n,yy}} \left(\frac{\rho S_w c_w^2 (-C_{m\dot{\alpha}}) U}{4 J_{yy}} \right) = \sqrt{\frac{J_{yy}}{4 S_w c_w (-C_{m\alpha}) q} \frac{\rho^2 S_w^2 c_w^4 (-C_{m\dot{\alpha}})^2 U^2}{16 J_{yy}^2}}$$

$$\zeta_{yy} = \sqrt{\frac{\rho S_w c_w^3 (-C_{m\dot{\alpha}})^2}{32 J_{yy} (-C_{m\alpha})}} \qquad C_{m\alpha} \le 0 \qquad C_{m\dot{\alpha}} \le 0 \tag{2.3.69}$$

Before proceeding with the analysis, it is useful to introduce the nondimensional radius of inertia. The radius of gyration is defined as:

$$R_{yy} \equiv \sqrt{\frac{J_{yy}}{m}} \tag{2.3.70}$$

Nondimensionalizing with respect to half the fuselage length l_f gives the nondimensional radius of gyration r_{yy}:

$$r_{yy} \equiv \frac{R_{yy}}{\left(\frac{1}{2} l_f\right)} = \frac{2}{l_f} \sqrt{\frac{J_{yy}}{m}} \tag{2.3.71}$$

This gives the following expression for the undamped natural pitch frequency and the damping ratio:

$$\omega_{n,yy} = \sqrt{\frac{4 S_w c_w (-C_{m\alpha}) q}{l_f^2 r_{yy}^2 m}} \qquad C_{m\alpha} \le 0 \tag{2.3.72}$$

$$\zeta_{yy} = \sqrt{\frac{\rho S_w c_w^3 (-C_{m\dot{\alpha}})^2}{8 l_f^2 r_{yy}^2 m (-C_{m\alpha})}} \qquad C_{m\alpha} \le 0 \qquad C_{m\dot{\alpha}} \le 0 \tag{2.3.73}$$

Since the vehicle mass scales with the cube of the vehicle size and wing area scales with the square of the vehicle size, it follows that the undamped natural pitch frequency is:

- Proportional to the airspeed.
- Independent of altitude (air density) at constant dynamic pressure.
- Proportional to the inverse of the vehicle size.
- Proportional to the square root of $(-C_{m\alpha})$.
- Proportional to the square root of inverse of the wing loading m/S_w.

Similarly the damping ratio is:

- Independent of airspeed.
- Independent of vehicle size.
- Proportional to the square root of the air density (i.e. decreases with altitude).

- Proportional to $(-C_{m\dot{\alpha}})$.
- Proportional to the square root of inverse of the wing loading m/S_w.

Before proceeding, we can gain a better understanding of the relationship between the vehicle geometry and the dynamics by introducing two new related quantities; the Aerodynamic Center (AC) and the Stability Margin (SM). The AC is defined as the geometric position on the vehicle where the aerodynamic pitching moment is independent of angle of attack.

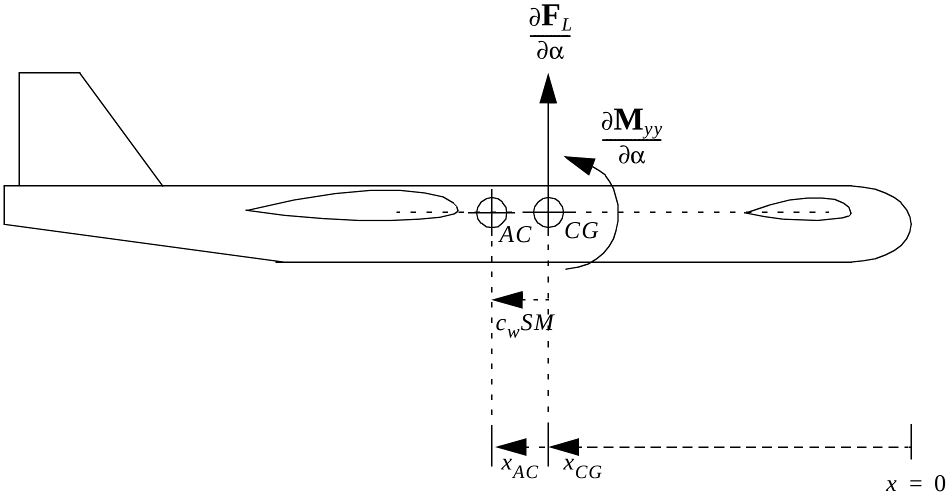

FIGURE 2.14 Longitudinal UAV aerodynamic center (AC).

Figure 2.14 shows the lift and pitching moment angle of attack derivatives $(\partial \mathbf{F}_L)/(\partial\alpha)$ and $(\partial \mathbf{M}_{yy})/(\partial\alpha)$. The Stability Margin (SM) is defined as the nondimensional distance between the AC and the CG:

$$SM = \frac{x_{AC} - x_{CG}}{c_w} \tag{2.3.74}$$

The stability margin can then be determined from its definition using Figure 2.14:

$$(c_wSM)\frac{\partial \mathbf{F}_L}{\partial\alpha} = -\frac{\partial \mathbf{M}_{yy}}{\partial\alpha} \tag{2.3.75}$$

This can be converted into nondimensional form:

$$\begin{aligned} (c_wSM)(qS_wC_{L\alpha}) &= -qS_wc_wC_{m\alpha} \\ C_{m\alpha} &= -C_{L\alpha}SM \end{aligned} \tag{2.3.76}$$

This means that we can use the SM as a nondimensional measure of stability.

From the definition of the aerodynamic center (AC), it follows that the pitching moment derivative with respect to the angle of attack around the AC position must be zero:

$$0 = S_{w1}C_{L\alpha1}(x_{w1} - x_{AC}) + S_wC_{L\alpha2}(x_{w2} - x_{AC}) \tag{2.3.77}$$

This can be rearranged to yield an explicit expression for the AC position:

$$x_{AC} = \frac{S_{w1}C_{L\alpha 1}x_{w1} + S_w C_{L\alpha 2}x_{w2}}{S_w C_{L\alpha}} = \frac{\sum\{S_{wn}C_{L\alpha n}x_{wn}\}}{\sum\{S_{wn}C_{L\alpha n}\}} \tag{2.3.78}$$

Where “*n*” is the lifting surface designator.

Apart from *short period* stability, another very important practical characteristic is the ability to *trim* the vehicle. In aeronautical terms, trim is used to describe the process of obtaining static equilibrium in (usually straight) flight. Neglecting pitching moment contributions from the propeller or other propulsion systems, it is apparent from the definition of the aerodynamic pitching moment that the condition for trim in straight flight is simply:

$$C_m\Big|_{\dot{\alpha} = \kappa_a = 0} = 0 \tag{2.3.79}$$

Given a certain CG position, the equilibrium lift coefficient ratio between the canard and main wing can be determined using Eq. 2.3.39:

$$\frac{C_{Lw1}}{C_{Lw2}} = -\frac{S_w}{S_{w1}}\frac{\Delta x_{w2}}{\Delta x_{w1}} = -\frac{S_w}{S_{w1}}\frac{(x_{w2} - x_{CG})}{(x_{w1} - x_{CG})} \tag{2.3.80}$$

Notice that $(x_{w1} - x_{CG})$ is normally negative.

Using Eq. 2.3.76 (stability margin) and Eq. 2.3.57 ($C_{m\alpha}$) gives an explicit expression for the CG position as a function of the stability margin:

$$\begin{aligned} C_{L\alpha}SM &= \frac{S_{w1}}{S_w}\frac{\Delta x_{w1}}{c_w}C_{L\alpha 1} + \frac{\Delta x_{w2}}{c_w}C_{L\alpha 2} \\ x_{CG} &= \frac{S_{w1}x_{w1}C_{L\alpha 1} + S_w x_{w2}C_{L\alpha 2} - S_w c_w SMC_{L\alpha}}{S_w C_{L\alpha}} \end{aligned} \tag{2.3.81}$$

Substitution of Eq. 2.3.81 into Eq. 2.3.80 gives the desired expression (after some algebra!):

$$\frac{C_{Lw1}}{C_{Lw2}} = \frac{S_{w1}(x_{w2} - x_{w1})C_{L\alpha 1} + S_w c_w SMC_{L\alpha}}{S_{w1}(x_{w2} - x_{w1})C_{L\alpha 2} - S_{w1}c_w SMC_{L\alpha}} \tag{2.3.82}$$

Notice the intuitive special case for SM equal to zero.

Since $S_{w1} \ll S_w$ for a canard configuration, it follows that an increase in the SM also increases the ratio C_{Lw1}/C_{Lw2}. Since the lift coefficient of the canard is limited by non-linear aerodynamic phenomena (stall) it is apparent that the lift coefficient of the entire vehicle will be limited if an excessive SM is used. On the other hand it is very desirable for prevention of main wing stall that the canard stalls before the main wing. This means that the desired (“optimal”) stability margin is a small positive value. However as we shall see later, it may be necessary to increase the nominal stability margin to ensure static stability in case of modelling errors.

We have now determined the short period mode eigensolution, introduced the stability margin and looked at the link between the stability margin and the maximum attainable vehicle lift coefficient. In order to complete the analysis of the short period mode, we should also determine the response to aerodynamic control inputs. The most obvious aerodynamic control input is the elevator angle δ_e. The complete ODE of the short period mode is obtained by keeping the flight path angle $\gamma_e(t)$ constant $\gamma_e(t) = \gamma_{e0}$ in Eq. 2.3.63:

$$\ddot{\theta}_e - \frac{\rho S_w c_w^2 C_{m\dot{\alpha}} U}{4J_{yy}}\dot{\theta}_e - \frac{\rho S_w c_w C_{m\alpha} U^2}{2J_{yy}}\theta_e = \frac{\rho S_w c_w U^2}{2J_{yy}}(-C_{m\alpha}\gamma_{e0} + C_{m\delta_e}\delta_e + C_{m0}) \tag{2.3.83}$$

Since Eq. 2.3.83 is already linear, we can investigate the response to elevator inputs by setting γ_{e0} and C_{m0} equal to zero:

$$\ddot{\theta}_e - \frac{\rho S_w c_w^2 C_{m\dot{\alpha}} U}{4J_{yy}}\dot{\theta}_e - \frac{\rho S_w c_w C_{m\alpha} U^2}{2J_{yy}}\theta_e = \frac{\rho S_w c_w U^2}{2J_{yy}}C_{m\delta_e}\delta_e = \frac{\rho S_w c_w U^2}{2J_{yy}}\frac{S_{w1}}{S_w}\frac{\Delta x_{w1}}{c_w}C_{L\alpha 1}\frac{\partial\alpha_{0L1}}{\partial\delta_e}\delta_e \tag{2.3.84}$$

Using the just introduced stability margin (Eq. 2.3.76) and the nondimensional radius of gyration (Eq. 2.3.71) gives:

$$\ddot{\theta}_e - \frac{\rho S_w c_w^2 C_{m\dot{\alpha}} U}{r_{yy}^2 l_f^2 m}\dot{\theta}_e + \frac{2\rho S_w c_w C_{L\alpha} U^2 SM}{r_{yy}^2 l_f^2 m}\theta_e = \frac{2\rho S_w c_w U^2}{r_{yy}^2 l_f^2 m}\frac{S_{w1}}{S_w}\frac{\Delta x_{w1}}{c_w}C_{L\alpha 1}\frac{\partial\alpha_{0L1}}{\partial\delta_e}\delta_e \tag{2.3.85}$$

Since there are no derivatives of δ_e in the ODE it follows that the transfer function from δ_e to θ_e has no zeros. The laplace transform of Eq. 2.3.85 is given by:

$$\left(s^2 - \frac{\rho S_w c_w^2 C_{m\dot{\alpha}} U}{r_{yy}^2 l_f^2 m}s + \frac{2\rho S_w c_w C_{L\alpha} U^2 SM}{r_{yy}^2 l_f^2 m}\right)\theta_e(s) = \frac{2\rho S_w c_w U^2}{r_{yy}^2 l_f^2 m}\frac{S_{w1}}{S_w}\frac{\Delta x_{w1}}{c_w}C_{L\alpha 1}\frac{\partial\alpha_{0L1}}{\partial\delta_e}\delta_e(s) \tag{2.3.86}$$

The transfer function can then immediately be determined as:

$$\frac{\theta_e(s)}{\delta_e(s)} = \frac{\dfrac{2\rho S_w c_w U^2}{r_{yy}^2 l_f^2 m}\dfrac{S_{w1}}{S_w}\dfrac{\Delta x_{w1}}{c_w}C_{L\alpha 1}\dfrac{\partial\alpha_{0L1}}{\partial\delta_e}}{s^2 - \dfrac{\rho S_w c_w^2 C_{m\dot{\alpha}} U}{r_{yy}^2 l_f^2 m}s + \dfrac{2\rho S_w c_w C_{L\alpha} U^2 SM}{r_{yy}^2 l_f^2 m}} = \frac{K_{\delta_e}\omega_{n,yy}^2}{s^2 + 2\zeta_{yy}\omega_{n,yy}s + \omega_{n,yy}^2} \tag{2.3.87}$$

Where:

$$\omega_{n,yy} = \sqrt{\frac{4S_w c_w C_{L\alpha} SMq}{l_f^2 r_{yy}^2 m}} \qquad \zeta_{yy} = \sqrt{\frac{\rho S_w c_w^3 (-C_{m\dot{\alpha}})^2}{8 l_f^2 r_{yy}^2 m C_{L\alpha} SM}}$$

$$K_{\delta_e} = \frac{S_{w1}}{S_w}\frac{\Delta x_{w1}}{c_w}\frac{C_{L\alpha 1}}{C_{L\alpha} SM}\frac{\partial\alpha_{0L1}}{\partial\delta_e} \tag{2.3.88}$$

It is apparent that the stability margin has a large influence on both the dynamic and static short period mode response.

In fact the pitch response ($\theta_e(t)$ or $\theta_e(s)$) by itself is not of primary interest for vehicle guidance. However since the lift coefficient is proportional to the angle of attack and the angle of attack rate is equal to the pitch rate $(\dot{\alpha}(t) = \dot{\theta}_e(t))$ for the short period mode, it follows that the lift and lift coefficient dynamics are the same as the pitch dynamics for the short period. The static lift coefficient elevator gain can then be determined by combining Eq. 2.3.88 and Eq. 2.3.54:

$$\left(\frac{\partial C_L}{\partial \delta_e}\right)_{\text{static}} = K_{\delta_e} C_{L\alpha} = \frac{S_{w1}}{S_w}\frac{\Delta x_{w1}}{c_w}\frac{C_{L\alpha 1}}{C_{L\alpha} SM}\frac{\partial \alpha_{0L1}}{\partial \delta_e} C_{L\alpha} = \frac{S_{w1}}{S_w}\frac{\Delta x_{w1}}{c_w}\frac{C_{L\alpha 1}}{SM}\frac{\partial \alpha_{0L1}}{\partial \delta_e} \tag{2.3.89}$$

Again we can see the importance of the numerical value of the stability margin.

The other main longitudinal control input is the propeller power (or thrust). However the short period approximation does not predict any power or thrust effect since the thrust in the simple model does not change the trim. However since the thrust changes the airspeed and thus the dynamic pressure, an increase in thrust will increase the lift and thus the normal acceleration. The effect of a thrust change is thus to change the flight path angle derivative. A complete dynamic analysis where the straight flight path approximation is dropped would thus give a small pitch and lift transient response as the result of a thrust change.

2.3.7.2 Phugoid mode

The phugoid mode is determined by assuming that the vehicle is trimmed to equilibrium in straight flight at constant airspeed. It is furthermore assumed that the angular pitch acceleration can be ignored. These two conditions imply a constant (trim) angle of attack, which in turn means that the lift coefficient (Eq. 2.3.54) and thus also the drag coefficient (Eq. 2.3.56) must be constant for the phugoid mode.

Assuming a small flight path angle $|\gamma| \ll 1$, the normal acceleration of the vehicle can be expressed as:

$$a_N = \frac{F_L}{m} - g \tag{2.3.90}$$

Where $g \cong 9.82 m/s^2$ is the magnitude of the acceleration of gravity.

Since the flight path angle derivative is the change in flight path angle per unit time, we can write:

$$\dot{\gamma} = \frac{a_N}{U} = \frac{F_L}{mU} - \frac{g}{U} = \frac{\rho C_L S_w U^2}{2mU} - \frac{g}{U} = \frac{\rho C_L S_w U}{2m} - \frac{g}{U} \tag{2.3.91}$$

Where we have assumed constant atmospheric wind.

The axial acceleration (in the flight path direction) for constant atmospheric wind and small flight path angles can be expressed as:

$$\dot{U} = \frac{F_{th} - F_D}{m} - g\gamma \tag{2.3.92}$$

For the moment we will assume that the combined motor and propeller efficiency is constant and that the dynamics of the propeller rotational speed is negligible:

$$F_{th} = \eta_p \eta_m \frac{W_e}{U} \tag{2.3.93}$$

Where η_p is the propeller efficiency, η_m is the DC motor efficiency and W_e is the electric power applied to the motor terminals (assumed constant for this analysis).

An explicit expression for the axial acceleration as a function of the flight speed and the flight path angle, can then be determined using the definition of the drag coefficient (Eq. 2.3.5):

$$\dot{U} = \frac{\eta_p \eta_m \frac{W_e}{U} - \frac{1}{2}\rho C_D S_w U^2}{m} - g\gamma \tag{2.3.94}$$

Before proceeding with a stability analysis we obviously have to linearize Eq. 2.3.91 and Eq. 2.3.94 around a suitable trim operating point. We will define the operating point in terms of the trim speed U_0 and the trim flight path angle γ_0. Since $\dot{\gamma}$ is obviously zero for the trim condition, we can obtain the trim lift coefficient C_{L0} from Eq. 2.3.91:

$$C_{L0} = \frac{2mg}{\rho S_w U_0^{\ 2}} \tag{2.3.95}$$

For a particular vehicle we could now use Eq. 2.3.56 to calculate the trim drag coefficient C_{D0}. However in this analysis we will keep C_{D0} as a parameter.

We are now able to use Eq. 2.3.94 to determine the trim electric power W_{e0}:

$$W_{e0} = \frac{U_0}{\eta_p \eta_m}\left(\frac{1}{2}\rho C_D S_w U_0^{\ 2} + mg\gamma_0\right) \tag{2.3.96}$$

We are now able to linearize by introducing deviation variables for flight path angle and airspeed:

$$U = \delta U + U_0 \qquad \gamma = \delta\gamma + \gamma_0 \tag{2.3.97}$$

Since by definition $\delta\dot{U} = \dot{U}$ and $\delta\dot{\gamma} = \dot{\gamma}$, we can linearize Eq. 2.3.91 and Eq. 2.3.94 as:

Flight path angle:

$$\delta\dot{\gamma} = \frac{\rho C_{L0} S_w}{2m}\delta U + \frac{g}{U_0^2}\delta U = \left(\frac{\rho C_{L0} S_w}{2m} + \frac{g}{U_0^2}\right)\delta U = \left(\frac{g}{U_0^{\ 2}} + \frac{g}{U_0^2}\right)\delta U = \frac{2g}{U_0^{\ 2}}\delta U \tag{2.3.98}$$

Axial acceleration:

$$\delta\dot{U} = -\left(\eta_p \eta_m \frac{W_{e0}}{U_0^2} + \rho C_D S_w U_0\right)\frac{\delta U}{m} - g\delta\gamma = -\left(\frac{3}{2}\rho C_D S_w U_0 + \frac{mg\gamma_0}{U_0}\right)\frac{\delta U}{m} - g\delta\gamma \tag{2.3.99}$$

A linearized state space ODE for the phugoid mode can then be expressed as:

$$\begin{bmatrix}\delta\dot{\gamma} \\ \delta\dot{U}\end{bmatrix} = \begin{bmatrix} 0 & \dfrac{2g}{U_0^{\;2}} \\ -g & -\dfrac{1}{m}\left(\dfrac{3}{2}\rho C_D S_w U_0 + \dfrac{mg\gamma_0}{U_0}\right) \end{bmatrix} \begin{bmatrix}\delta\gamma \\ \delta U\end{bmatrix} \qquad (2.3.100)$$

The characteristic equation of Eq. 2.3.100 can then be determined directly as (Ref. 10, p. 34):

$$0 = det\left(\begin{bmatrix} s & -\dfrac{2g}{U_0^{\;2}} \\ g & s + \dfrac{1}{m}\left(\dfrac{3}{2}\rho C_D S_w U_0 + \dfrac{mg\gamma_0}{U_0}\right) \end{bmatrix}\right) = s\left(s + \frac{1}{m}\left(\frac{3}{2}\rho C_D S_w U_0 + \frac{mg\gamma_0}{U_0}\right)\right) + \frac{2g^2}{U_0^{\;2}}$$

$$0 = s^2 + \frac{1}{m}\left(\frac{3}{2}\rho C_D S_w U_0 + \frac{mg\gamma_0}{U_0}\right)s + \frac{2g^2}{U_0^{\;2}} \qquad (2.3.101)$$

The undamped natural frequency ω_n and damping ratio ζ are then given by:

$$\omega_n = \sqrt{2}\frac{g}{U_0} \qquad \zeta = \frac{1}{2\omega_n m}\left(\frac{3}{2}\rho C_D S_w U_0 + \frac{mg\gamma_0}{U_0}\right) = \frac{1}{2\sqrt{2}}\left(\frac{3\rho C_D S_w U_0^2}{2mg} + \gamma_0\right) \qquad (2.3.102)$$

Since $mg = \frac{1}{2}\rho C_{L0} S_w U_0^2$, this can further be simplified as:

$$\omega_n = \sqrt{2}\frac{g}{U_0} \qquad \zeta = \frac{1}{2\sqrt{2}}\left(3\left(\frac{C_{L0}}{C_{D0}}\right)^{-1} + \gamma_0\right) \qquad (2.3.103)$$

Since C_{L0}/C_{D0} is equal to the *lift to drag ratio*, which is normally greater then 10 for a well designed subsonic vehicle, the damping ratio of the phugoid mode is generally below 0.1 in level flight ($\gamma_0 = 0$). At the same time it can be seen that the phugoid damping increases during a steady climb ($\gamma_0 > 0$) and decreases during a steady descent ($\gamma_0 < 0$). This means that for a reasonably clean aerodynamic vehicle it is possible that the damping of the phugoid becomes negative in a dive.

We can conclude that the undamped frequency of the phugoid mode is:

- Independent of the airframe geometry and size.
- Proportional to the inverse of the airspeed.

The damping ratio of the phugoid mode is:

- Small but generally positive.
- Smaller for an aerodynamically effective vehicle (i.e. high lift to drag ratio).
- Smaller for a dive and higher for a climb.
- Independent of the airspeed (for constant lift to drag ratio).

Since the phugoid is only lightly damped, it is of particular interest to increase the damping using closed loop control. In order evaluate the possibilities of this, it is necessary to determine the phugoid mode response to elevator angle and propeller power inputs.

Since we know from the short period mode approximation that the lift coefficient can be directly controlled by the elevator deflection angle (Eq. 2.3.89), we can investigate the response of the phugoid mode to changes in lift coefficient, in order to determine the effects of elevator input.

The derivative of the flight path angle rate with respect to the lift coefficient, can be determined from Eq. 2.3.91:

$$\frac{\partial(\dot{\gamma})}{\partial C_L} = \frac{\rho S_w U}{2m} \tag{2.3.104}$$

It is apparent from Eq. 2.3.94 that the derivative of the axial acceleration with respect to the lift coefficient is zero:

$$\frac{\partial(\dot{U})}{\partial C_L} = 0 \tag{2.3.105}$$

The derivative of the axial acceleration with respect to the propeller power, can be determined from Eq. 2.3.94:

$$\frac{\partial(\dot{U})}{\partial W_e} = \frac{\eta_p \eta_m}{mU} \tag{2.3.106}$$

The derivative of the flight path angle rate with respect to the propeller power is zero according to Eq. 2.3.91:

$$\frac{\partial(\dot{\gamma})}{\partial W_e} = 0 \tag{2.3.107}$$

We can now extend the linearized phugoid mode ODE (Eq. 2.3.100) to include lift coefficient and propeller power inputs:

$$\begin{bmatrix} \delta\dot{\gamma} \\ \delta\dot{U} \end{bmatrix} = \begin{bmatrix} 0 & \dfrac{2g}{U_0^{\,2}} \\ -g & -\dfrac{1}{m}\left(\dfrac{3}{2}\rho C_D S_w U_0 + \dfrac{mg\gamma_0}{U_0}\right) \end{bmatrix} \begin{bmatrix} \delta\gamma \\ \delta U \end{bmatrix} + \begin{bmatrix} \dfrac{\rho S_w U_0}{2m} & 0 \\ 0 & \dfrac{\eta_p \eta_m}{mU_0} \end{bmatrix} \begin{bmatrix} \delta C_L \\ \delta W_e \end{bmatrix} \tag{2.3.108}$$

Where δC_L and δW_e are deviation variables.

The (matrix) transfer function from the input vector $\begin{bmatrix} \delta C_L & \delta W_e \end{bmatrix}^T$ to the output vector $\begin{bmatrix} \delta\gamma & \delta U \end{bmatrix}^T$, can be determined as (Ref. 10, Table 2.1-1):

$$\begin{bmatrix} \dfrac{\delta\gamma(s)}{\delta C_L(s)} & \dfrac{\delta\gamma(s)}{\delta W_e(s)} \\ \dfrac{\delta U(s)}{\delta C_L(s)} & \dfrac{\delta U(s)}{\delta W_e(s)} \end{bmatrix} = \begin{bmatrix} s & -\dfrac{2g}{U_0^{\,2}} \\ g & s + \dfrac{1}{m}\left(\dfrac{3}{2}\rho C_D S_w U_0 + \dfrac{mg\gamma_0}{U_0}\right) \end{bmatrix}^{-1} \begin{bmatrix} \dfrac{\rho S_w U_0}{2m} & 0 \\ 0 & \dfrac{\eta_p \eta_m}{mU_0} \end{bmatrix} \tag{2.3.109}$$

Which reduces to:

$$\begin{bmatrix} \dfrac{\delta\gamma(s)}{\delta C_L(s)} & \dfrac{\delta\gamma(s)}{\delta W_e(s)} \\ \dfrac{\delta U(s)}{\delta C_L(s)} & \dfrac{\delta U(s)}{\delta W_e(s)} \end{bmatrix} = \frac{\begin{bmatrix} \left(s + \dfrac{1}{m}\left(\dfrac{3}{2}\rho C_D S_w U_0 + \dfrac{mg\gamma_0}{U_0}\right)\right)\dfrac{\rho S_w U_0}{2m} & \dfrac{2g}{U_0^{\ 2}}\dfrac{\eta_p\eta_m}{mU_0} \\ -g\dfrac{\rho S_w U_0}{2m} & s\dfrac{\eta_p\eta_m}{mU_0} \end{bmatrix}}{s^2 + \dfrac{1}{m}\left(\dfrac{3}{2}\rho C_D S_w U_0 + \dfrac{mg\gamma_0}{U_0}\right)s + \dfrac{2g^2}{U_0^{\ 2}}} \qquad (2.3.110)$$

Notice that the static gain of $\delta U(s)/\delta W_e(s)$ is zero! This apparently counter intuitive result is due to the fact that a power setting change will eventually lead to a new steady flight path angle, but since the lift must be equal to the weight for moderate flight path angles, the airspeed must be constant (neglecting air density change) since the trim lift coefficient is independent of the power setting for this aerodynamic model.

This results in the conclusion that in order to change the airspeed it is necessary to change both the propeller power setting and the elevator deflection angle (i.e the trim lift coefficient).

2.3.8 Linear aerodynamic coefficients for real configurations

In the simple longitudinal aerodynamic model presented in Section 2.3.6, only the lift and drag forces from the canard and main wing was considered. This model was used in Section 2.3.7 to determine the approximate longitudinal dynamics of the vehicle. This analysis showed that the Stability Margin (SM) has a significant influence on the short period mode. Since the stability margin is defined as the nondimensional difference between the position of the Center of Gravity (CG) and the Aerodynamic Center (AC), any errors in the CG or AC position will have a large influence on the SM. This is especially compounded by the fact that the “optimal” SM for aerodynamic efficiency, is a small positive value. This means that any uncertainty in the CG or AC position has the potential to seriously effect the longitudinal vehicle dynamics, even to the extent of producing longitudinal aerodynamic instability. For this reason it is prudent to obtain an answer to two questions; how is the position of the AC affected by aerodynamic forces on other vehicle components and what is the estimated uncertainty of the AC position.

2.3.8.1 Wing lift coefficient curve slope and aerodynamic center

Before proceeding we will return to the problem of determining the lift curve slopes $C_{L\alpha 1}$ and $C_{L\alpha 2}$ of the canard and wing respectively. As noted in Section 2.3.6, the theoretical lift curve slope of a 2 dimensional wing is $2\pi/\mathrm{rad}$. This value is approached for an ideal 3 dimensional wing of large *aspect ratio*. The general trapezoidal wing platform is defined in Figure 2.15 below:

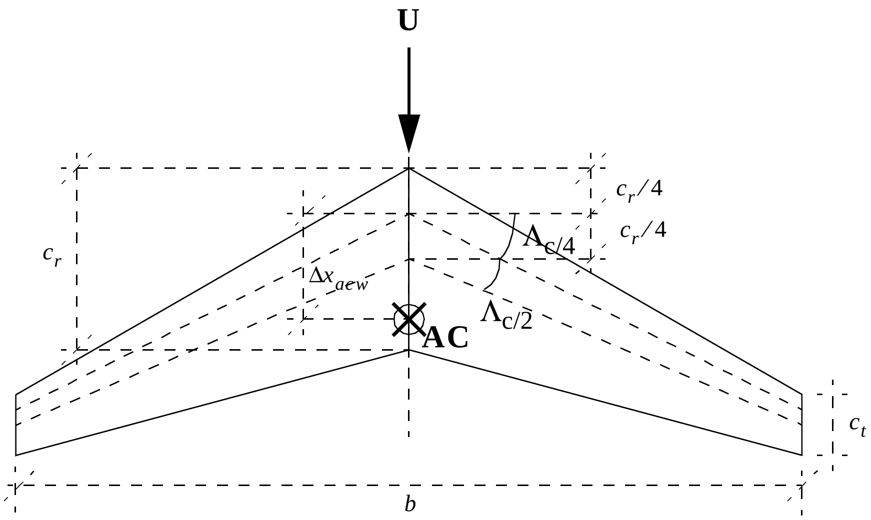

FIGURE 2.15 Trapezoidal wing geometry.

We can see that the wing geometry can be defined by 4 parameters; the wing span b, the root chord c_r, the tip chord c_t and the quarter chord sweep angle $\Lambda_{c/4}$. The longitudinal distance between the root $c_r/4$ position and the aerodynamic center of the wing is defined as Δx_{acw}.

In the following we will also need some derived geometric properties of the wing:

Taper ratio:

$$\lambda = c_t/c_r \tag{2.3.111}$$

Mean aerodynamic chord (Ref. 8, Eq. 7.8):

$$c_w = \frac{2}{3}c_r\frac{1+\lambda+\lambda^2}{1+\lambda} \tag{2.3.112}$$

Notice that c_w is not the algebraic mean of the tip and root chords. This is because c_w is the chord measured at the spanwise wing panel center of area position y_w.

Spanwise wing panel center of area position (Ref. 8, Eq. 7.9) (measured outboard from the wing root):

$$y_w = \frac{b}{6}\left(\frac{1+2\lambda}{1+\lambda}\right) \tag{2.3.113}$$

Wing area:

$$S_w \equiv \left(\frac{c_r+c_t}{2}\right)b \neq c_w b \tag{2.3.114}$$

Aspect ratio:

$$A_w \equiv \frac{b^2}{S_w} \neq \frac{b}{c_w} \tag{2.3.115}$$

Half chord sweep:

$$\Lambda_{c/2} = \operatorname{atan}\left(\tan(\Lambda_{c/4}) - \frac{(1-\lambda)}{A_w(1+\lambda)}\right) \tag{2.3.116}$$

Trailing edge (TE) sweep:

$$\Lambda_{TE} = \operatorname{atan}\left(\tan(\Lambda_{c/4}) - \frac{3(1-\lambda)}{A_w(1+\lambda)}\right) \tag{2.3.117}$$

The lift curve slope of the entire wing $C_{L\alpha w}$ can then be determined using the following empirical equation (Ref. 4, 4.1.3.2-49):

$$C_{L\alpha w} = \frac{2\pi A_w}{2 + \sqrt{\frac{A_w^2}{\kappa^2}(1 + \tan(\Lambda_{c/2})^2) + 4}} \tag{2.3.118}$$

Where $\kappa = C_{l\alpha}/(2\pi)$ is the ratio of the wing profile section lift curve slope to $2\pi/\text{rad}$.

The aerodynamic center position of each lifting surface is important for determining the overall vehicle AC. For the wing alone, it can safely be assumed that the aerodynamic center of a high aspect ratio wing is close to the quarter chord line. This means that the AC position for a straight (nonswept) wing is located at the quarter chord point on the wing root. For a swept wing it is necessary to determine the spanwise lift distribution in order to find the longitudinal AC of the wing. For moderate sweep and high aspect ratio, it is sufficient to assume an elliptic lift distribution (Ref. 1, Eq. III.3.18):

$$\Delta x_{acw} = \frac{2}{3\pi} A_w \tan(\Lambda_{c/4}) c_w \tag{2.3.119}$$

Notice that the definition of the wing AC implies that the pitching moment coefficient around the AC is independent of the relative angle of attack (and thus independent of the lift coefficient). However it does not imply that the pitching moment is zero. In fact, if the wing section is cambered and/or the wing is twisted and swept, the pitching moment coefficient referenced to the AC will be nonzero. Neglecting the combined effect of wing twist *and* sweep, the wing alone pitching moment can be expressed as (Ref. 8, Eq. 16.18):

$$C_{mw} = C_{mp0}\left(\frac{A_w \cos(\Lambda_{c/4})^2}{A_w + 2\cos(\Lambda_{c/4})}\right) \tag{2.3.120}$$

Where C_{mp0} is the wing profile pitching moment referenced to the profile AC (c/4 point).

Trailing edge flap:

The lift coefficient of a 2 dimensional airfoil can be altered by a nonextending trailing edge flap as described by Eq. 2.3.23. For a 2 dimensional airfoil the influence of a nonextending trailing edge flap is to alter the zero lift angle of attack of the complete airfoil. Since the flap is nonextending, the lift curve slope (with fixed flap) is not altered by flap deflection. For a 3 dimensional wing, the effects of the flap, on the lift coefficient of the complete wing can be approximated as proportional to the "flapped" wing area (Ref. 8, p. 339-340).

$$\frac{\partial\alpha_{0Lw}}{\partial\delta_e} \cong \frac{S_{flapped}}{S_w}\frac{\partial\alpha_{0L}}{\partial\delta_e} \tag{2.3.121}$$

Where $(\partial\alpha_{0Lw})/(\partial\delta_e)$ is the change in zero lift angle of attack of the complete wing, while $(\partial\alpha_{0L})/(\partial\delta_e)$ is the change in zero lift angle of attack of the airfoil of the 2 dimensional flapped airfoil.

The flapped wing area $S_{flapped}$ is defined in Figure 2.16 below:

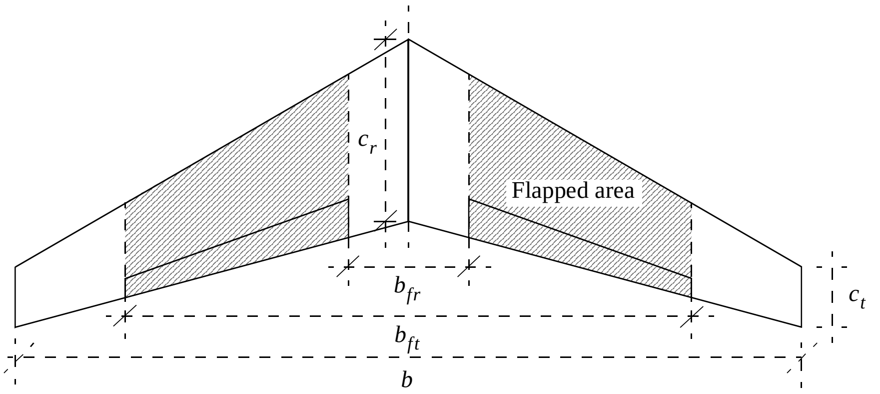

FIGURE 2.16 Flapped wing area.

Deflection of a trailing edge flap causes a change in the wing (or canard) lift, which can be expressed as:

$$C_{L\delta_e w} \equiv \frac{\partial C_{Lw}}{\partial\delta_e} = -C_{L\alpha w}\frac{\partial\alpha_{0Lw}}{\partial\delta_e} \tag{2.3.122}$$

However the center of pressure (CP) for the lift increment due to change of flap angle is not the same as the aerodynamic center. For a two dimensional airfoil, the CP due to flap deflection can be approximated as (Ref. 8, Fig. 16.9):

$$\frac{(\Delta x_{cp})_{\text{flap}}}{c} = 0.5\left(1 - 0.5\frac{c_f}{c}\right) \tag{2.3.123}$$

Where c is the total airfoil chord, c_f is the flap chord and $(\Delta x_{cp})_{\text{flap}}$ is the airfoil CP distance behind the airfoil leading edge, due to flap deflection.

For a 3 dimensional wing with a partial span flap (see Figure 2.16) the mean aerodynamic chord of the flapped part of the wing c_{wf} is given by (see Eq. 2.3.112):

$$c_{wf} = \frac{2}{3}c_{wfr}\frac{1 + \lambda_{wf} + \lambda_{wf}^2}{1 + \lambda_{wf}} \tag{2.3.124}$$

Where the root chord of the flapped part of the wing c_{wfr} is given by:

$$c_{wfr} = c_t + (c_r - c_t)\frac{b_{fr}}{b} \tag{2.3.125}$$

The tip chord of the flapped part of the wing c_{wft} is given by:

$$c_{wft} = c_t + (c_r - c_t)\frac{b_{ft}}{b} \tag{2.3.126}$$

The taper ratio λ_{wf} of the flapped part of the wing is given by:

$$\lambda_{wf} = \frac{c_{wft}}{c_{wfr}} \tag{2.3.127}$$

The spanwise position y_{wf} of the mean aerodynamic chord of the flapped part of the wing is given by (see Eq. 2.3.113):

$$y_{wf} = \frac{(b_{ft} - b_{fr})}{6}\left(\frac{1 + 2\lambda_{wf}}{1 + \lambda_{wf}}\right) + \frac{b_{fr}}{2} \tag{2.3.128}$$

For a three dimensional wing, the CP due to flap deflection will be computed using Eq. 2.3.123 with the flap and wing chords taken at the mean aerodynamic flap position:

$$\frac{(\Delta x_{cp})_{\text{flap}}}{c_{wf}} = 0.5\left(1 - 0.5\frac{c_f}{c_{wf}}\right) \tag{2.3.129}$$

Where c_f is the mean aerodynamic flap chord and $(\Delta x_{cp})_{\text{flap}}$ is the airfoil CP distance behind the airfoil leading edge, due to flap deflection.

This gives the longitudinal position of the CP due to flap deflection Δx_{cpwf} for the 3-dimensional wing as:

$$\Delta x_{cpwf} = \tan(\Lambda_{c/4})y_{wf} + (\Delta x_{cp})_{\text{flap}} - \frac{c_{wf}}{4} \tag{2.3.130}$$

Where Δx_{cpwf} is the distance behind the root quarter chord position.

2.3.8.2 Wing-body lift

On (almost) any real vehicle, the lifting surfaces (i.e. canard or wing) are mounted on some sort of fuselage or body. The general geometry of such a wing-body combination is defined in Figure 2.17 below:

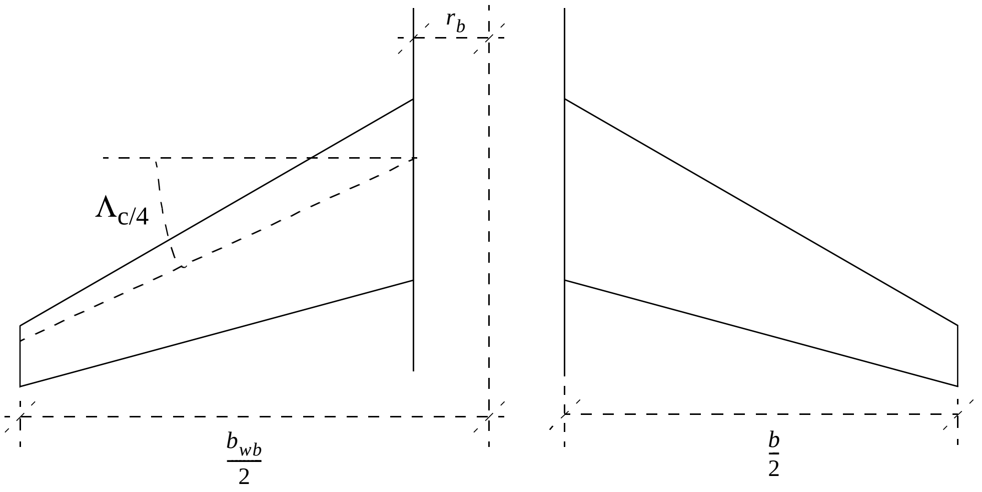

FIGURE 2.17 Wing-body geometry.

The body effects the lift in two ways. The presence of the body at an angle of attack forces the air to flow at faster speeds around the sides of the body, thus increasing the angle of attack of any lifting surface mounted on the body sides. This *wing in presence of body* effect can be expressed as the coefficient $K_{W(B)}$ that increases the lift curve slope of the wing-body combination. In addition, the presence of the wings on the body produces an "image" of the wing lift on the body which can be expressed as the coefficient $K_{B(W)}$. The combined wing-body combination thus has a lift curve slope that can be expressed as:

$$C_{L\alpha wb} = (K_{W(B)} + K_{B(W)})C_{L\alpha w} \tag{2.3.131}$$

It is possible to derive explicit relationships for $K_{W(B)}$ and $K_{B(W)}$ for cylindrical bodies with side mounted wings (Ref. 2):

$$K_{W(B)} = \frac{2}{\pi}\frac{\left\{\left(1+\frac{r_b^4}{s_{wb}^4}\right)\left[\frac{1}{2}\operatorname{atan}\left(\frac{1}{2}\left(\frac{s_{wb}}{r_b}-\frac{r_b}{s_{wb}}\right)\right)+\frac{\pi}{4}\right]-\frac{r_b^2}{s_{wb}^2}\left[\left(\frac{s_{wb}}{r_b}-\frac{r_b}{s_{wb}}\right)+2\operatorname{atan}\left(\frac{r_b}{s_{wb}}\right)\right]\right\}}{\left(1-\frac{r_b}{s_{wb}}\right)^2} \tag{2.3.132}$$

And:

$$K_{B(W)} = \frac{\left(1-\frac{r_b^2}{s_{wb}^2}\right)^2-\frac{2}{\pi}\left\{\left(1+\frac{r_b^4}{s_{wb}^4}\right)\left[\frac{1}{2}\operatorname{atan}\left(\frac{1}{2}\left(\frac{s_{wb}}{r_b}-\frac{r_b}{s_{wb}}\right)\right)+\frac{\pi}{4}\right]-\frac{r_b^2}{s_{wb}^2}\left[\left(\frac{s_{wb}}{r_b}-\frac{r_b}{s_{wb}}\right)+2\operatorname{atan}\left(\frac{r_b}{s_{wb}}\right)\right]\right\}}{\left(1-\frac{r_b}{s_{wb}}\right)^2} \tag{2.3.133}$$

Where $r_b = d/2$ is the body radius and $s_{wb} = b_{wb}/2$ is the wing-body *semispan*. Graphs of $K_{W(B)}$ and $K_{B(W)}$ as a function of r/s_{wb} can be found in (Ref. 2, chart #1).

Since we don't have any data for noncylindrical bodies, we will use Eq. 2.3.132 and Eq. 2.3.133, but with the knowledge that these expressions are only approximations for vehicles with noncylindrical bodies.

The AC of a wing-body combination can be determined as the mean of the AC of the wing in the presence of the body and the body in the presence of the wing. The simplest approach is to assume that the wing AC in the presence of the body is the same as the wing alone AC. This approach is recommended in (Ref. 2, p. 17). For highly swept back wings it should however be remembered that the upwash from the body is largest at the wing root. Thus the AC for swept back wings in presence of the body can be expected to be more forward then for the wing alone. This can be summarized as:

$$(\Delta x_{acw(b)})_{nom} = \Delta x_{acw} \tag{2.3.134}$$

$$(\Delta x_{acw(b)})_{min} = \frac{\Delta x_{acw} C_{L\alpha w}}{K_{W(B)} C_{L\alpha w}} = \frac{\Delta x_{acw}}{K_{W(B)}} \qquad \Lambda_{c/4} > 0 \tag{2.3.135}$$

Where $(\Delta x_{acw(b)})_{nom}$ is the nominal wing AC position in the presence of the body and $(\Delta x_{acw(b)})_{min}$ is the minimum (i.e. most forward) wing AC position.

The body AC position in the presence of the wing can for moderate sweep angles be assumed to coincide with the wing root chord quarter chord point. This gives a slightly to far forward position according to (Ref. 2, chart #16), however the impact of this error on the vehicle AC is small due to the small percentage of lift carried on the body for most UAV configurations. Anyway the error will be on the "safe" side in that it under predicts the vehicle stability margin:

$$\Delta x_{acb(w)} = 0 \tag{2.3.136}$$

The net wing-body AC of a lifting surface (i.e. canard or main wing) can thus be expressed as:

$$(\Delta x_{acwb})_{max} = (\Delta x_{acwb})_{nom} = \frac{\Delta x_{acw} K_{W(B)} + \Delta x_{acb(w)} K_{B(W)}}{K_{W(B)} + K_{B(W)}} = \frac{\Delta x_{acw} K_{W(B)}}{K_{W(B)} + K_{B(W)}} \tag{2.3.137}$$

$$(\Delta x_{acwb})_{min} = \frac{\Delta x_{acw} + \Delta x_{acb(w)} K_{B(W)}}{K_{W(B)} + K_{B(W)}} = \frac{\Delta x_{acw}}{K_{W(B)} + K_{B(W)}} \qquad \Lambda_{c/4} > 0 \tag{2.3.138}$$

The wing-body pitching moment referenced to the wing body AC will be approximated by the wing alone value:

$$C_{mwb} = C_{mw} \tag{2.3.139}$$

Since C_{mwb} is independent of angle of attack by definition (in the linear lift range), it does not have an immediate effect upon the stability, but only on the trim. For this reason it is not essential to model the uncertainty of C_{mwb}.

When the lift of the wing varies independently of the angle of attack of the body (i.e. wing incidence and flap deflection) we should use $k_{W(B)}$ and $k_{B(W)}$ instead of $K_{W(B)}$ and $K_{B(W)}$.

For large aspect ratios, the lift on the wing in the presence of the body at zero angle of attack, is nearly the same as for the wing alone (Ref. 2):

$$k_{W(B)} \cong 1 \qquad A_w \gg 1 \tag{2.3.140}$$

Furthermore it can be shown (Ref. 2) that the lift on the body in the presence of the wing, is approximately given by:

$$k_{B(W)} \cong \frac{K_{B(W)}}{K_{W(B)}} \tag{2.3.141}$$

This concludes the treatment of isolated wing-body combinations.

2.3.8.3 Fuselage lift and pitching moment

In the preceding analysis, wing-body interference was accounted for. However even without a wing, a body produces aerodynamic forces. For a positive angle of attack a positive lift force is in general developed on the nose of a slender body. If the body is sufficiently streamlined and ends in a point (so that the flow remains attached to the end) it can furthermore be shown that an equal but negative lift is developed on the afterbody. The net lift curve slope is thus zero on a perfectly streamlined body, while the pitching moment is destabilizing ($C_{mb\alpha} > 0$). In reality even a streamlined body has a certain amount of separation near the tail, thus the net left curve slope of any slender body is positive. Since the body lift is only a small percentage of the total lift for the anticipated low speed UAV’s considered herein, we will neglect the body lift and only consider the body pitching moment curve slope and its influence on the vehicle AC. For the case of a slender rotational symmetrical body, the pitching moment around the nose apex is given by (Ref. 12, Eq. 27):

$$C_{mb} = -2\alpha\left(1 - \frac{S_{bm}}{S_{bb}}\right) \tag{2.3.142}$$

Where S_{bm} is the mean body crossection area and S_{bb} is the body base area (i.e. the crossection area of the “cut” tail). The moment C_{mb} is based on the product of the base area and the body length.

When the base area is reduced to near zero it is inconvenient to use the base area as the reference area as in Eq. 2.3.142. Instead we can use the maximum body crossection area S_{bmax}:

$$C_{mb} = -2\alpha\left(1 - \frac{S_{bm}}{S_{bb}}\right)\frac{S_{bb}}{S_{bmax}} = -2\alpha\left(\frac{S_{bb}}{S_{bmax}} - \frac{S_{bm}}{S_{bmax}}\right) = 2\alpha\left(\frac{S_{bm} - S_{bb}}{S_{bmax}}\right) \tag{2.3.143}$$

Which is thus based on the maximum body crossection area and the body length.

In (Ref. 12) it is shown that the same result (as Eq. 2.3.142) is obtained for a slender wing with a planform equal to the silhouette of the rotational symmetrical body. This leads to the approximation, that for a crossection shape other then that of a circle, we may use the square of the fuselage width instead of the crossection area in Eq. 2.3.143:

$$C_{mf} = \frac{\pi}{2}\alpha\left(\frac{B_{fmean} - B_{fbase}}{B_{fmax}}\right) \tag{2.3.144}$$

Where we have used the following virtual “crossection” areas:

$$B_{fmax} \equiv b_{fmax}^2 \qquad B_{fbase} \equiv b_{fbase}^2 \qquad B_{fmean} \equiv \frac{1}{l_f}\int_0^{l_f} (b_f(x))^2 dx \tag{2.3.145}$$

Which is based on the maximum fuselage width squared $B_{fmax} \equiv b_{fmax}^2$.

It can be shown that the pitching moment obtained from Eq. 2.3.145 is equal to that obtained from Eq. 2.3.143 when the fuselage is a rotational symmetric body.

The pitching moment curve slope of the fuselage is thus given by:

$$C_{mf\alpha} = \frac{\pi}{2}\left(\frac{B_{fmean} - B_{fbase}}{B_{fmax}}\right) \tag{2.3.146}$$

Which is based on the area b_{fmax}^2 and the fuselage length l_f.

Given the tentative nature of the above analysis, we might as well make the reasonable assumption that the maximum fuselage pitching moment curve slope is given by:

$$(C_{mf\alpha})_{max} = \frac{\pi}{2}\left(\frac{B_{fmean}}{B_{fmax}}\right) \tag{2.3.147}$$

With the nominal and minimum values given by:

$$\begin{aligned} (C_{mf\alpha})_{nom} &= 0.5(C_{mf\alpha})_{max} \\ (C_{mf\alpha})_{min} &= 0.25(C_{mf\alpha})_{max} \end{aligned} \tag{2.3.148}$$

2.3.8.4 Canard-wing interference

Since the main wing is placed behind the canard, the flowfield at the main wing is altered by the canard. What qualitatively happens is that the lift on the canard produces a downward force on the air. This downward force produces a downwash behind the wing.

It can be shown that a short distance (compared to the wing span) behind a high aspect ratio wing with elliptic lift distribution, the downwash angle is (Ref. 13, p. 7.1 & 7.2):

$$\alpha_{dw} = \frac{2C_L}{\pi A} \tag{2.3.149}$$

The downwash can be modelled as the velocity induced by an infinite number of vortexes (a “vortex sheet”) streaming back from the wing trailing edge in the local freestream direction.

Some distance further downstream the vortex sheet will have “rolled up” into two discrete vortexes in the freestream direction with a lateral spacing of approximately $0.75b$.

In this case the downwash can be calculated as originating from the two discrete vortexes, see (Ref. 13) and (Ref. 2) for details.

For configurations where the canard span is approximately the same as the canard-wing spacing, it is unlikely that much “roll up” of the canard vortex sheet has occurred. In this common practical case we can use Eq. 2.3.149 to estimate the influence of canard- wing interference on the location of the vehicle AC.

Letting the canard-body lift curve slope be denoted by $C_{L\alpha wb1}$, the downwash angle derivative $\alpha_{dw\alpha_1}$ behind the canard can then be determined from Eq. 2.3.149 as:

$$\alpha_{dw\alpha_1} = \left(\frac{\partial \alpha_{dw}}{\partial \alpha_1}\right) = \frac{2C_{L\alpha wb1}}{\pi A_1} \qquad (2.3.150)$$

Where A_1 is the canard span (without the body).

The downwash calculated by Eq. 2.3.150 only affects the main wing inboard of the canard wingtips, as indicated in Figure 2.18 below:

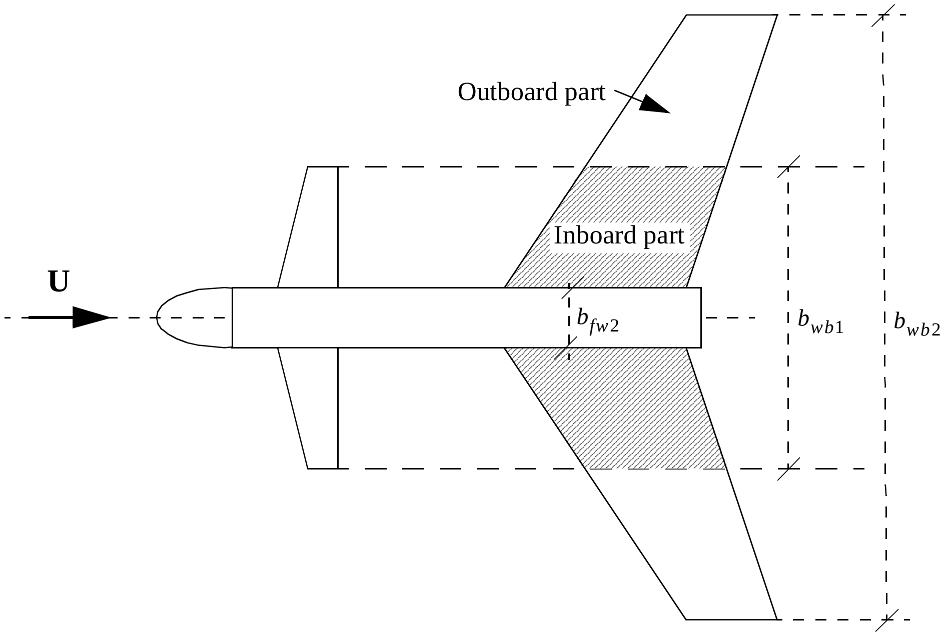

FIGURE 2.18 Area of main wing affected by uniform canard downwash.

Since the effective angle of attack of the main wing is reduced by α_{dw}, it follows that the effective lift curve slope of the inboard part of the main wing ($|y| \le \pm\frac{b_{wb1}}{2}$) can be expressed as:

$$(C_{L\alpha wb2})_{inboard} = C_{L\alpha wb2}(1-\alpha_{dw\alpha_1}) = C_{L\alpha wb2}\left(1-\frac{2C_{L\alpha wb1}}{\pi A_1}\right) \qquad (2.3.151)$$

The area of the inboard part of the main wing can be determined using Figure 2.15 and Figure 2.18 as:

$$(S_{w2})_{inboard} = \frac{c_r}{2}\left(2+(\lambda_2-1)\frac{b_{wb1}-b_{fw2}}{b_2}\right)(b_{wb1}-b_{fw2}) \qquad (2.3.152)$$

On the outboard part of the wing ($|y| > \pm\frac{b_{wb1}}{2}$) we will assume that the lift is unaffected by the canard. This gives the following expression for the main wing-body-canard lift coefficient slope $C_{L\alpha wbc2}$:

$$\begin{aligned} C_{L\alpha wbc2} &= \frac{(S_{w2})_{inboard} C_{L\alpha wb2}(1-\alpha_{dw\alpha_1}) + (S_{w2} - (S_{w2})_{inboard}) C_{L\alpha wb2}}{S_{w2}} \\ C_{L\alpha wbc2} &= \frac{S_{w2} - (S_{w2})_{inboard}\alpha_{dw\alpha_1}}{S_{w2}} C_{L\alpha wb2} \end{aligned} \qquad (2.3.153)$$

In reality it can be shown that immediately outside of the downwash area, there is a strong upwash. For canard configurations (i.e. larger main wing then canard span), this upwash will partly counteract the effects of the downwash on the inboard part of the main wing. For this reason we should regard Eq. 2.3.153 as the worst case lift coefficient curve slope of the main wing-body in the presence of canard downwash:

$$\begin{aligned} (C_{L\alpha wbc2})_{min} &= \frac{S_{w2} - (S_{w2})_{inboard}(\alpha_{dw\alpha_1})_{max}}{S_{w2}} (C_{L\alpha wb2})_{min} \\ (C_{L\alpha wbc2})_{nom} &= \frac{(C_{L\alpha wb2})_{nom} + (C_{L\alpha wbc2})_{min}}{2} \\ (C_{L\alpha wbc2})_{max} &= (C_{L\alpha wb2})_{max} \end{aligned} \qquad (2.3.154)$$

The nominal value of $C_{L\alpha wbc2}$ is guessed as the value corresponding to the effect of only half the calculated downwash, since we have knowingly neglected the upwash on the outboard main wing parts in the above analysis. In calculating the maximum value of $C_{L\alpha wbc2}$, the canard downwash has been neglected altogether.

Since the lift curve slope of the inboard part of the main wing is decreased by canard downwash, the resulting aerodynamic center of the main wing is displaced slightly backwards if the wing sweep is positive. However since this effect is small and stabilizing for moderate main wing sweep angles, it will be neglected in this analysis:

$$\Delta x_{acwbc2} = \Delta x_{acwb2} \qquad (2.3.155)$$

The absolute positions of the canard and main wing AC's can then be determined as:

$$x_{wb1} = l_{wb1} + \Delta x_{acwb1} \qquad x_{wbc2} = l_{wb2} + \Delta x_{acwb2} \qquad (2.3.156)$$

Where l_{wb1} and l_{wb2} are the longitudinal positions of the quarter chord root point of the canard and main wing respectively.

In order to calculate the pitching moment due to canard flap deflection (i.e. elevator control), the distance from the CG to the CP due to flap deflection is needed:

$$\Delta x_{wf1} = (l_{wb1} + \Delta x_{cpwf1}) - x_{CG} \qquad (2.3.157)$$

Notice that wing-body interference is neglected.

2.3.8.5 Complete vehicle coefficients:

The lift curve slope uncertainty range for the complete vehicle can now be determined simply as:

$$\begin{aligned}(C_{L\alpha})_{min} &= \frac{S_{w1}}{S_w}(C_{L\alpha wb1})_{min} + (C_{L\alpha wbc2})_{min} \\ (C_{L\alpha})_{nom} &= \frac{S_{w1}}{S_w}(C_{L\alpha wb1})_{nom} + (C_{L\alpha wbc2})_{nom} \\ (C_{L\alpha})_{max} &= \frac{S_{w1}}{S_w}(C_{L\alpha wb1})_{max} + (C_{L\alpha wbc2})_{max}\end{aligned} \qquad (2.3.158)$$

As discussed above, the fuselage alone lift is ignored.

It is important to realize that $(C_{L\alpha})_{min}$ and $(C_{L\alpha})_{max}$ are worst case approximations to the uncertainty boundaries, since Eq. 2.3.158 assumes that the lift extremes of the canard and main wing occur at the same time. In other words it is assumed that $C_{L\alpha wb1}$ are $C_{L\alpha wbc2}$ correlated.

The AC of the vehicle with just one canard and main wing is given by Eq. 2.3.78. Since the numerator of Eq. 2.3.78 is really just the sum of the weighted downwards (i.e. negative) pitching moments around the nose apex ($x = 0$), it follows that the theoretical AC of the complete vehicle (including the fuselage) can be expressed as:

$$x_{AC} = \frac{S_{w1}C_{L\alpha wb1}x_{wb1} + S_w C_{L\alpha wbc2}x_{wbc2} - b_{fmax}^2 C_{mf\alpha} l_f}{S_w C_{L\alpha}} \qquad (2.3.159)$$

The vehicle AC uncertainty range can then be determined as:

$$\begin{aligned}(x_{AC})_{min} &= \frac{S_{w1}(C_{L\alpha wb1})_{max}(x_{wb1})_{min} + S_w(C_{L\alpha wbc2})_{min}(x_{wbc2})_{min} - b_{fmax}^2(C_{mf\alpha})_{max} l_f}{S_{w1}(C_{L\alpha wb1})_{max} + S_w(C_{L\alpha wbc2})_{min}} \\ (x_{AC})_{nom} &= \frac{S_{w1}(C_{L\alpha wb1})_{nom}(x_{wb1})_{nom} + S_w(C_{L\alpha wbc2})_{nom}(x_{wbc2})_{nom} - b_{fmax}^2(C_{mf\alpha})_{nom} l_f}{S_{w1}(C_{L\alpha wb1})_{nom} + S_w(C_{L\alpha wbc2})_{nom}} \\ (x_{AC})_{max} &= \frac{S_{w1}(C_{L\alpha wb1})_{min}(x_{wb1})_{max} + S_w(C_{L\alpha wbc2})_{max}(x_{wbc2})_{max} - b_{fmax}^2(C_{mf\alpha})_{min} l_f}{S_{w1}(C_{L\alpha wb1})_{min} + S_w(C_{L\alpha wbc2})_{max}}\end{aligned} \qquad (2.3.160)$$

Notice that we have assumed that the vehicle AC is situated between the AC of the canard and that of the main wing.

In this case the AC uncertainty range is determined assuming the worst case situation where the correlation between $C_{L\alpha wb1}$ and $C_{L\alpha wbc2}$ is negative. Notice that this is not compatible with the assumption used in Eq. 2.3.158. This means that results based on uncorrelated combinations of Eq. 2.3.158 and Eq. 2.3.160 will include unphysical instances. This may lead to a too conservative estimate of the effects of uncertain aerodynamics. This is a good reason to use a model which includes only the major sources of uncertainty.

A simple expression for the dynamic pitching moment derivative $C_{m\dot{\alpha}}$ was determined in Eq. 2.3.43. This was based on the assumption that the dynamic pitching moment is generated entirely by linear quasi steady lift forces at the AC's of two aerodynamically independent lifting surfaces. For canard configurations with high aspect ratio wings, it is probably a reasonable assumption to ignore wing alone pitching moment damping since the chord is small compared to the longitudinal separation between the canard and main wing. However the assumption of no aerodynamic interaction between the canard and main wing has been shown in Section 2.3.8.4 to be not completely true. Unfortunately the downwash from the canard on the main wing is not instantaneous. This is principally due to the fact that the downwash inducing vortexes from the canard propagate at approximately the freestream velocity from the canard to the main wing. This has the effect that for slow pitching motions, the downwash at the main wing will be in phase with the canard lift. However for faster pitching motions we may in effect have a downwash that is $180°$ out of phase with the canard lift.

For the case of no canard-wing interaction (corresponding to $90°$ phase shift between canard lift and downwash at main wing), we have directly from Eq. 2.3.43:

$$C_{m\dot{\alpha}} = -2\left(\frac{S_{w1}}{S_w}\left(\frac{\Delta x_{w1}}{c_w}\right)^2 C_{L\alpha wb1} + \left(\frac{\Delta x_{w2}}{c_w}\right)^2 C_{L\alpha wb2}\right) \qquad \text{no canard-wing interaction} \tag{2.3.161}$$

For the limit of very slow pitching motions, the downwash at the main wing will be in complete phase with the canard lift. As an example we can look at the situation for positive $\dot{\alpha}$. In this case the canard lift due to pitching motion will be negative, while the main wing lift will be positive. However since the downwash will be *negative* in this case, the result is a larger main wing lift. The net result is thus a larger pitch damping coefficient, then for the case without canard-wing interaction:

$$C_{m\dot{\alpha}} = -2\left(\frac{S_{w1}}{S_w}\left(\frac{\Delta x_{w1}}{c_w}\right)^2 C_{L\alpha wb1} + \left(\frac{\Delta x_{w2}}{c_w}\right)^2\left(\frac{S_w + (S_w)_{inboard}\alpha_{dw\alpha_1}}{S_w}\right) C_{L\alpha wb2}\right) \qquad \text{downwash in phase} \tag{2.3.162}$$

The other extreme case is given by a downwash $180°$ out of phase with the canard lift. In this case the pitch damping coefficient will be reduced by downwash:

$$C_{m\dot{\alpha}} = -2\left(\frac{S_{w1}}{S_w}\left(\frac{\Delta x_{w1}}{c_w}\right)^2 C_{L\alpha wb1} + \left(\frac{\Delta x_{w2}}{c_w}\right)^2\left(\frac{S_w - (S_w)_{inboard}\alpha_{dw\alpha_1}}{S_w}\right) C_{L\alpha wb2}\right) \qquad \text{downwash out of phase} \tag{2.3.163}$$

Since the downwash propagates at approximately the freestream velocity, we could in principle determine the phase shift of the downwash for a certain flight speed and eigenfrequency. However in practice this would complicate the model further. Thus for the time being we will treat the downwash influence as model uncertainty, reflected in an uncertain $C_{m\dot{\alpha}}$ value.

The $C_{m\dot{\alpha}}$ uncertainty range can then be determined as:

$$\begin{aligned}
(C_{m\dot{\alpha}})_{max} &= -2\left(\frac{S_{w1}}{S_w}\left(\frac{\Delta x_{w1}}{c_w}\right)^2(C_{L\alpha wb1})_{min} + \left(\frac{\Delta x_{w2}}{c_w}\right)^2\left(\frac{S_w-(S_w)_{inboard}\alpha_{dw\alpha_1}}{S_w}\right)(C_{L\alpha wb2})_{min}\right) \\
(C_{m\dot{\alpha}})_{nom} &= -2\left(\frac{S_{w1}}{S_w}\left(\frac{\Delta x_{w1}}{c_w}\right)^2(C_{L\alpha wb1})_{nom} + \left(\frac{\Delta x_{w2}}{c_w}\right)^2(C_{L\alpha wb2})_{nom}\right) \\
(C_{m\dot{\alpha}})_{min} &= -2\left(\frac{S_{w1}}{S_w}\left(\frac{\Delta x_{w1}}{c_w}\right)^2(C_{L\alpha wb1})_{max} + \left(\frac{\Delta x_{w2}}{c_w}\right)^2\left(\frac{S_w+(S_w)_{inboard}\alpha_{dw\alpha_1}}{S_w}\right)(C_{L\alpha wb2})_{max}\right)
\end{aligned} \tag{2.3.164}$$

As discussed in Section 2.3.7, the dynamic derivatives $C_{m\kappa_a}$, $C_{L\dot{\alpha}}$ and $C_{L\kappa_a}$ do not affect the phugoid or short period modes. As a result we will use the approximation given by Eq. 2.3.58 for the dynamic pitching moment derivatives, pending an investigation of the complete longitudinal dynamics:

$$C_{m\kappa_a} = C_{m\dot{w}_{gfz}} = C_{m\dot{\alpha}} \tag{2.3.165}$$

Notice that Eq. 2.3.165 implies that the dynamic pitching moment derivatives are completely correlated and thus has identical numerical values for a certain instance.

At the same time we will ignore the dynamic lift derivatives:

$$C_{L\kappa_a} = C_{L\dot{w}_{gfz}} = C_{L\dot{\alpha}} \cong 0 \tag{2.3.166}$$

For simplicity, the dynamic pitching moment derivative $C_{m\dot{U}}$ due to axial wind gradient will be expressed using the nominal value (from Eq. 2.3.59):

$$(C_{m\dot{U}})_{nom} = 4\left(\frac{S_{w1}}{S_w}\left(\frac{\Delta x_{w1}}{c_w}\right)^2 C_{Lwb1} + \left(\frac{\Delta x_{w2}}{c_w}\right)^2 C_{Lwb2}\right) \tag{2.3.167}$$

The aerodynamic pitching moment around the vehicle AC can be determined by summing the individual contributions from the canard, main wing and fuselage. The AC of the complete vehicle is defined as the position of zero pitching moment variation with angle of attack. The angle of attack independent pitching moment C_{m0} of the complete vehicle can then be determined by summing the angle of attack independent contributions. Eq. 2.3.41 already contains the contributions from the lift of the canard and main wing. The fuselage contribution will be assumed negligible compared to the lifting surface contributions (this is exact if the fuselage is top-bottom symmetric). What remains to be included is the pitching moment contributions due to airfoil camber, elevator deflection and wing incidence. For practical reasons we will separate the angle of attack independent pitching moment into two parts:

The elevator (canard flap) pitching moment derivative $C_{m\delta_e}$:

$$C_{m\delta_e} = \frac{S_{w1}}{S_w}\frac{\Delta x_{wf1}}{c_w}(1 + k_{B(W)1})C_{L\alpha w1}\frac{\partial\alpha_{0Lw1}}{\partial\delta_e} \tag{2.3.168}$$

Notice $C_{m\delta_e}$ is referenced to the CG position.

The pitching moment coefficient due to camber and lifting surface incidence:

$$
\begin{aligned}
C_{m0} = {} & -\frac{S_{w1}}{S_w}\left(\frac{x_{wb1}-x_{ac}}{c_w}(1+k_{B(W)1})C_{L\alpha w1}(i_{w1}-\alpha_{0L1})-\frac{c_{w1}}{c_w}C_{mwb1}\right) \\
& -\left(\frac{x_{wbc2}-x_{ac}}{c_w}(1+k_{B(W)2})C_{L\alpha w2}(i_{w2}-\alpha_{0L2})-C_{mwb2}\right)
\end{aligned}
\qquad (2.3.169)
$$

Notice that C_{m0} is referenced to the AC position.

The lift coefficient due to camber and lifting surface incidence:

$$C_{L0} = \frac{S_{w1}}{S_w}(1+k_{B(W)1})C_{L\alpha w1}(i_{w1}-\alpha_{0L1})+(1+k_{B(W)2})C_{L\alpha w2}(i_{w2}-\alpha_{0L2}) \qquad (2.3.170)$$

The elevator (canard flap) lift coefficient derivative $C_{L\delta_e}$:

$$C_{L\delta_e} = -\frac{S_{w1}}{S_w}(1+k_{B(W)1})C_{L\alpha w1}\frac{\partial\alpha_{0Lw1}}{\partial\delta_e} \qquad (2.3.171)$$

For simplicity we have ignored canard-wing interference in deriving C_{L0}, C_{m0}, $C_{m\delta_e}$ and $C_{L\delta_e}$, since it probably only has a relative small effect on these coefficients. As an example the derivative $C_{m\delta_e}$ will be increased slightly by canard-wing interference since a positive canard flap deflection will give a small down load on the main wing. However unlike the stability margin issue, the interference will not change the stability or open loop dynamics significantly.

The total static aerodynamic pitching moment coefficient referenced to the CG can then be determined as:

$$C_m(\alpha,\delta_e) = C_{m0}+C_{m\delta_e}\delta_e-SM(C_{L\alpha}\alpha+C_{L0}) \qquad (2.3.172)$$

Similarly the total lift can be expressed as the sum of the lift due to angle of attack and the lift due to profile camber and wing incidence. Starting with Eq. 2.3.30, the angle of attack independent lift coefficient can be expressed as the sum of two contributions:

The total static lift coefficient can then be determined as:

$$C_L(\alpha,\delta_e) = C_{L0}+C_{L\delta_e}\delta_e+C_{L\alpha}\alpha \qquad (2.3.173)$$

Comparing $C_{L\delta_e}$ with $C_{m\delta_e}$ shows that:

$$C_{m\delta_e} = -\frac{\Delta x_{wf1}}{c_w}C_{L\delta_e} \qquad (2.3.174)$$

The advantage of the formulations in Eq. 2.3.172 and Eq. 2.3.173 is that C_{m0} and C_{L0} are constants in the equations of motion, this means that they have no first order influence on the dynamics and stability of the vehicle. Due to their minor influence on the stability, they can be treated as fixed values without any uncertainty.

Since both $C_{L\delta_e}$ and $C_{m\delta_e}$ have a large influence on the open loop aerodynamic gains, uncertainties in these derivatives may affect the closed loop dynamics and stability. It is thus appropriate to introduce an uncertainty range on both coefficients. The uncertainty range on $C_{L\delta_e}$ can be determined as:

$$\begin{aligned}
(C_{L\delta_e})_{min} &= \frac{S_{w1}}{S_w}(1 + k_{B(W)1})(C_{L\alpha w1})_{min}\left(\frac{\partial\alpha_{0Lw1}}{\partial\delta_e}\right)_{min} \\
(C_{L\delta_e})_{nom} &= \frac{S_{w1}}{S_w}(1 + k_{B(W)1})(C_{L\alpha w1})_{nom}\left(\frac{\partial\alpha_{0Lw1}}{\partial\delta_e}\right)_{nom} \\
(C_{L\delta_e})_{max} &= \frac{S_{w1}}{S_w}(1 + k_{B(W)1})(C_{L\alpha w1})_{max}\left(\frac{\partial\alpha_{0Lw1}}{\partial\delta_e}\right)_{max}
\end{aligned} \tag{2.3.175}$$

Notice that the uncertainties of $C_{L\alpha wb1}$ and $C_{L\delta_e}$ are correlated.

We can then determine the uncertainty range of $C_{m\delta_e}$ as:

$$\begin{aligned}
(C_{m\delta_e})_{min} &= \left(\frac{\Delta x_{wf1}}{c_w}\right)_{min}(C_{L\delta_e})_{min} \\
(C_{m\delta_e})_{nom} &= \left(\frac{\Delta x_{wf1}}{c_w}\right)_{nom}(C_{L\delta_e})_{nom} \\
(C_{m\delta_e})_{max} &= \left(\frac{\Delta x_{wf1}}{c_w}\right)_{max}(C_{L\delta_e})_{max}
\end{aligned} \tag{2.3.176}$$

Since the relative uncertainty of $\Delta x_{wf1}/c_w$ is generally small, the uncertainty of $C_{m\delta_e}$ is highly correlated with the uncertainty of $C_{L\delta_e}$.

2.3.8.6 Zero lift drag

In the simple aerodynamic model presented in Section 2.3.6, only the drag of the lifting surfaces where included. Unfortunately from a performance point of view, a major part of the drag of most vehicles is caused by nonlifting airframe parts such as the fuselage, landing gear (if not retracted) and other protrusions into the airstream. The drag of vehicle airframe components can be treated as two contributions; zero lift drag and drag due to lift. For this analysis we will assume that only the canard and main wing creates drag due to lift, while all other airframe components only create lift independent drag.

For streamlined airframe components, the best simple zero lift drag estimation method is based on flat plate drag data (Ref. 8, chapter 12.5). The drag of a smooth flat plate parallel to the airstream is expressed by the *skin friction* coefficient C_f which is the drag coefficient of the plate based on the *wetted* surface area. Unfortunately from a computational point of view, the skin friction coefficient depends on whether the flow is laminar or turbulent. This can only be judged from such flow features as the surface roughness, freestream turbulence and pressure distribution. However since the skin friction coefficient of turbulent flow is always higher then that of laminar flow, we can conservatively estimate the skin friction coefficient of streamlined airframe components by using the turbulent skin friction coefficient (Ref. 8, Eq. 12.27):

$$C_f \cong (C_f)_{turbulent} = \frac{0.455}{(\log(Re))^{2.58}} \tag{2.3.177}$$

Where $Re \equiv \frac{\rho U l}{\mu}$ is the Reynolds number based on the length l in the flow direction of the airframe component.

Since the flow around any 3 dimensional body also exerts a pressure drag which is not found in ideal flat plate flow, the drag coefficient of an airframe component can be corrected by the empirical *Form Factor* (FF) that depends on the slenderness of the component (Ref. 8, p. 344&345). Lastly the drag may also be increased by the presence of other airframe components that increase the local flow speed and thus the drag. This is expressed by the *interference factor* Q (Ref. 8, p. 346). A more complete discussion of these concepts is provided in (Ref. 8, chapter 12.5). Below we will use some of the results from this reference, with the implicit assumption that the mach number is small.

The drag coefficient of the fuselage referenced to the main wing area is given by:

$$C_{Df} = \frac{C_{ff}FF_f S_{wet,f} + C_{Dbase,f} S_{base,f}}{S_w} \tag{2.3.178}$$

Where the fuselage skin friction coefficient is computed using the Reynolds number corresponding to the fuselage length l_f. The fuselage interference factor is 1.0. The fuselage form factor is a function of the slenderness f_f:

$$FF_f = 1 + \frac{60}{f_f^3} + \frac{f_f}{400} \qquad f_f = \frac{l_f}{\sqrt{(4/\pi)S_{fmax}}} \tag{2.3.179}$$

Where S_{fmax} is the maximum fuselage crossection area.

The wetted fuselage area is denoted by $S_{wet,f}$. The drag due to a cut off, aft facing surface with the projected area $S_{base,f}$ on the fuselage is given by $C_{Dbase,f}$, which can be approximated by:

$$C_{Dbase,f} = 0.139 \tag{2.3.180}$$

The zero lift drag on the canard, wing and vertical fin can also be estimated using the skin friction coefficient. For a streamlined lifting surface, the form factor can be determined as:

$$FF_w = \left(1 + \frac{0.6}{(x/c)_m}\left(\frac{t}{c_w}\right) + 100\left(\frac{t}{c_w}\right)^4\right)(\cos(\Lambda_m))^{0.28} \tag{2.3.181}$$

Where $(x/c)_m$ is the longitudinal position of the maximum wing profile thickness, (t/c_w) is the mean wing profile maximum thickness ratio and Λ_m is the sweep of the maximum wing profile thickness line. For simplicity we can use $(x/c)_m \cong 0.3$ and $\Lambda_m \cong \Lambda_{c/4}$ for subsonic airfoils.

The interference factor Q_w can be taken as equal to one for a high or mid wing, while it may be greater then one for a low wing.

The zero lift drag coefficient of the wing is then given by:

$$C_{D0w} = \frac{C_{fw}FF_w Q_w S_{wet,w}}{S_w} \tag{2.3.182}$$

Where the skin friction coefficient is based on the Reynolds number of the mean aerodynamic wing chord c_w.

We will assume that the wetted area of a wing with a typical wing profile is equal to twice the exposed wing area:

$$S_{wet,\,w} = 2S_w \tag{2.3.183}$$

The last major drag contribution is “miscellaneous” drag. This is drag due to airframe components that have a shape that is too irregular to be analysed using the skin friction coefficient. The most important miscellaneous item drag for many aircraft is a fixed landing gear. The miscellaneous drag is expressed in terms of the “drag area” of a component, for a normal landing gear wheel the drag area is (Ref. 8, Table 12.5):

$$(D/q)_{wheel} = 0.25S_{wheel} \tag{2.3.184}$$

Where (D/q) is the drag pr. unit dynamic pressure q and S_{wheel} is the projected frontal area of the wheel.

If the wheels are mounted on a strut with circular crossection, the drag area of this can be approximated as:

$$(D/q)_{strut} = 0.3S_{strut} \tag{2.3.185}$$

Where S_{strut} is the projected frontal area of the strut.

Miscellaneous drag contributions from other airframe components can be found in (Ref. 8, p. 346-351).

The zero lift drag of the complete vehicle can then be determined by adding the contributions from the individual airframe components:

$$C_{D0} = C_{Df} + C_{D0w1} + C_{D0w2} + C_{D0fin} + \frac{\sum (D/q)}{S_W} \tag{2.3.186}$$

Where $\sum (D/q)$ is the sum of all miscellaneous drag areas and C_{D0fin} is the zero lift drag of the vertical fin.

2.3.8.7 Induced drag

As mentioned in Section 2.3.6, the induced drag coefficient (i.e. the drag due to lift) of a lifting surface is approximately proportional to the square of the lift coefficient. For a wing of reasonable aspect ratio with elliptic lift distribution, the induced drag can be determined as (Ref. 8, p. 360):

$$(C_{Dw,\,induced})_{ideal} = \frac{C_{Lw}^2}{\pi A_w} = K_{ideal} C_{Lw}^2 \qquad K_{ideal} = \frac{1}{\pi A_w} \tag{2.3.187}$$

This is the minimum induced drag coefficient of a wing with prescribed lift coefficient and aspect ratio. Any deviation from the elliptic lift distribution will make the induced drag coefficient higher.

This can be quantified by the Oswald span efficiency "e"(Ref. 8, p. 360). Using the Oswald span efficiency, the constant K can be expressed as:

$$K = \frac{1}{\pi A_w e} \tag{2.3.188}$$

For wings with little or no sweep, the Oswald span efficiency can be determined using the following empirically derived expression (Ref. 8, Eq. 12.49):

$$e = 1.78(1 - 0.045A_w^{0.68}) - 0.64 \tag{2.3.189}$$

Since we have two lifting surfaces, the canard and the main wing, we can determine the total induced drag of the vehicle as:

$$C_{D,\,induced} = \frac{S_{w1}}{S_w} K_{w1} C_{Lw1}^2 + K_{w2} C_{Lw2}^2 \tag{2.3.190}$$

Which is based on the main wing area S_w.

2.3.9 UAV case study:

The theory derived above will be used to determine the aerodynamic characteristics of a small unmanned aerial vehicle with canard configuration. The vehicle planform geometry is shown in Figure 2.19 below:

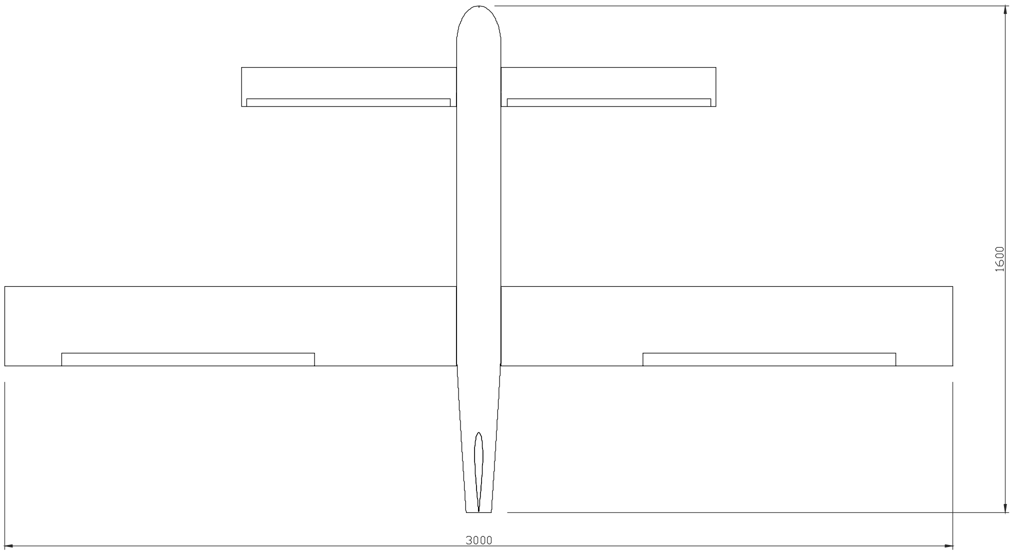

FIGURE 2.19 Electric UAV concept study (dimensions in mm).

The main aerodynamic dimensions and parameters of the vehicle are listed in Table 2.1 below:

Total main wing span	$b_{wb} = 3.0m$
Main wing area	$S_w = 0.715m^2$
Main wing chord	$c_w = 0.25m$

Tabel 2.1 UAV case study.

Main wing aspect ratio	$A_w = 11.4$
Total canard span	$b_{wb1} = 1.5m$
Canard area	$S_{w1} = 0.17m^2$
Canard chord	$c_{w1} = 0.125m$
Canard aspect ratio	$A_{w1} = 10.9$
Fuselage width	$b_{fmax} = 0.14m$
Fuselage length	$l_f = 1.6m$
Fuselage wetted area	$S_{wet,f} = 0.7759m^2$
Fuselage base area	$S_{base,f} = 0.0062m^2$
Vertical fin area[a]	$S_{fin} = 0.0437m^2$
Vertical fin chord	$c_{fin} = 0.1857m^2$
Vertical fin aspect ratio	$A_{fin} = 1.43$
Total wetted area	$S_{wet,t} = 2.6333m^2$
Misc. drag wheels	$(D/q)_{wheels} = 0.0014m^2$
Misc. drag wheel struts	$(D/q)_{struts} = 0.0018m^2$
Total misc. drag area	$(D/q)_{total} = 0.0032m^2$
Maximum mass	$m = 7.0kg$
Total wing loading	$\frac{m}{S_{w1} + S_w} = 7.9kg/m^2$

Tabel 2.1 UAV case study.

---

[a] Vertical fin size is quessed at this point, the final fin size is determined later.

Canard airfoil name	Mod. Clark-Y 16%
Percent thickness	16% of chord
Percent flap chord	25% of chord

Tabel 2.2 Canard airfoil geometry.

Main wing airfoil name	Clark-Y
Percent thickness	11.72% of chord
Percent aileron chord	20% of chord

Tabel 2.3 Main wing airfoil geometry.

The aerodynamic properties of the airfoils used for the canard and main wing have been computed using the xfoil program (Ref. 17). Due to the relative low speed of the UAV, compared to larger aircraft, the Reynolds number, airfoil surface roughness and freestream turbulence has a significant influence on not only the drag but also on the lift coefficient curve slope of the airfoils. This is shown in Figure 2.20 below:

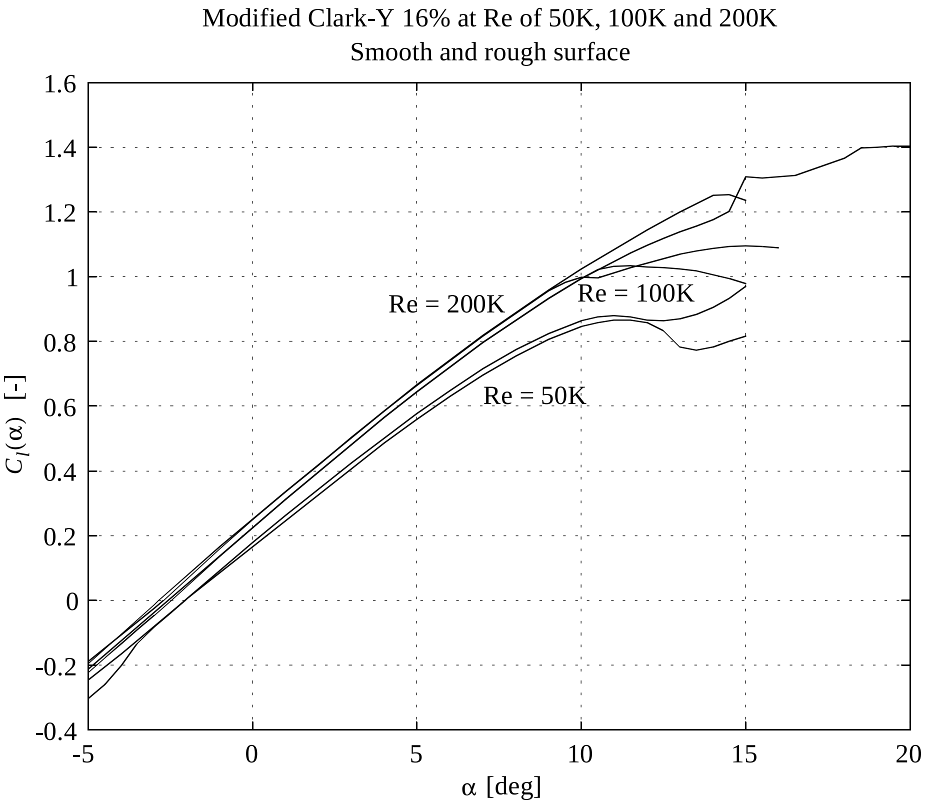

FIGURE 2.20 Computed canard wing profile lift coefficient polars (zero flap deflection).

The main aerodynamic properties of the canard and main wing airfoils in the expected Reynolds number range is summarized in the following tables:

Name	Value		
	Min	Nominal	Max
Re [a]	50×10^3	-	200×10^3
$C_{l\alpha}$ [rad^{-1}]	4.71	5.65	6.28
α_{0L}	$-3.0°$	$-2.5°$	$-2.0°$
$C_{l,\,max}$	0.9	1.0	1.4
$(\partial\alpha_{0L})/(\partial\delta_e)$	-0.36	-0.30	-0.24
$(C_{l,\,max})/(\partial\delta_e)$ [rad^{-1}]	0.0	0.5	1.15

Tabel 2.4 Canard airfoil properties.

---

a. Based on the canard chord.

Name	Value		
	Min	Nominal	Max
Re [a]	100×10^3	-	400×10^3
$C_{l\alpha}$ [rad^{-1}]	5.25	5.90	6.28
α_{0L}	$-5.2°$	$-4.3°$	$-3.5°$
$C_{l,\,max}$	1.20	1.25	1.35

Tabel 2.5 Main wing airfoil properties.

---

[a] Based on the wing chord.

Using the aerodynamic airfoil properties listed in Table 2.4 and Table 2.5 and the equations for the linear aerodynamic coefficients given in Section 2.3.8, gives the following numerical values:

Name	Value		
	Min	Nominal	Max
x_{AC} **[m]**	0.7466	0.7848	0.8261
$C_{l\alpha}$	5.2740	6.1602	7.2687

Tabel 2.6 UAV AC position and lift curve slope range (angles in radians).

At first it seems like the relative uncertainty for the AC and the lift curve slope are more or less the same, however this is deceiving. According to Section 2.3.7.1, the important aerodynamic parameter is the stability margin (SM). Since the stability margin must be small but positive to achieve both static stability and a reasonable maximum lift coefficient, it follows that the impact of the AC uncertainty on the dynamics of the vehicle will generally be much larger then that of the lift curve slope uncertainty.

The AC uncertainty range is shown on a side view of the UAV below:

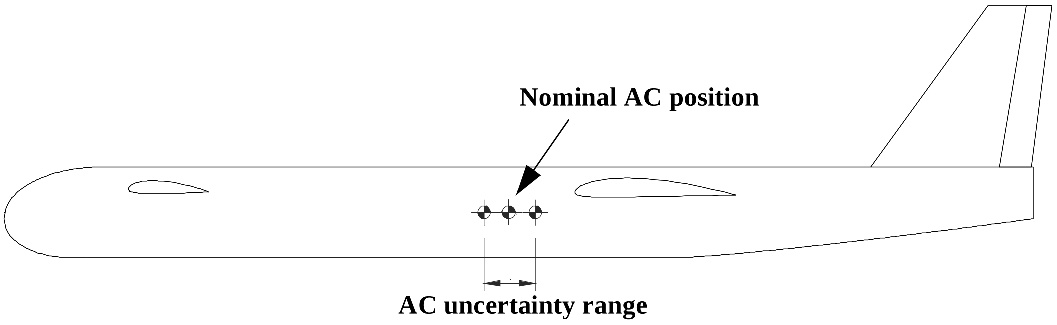

FIGURE 2.21 UAV AC uncertainty range.

Before we can proceed with the dynamic analysis, we need to determine the CG position. The CG position will be chosen by defining a minimum value for the stability margin. Based on (Ref. 8, Fig. 16.4), the following minimum stability margin will be used for the rest of this case study:

$$(SM)_{min} \equiv 0.05 \tag{2.3.191}$$

Using the AC position uncertainty range from Table 2.6, places the desired CG at the following position:

$$x_{CG} = (x_{AC})_{min} - c_w(SM)_{min} = 0.734m \tag{2.3.192}$$

We will not use any uncertainty for the CG since the CG position is fixed during a flight and is easily determined with an accuracy better then 1 mm using a simple balancing procedure.

We are now able to determine the uncertainty range for all the important static and dynamic linear aerodynamic coefficients:

Name	Value			
	Min	Nominal	Max	Percent uncertainty
x_{AC} **[m]**	0.7466	0.7848	0.8261	+5.3%/-4.9%
SM	0.050	0.203	0.368	+81.3%/-75.4%
$C_{l\alpha}$	5.274	6.160	7.269	+18.0%/-14.4%
$C_{m\dot{\alpha}}$	-22.46	-19.49	-15.81	+18.9%/-15.2%
$(\partial\alpha_{0Lw1})/(\partial\delta_e)$	-0.342	-0.285	-0.228	+20%/-20.0%
Δx_{wf1} [m]	-0.486	-0.486	-0.486	0%

Tabel 2.7 UAV linear longitudinal aerodynamic properties (angles in radians).

Notice that since the wing and canard sweeps are zero, the uncertainty on the canard AC position and thus on Δx_{wf1} is zero according to the model.

It is readily apparent that the relative stability margin uncertainty is much larger then the relative uncertainty of any other aerodynamic coefficient or parameter. Since the stability margin is a very important parameter for the open loop stability and response of the short period mode, it follows that the longitudinal control system should at least be checked for robustness against the stability margin variations from Table 2.7.

2.3.10 Lift to drag ratio

The lift to drag ratio is a very important indicator of the performance of the complete UAV. The drag “polar” of the vehicle is constructed assuming steady flight at constant altitude. This means that the drag is determined using the following conditions:

- The total lift is equal to the weight of the UAV.
- The aerodynamic pitching moment referenced to the CG is zero.

The lift equilibrium equation is given by:

$$mg = q(C_{L0} + C_{L\delta_e}\delta_e + C_{L\alpha}\alpha)S_w \tag{2.3.193}$$

The equation for pitching moment equilibrium is:

$$0 = C_{m0} + C_{m\delta_e}\delta_e - SM(C_{L\alpha}\alpha + C_{L0}) = C_{m0} - \frac{\Delta x_{wf1}}{c_w}C_{L\delta_e}\delta_e - SM(C_{L\alpha}\alpha + C_{L0}) \tag{2.3.194}$$

The problem is thus to determine the elevator angle δ_e in such a way that both Eq. 2.3.193 and Eq. 2.3.194 are satisfied at a given dynamic pressure q. The derivative $C_{L\delta_e}$ is given by Eq. 2.3.175.

The total lift coefficient C_L can be determined directly using vertical equilibrium:

$$C_L = \frac{mg}{qS_w} \tag{2.3.195}$$

It is apparent from Eq. 2.3.193 and Eq. 2.3.194, that this results in a linear equation with two unknowns:

$$\begin{bmatrix} C_{L\delta_e} & C_{L\alpha} \\ \frac{\Delta x_{wf1}}{c_w}C_{L\delta_e} & SMC_{L\alpha} \end{bmatrix} \begin{bmatrix} \delta_e \\ \alpha \end{bmatrix} = \begin{bmatrix} \frac{mg}{qS_w} - C_{L0} \\ C_{m0} - SMC_{L0} \end{bmatrix} \Leftrightarrow \tag{2.3.196}$$

$$\begin{bmatrix} \delta_e \\ \alpha \end{bmatrix} = \begin{bmatrix} C_{L\delta_e} & C_{L\alpha} \\ \frac{\Delta x_{wf1}}{c_w}C_{L\delta_e} & SMC_{L\alpha} \end{bmatrix}^{-1} \begin{bmatrix} C_L - C_{L0} \\ C_{m0} - SMC_{L0} \end{bmatrix}$$

According to the discussion in Section 2.3.9, the stability margin (SM) uncertainty is the single most important longitudinal aerodynamic uncertainty. For this reason, we will compute δ_e and α using nominal values of all coefficients, except the stability margin. This gives δ_e and α for 3 instances; low, nominal and high stability margin.

Having determined equilibrium values of δ_e and α the lift coefficient of the canard can be determined as:

$$C_{Lwb1} = C_{L\alpha wb1}\alpha + (1 + k_{B(W)1})C_{L\alpha w1}(i_{w1} - \alpha_{0Lw1}) + \frac{S_w}{S_{w1}}C_{L\delta_e}\delta_e \tag{2.3.197}$$

The main wing lift coefficient can then be determined as:

$$C_{Lwbc2} = C_L - \frac{S_{w1}}{S_w}C_{Lwb1} \tag{2.3.198}$$

Where the lift coefficient C_L of the complete vehicle is determined using Eq. 2.3.195.

Using this procedure for the concept vehicle in Section 2.3.9 gives trim lift coefficients of the canard and main wing as function of indicated airspeed for 3 values of the stability margin; low, nominal and high:

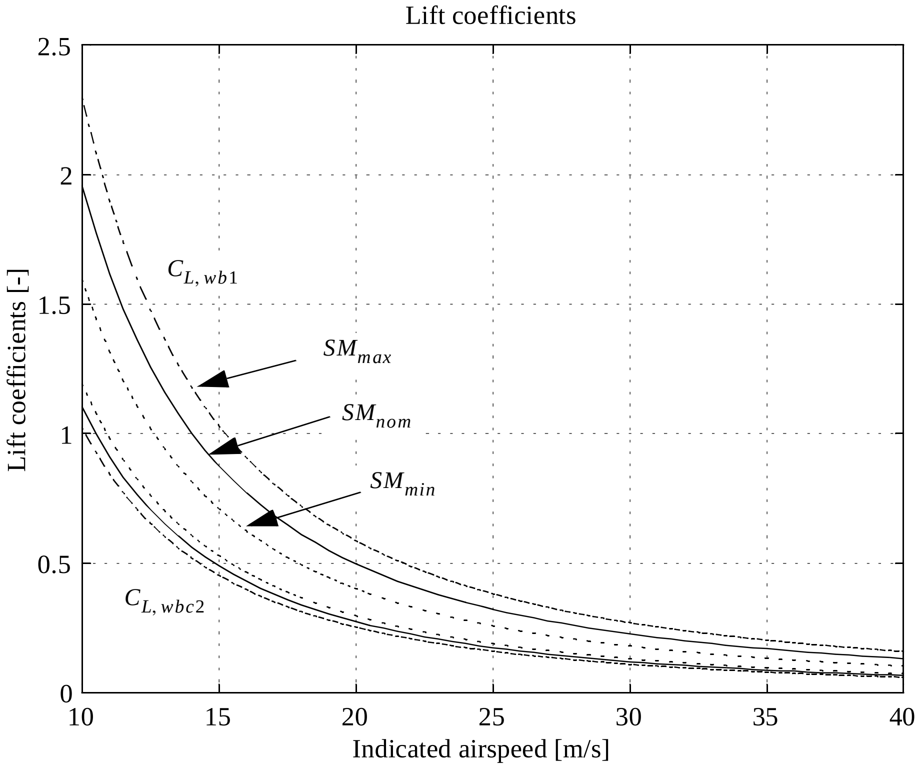

FIGURE 2.22 Lift coefficients of canard and main wing of UAV case study as function of indicated airspeed and stability margin.

Since the lift of canard is limited due to flow separation (stall), the minimum level flight speed is limited by the maximum stability margin and the minimum value of the canard stall lift coefficient. This means that while the lowest limit of the stability margin is critical for static stability, the highest limit of the stability margin is critical for available lift. Since the minimum value of the maximum canard lift coefficient is approximately 0.9 according to Table 2.4, Figure 2.22 shows that the guaranteed minimum flight speed is approximately equal to 16 m/s.

Knowing the distribution of lift between the canard C_{Lwb1} and the main wing C_{Lwbc2}, we can determine the induced drag using Eq. 2.3.190:

$$C_{D,\,induced} = \frac{S_{w1}}{S_w} K_{w1} C_{Lwb1}^2 + K_{w2} C_{Lwbc2}^2 \qquad (2.3.199)$$

Notice that the wing-body lift coefficient is used instead of the wing alone lift, this should give a conservative estimate of the induced drag.

The zero lift drag is computed using flat plate drag data for the wings and fuselage and drag area data for the undercarriage. The total drag $C_{D,\,total}$ is then computed as the sum of the induced and zero lift drag contributions.

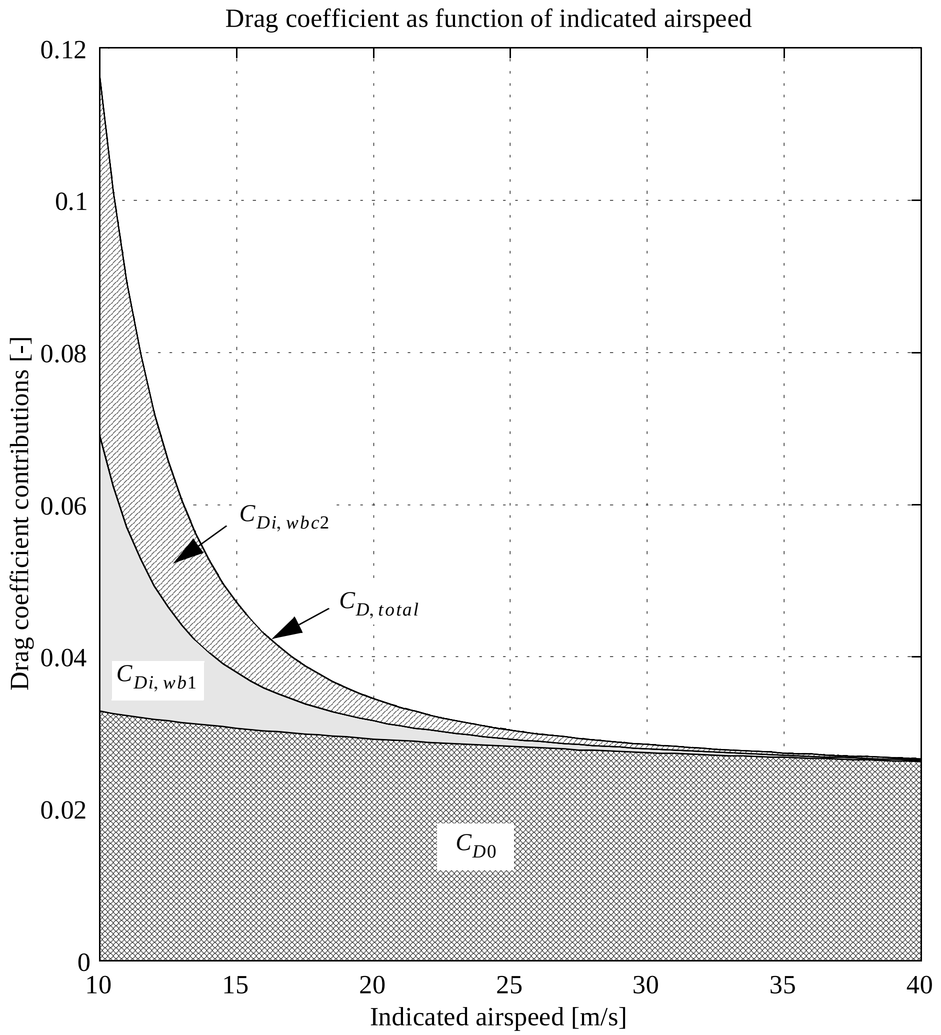

FIGURE 2.23 Drag of UAV case study as function of airspeed at standard sealevel conditions.

Where $C_{Di,\,wb1}$ is the induced drag of the canard referenced to the main wing area and $C_{Di,\,wbc2}$ is the induced drag of the main wing. Figure 2.23 shows that the induced drag is only important at low flight speeds. Notice that Figure 2.23 is based on the nominal SM margin.

It is standard practice to express the aerodynamic efficiency in terms of the lift to drag ratio in level flight. This gives the following results for the concept study UAV:

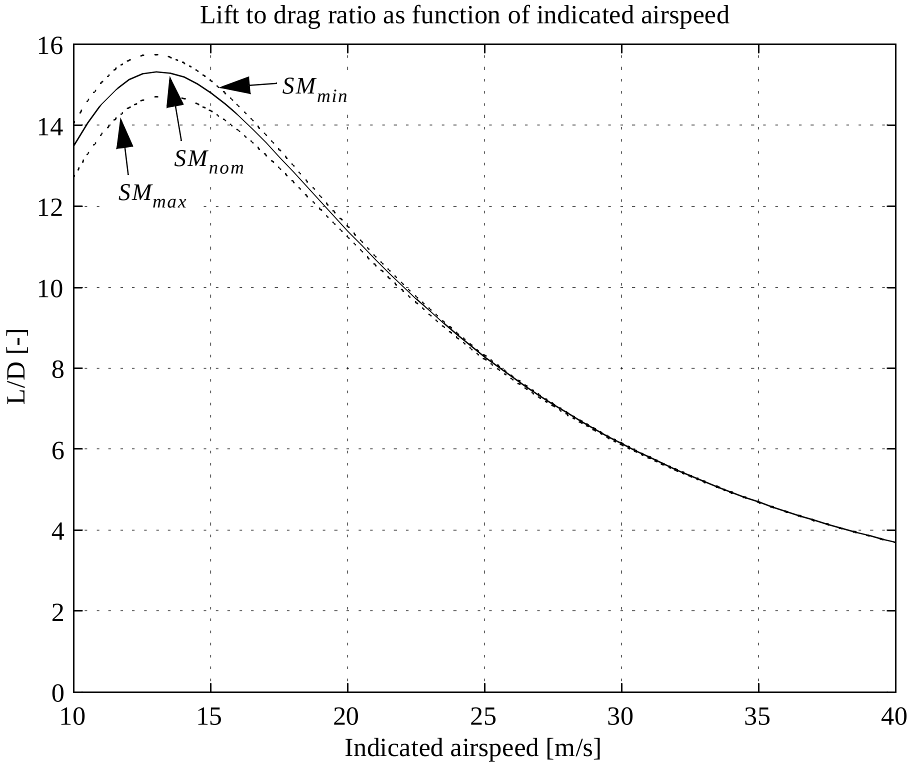

FIGURE 2.24 Lift to drag ratio of UAV case study as function of airspeed at standard sealevel conditions.

It is apparent from Figure 2.24 that the effect of the stability margin uncertainty on the predicted performance is small compared to the inherent uncertainty in the model used to predict the total drag. We can thus conclude that for the vehicle used in this analysis, the drag can be adequately predicted without including the aerodynamic center uncertainty. This conclusion will be used in the following analysis of the propulsion system.

2.3.11 Electric propulsion system model

The electric propulsion system consists of two DC-motors connected in series. Each motor drives a relatively large propeller at a relatively slow speed through a fixed mechanical gearing. The details of the propulsion system mathematical models are described in Appendix A. In this section we will describe the main characteristics of the system.

A schematic drawing of the propulsion system is shown below:

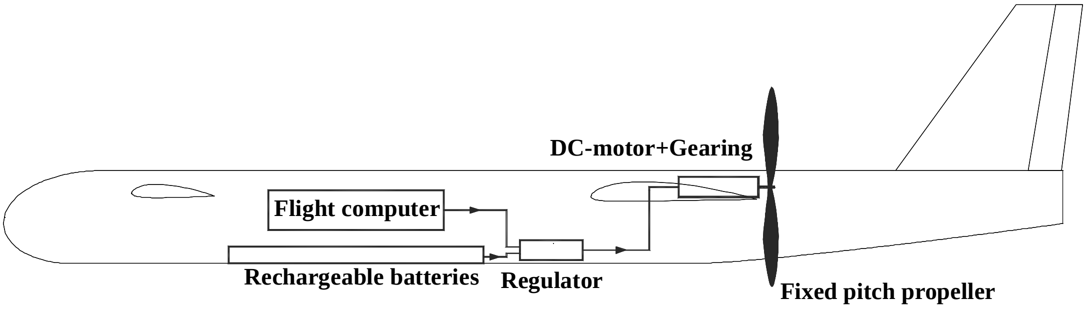

FIGURE 2.25 UAV propulsion system.

As shown in Figure 2.25 one propulsion unit consisting of a motor with fixed gearing and a fixed pitched propeller, is mounted on each side of the fuselage on the main wing.

A simple model of the available torque τ_m from a permanent magnet DC-motor with motor current I_m is given by (Ref. 18):

$$\tau_m = k_m I_m - \tau_c = k_m \frac{V_m - k_e \omega_m}{R_m} - \tau_c \qquad I_m = \frac{V_m - k_e \omega_m}{R_m} \tag{2.3.200}$$

Where V_m is the voltage at the motor terminals, ω_m is the angular velocity of the motor shaft, R_m is the combined resistance of the motor windings and commutators, k_m is the motor "torque" constant, k_e is the motor "induced voltage" constant and τ_c is the constant motor coulomb friction torque. It can be shown that if a consistent set of units are used, the numerical value (but not the dimension) of k_m and k_e will be the same.The net result is that the static (constant speed) and dynamic (variable speed) characteristics of the DC motor can be described by three parameters: k_m, R_m and τ_c.

The characteristics of a typical DC-motor designed for electric propulsion of model aircraft are shown below:

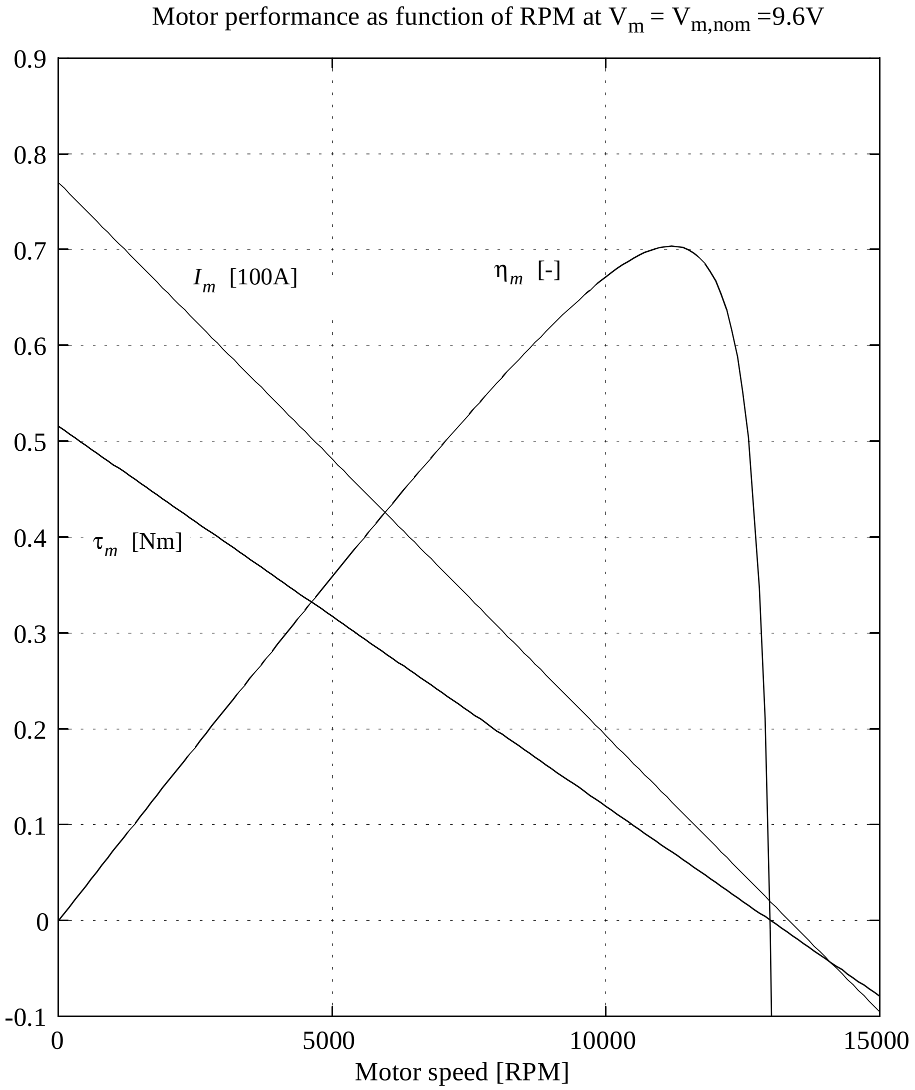

FIGURE 2.26 Typical DC-motor characteristics.

Figure 2.26 shows that for this particular motor, the maximum efficiency at nominal voltage is just over 70%. It is also worth noting two other typical DC-motor characteristics at constant voltage; the maximum efficiency occurs close to the idle speed at low loading and the available torque at low speeds is very large. This means that if the power system is optimized for efficient cruise, there will still be a large reserve power available to turn a fixed pitch propeller at low speed conditions during takeoff. Thus in this respect an electric motor has an advantage over internal combustion engines for driving fixed pitch propellers.

The fixed gearing between the motor and propeller makes it possible to use a larger and more aerodynamically efficient propeller.

The gear ratio N_{gear} is defined as the ratio between the output angular velocity ω_{out} and the input angular velocity ω_{in}:

$$\omega_{out} = N_{gear}\omega_{in} \tag{2.3.201}$$

The gear efficiency η_g is assumed constant:

$$\tau_{out} = \eta_g \frac{\omega_{in}}{\omega_{out}}\tau_{in} = \eta_g \frac{\tau_{in}}{N_{gear}} \tag{2.3.202}$$

Where τ_{out} is the output torque and τ_{in} is the input torque.

The propeller thrust F_{th} and shaft power W_p are determined as:

$$F_{th} = k_T \rho f_p^2 D_p^4 \tag{2.3.203}$$

And:

$$W_p = k_P \rho f_p^3 D_p^5 \tag{2.3.204}$$

Where k_T is the nondimensional propeller thrust coefficient and k_P is the nondimensional propeller power coefficient. The atmospheric air density is ρ, f_p is the number of revolutions pr. second of the propeller and D_p is the propeller diameter.

It can be shown the nondimensional propeller characteristics k_T and k_P are functions of the *advance ratio* J defined by (Ref. 19, p. 467):

$$J \equiv \frac{U}{f_p D_p} = \frac{U}{2\pi\omega_p D_p} \tag{2.3.205}$$

Where f_p is the number of revolutions pr. second of the propeller and ω_p is the corresponding propeller angular velocity. The free airspeed (i.e. the UAV airspeed) is given by U.

It is important to note the extreme dependence on the propeller diameter for geometrically similar propellers under similar operating conditions.

The propeller efficiency η_p can be determined from k_T and k_P as (Ref. 19, p. 467):

$$\eta_p = \frac{k_T}{k_P} J \tag{2.3.206}$$

From which the intuitive conclusion can be drawn that the efficiency is maximized by increasing the ratio between the thrust and torque, at a given operating point.

The shapes of $k_T(J)$ and $k_P(J)$ can be calculated from the propeller geometry using blade element theory (see Appendix A.2). However this is quit tedious because of the effort involved in determining the propeller geometry. The main problem being that the detailed geometry of commercially available model airplane propellers is not readily available.

What is generally available is the diameter and the pitch P (conceptually equivalent to the pitch of a screw) of model airplane propellers. From these two parameters we may define the nondimensional pitch P' as:

$$P' \equiv \frac{P}{D_p} \tag{2.3.207}$$

Using correlation rules proposed in Appendix A.3, we will correlate $k_T(J)$ and $k_P(J)$ of our propeller to that of a low pitch two bladed propeller with known thrust and power coefficients (from measured data in (Ref. 20, Fig. 5)).

The correlated characteristics of a typical low pitch propeller are shown below

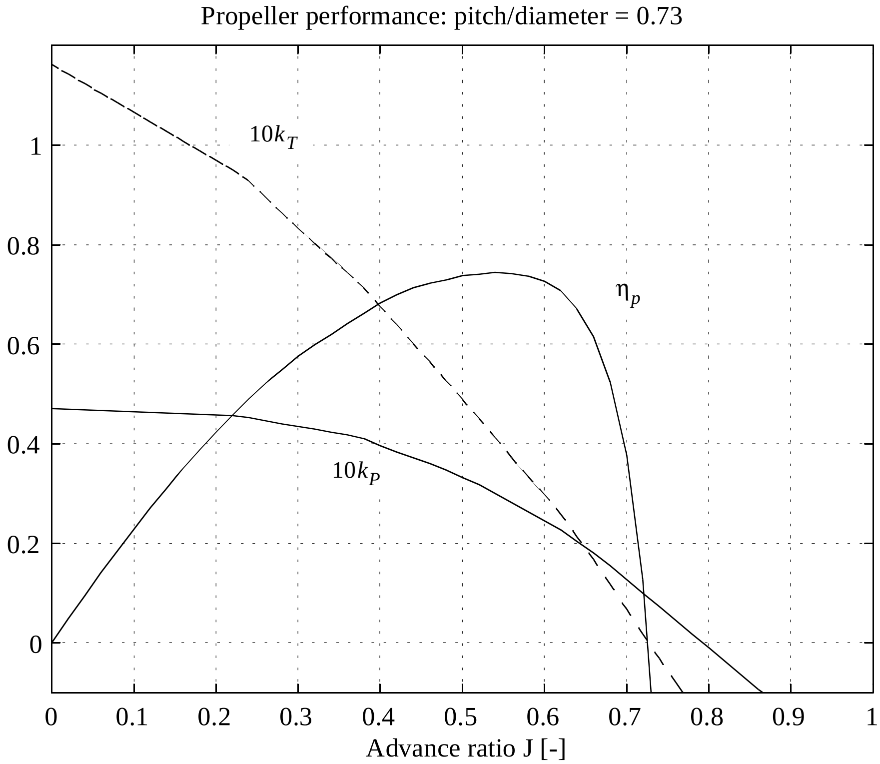

FIGURE 2.27 Typical characteristics of a low pitch propeller ($0 < P' \leq 1$).

For UAV performance analysis, the steady state performance of the propulsion system is of particular interest. Lets assume that we want to compute the propulsion system performance at a specified airspeed U.

For steady level flight, the total propulsion system thrust $F_{th,\text{total}}$ must be equal to the total drag of the trimmed vehicle:

$$F_{th,\text{total}} = qC_D S_w \qquad q \equiv \frac{1}{2}\rho U^2 \tag{2.3.208}$$

Where the total drag coefficient C_D for level flight is computed in Section 2.3.10.

Combining this with Eq. 2.3.203 gives:

$$k_T f_p^2 D_p^4 = \frac{F_{th,\text{total}}}{N_p} = F_{th} \tag{2.3.209}$$

This nonlinear equation can then be solved for the propeller speed f_p, since the thrust coefficient is obtained from the advance ratio. The total number of identical propeller-motor systems is given by N_p.

Having determined the propeller speed, the next step is to determine the propeller power W_p using Eq. 2.3.204. Since the propeller is connected to the motor using a fixed transmission with a gear ratio of N_{gear} and an efficiency of η_g, the motor shaft power and speed can be determined as:

$$\omega_m = \frac{\omega_p}{N_{gear}} = \frac{2\pi f_p}{N_{gear}} \qquad W_m = \frac{W_p}{\eta_g} \tag{2.3.210}$$

Where $N_{gear} < 1$ if the motor is to operate at a higher speed then the propeller and W_m is the available motor shaft power.

Since the available motor power can be determined as $W_m = \tau_m \omega_m$, Eq. 2.3.200 can be used to determine the necessary motor voltage V_m as:

$$W_m = \left(k_m \frac{V_m - k_e \omega_m}{R_m} - \tau_c\right)\omega_m \quad \Leftrightarrow \quad V_m = \frac{R_m}{k_m}\left(\frac{W_m}{\omega_m} + \tau_c\right) + k_e \omega_m \tag{2.3.211}$$

The corresponding motor current I_m can be determined as:

$$I_m = \frac{V_m - k_e \omega_m}{R_m} \tag{2.3.212}$$

We can now determine the motor efficiency from the definition given by Eq. A.6:

$$\eta_m \equiv \frac{W_m}{W_e} = \frac{\tau_m \omega_m}{V_m I_m} \tag{2.3.213}$$

The overall propulsion system efficiency is similarly given by:

$$\eta_{propsys} \equiv \frac{F_{th} U}{W_e} = \frac{F_{th} U}{V_m I_m} \tag{2.3.214}$$

The results of these calculations can then be shown in graphical form as function of airspeed:

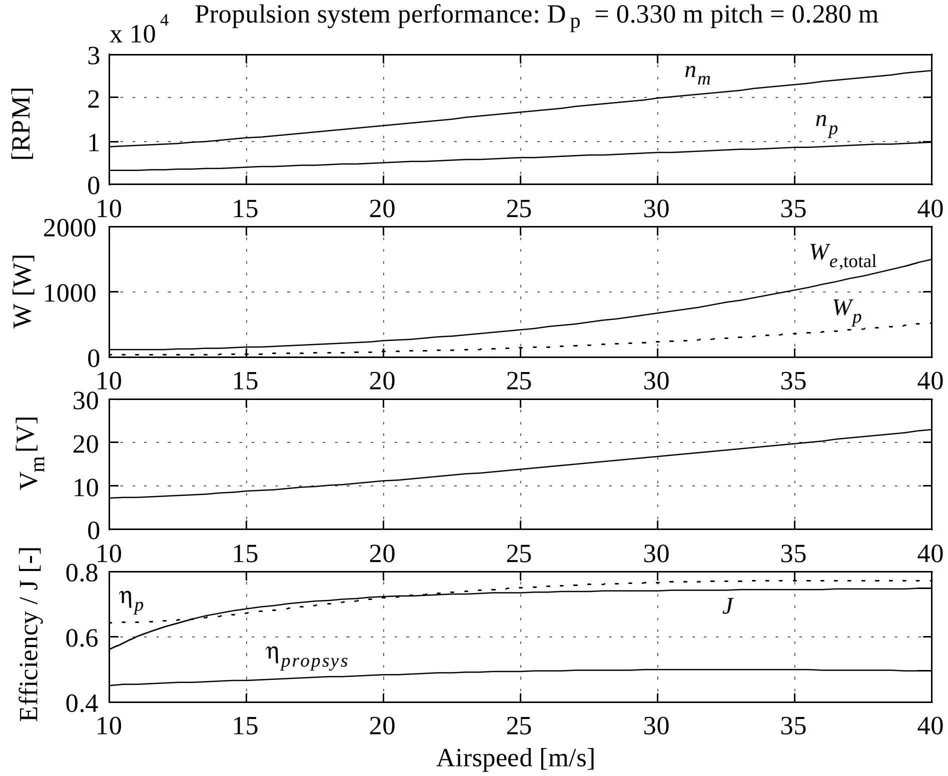

FIGURE 2.28 Concept study UAV propulsion system characteristics for level flight at sea level conditions.

Since the available electric energy from rechargeable batteries is limited, it is important for maximum range of the UAV to maximize the amount of propulsive work done for a unit amount of electric energy. In theory this should be done using a complete typical mission profile consisting of takeoff, climb, cruise, descent and landing. In practice it is easier and more transparent to maximize the efficiency at cruise, while checking that the system has sufficient thrust for takeoff, climb and aborted landings.

Because the propulsion system designer in practice has to use standard components, the objective is to choose a suitable propeller based on the diameter and pitch and a suitable motor-gear combination. Since the gearing and motor is typically integrated into one unit, the design problem has three variables. Figure 2.28 shows the propulsion system performance for steady level flight at sealevel conditions for the concept UAV powered by two identical electric motors. The total electric power supplied to the propulsion motors is denoted by $W_{e,\text{total}}$. Notice that since the induced drag is negligible at high speeds, the necessary propulsive power is roughly proportional to the cube of the airspeed. In practice the optimum cruise speed of the vehicle as designed would probably be close to the minimum flight speed, since the lift to drag ratio is best at low speeds (see Figure 2.24). For a cruise speed of 20 m/s, Figure 2.28 shows that the total electric power required is equal to approximately 250 W.

For good takeoff and climb performance, there needs to be an adequate thrust reserve. We will assumme that the maximum motor power is limited by the available terminal voltage $V_{m,\,max}$ (it could also be limited by power dissipation in the motor windings). However given $V_{m,\,max}$ and the airspeed U, we can determine the equilibrium propeller speed f_p by solving the following equations:

The propeller power:

$$W_p = k_P \rho f_p^3 D_p^5 \tag{2.3.215}$$

The motor power and speed:

$$\omega_m = \frac{2\pi f_p}{N_{gear}} \qquad W_m = \frac{W_p}{\eta_g} \tag{2.3.216}$$

The motor voltage:

$$V_m = \frac{R_m}{k_m}\left(\frac{W_m}{\omega_m} + \tau_c\right) + k_e \omega_m \tag{2.3.217}$$

The method consists of adjusting f_p and thus the advance ratio J iteratively until the motor voltage calculated by Eq. 2.3.217 is equal to the maximum motor voltage $V_{m,\,max}$.

The total thrust $F_{th,\mathrm{total}}$ is then determined from Eq. 2.3.203:

$$F_{th,\mathrm{total}} = N_p F_{th} = N_p k_T \rho f_p^2 D_p^4 \tag{2.3.218}$$

The results of these calculations are shown below:

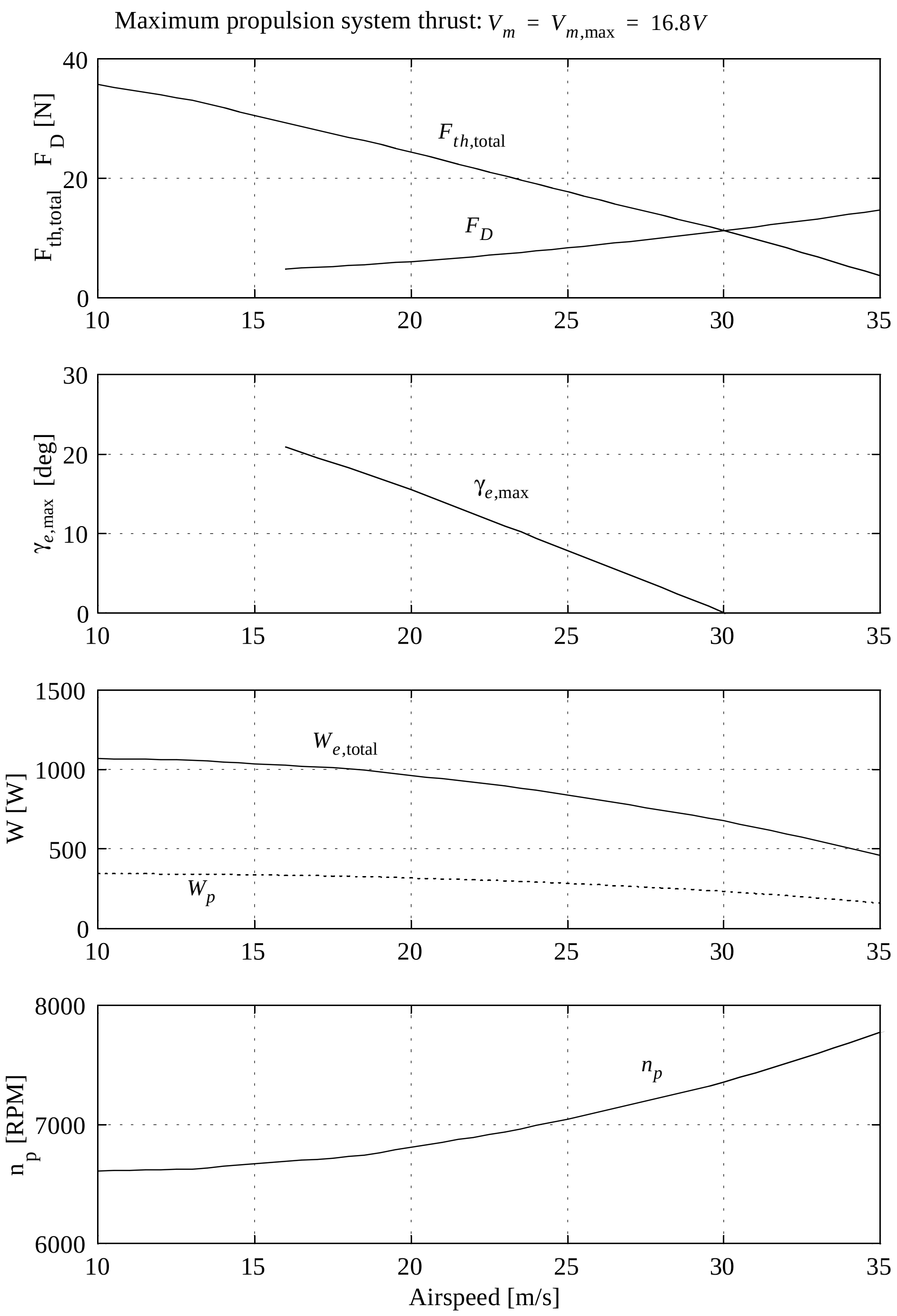

FIGURE 2.29 Concept study UAV propulsion system thrust capability at sea level conditions.

Figure 2.29 shows that at a cruise speed of 20 m/s, the maximum steady state climb angle with motor terminal voltage of 16.8V is approximately 15^{o}. This is a descent performance for a vehicle designed for cruise efficiency. Figure 2.29 also shows that during the takeoff run the thrust is over 30N, corresponding to a thrust to weight ratio in excess of 40%. This should be adequate for takeoff from a grass surface runway.

In order to obtain a dynamic model of the propulsion system, it is necessary to know the effective moment of inertia $J_{m.\mathrm{eff}}$ of the propeller and motor, referenced to the motor shaft. If the propeller moment of inertia is denoted by J_{prop} (not to be confused with the advance ratio J) and the motor rotor moment of inertia is denoted by J_m, the effective moment of inertia can be expressed as (Ref. 18, p. 4-3):

$$J_{m.\mathrm{eff}} = J_m + \left(\frac{1}{N_{gear}}\right)^2 J_{prop} \tag{2.3.219}$$

Where the moment of inertia of the gear has been ignored and the gear efficiency for simplicity is assumed close to unity.

As “usual” it is not possible to obtain published values of propeller and model airplane electric motor moment of inertias. Instead we will try to obtain realistic maximum values of the moment of inertias.

Lets assume that we know the outside diameter of the motor D_m and the total motor mass M_m. We will then assume that the rotor has an maximum outside diameter of 75% of the total motor diameter and that the maximum rotor mass is 50% of the total motor mass. In addition we will assume that the rotor mass distribution is in the form of a solid round cylinder, this gives (Ref. 21, Table 7.1):

$$J_{m,\max} \approx \frac{1}{8}(0.5M_m)(0.75D_m)^2 \tag{2.3.220}$$

The propeller mass distribution will be modelled as uniform with respect to the radius, since the propeller blades generally have a thick crossection close to the hub because of the large centrifugal forces, this will give an upper bound for the propeller moment of inertia:

$$J_{prop,\max} \approx \frac{1}{12}M_{prop}D_p^2 \tag{2.3.221}$$

Where M_{prop} is the total propeller mass.

An upper bound of the effective moment of inertia can then be determined as:

$$(J_{m,\,\mathrm{eff}})_{\max} = \frac{1}{8}(0.5M_m)(0.75D_m)^2 + \frac{1}{12}M_{prop}D_p^2 \tag{2.3.222}$$

We can now determine the overall dynamic model of the UAV propulsion system. The angular acceleration $\dot{\omega}_m$ of the motor is given by:

$$\dot{\omega}_m = \frac{1}{J_{m,\,\mathrm{eff}}}\left(\tau_m - \frac{W_p}{\eta_g\omega_m}\right) = \frac{1}{J_{m,\,\mathrm{eff}}}\left(k_m\frac{V_m - k_e\omega_m}{R_m} - \tau_c - \frac{W_p}{\eta_g\omega_m}\right) \tag{2.3.223}$$

According to Eq. 2.3.204, the applied propeller power can be expressed as:

$$W_p = k_P\rho\left(\frac{\omega_p}{2\pi}\right)^3 D_p^5 = k_P\rho\left(\frac{N_{gear}\omega_m}{2\pi}\right)^3 D_p^5 = \frac{k_P\rho N_{gear}^3{\omega_m}^3 D_p^5}{8\pi^3} \tag{2.3.224}$$

Where the power coefficient is given by:

$$k_P = k_P(J) \qquad J = \frac{2\pi U}{N_{gear}\omega_m D_p} \tag{2.3.225}$$

Where U is the airspeed.

The dynamic model of the motor speed is then given by:

$$\dot{\omega}_m = \frac{1}{J_{m,\,\mathrm{eff}}}\left(\frac{k_m V_m}{R_m} - \frac{k_m^2\omega_m}{R_m} - \frac{k_P \rho N_{gear}^3 \omega_m^2 D_p^5}{8\pi^3\eta_g} - \tau_c\right) \tag{2.3.226}$$

The propeller dynamics is thus a first order nonlinear ODE.

Since the thrust and power coefficients are computed on the basis of the propeller speed rather then the motor speed, it may be convenient to convert Eq. 2.3.226 into an ODE of the propeller speed (frequency) f_p:

$$\dot{f}_p = \frac{N_{gear}}{2\pi}\dot{\omega}_m = \frac{N_{gear}}{2\pi J_{m,\,\mathrm{eff}}}\left(\frac{k_m V_m}{R_m} - \frac{2\pi k_m^2 f_p}{N_{gear} R_m} - \frac{k_P \rho N_{gear} f_p^2 D_p^5}{2\pi\eta_g} - \tau_c\right) \tag{2.3.227}$$

Notice that it is implicitly assumed in the above equations that the net power transfer is from the motor to the propeller. In other words if the propeller is driving the motor through the gear (windmilling), the definition of the gear efficiency should be changed. However since the gear efficiency η_g is close to unity, this error will probably be of minor importance. The instantaneous thrust per propeller is then given by Eq. 2.3.203.

The preceding equations can be used as a nonlinear simulation model of the propulsion system. However for control system design we need a linearized model which essentially describes the “gain” of the propulsion system.

Assuming that the propulsion system dynamics are primarily affected by changes in airspeed and propeller speed, with the motor voltage as an independent controlled input, the linearized propulsion system dynamics can be described using the following mathematical model:

$$\begin{aligned} \delta F_{th} &= \left(\frac{\partial F_{th}}{\partial f_p}\right)\delta f_p + \left(\frac{\partial F_{th}}{\partial U}\right)\delta U \\ \dot{f}_p &= \left(\frac{\partial \dot{f}_p}{\partial f_p}\right)\delta f_p + \left(\frac{\partial \dot{f}_p}{\partial U}\right)\delta U + \left(\frac{\partial \dot{f}_p}{\partial V_m}\right)\delta V_m \end{aligned} \tag{2.3.228}$$

The derivatives of Eq. 2.3.228 can be determined from Eq. 2.3.227:

Propeller speed derivatives:

$$\left(\frac{\partial \dot{f}_p}{\partial f_p}\right) = -\frac{N_{gear}}{2\pi J_{m,\,\mathrm{eff}}}\left(\frac{2\pi k_m^2}{N_{gear}R_m} + \frac{\rho N_{gear}D_p^5}{2\pi\eta_g}\left(2k_P f_p + f_p^2\frac{\partial k_P}{\partial f_p}\right)\right) \tag{2.3.229}$$

$$\left(\frac{\partial \dot{f}_p}{\partial U}\right) = -\frac{\rho N_{gear}^2 f_p^2 D_p^5}{4\pi^2\eta_g J_{m,\,\mathrm{eff}}}\left(\frac{\partial k_P}{\partial U}\right) \tag{2.3.230}$$

$$\left(\frac{\partial \dot{f}_p}{\partial V_m}\right) = \frac{N_{gear}k_m}{2\pi J_{m,\,\mathrm{eff}}R_m} \tag{2.3.231}$$

Thrust derivatives:

$$\left(\frac{\partial F_{th}}{\partial f_p}\right) = \rho D_p^4\left(2k_T f_p + f_p\frac{\partial k_T}{\partial f_p}\right) \tag{2.3.232}$$

$$\left(\frac{\partial F_{th}}{\partial U}\right) = \rho f_p^2 D_p^4\left(\frac{\partial k_T}{\partial U}\right) \tag{2.3.233}$$

2.4 Atmospheric wind and gusts

When the UAV moves through the atmosphere, it may encounter fluctuating wind velocities. These fluctuations are generally due to atmospheric turbulence. The turbulence may be generated by a number of factors:

- “Ground turbulence” due the flow of wind over the landscape, with various degrees of roughness. Due to the similarity with flow over rough plates, this effect can be quantitatively predicted by semi empirical theory for such flows. For this reason, this flow regime is called the Atmospheric Boundary Layer (ABL).
- “Thermal turbulence” is generated by air rising due to thermal differences. This is the same phenomenon responsible for generating the familiar “cumulous” clouds. This kind of turbulence is especially severe inside clouds.
- “Clear air turbulence” is the general term for turbulence not directly associated with clouds or the ABL, especially severe cases are found at edges of “jet streams” and on the leeward side of mountains.

Since atmospheric turbulence is random in nature, it must be described statistically. In general such a description must include both the statistical distribution and frequency content of the turbulence.

It is readily appreciated that atmospheric turbulence is a complex spatial and temporal function. However in order to analyse the effects of turbulence on a moving aeroplane, it is a generally accepted practice (Ref. 1, section III.13) to use the following approximations:

- “Frozen gust”: The atmospheric gust at a fixed position is assumed constant during the time span that the vehicle transverses the gust. This approximation is reasonable if the velocity of the vehicle is significantly larger then the gust wind speed.
- The time function of the gusts in moving vehicle coordinates are continues.

- The gusts are stationary stochastic processes.

There are two types of gust models that are in general use (Ref. 1, section III.13):

- Stochastic gust models, where the gusts are described as stochastic processes using power spectrum models.
- Discrete gusts, where the gust velocity profiles are deterministic functions of time.

The stochastic gust models are generally good for describing the most frequently encountered gusts, while the discrete gust models are useful for describing the rare occurrence of large gusts. This stems from the fact that the gaussian probability distributions used in the stochastic gust models do not adequately model the probability of extreme gusts (Ref. 1, section III.13.6).

2.4.1 Mean wind and the atmospheric boundary layer:

The mean atmospheric wind is basically driven by areas of high and low pressure in the atmosphere (the "weather"). Due to the coriolis force, the wind direction is not directly from areas of low pressure towards areas of high pressure. Instead the wind direction generally follows the isobars in a clockwise direction around regions of low pressure in the northern hemisphere and a counter clockwise direction in the southern hemisphere. Due to the presence of the ground, the mean wind speed is slowed down as the height about the earth's surface is reduced. At the same time the wind direction in general seems to be more in the direction of the low pressure region as the surface is approached.

Due to the extreme complexity of the real flow around natural and man made obstacles on the ground, a simple stochastic model of the atmospheric boundary layer (ABL) seems to be more suited for studying the effects of the ABL on aeroplanes, rather then attempt to use a complex model which may after all not give a more accurate result.

A simple model of the mean atmospheric wind is given in (Ref. 15):

$$\bar{w}(h) = \begin{cases} \ln(h/h_0)\dfrac{\bar{w}_{meas}}{\ln(h_{meas}/h_0)} & h \geq h_{min} \\ \ln(h_{min}/h_0)\dfrac{\bar{w}_{meas}}{\ln(h_{meas}/h_0)} & h < h_{min} \end{cases} \tag{2.4.1}$$

Where h_0 and h_{min} depends on the roughness of the terrain. $\bar{w}_{meas}$ is the mean wind speed (10 minute mean) measured at the height $h_{meas} \geq h_{min}$. If $h_{meas} < h_{min}$, then h_{meas} must be replaced with h_{min} in Eq. 2.4.1. It should be noted that since $\bar{w}_{meas}$ is assumed to be parallel to the mean surface of the ground, it is most conveniently expressed in earth coordinates.

The mean wind velocity $\mathbf{w}_{\mathrm{e}}(h)$ in earth coordinates can then be expressed as:

$$\mathbf{w}_{\mathrm{e}}(h) = -(\mathbf{e}_{\mathrm{ex}}\cos(\theta_{\mathrm{w}}) + \mathbf{e}_{\mathrm{ey}}\sin(\theta_{\mathrm{w}}))\bar{w}(h) = \mathbf{e}_{\mathrm{ex}}w_{ex} + \mathbf{e}_{\mathrm{ey}}w_{ey} \tag{2.4.2}$$

Where θ_{w} is the wind direction expressed according to usual meteological convention, i.e. the direction that the wind appears to be coming from, as viewed by a fixed observer. The local north unit vector is given by $\mathbf{e}_{\mathrm{ex}}$ and the local east unit vector by $\mathbf{e}_{\mathrm{ey}}$.

In the next subsection, the turbulence levels associated with the ABL will be discussed.

2.4.2 Power spectrum model

The power spectrum models describe the gust time functions as a linear dynamic system driven by white gaussian noise. If the gust process is assumed statistically stationary, the power spectral density (PSD) of the gust autocorrelation function can be defined and computed. In this thesis we will not go into the details of determining the PSD's of atmospheric gusts, instead the interested reader is referred to (Ref. 1, section III.13). From this reference, an approximation due to Dryden of the vertical gust PSD is:

$$\Phi_w(\omega) = \frac{\sigma_w^2 L_w}{\pi U_w} \frac{1 + 3\left(\frac{L_w \omega}{U_w}\right)^2}{\left(1 + \left(\frac{L_w \omega}{U_w}\right)^2\right)^2} \tag{2.4.3}$$

Where $\Phi_w(\omega)$ is the temporal gust PSD for vertical gusts with respect to the angular frequency ω, L_w is the vertical turbulence length scale, σ_w is the vertical gaussian turbulence intensity and U_w is the flight speed through the quasisteady atmosphere. The flight speed U_w is defined as the speed relative to the atmosphere *without* wind gusts, but *including* steady wind.$\bar{w}(h)$.

A time domain gust signal with the specified PSD can be generated by passing a continues white noise signal through a stable linear filter with transfer function $G_w(s)$ given by (Ref. 11, p. 118):

$$\Phi_w(\omega) = G_w(j\omega) G_w(-j\omega) \sigma_w^2 \tag{2.4.4}$$

Where σ_w^2 is formally the power density of a continues white noise signal applied to the input of the filter.

As shown in Appendix B, the filter $G_w(s)$ can be determined as:

$$G_w(s) = \frac{b_1 s + b_2}{s^2 + 2\alpha s + \omega_n^2} \tag{2.4.5}$$

With the coefficients given by:

$$\omega_n = \frac{U_w}{L_w} \qquad \alpha = \frac{U_w}{L_w} = \omega_n \qquad b_1 = \sqrt{\frac{3U_w}{\pi L_w}} \qquad b_2 = \sqrt{\frac{U_w^3}{\pi L_w^3}} \tag{2.4.6}$$

A continues state space implementation of the filter in canonic reachable form is determined as:

$$\begin{aligned}\dot{\mathbf{x}}_w &= \mathbf{A}_w\mathbf{x}_w + \mathbf{B}_w\mathbf{u}_w = \begin{bmatrix} 0 & 1 \\ -\omega_n^2 & -2\alpha \end{bmatrix}\mathbf{x}_w + \begin{bmatrix} 0 \\ 1 \end{bmatrix} u_w \\ w_{gz} &= \mathbf{C}_w\mathbf{x}_w = \begin{bmatrix} b_2 & b_1 \end{bmatrix}\mathbf{x}_w \end{aligned} \tag{2.4.7}$$

This implements the filter $G_w(s) = \frac{W_{gz}(s)}{U(s)}$, where $W_{gz}(s)$ is the Laplace transform of the filter gust output $w_{gz}(t)$ and $U(s)$ is the Laplace transform of the filter input $u_w(t)$.

For horizontal gusts in the axial flight path direction, the following model due to Dryden can be used:

$$\Phi_u(\omega) = \frac{2\sigma_u^2 L_u}{\pi U_w} \frac{1}{1 + \left(\frac{L_u\omega}{U_w}\right)^2} \tag{2.4.8}$$

Where $\Phi_u(\omega)$ is the temporal gust PSD for longitudinal gusts, L_u is the longitudinal turbulence length scale and σ_u is the longitudinal gaussian turbulence intensity.

This can be factorized as:

$$\Phi_u(\omega) = G_u(j\omega)G_u(-j\omega)\sigma_u^2 \tag{2.4.9}$$

It is then apparent that we should be able to realize $G_u(s)$ as a first order filter. A general continues first order filter can be expressed as:

$$G_u(s) = \frac{b_1}{s + a_1} \tag{2.4.10}$$

Where a_1 can be interpreted as the inverse of the filter time constant.

The coefficients in Eq. 2.4.10 are then determined as (see Appendix B):

$$a_1 = \frac{U_w}{L_u} \qquad b_1 = \sqrt{\frac{2U_w}{\pi L_u}} \tag{2.4.11}$$

The reachable canonical state space form of $G_u(s)$ can then be determined as:

$$\begin{aligned}\dot{\mathbf{x}}_u &= \mathbf{A}_u\mathbf{x}_u + \mathbf{B}_u\mathbf{u}_u = \begin{bmatrix} -a_1 \end{bmatrix}\mathbf{x}_u + \begin{bmatrix} 1 \end{bmatrix} u_u \\ w_{gx} &= \mathbf{C}_u\mathbf{x}_u = \begin{bmatrix} b_1 \end{bmatrix}\mathbf{x}_u \end{aligned} \tag{2.4.12}$$

Where $w_{gx}(t)$ is the axial gust noise signal.

Notice that both the “vertical” and “longitudinal” gusts are defined relative to flight axes without wind gusts but including the quasisteady wind. In theory, the PSD’s are only valid for flight parallel to the ground, however according to REF they can be used with good accuracy when the flight path angle γ_e is in the range of $\pm 30°$. For the purpose of the present analysis, we are mostly interested in flight at moderate flight path angles during cruise, approach and landing. Thus we will use the PSD’s for horizontal flight throughout the flight envelope.

There are several ways to determine the applicable turbulence intensities for a given mission or flight profile. Either the turbulence intensities can be classified/defined using a grading system or it can be correlated to an easily measured quantity such as the wind speed.

One grading system is given by (Ref. 14, Table2)

Nominal grade of turbulence	Turbulence reference intensity $\bar{\sigma}$
Light	0.9 m/s
Moderate	1.8 m/s
Severe	3.7 m/s
Extreme	7.3 m/s

Tabel 2.8 Turbulence grades.

When using the mean wind speed $\bar{w}(h)$ at altitude h to define the turbulence levels in the Atmospheric Boundary Layer (ABL), the turbulence levels are correlated with the *Surface Roughness Length* h_0. One expression for this correlation is defined in (Ref. 15):

$$\sigma_u = \begin{cases} \dfrac{w(h)}{\ln(h/h_0)} & h \geq h_{min} \\[2ex] \dfrac{\bar{w}(h)}{\ln(h_{min}/h_0)} & h < h_{min} \end{cases} \qquad (2.4.13)$$
$$\sigma_v = 0.8\sigma_u$$
$$\sigma_w = 0.5\sigma_u$$

Where h_{min} depends on the type of terrain surface. It is generally assumed that the vertical and longitudinal gusts are uncorrelated (Ref. 14, p. 6).

The turbulence length scales L_w and L_u are generally functions of the height h above ground level. According to (Ref. 14, p.7), the following expressions for the turbulence length scales can be used:

$$L_w = L_u = L_v = 750m \qquad h \geq 750m$$
$$\left.\begin{aligned} L_u &= L_v = (82.5m^{2/3})\sqrt[3]{h} \\ L_w &= h \end{aligned}\right\} \quad h < 750m \qquad (2.4.14)$$

Where L_v is the turbulence length scale for lateral gusts.

It is notable the vertical gust turbulence length scale is significantly reduced at lower heights, this means that the frequency of the vertical turbulence increases as the ground is approached during approach and landing.

2.4.3 Discrete gust models

The stochastic process gust models given above, are well suited for evaluating the continues response to “ordinary” gusts. However the discrete gust model is better suited for evaluating the response to the rare “extreme” gusts encountered during flight (Ref. 14, p.6). The discrete gust model is composed of a shaped ramp gust, which can be followed a similar gust of opposite direction. The single ramp gust can be modelled by the expression (Ref. 14, p. 9):

$$V_g(s) = \begin{cases} 0 & s < s_0 \\ \dfrac{V_{gm}}{2}\left(1 - \cos\left(\dfrac{\pi(s - s_0)}{\Delta s}\right)\right) & s_0 \le s \le s_0 + \Delta s \\ V_{gm} & s > s_0 + \Delta s \end{cases} \tag{2.4.15}$$

Where $V_g(s)$ is the gust strength as a function of the longitudinal position s of the vehicle, s_0 is the position of the start of the gust, Δs is the length of the gust and V_{gm} is the gust amplitude. $V_g(s)$ can be applied to any of the spatial gust components.

When flying into a gust, the gust gradient $\frac{\partial}{\partial s}(V_g(s))$ may also contribute to the response of the vehicle. The gust gradient for a discrete gusts given by Eq. 2.4.15, can be determined as:

$$\frac{\partial}{\partial s}(V_g(s)) = \begin{cases} 0 & s < s_0 \\ \dfrac{\pi V_{gm}}{2\Delta s}\sin\left(\dfrac{\pi(s - s_0)}{\Delta s}\right) & s_0 \le s \le s_0 + \Delta s \\ 0 & s > s_0 + \Delta s \end{cases} \tag{2.4.16}$$

It is apparent that the gust gradient is strongest for short gusts $(\Delta s \to 0)$.

The amplitudes of discrete gusts in the longitudinal, vertical and lateral directions, can be determined as functions of the reference turbulence intensity and length scales, using the following relationships (Ref. 14, p. 10):

$$u_{gm} = \begin{cases} 5\bar{\sigma}\left(\dfrac{\Delta s}{750m}\right)^{1/3} & \Delta s \le L_u \\ 5\bar{\sigma}\left(\dfrac{L_u}{750m}\right)^{1/3} & \Delta s > L_u \end{cases}$$

$$v_{gm} = \begin{cases} 5.8\bar{\sigma}\left(\dfrac{\Delta s}{750m}\right)^{1/3} & \Delta s \le L_v \\ 5.8\bar{\sigma}\left(\dfrac{L_v}{750m}\right)^{1/3} & \Delta s > L_v \end{cases} \tag{2.4.17}$$

$$w_{gm} = \begin{cases} 5.8\bar{\sigma}\left(\dfrac{\Delta s}{750m}\right)^{1/3} & \Delta s \le L_w \\ 5.8\bar{\sigma}\left(\dfrac{L_w}{750m}\right)^{1/3} & \Delta s > L_w \end{cases}$$

Where u_{gm}, v_{gm} and w_{gm} are respectively the longitudinal, lateral and vertical gust amplitudes.

The gusts defined by varying the *gradient distance* Δs in Eq. 2.4.17, have equal probabilities of occurring (Ref. 14, p. 8). The worst case response at given $\bar{\sigma}$ and length scale L can then be determined by varying the gradient distance Δs.

In addition to the single ramp gust given above, the response to a pair of ramp gusts should also be considered. In this case two single ramp gusts of opposite sign occur at a given interval Δs_{12}. The *gradient distances* of the two gusts are denoted by Δs_1 and Δs_2 and the gust sizes by V_{gm1} and $-V_{gm2}$. The worst case response is determined by varying Δs_1, Δs_2 and Δs_{12} until the worst response is found. Since the probability of occurrence of a pair of ramp gusts is smaller then the probability of a single ramp gust, the gust amplitudes obtained from Eq. 2.4.17 may be multiplied by a factor of 0.85 (Ref. 14, p. 10).

2.5 Complete linear longitudinal aerodynamic model

Having derived a linear longitudinal aerodynamic model, it is possible to determine a linear longitudinal ordinary differential state space equation describing the complete longitudinal dynamics of the UAV.

We will define the longitudinal state vector as consisting of the following states:

- The body pitch angle θ_e.
- The body pitch rate ω_y.
- The UAV speed U in earth fixed coordinates.
- The flight path angle γ_e (direction of U) in earth coordinates.
- The propeller rotational frequency f_p.
- The horizontal UAV position x.
- The UAV altitude h (relative to the mean sealevel).

The independent longitudinal control inputs are:

- The canard flap angle δ_e (i.e. the elevator angle).
- The electric propulsion system motor terminal voltage V_m.

The independent longitudinal disturbance inputs are:

- The horizontal quasisteady wind velocity w_{ex} in earth coordinates.
- The axial gust velocity w_{gfx} in flight coordinates.
- The “vertical” gust velocity w_{gfz} in flight coordinates.

According to the results of Section 2.3.7 the dynamic lift derivatives can probably be ignored. The total lift coefficient is thus equal to the static lift coefficient given by Eq. 2.3.173:

$$C_L = C_{L0} + C_{L\delta_e}\delta_e + C_{L\alpha}\alpha \qquad (2.5.1)$$

The total drag coefficient C_D can be determined as the sum of the zero lift and induced drag coefficients:

$$C_D = C_{D0} + C_{Di,\,wb1} + C_{Di,\,wb2} = C_{D0} + \frac{S_{w1}}{S_w} K_{w1} C_{Lwb1}^2 + K_{w2} C_{Lwbc2}^2 \tag{2.5.2}$$

The equation for the total pitching moment coefficient is obtained by combining the static pitching moment coefficient with the nonsteady contributions:

$$C_m = C_{m0} + \frac{\Delta x_{wf1}}{c_w} C_{L\delta_e}\delta_e - SMC_{L\alpha}\alpha + C_{m\dot{\alpha}}\frac{\dot{\alpha}c_w}{2U} + C_{m\kappa_a}\frac{\kappa_a c_w}{2} + C_{m\dot{w}_{gfz}}\frac{\dot{w}_{gfz}c_w}{2U^2} + C_{m\dot{U}}\frac{\dot{U}c_w}{2U^2} \tag{2.5.3}$$

In the context of longitudinal kinematics, the aerodynamic variables can be determined from Figure 2.13, remembering that we have chosen the body pitch θ_e and longitudinal flight path angle γ_e as independent states:

For the no wind condition ($\mathbf{w}_g = \mathbf{0}$), Figure 2.13 gives the following relation:

$$\theta_e = \alpha + \gamma \tag{2.5.4}$$

Since the derivative of θ_e is equal to the body pitch rate ω_y, the derivative of Eq. 2.5.4 can be expressed as:

$$\omega_y = \dot{\alpha} + \dot{\gamma} \tag{2.5.5}$$

This can be used to simplify the dynamic terms of Eq. 2.5.3:

$$C_{m\dot{\alpha}}\frac{\dot{\alpha}c_w}{2U} + C_{m\kappa_a}\frac{\kappa_a c_w}{2} = \frac{C_{m\dot{\alpha}}c_w}{2}\left(\frac{\dot{\alpha}}{U} + \kappa_a\right) = \frac{C_{m\dot{\alpha}}c_w}{2}\left(\frac{\dot{\alpha}}{U} + \frac{\dot{\gamma}_e}{U}\right) = \frac{C_{m\dot{\alpha}}c_w}{2}\frac{\omega_y}{U} \tag{2.5.6}$$

Where we have used the fact that $C_{m\kappa_a}$ can be approximated by $C_{m\dot{\alpha}}$ and that κ_a is equal to $\dot{\gamma}_e/U$ for purely longitudinal motion without wind.

The derivatives $C_{m\dot{w}_{gfz}}$ and $C_{m\dot{U}}$ are mainly of importance to the dynamic gust response. They account for the fact that when the vehicle travels into a sudden gust, the canard incidence and dynamic pressure changes before that of the main wing. However for this effect to be of any importance, the gust edge must be very sharp and the travel time of the gust from the canard to the main wing must be of the same order of magnitude as the dynamic response time of the vehicle. As we shall see below, real gusts are not infinitely sharp like i.e. a step input. In addition given the estimated velocity of the vehicle and the small canard to main wing distance, the time delay from when the canard enters the gust, to when the main wing enters the gust, is very small. This means that we can simplify the model by neglecting purely dynamic gust response due to penetration time into vertical and axial wind gusts. This gives the following simplified pitching moment coefficient:

$$C_m = C_{m0} + \frac{\Delta x_{wf1}}{c_w} C_{L\delta_e}\delta_e - SMC_{L\alpha}\alpha + C_{m\dot{\alpha}}\frac{c_w}{2U_{TAS}}\omega_y \tag{2.5.7}$$

Where we have used the true airspeed U_{TAS} (relative to the atmosphere) to indicate that the airspeed used in determining the aerodynamic forces and moments are relative to the moving atmosphere and not the earth.

Since the vehicle velocity relative to the earth is denoted by $\mathbf{U}$, the quasisteady wind velocity by $\mathbf{w}(h)$ and the gust velocity by $\mathbf{w}_g$, we can determine the true airspeed vector $\mathbf{U}_{TAS}$ as:

$$\mathbf{U}_{TAS} = \mathbf{U} - \mathbf{w}(h) - \mathbf{w}_g \tag{2.5.8}$$

The airspeed vector without gusts can be defined as:

$$\mathbf{U}_w = \mathbf{U} - \mathbf{w}(h) \tag{2.5.9}$$

From which we can determine the airspeed without gusts as:

$$U_w = \|\mathbf{U}_w\| \tag{2.5.10}$$

The airspeed U_w is used in Eq. 2.4.3 and Eq. 2.4.8 to determine the gust PSD's.

According to Section 2.4.2, the gust velocity is determined in flight path coordinates, while the vehicle velocity and quasisteady wind is determined in earth coordinates.

The instantaneous angle of attack α can then be expressed as the angle between the $\mathbf{e}_{\mathrm{bx}}$ vector (longitudinal body axis) and the true airspeed vector $\mathbf{U}_{TAS}$. One way to determine this angle is to transform the $\mathbf{U}_{TAS}$ vector into body coordinates:

$$\mathbf{U}_{TAS,\mathrm{b}} = \mathbf{M}_{\mathrm{eb}}\mathbf{U}_{w,\mathrm{e}} - \mathbf{M}_{\mathrm{fb}}\mathbf{w}_{g,\mathrm{f}} \tag{2.5.11}$$

Where $\mathbf{M}_{\mathrm{eb}}$ is the transformation matrix from earth to body coordinates and $\mathbf{M}_{\mathrm{fb}}$ is the transformation matrix from flight to body coordinates. In this and the following equations, we will define the flight path coordinate system as a cartesian coordinate system with the x-axis in the direction of the relative velocity vector without wind gusts, but including quasisteady wind.

The angle of attack in the longitudinal motion case is then simply determined as:

$$\alpha = \tan\left(\frac{U_{TAS,\mathrm{bz}}}{U_{TAS,\mathrm{bx}}}\right) \tag{2.5.12}$$

Where $U_{TAS,\mathrm{bz}}$ is the "z" component of $\mathbf{U}_{TAS,\mathrm{b}}$ and $U_{TAS,\mathrm{bx}}$ is the "x" component.

The transformation $\mathbf{M}_{\mathrm{eb}}$ from earth $(x, z)_{\mathrm{e}}$ to body $(x, z)_{\mathrm{b}}$ coordinates can be determined as a function of the body pitch angle θ_e:

$$\mathbf{M}_{\mathrm{eb}} = \begin{bmatrix} \cos(\theta_e) & \sin(\theta_e) \\ -\sin(\theta_e) & \cos(\theta_e) \end{bmatrix} \tag{2.5.13}$$

The transformation $\mathbf{M}_{\mathrm{fb}}$ from flight $(x, z)_{\mathrm{f}}$ to body $(x, z)_{\mathrm{b}}$ coordinates can be determined as a function of the flight path angle γ_e and the quasisteady (horizontal) wind w_{ex}:

$$\mathbf{M}_{\mathrm{fb}} = \begin{bmatrix} \cos(\gamma_w) & \sin(\gamma_w) \\ -\sin(\gamma_w) & \cos(\gamma_w) \end{bmatrix} \tag{2.5.14}$$

Where γ_w is the flight path angle relative to the atmosphere with quasisteady wind:

$$\gamma_w = \tan\left(-\frac{U_{w,\mathrm{ez}}}{U_{w,\mathrm{ex}}}\right) \tag{2.5.15}$$

With $\mathbf{U}_w$ defined by Eq. 2.5.9. Notice that if $\mathbf{w}(h)$ is zero, then γ_w is equal to γ_e.

Since the aerodynamic lift is defined as normal to the true airspeed vector $\mathbf{U}_{TAS}$ and the drag is defined as parallel to $\mathbf{U}_{TAS}$, in theory we thus need to transform the aerodynamic forces into a coordinate system which is aligned with the vehicle velocity vector $\mathbf{U}$ relative to the earth in order to determine the derivatives of the vehicle speed U and the flight path angle γ_e. However as discussed previously we probaly do not need to account exactly for the effects of gusts. Thus we can for simplicy assumme that the lift and drag vectors are aligned with flight axis system and not the instantanous “wind” axis system.

Since the flight path angle is defined by γ_e and the flight path angle relative to the atmosphere is defined by γ_w, it follows that the flight path angle difference γ_d due to wind is given by:

$$\gamma_d = \gamma_w - \gamma_e \tag{2.5.16}$$

The exact direction of the propeller thrust vector is probaly close to the longitudinal body axis direction $\mathbf{e}_{\mathrm{bx}}$. For simplicy we will assumme that the thrust vector is in the general flight path direction relative to the atmosphere. This is probaly a good approximation since the angle of attack is always close to zero in normal flight.

The acceleration $\dot{U}$ in the flight path direction can then be determined as:

$$\dot{U} = \frac{1}{m}(\cos(\gamma_d)F_{th} - \cos(\gamma_d)F_D - \sin(\gamma_d)F_L - \sin(\gamma_e)mg) \tag{2.5.17}$$

The derivative of the flight path angle $\dot{\gamma}_e$ can be determined as:

$$\dot{\gamma}_e = \frac{a_N}{U} = \frac{1}{mU}(\sin(\gamma_d)F_{th} + \cos(\gamma_d)F_L - \sin(\gamma_d)F_D - \cos(\gamma_d)mg) \tag{2.5.18}$$

The body pitch rate acceleration $\dot{\omega}_y$ can be determined from the aerodynamic pitching moment C_m as:

$$\dot{\omega}_y = \frac{\frac{1}{2}\rho U_{TAS}^2 S_w c_w C_m}{J_{yy}} = \frac{\frac{1}{2}\rho U_{TAS}^2 S_w c_w}{J_{yy}}\left(C_{m0} + \frac{\Delta x_{wf1}}{c_w}C_{L\delta_e}\delta_e - SMC_{L\alpha}\alpha + C_{m\dot{\alpha}}\frac{c_w}{2U_{TAS}}\omega_y\right) \tag{2.5.19}$$

As pointed out previosly we have:

$$\dot{\theta}_e \equiv \omega_y \tag{2.5.20}$$

The propeller dynamics are described in Section 2.3.11. It is shown that the dynamics of the propulsion system can be described as a first order nonlinear ODE with the propeller speed f_p as the only state.

The derivative of the horizontal position $\dot{x}$ (i.e. the horizontal speed relative to the ground can be determined geometrically from the speed relative to the ground and the flight path angle relative to the ground:

$$\dot{x} = \cos(\gamma_e)U \tag{2.5.21}$$

This also applies to the derivative of the UAV altitude (relative to mean sealevel):

$$\dot{h} = \sin(\gamma_e)U \tag{2.5.22}$$

This completes the longitudinal model with nonlinear kinematics and linear aerodynamics.

In order to analyse the linear response of the UAV to control and disturbance inputs and subsequently design a linear control system, it is usefull to have a linearized dynamic model.

We can linearize the nonlinear kinematics by assumming a near horizontal flight path and zero steady state wind ($\mathbf{w}(h) = 0$).

This gives the following simplifications:

$$\gamma_w = \gamma_e \qquad \gamma_d = 0 \qquad \|\gamma_e\| \ll 1 \qquad \cos(\gamma_e) \cong 1 \qquad \sin(\gamma_e) \cong \gamma_e \qquad \alpha \cong \theta_e - \gamma_e - \frac{w_{gfz}}{U_0} \tag{2.5.23}$$

We also need to assumme an equilibrium flight speed U_0 and air density ρ_0, from which we can determine the corresponding dynamic pressure as:

$$q_0 = \frac{1}{2}\rho_0 U_0^2 \tag{2.5.24}$$

Linearized versions of the above equations can then be derived:

Body pitch rate acceleration $\dot{\omega}_y$ with $\alpha \cong \theta_e - \gamma_e - \frac{w_{gfz}}{U_0}$:

$$\dot{\omega}_y \cong \frac{\frac{1}{2}\rho U_{TAS}^2 S_w c_w}{J_{yy}}\left(C_{m0} + \frac{\Delta x_{wf1}}{c_w}C_{L\delta_e}\delta_e - SMC_{L\alpha}\left(\theta_e - \gamma_e - \frac{w_{gfz}}{U_0}\right) + C_{m\dot{\alpha}}\frac{c_w}{2U_{TAS}}\omega_y\right) \tag{2.5.25}$$

This can further be simplified as:

$$\dot{\omega}_y \cong \frac{q_0 S_w c_w}{J_{yy}}\left(C_{m0} + \frac{\Delta x_{wf1}}{c_w}C_{L\delta_e}\delta_e - SMC_{L\alpha}\left(\theta_e - \gamma_e - \frac{w_{gfz}}{U_0}\right) + C_{m\dot{\alpha}}\frac{c_w}{2U_0}\omega_y\right) \tag{2.5.26}$$

Where the direct body pitch rate due changes in airspeed is ignored.

The partial derivatives of $\dot{\omega}_y$ can then be determined as:

$$\begin{gathered}\frac{\partial\dot{\omega}_y}{\partial\omega_y} = \frac{q_0 S_w c_w^2 C_{m\dot{\alpha}}}{2U_0 J_{yy}} \qquad \frac{\partial\dot{\omega}_y}{\partial\gamma_e} = \frac{q_0 S_w c_w SMC_{L\alpha}}{J_{yy}} \qquad \frac{\partial\dot{\omega}_y}{\partial\theta_e} = -\frac{q_0 S_w c_w SMC_{L\alpha}}{J_{yy}} \\ \frac{\partial\dot{\omega}_y}{\partial\delta_e} = \frac{q_0 S_w \Delta x_{wf1} C_{L\delta_e}}{J_{yy}} \qquad \frac{\partial\dot{\omega}_y}{\partial w_{gfz}} = \frac{q_0 S_w c_w SMC_{L\alpha}}{J_{yy}U_0}\end{gathered} \tag{2.5.27}$$

The acceleration $\dot{U}$ in the flight path direction:

$$\dot{U} \cong \frac{1}{m}(F_{th} - F_D - mg\gamma_e) = \frac{1}{m}\left(F_{th} - \frac{1}{2}\rho_0 U^2 S_w (C_{D0} + C_{Di}) - mg\gamma_e\right) \tag{2.5.28}$$

Where the induced drag C_{Di} can be determined according to Eq. 2.3.199:

$$C_{Di} = \frac{S_{w1}}{S_w} K_{w1} C_{Lwb1}^2 + K_{w2} C_{Lwbc2}^2 \tag{2.5.29}$$

In order to determine the partial derivatives of C_{Di} with respect to the states and inputs, it is important to realize that even though the canard and main wing lift coefficients and thus the induced drag changes with trim speed, the partial derivative of the lift coefficients with respect to the airspeed is negligibel. This is due to the fact that the lift coefficients are determined directly by the angle of attack and the elevator angle:

$$\frac{\partial C_{Di}}{\partial U} \cong 0 \tag{2.5.30}$$

According to Figure 2.23, the zero lift drag coefficient only varies slightly with airspeed:

$$\frac{\partial C_{D0}}{\partial U} \cong 0 \tag{2.5.31}$$

This gives the following partial derivatives of $\dot{U}$:

$$\begin{gathered}
\frac{\partial \dot{U}}{\partial U} = -\frac{\rho_0 U S_w C_D}{m} + \frac{\partial F_{th}}{\partial U} \qquad \frac{\partial \dot{U}}{\partial \gamma_e} = -g - \frac{\rho_0 U^2 S_w}{2m}\frac{\partial C_{Di}}{\partial \alpha}\frac{\partial \alpha}{\partial \gamma_e} = -g + \frac{\rho_0 U^2 S_w}{2m}\frac{\partial C_{Di}}{\partial \alpha} \\
\frac{\partial \dot{U}}{\partial \theta_e} = -\frac{\rho_0 U^2 S_w}{2m}\frac{\partial C_{Di}}{\partial \alpha}\frac{\partial \alpha}{\partial \theta_e} = -\frac{\rho_0 U^2 S_w}{2m}\frac{\partial C_{Di}}{\partial \alpha} \\
\frac{\partial \dot{U}}{\partial w_{gfx}} = \frac{\rho_0 U S_w C_D}{m} - \frac{\partial F_{th}}{\partial U} \qquad \frac{\partial \dot{U}}{\partial w_{gfz}} = \frac{\rho_0 U^2 S_w}{2mU_0}\frac{\partial C_{Di}}{\partial \alpha} = \frac{\rho_0 U_0 S_w}{2m}\frac{\partial C_{Di}}{\partial \alpha}
\end{gathered} \tag{2.5.32}$$

And:

$$\frac{\partial \dot{U}}{\partial \delta_e} = -\frac{\rho_0 U^2 S_w}{2m}\frac{\partial C_{Di}}{\partial \delta_e} \qquad \frac{\partial \dot{U}}{\partial f_p} = \frac{1}{m}\frac{\partial F_{th}}{\partial f_p} \tag{2.5.33}$$

The linearized propulsion system model is given by Eq. 2.3.228, repeated below for convenience:

$$\begin{aligned}
\delta F_{th} &= \left(\frac{\partial F_{th}}{\partial f_p}\right)\delta f_p + \left(\frac{\partial F_{th}}{\partial U}\right)\delta U \\
\dot{f}_p &= \left(\frac{\partial \dot{f}_p}{\partial f_p}\right)\delta f_p + \left(\frac{\partial \dot{f}_p}{\partial U}\right)\delta U + \left(\frac{\partial \dot{f}_p}{\partial V_m}\right)\delta V_m
\end{aligned} \tag{2.5.34}$$

The partial derivatives are determined in Section 2.3.11.

The derivative of the flight path angle $\dot{\gamma}_e$:

$$\dot{\gamma}_e = \frac{a_N}{U} = \frac{1}{mU}(F_L - mg) = \frac{1}{mU}\left(\frac{1}{2}\rho_0 U^2 S_w (C_{L0} + C_{L\delta_e}\delta_e + C_{L\alpha}\alpha) - mg\right) \qquad (2.5.35)$$

The partial derivatives of $\dot{\gamma}_e$:

$$\begin{gathered}
\frac{\partial\dot{\gamma}_e}{\partial U} = \frac{\rho_0 S_w C_L}{2m} + \frac{g}{U^2} = \frac{2g}{U^2} \qquad \frac{\partial\dot{\gamma}_e}{\partial\gamma_e} = \frac{\rho_0 U S_w C_{L\alpha}}{2m}\frac{\partial\alpha}{\partial\gamma_e} = -\frac{\rho_0 U S_w C_{L\alpha}}{2m} \\
\frac{\partial\dot{\gamma}_e}{\partial w_{gfx}} = -\frac{2g}{U^2} \qquad \frac{\partial\dot{\gamma}_e}{\partial w_{gfz}} = -\frac{\rho_0 U S_w C_{L\alpha}}{2mU_0} = -\frac{\rho_0 S_w C_{L\alpha}}{2m} \\
\frac{\partial\dot{\gamma}_e}{\partial\theta_e} = \frac{\rho_0 U S_w C_{L\alpha}}{2m}\frac{\partial\alpha}{\partial\theta_e} = \frac{\rho_0 U S_w C_{L\alpha}}{2m}
\end{gathered} \qquad (2.5.36)$$

And:

$$\frac{\partial\dot{\gamma}_e}{\partial\delta_e} = \frac{\rho_0 U S_w C_{L\delta_e}}{2m} \qquad (2.5.37)$$

We can now express the longitudinal linear kinematic and dynamic model as:

$$\delta\dot{\mathbf{X}}_{\text{long}} = \mathbf{A}_{\text{long}}\delta\mathbf{X}_{\text{long}} + \mathbf{B}_{\text{long1}}\delta\mathbf{U}_{\text{long}} + \mathbf{B}_{\text{long2}}\delta\mathbf{W}_{\text{long}} \qquad (2.5.38)$$

Where the longitudinal state vector $\mathbf{X}_{\text{long}}$, the control input vector $\mathbf{U}_{\text{long}}$ and the distrubance vector $\mathbf{W}_{\text{long}}$ are defined as:

$$\mathbf{X}_{\text{long}} \equiv \begin{bmatrix} \gamma_e \\ \theta_e \\ \omega_y \\ U \\ x \\ h \\ f_p \end{bmatrix} \qquad \mathbf{U}_{\text{long}} \equiv \begin{bmatrix} \delta_e \\ V_m \end{bmatrix} \qquad \mathbf{W}_{\text{long}} \equiv \begin{bmatrix} w_{gfx} \\ w_{gfz} \end{bmatrix} \qquad (2.5.39)$$

The deviation vectors $\delta\mathbf{X}_{\text{long}}$, $\delta\mathbf{U}_{\text{long}}$ and $\delta\mathbf{W}_{\text{long}}$ are defined as the difference between the instantanous vectors $\mathbf{X}_{\text{long}}$, $\mathbf{U}_{\text{long}}$ and $\mathbf{W}_{\text{long}}$ and the equilibrium values of these vectors.

The longitudinal system matrix $\mathbf{A}_{\mathrm{long}}$ can then be determined as:

$$\mathbf{A}_{\mathrm{long}} = \begin{bmatrix} -\frac{\rho_0 U S_w C_{L\alpha}}{2m} & \frac{\rho_0 U S_w C_{L\alpha}}{2m} & 0 & \frac{2g}{U_0^{\,2}} & 0 & 0 & 0 \\ 0 & 0 & 1 & 0 & 0 & 0 & 0 \\ \frac{q_0 S_w c_w SMC_{L\alpha}}{J_{yy}} & -\frac{q_0 S_w c_w SMC_{L\alpha}}{J_{yy}} & \frac{q_0 S_w c_w^2 C_{m\dot{\alpha}}}{2U_0 J_{yy}} & 0 & 0 & 0 & 0 \\ -g + \frac{\rho_0 U^2 S_w}{2m}\frac{\partial C_{Di}}{\partial \alpha} & -\frac{\rho_0 U^2 S_w}{2m}\frac{\partial C_{Di}}{\partial \alpha} & 0 & -\frac{\rho_0 U S_w C_D}{m} + \frac{\partial F_{th}}{\partial U} & 0 & 0 & \frac{\partial F_{th}}{\partial f_p} \\ -\sin(\gamma_e) U_0 & 0 & 0 & \cos(\gamma_e) & 0 & 0 & 0 \\ \cos(\gamma_e) U_0 & 0 & 0 & \sin(\gamma_e) & 0 & 0 & 0 \\ 0 & 0 & 0 & \left(\frac{\partial \dot{f}_p}{\partial U}\right) & 0 & 0 & \left(\frac{\partial \dot{f}_p}{\partial f_p}\right) \end{bmatrix} \qquad (2.5.40)$$

The longitudinal input matrix $\mathbf{B}_{\mathrm{long1}}$ is given by:

$$\mathbf{B}_{\mathrm{long1}} = \begin{bmatrix} \frac{\rho_0 U S_w C_{L\delta_e}}{2m} & 0 \\ 0 & 0 \\ \frac{q_0 S_w \Delta x_{wf1} C_{L\delta_e}}{J_{yy}} & 0 \\ -\frac{\rho_0 U^2 S_w}{2m}\frac{\partial C_{Di}}{\partial \delta_e} & 0 \\ 0 & 0 \\ 0 & 0 \\ 0 & \frac{\partial \dot{f}_p}{\partial V_m} \end{bmatrix} \qquad (2.5.41)$$

The longitudinal disturbance input matrix $\mathbf{B}_{\mathrm{long2}}$ is given by:

$$\mathbf{B}_{\mathrm{long2}} = \begin{bmatrix} -\frac{2g}{U^2} & -\frac{\rho_0 S_w C_{L\alpha}}{2m} \\ 0 & 0 \\ 0 & \frac{q_0 S_w c_w SMC_{L\alpha}}{J_{yy}U_0} \\ \frac{\rho_0 U S_w C_D}{m} - \frac{\partial F_{th}}{\partial U} & \frac{\rho_0 U_0 S_w}{2m}\frac{\partial C_{Di}}{\partial \alpha} \\ 0 & 0 \\ 0 & 0 \\ -\frac{\partial \dot{f}_p}{\partial U} & 0 \end{bmatrix} \tag{2.5.42}$$

2.6 Lateral aerodynamic coefficients

In the linear flow range, the lateral aerodynamic coefficients can be expressed as:

Side force:

$$C_Y = C_{Y\beta}(\alpha)\beta + C_{Y_{\dot\beta}}\frac{\dot\beta b_w}{2U} + C_{Y\kappa_\beta}\frac{\kappa_\beta b_w}{2} + C_{Y_p}(\alpha)\frac{(\omega_{rf} + \omega_w)b_w}{2U} + C_{Y\eta}(\alpha)\eta_{\beta j} \tag{2.6.1}$$

Where $C_{Y\beta}(\alpha)$, $C_{Y_p}(\alpha)$ and $C_{Y\eta}(\alpha)$, emphasize that these coefficients depend on the angle of attack α. "p" is used as a short hand notation for roll rate ω_{rf}. The side force coefficient is based on the main wing area S_w.

Rolling moment:

$$C_l = C_{l\beta}(\alpha)\beta + C_{l_{\dot\beta}}(\alpha)\frac{\dot\beta b_w}{2U} + C_{l\kappa_\beta}(\alpha)\frac{\kappa_\beta b_w}{2} + C_{l_p}(\alpha)\frac{(\omega_{rf} + \omega_w)b_w}{2U} + C_{l\eta}(\alpha)\eta_{\beta j} \tag{2.6.2}$$

The rolling moment coefficient is based on the product of the main wing area S_w and the total wing-body span b_{wb}.

Yawing moment:

$$C_n = C_{n_\beta}(\alpha)\beta + C_{n_{\dot\beta}}(\alpha)\frac{\dot\beta b_w}{2U} + C_{n\kappa_\beta}(\alpha)\frac{\kappa_\beta b_w}{2} + C_{n_p}(\alpha)\frac{(\omega_{rf} + \omega_w)b_w}{2U} + C_{n\eta}(\alpha)\eta_{\beta j} \tag{2.6.3}$$

The yawing moment coefficient is based on the product of the main wing area S_w and the total wing-body span b_{wb}.

Under normal circumstances, the above linear coefficients are adequate for predicting the lateral behaviour of the UAV. However under certain circumstances involving high angles of attack and/or high sideslip angles, these equations may need modification to represent the quantitative behaviour of the vehicle.

The following situations may need to be carefully considered:

1. At high sideslip angles $\beta > 10^0$, the coefficients $C_{Y\beta}(\alpha)$ and $C_{n\beta}(\alpha)$ may change sign leading to rapid divergence in yaw.
2. At high angles of attack, the coefficient $C_{l\eta}(\alpha)$ may change sign as a function of the aileron control deflection $\eta_{\beta j}$, leading to aileron control reversal.
3. At high angles of attack, the roll damping coefficient $C_{lp}(\alpha)$ may become negative, putting the UAV into a spin. This situation is however already modelled above.
4. At high angles of attack the coefficient $C_{lp}(\alpha)$ may change sign, which may also put the UAV into a spin.

Whether or not these modelling errors affect the behaviour of the vehicle, depends to a large extent on the following factors:

- Will the vehicle ever encounter these flight regimes.
- How adaptive is the automatic flight control.

As an example of the last issue, consider the situation where the aileron $C_{l\eta}(\alpha)$ changes sign at high angles of attack. If a linear feedback controller is used to control the vehicle roll, this will lead to divergence because the feedback path suddenly becomes positive. This problem can become even worse if the roll damping coefficient $C_{lp}(\alpha)$ is also negative.

From a closed loop control point, a change of sign in the feedback path is an especially serious problem because inherent modelling errors prevent the exact position of the sign change to be predicted. Thus a non adaptive controller can not provide any control in a region around the sign change. The only effective way to recover from this flight regime is thus to reduce the angle of attack.

2.7 References

1. G.J.Hancock: “An Introduction To The Flight Dynamics Of Rigid Aero planes”,1995.
2. W.C.Pitts, J.N.Nielsen and G.E.Kaattari: “Lift and center of pressure of wing-body-tail combinations at subsonic, transonic, and supersonic speeds”, NACA Report 1307.
3. Johs. Tejlgård:”Aeroplanlære”, AFM 1990,DTU,ISBN 0590-8809.
4. R.D.Finck: “USAF STABILITY AND CONTROL DATCOM”,1960, Global Engineering Documents, revised 1978.
5. F.M.White:”Viscous Fluid Flow”, International edition 1991, McGraw-Hill, Inc.
6. M.J.Queijo:”Theoretical span load distributions and rolling moments for sideslipping wings in incompressible flow”, NACA Report 1269.
7. T.A.Toll & M.J.Queijo:”Approximate relations and charts for low-speed stability derivatives of swept wings”, NACA Technical Note 1581, 1948.
8. D.P.Raymer:”Aircraft Design: A Conceptual Approach, Third Edition”, AIAA EDUCATION SERIES, AIAA 1999.
9. K. Ogata:”Modern Control Engineering”, Second edition, Prentice-Hall Inc. 1990.
10. F.L.Lewis:”Applied Optimal Control & Estimation, Digital Design & Implementation”, Prentice-Hall Inc. 1992.
11. F.L.Lewis:”Optimal Estimation, with an introduction to stochastic control theory”, John Wiley & Sons 1986.
12. J.R.Spreiter:”The aerodynamic forces on slender plane- and cruciform-wing and body combinations”, NACA Report 962.
13. S.F.Hoerner:”Fluid-Dynamic Drag”, Published by the Author, 1965.
14. Unknown author(s):”LEAFLET 5, General Requirements and Definitions, Atmospheric Disturbances”, DEF STAN 00-970, Part 1 Section2.
15. DS 472, (1992):”Code of Practice for Loads and Safety of Wind Turbine Constructions” DS 472, The Danish Society of Engineers and the Federation of Engineers.
16. DS 410, (1998):”Code of Practice for Loads for the Design of Structures” DS 410, The Danish Society of Engineers and the Federation of Engineers.
17. Mark Drela: “XFOIL” program, http://raphael.mit.edu/xfoil/.
18. N. Leth:”Servomekanismer, bind 1”(“Servo actuators, volume 1”), Servolaboratoriet 1979.
19. E.L.Houghton & P.W.Carpenter:”Aerodynamics for engineering students”,4’th edition, Edward Arnold.
20. E.P.Lesley:”NACA TN 698”, NACA Washington 1939.
21. G.Christian,E.Both,P.Ø.Sørensen:”Mekanik”(“Mechanics”),Laboratoriet for Teknisk Fysik, DTU 1990.

Chapter 3

UAV actuators

3.1 Overview:

This part of the thesis describes the basic properties of the electromechanical actuators used to control the aerodynamic surfaces and propulsion unit of the UAV. First the basic design and operating principles of the actuators are discussed. Then a detailed semiemperical dynamic model of the canard actuator is described. Finally the characteristics of the remaining actuators are briefly summarized.

3.2 Basic actuator design and properties:

All the electromechanical actuators used in UAV are commercial “model airplane” type servos. For reasons of performance and versatility, the actuators are of the “microprocessor” type. This means that each servo is a complete self contained digital servo system with some programmeable features. These features include various “fail safe” modes that the servo can be programmed to enter if the reference signal to the servo is lost. These features will not be described further in the following, as they are of no importance to regular operation.

The basic function of the servo is to generate a mechanical rotation of the output lever, in response to the reference input to the servo. The main distinction between the various servos, is in the maximum available torque on the output. Each servo is controlled by a Pulse Width Modulated (PWM) square wave signal. For the particular brand of servos used for the UAV, the properties of the PWM signal is given below (Ref. 22):

Nominal pulse frequency	40 Hz
Neutral position pulse width	1.6 ms
Pulse width range	1.0 ms to 2.2 ms

Tabel 3.1 Multiplex PWM signal characteristics.

Since each servo is a completely self contained unit, there is no external feedback of the actual position of the output lever. This means that the flight control system has no way of determining the actual output error. This property should be remembered when selecting the appropriate servo for a particular task and when designing the flight control system.

3.3 Semiemperical model of canard actuator:

The canard actuator is the largest servo in the multiplex product range. This choice is due to the large aerodynamic torque that may be generated by an “all moving” canard surface, as used in the original UAV design concept. In this way, the maximum torque that is available from the servo is considerably larger then the maximum aerodynamic torque produced under any normal circumstance. This eliminates some of the uncertainty caused by the lack of a direct output feedback to the flight control system. The somewhat scarce specifications which are obtainable from the datasheet (Ref. 22), are listed below:

Name	Jumbo mc/V2
Maximum rotational[a] torque	210 Ncm
Maximum blocking torque	-
“Speed”[b] under zero load	0.20 sec
Angular output range	$\pm 90^o$
Rated voltage range	4.8-6 V
Maximum current	-
Mass	162 g

Tabel 3.2 Canard servo datasheet.

---

a. The maximum torque that can be generated by the motor on the output.

b. The time required to rotate the output lever 90^o.

As can be seen the control specifications are only sketchy at best. For this reason we are forced to conduct some experiments to determine the actual control specifications of the servo.

3.3.1 Experimental test setup:

In order to determine the control specifications of the servo, an experimental test setup has been constructed as shown schematically below:

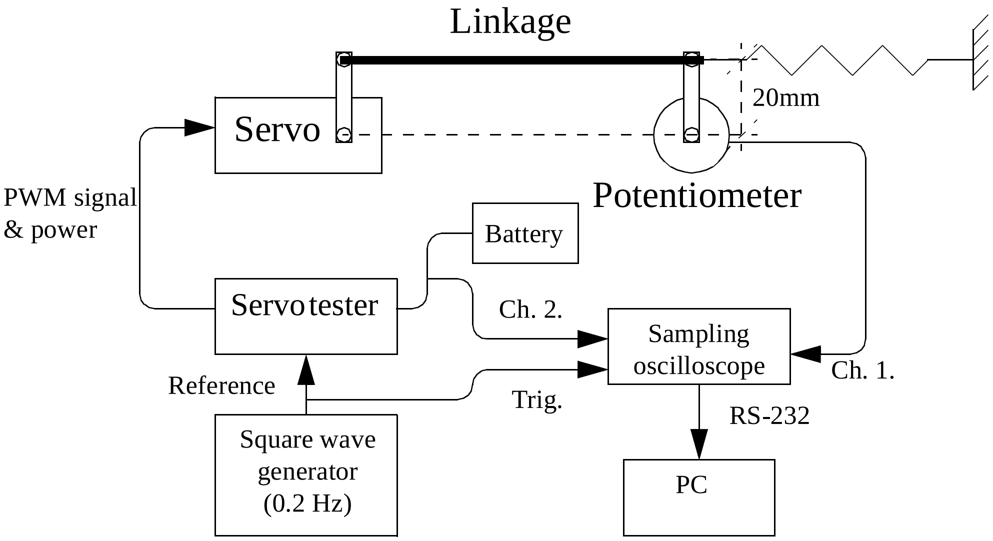

FIGURE 3.1 Servo test setup.

The part named “servo tester” is a commercially available product that generates a PWM signal which is compatible with multiplex servos. The PWM output of the servo tester is controlled by a build in potentiometer with a control knob. However for use in the test setup above, the servo tester has been modified so that an external voltage can be used to control the reference pulse length, and thus the position. This external voltage is a square wave signal with a frequency of approximately 0.2Hz. Using the two channel sampling oscilloscope it is thus possible to obtain and record the response of the servo to steps of various sizes. The particular oscilloscope also permits the obtained measurements to be transferred to a Personal Computer (PC), for subsequent analysis. In addition to the potentiometer position obtained using ch. #1 of the oscilloscope, the voltage of the servo drive battery is monitored using ch. #2.

The linkage shown in the setup is a rigid rod with “model airplane” type ball joints at each end. The linkage is adjusted in such a way that it is parallel to the line between the servo axle and the potentiometer axle. In this way the angular displacement of the potentiometer should ideally equal the angular displacement of servo output axle. Mechanical slack in the servo linkage is taken up be a pretensioned low stiffness spring.

3.3.2 Preliminary measurements:

In order to accurately determine the control specifications of the servo, it is necessary to calibrate the test setup.

The PWM pulse rate of the “servo tester” was measured using the oscilloscope:

$$f_{PWM} \cong 35.5Hz \tag{3.3.1}$$

This is somewhat smaller then the nominal frequency of 40Hz, but this deviation should have no significant influence on the response.

The sensitivity of the potentiometer has been determined as:

$$G_{\mathrm{POT}} \cong \begin{array}{l} 360^{o}/5.12V = 70.3^{o}/V \\ 2\pi/5.12V = 1.23\mathrm{rad/V} \end{array} \tag{3.3.2}$$

The potentiometer drive voltage is 5.12V.

3.3.3 Measured response:

Using the experimental setup just described, a number of step responses where recorded. 4 different step sizes where used to cover the likely operating area of the servo. Each stepsize was applied in both a positive and a negative direction. The stepsizes where approximately 10^o, 20^o, 40^o and 80^o, thus covering almost one magnitude in amplitude. The results for the “positive” steps are given below:

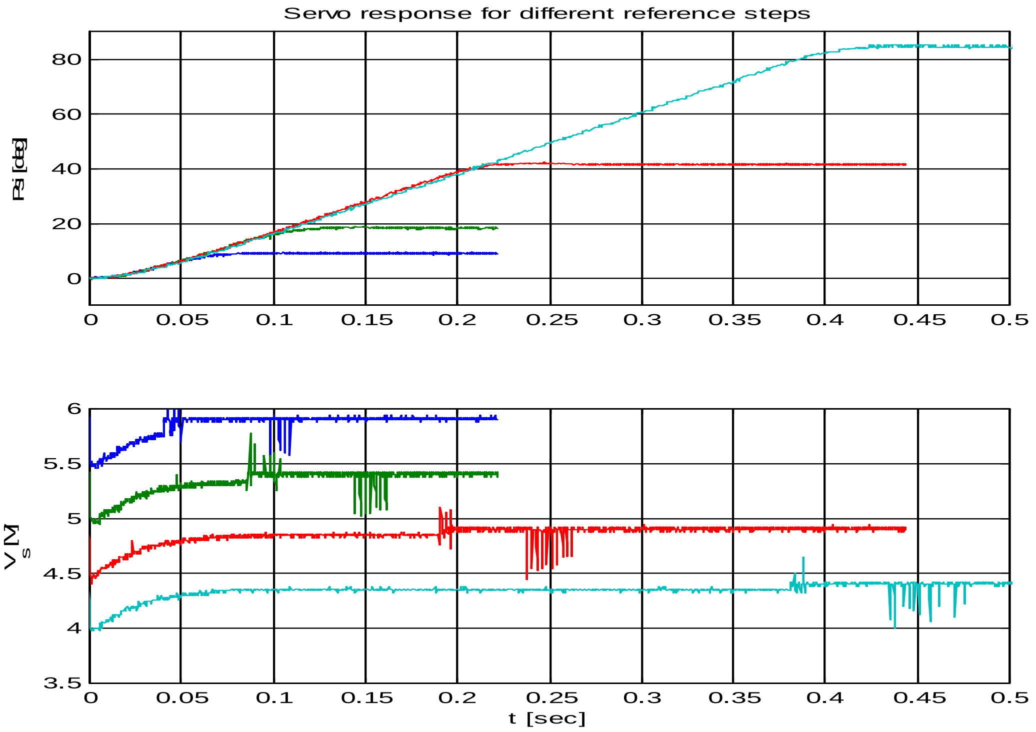

FIGURE 3.2 Measured positive steps.[a]

---

[a] For clarity, the different supply voltage plots have been shifted down by multiples of 0.5 V.

Inspection of the measured step responses, reveals two important phenomena; the first part of the response (the acceleration phase) is practically independent of the step size and the angular rates appear to approach a limiting value. The most simple explanation of these observations, is that the servo motor drive voltage is saturated for all the measured responses. The supply voltage plots ($V_S(t)$) confirm this conclusion since they show identical voltage drops for the acceleration phase of all the responses.

3.3.4 Semiemperical servo model:

Since it seems likely that the servo motor drive current is saturated for all practical responses, the most appropriate model of the servo includes a bang-bang type nonlinearity in the motor drive voltage. One simple controller scheme is Proportional Derivative (PD) controller with a bang-bang nonlinearity at the motor drive input. The bang-bang nonlinearity could be physically implemented by an on-off controlled H-bridge driver circuit.

The proposed semiemperical model is given in block diagram form below:

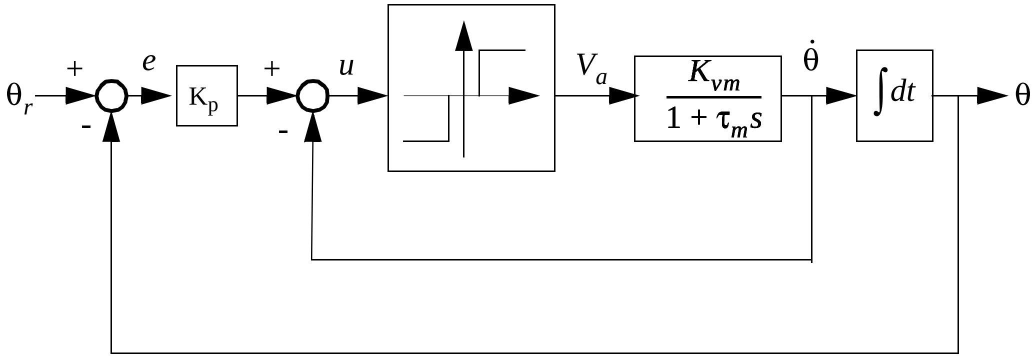

FIGURE 3.3 Semi empirical servo model.

The main features of the model is a linear PD feedback loop, a nonlinear bang-bang servo driver with a small amount of deadband and a linear DC motor model. The deadband is necessary to avoid a low amplitude limit cycle and associated excessive power consumption. The magnitude of the rate (tacho) feedback has been arbitrarily set to unity, since the absolute amplitude of the control signal u(t) is insignificant for ideal bang-bang control. It must be stressed we do not actually know whether the rate feedback signal $\dot{\theta}$ is obtained by direct measurement such as a tacho generator or by differentiation of the position θ.

3.3.5 Parameter estimation:

In the proposed semiemperical servo model, there are 4 a priori unknown parameters: The proportional gain K_p, the servo motor time constant τ_m, the servo output speed constant K_{vm} and lastly the bang-bang controller deadband Δu_0. These parameters have been determined using a nonlinear least mean squares parameter estimation method. The basic idea is to simulate the response of the servo to a reference step of a given magnitude using guessed parameters, the least mean square error between the measured and the guessed response can then be used as a scalar error function. An iterative method is then used to find a minima of the error function, corresponding to the "optimal" parameter estimate.

The relation between the angular deadband $\Delta\theta_0$ and controller deadband Δu_0, can relatively easily be determined as:

$$\Delta u_0 = K_p \Delta\theta_0 \qquad (3.3.3)$$

Since a small deadband only has a negligible influence on the transient response of the servo, we can not expect to able to estimate it from the measured step response. For this reason it is better to assume that the deadband is small but finite. We have thus fixed the angular deadband as:

$$\Delta\theta_0 = 0.05^o \qquad (3.3.4)$$

Using Eq. 3.3.3, the number of unknown parameters to be determined is reduced to 3, the proportional gain K_p, the servo motor time constant τ_m and the servo output speed constant K_{vm}. The parameter estimation problem can then be reduced to finding the minimum of:

$$\theta_{\mathrm{res,RMS}}(\mathbf{X}) = \frac{1}{t_1 - t_0}\left(\int_{t_0}^{t_1}\{\theta_e(\mathbf{X}, t) - \theta_m(t)\}^2 dt\right)^{1/2} \tag{3.3.5}$$

Where $\mathbf{X} \equiv [K_p, K_{vm}, \tau_m]$ is the parameter vector, $\theta_m(t)$ is the measured response, $\theta_e(\mathbf{X}, t)$ is the estimated response, $\theta_{\mathrm{res,RMS}}(\mathbf{X})$ is the Root Mean Square (RMS) error and $[t_0,t_1]$ is the response time interval.

It is obvious that the “optimal” solution $\tilde{\mathbf{X}}$ of Eq. 3.3.5 depends on the choice of time interval $[t_0,t_1]$. As shown in Figure 3.2, the step times coincide with t = 0. Thus the initial time should be taken as $t_0 = 0$. The “final” time t_1 should be chosen such that the response is “finished”, but on the other hand not too long, to avoid the estimate to be dominated by noise after “steady” state is reached. In addition due regard has to be taken to the fact that the response to a positive and negative going step of the same magnitude may not be perfect mirror images. This can be caused by variations in the saturation current of different parts of the internal H-bridge driver circuit.

In due regard to the above practical considerations, the actual parameter estimation has been done using two measured responses, with step sizes of approximately $\pm 84^o$. The actual error function is then the mean of the two root mean square errors. This of course requires two simulation runs for each minimization step, because the positive and negative steps are not necessarily of the exact same magnitude.

The actual parameter estimation was performed in MATLAB using a fourth order variable step size Runge-Kutta integrator (ODE45) to simulate the estimates step response and a simplex type (non derivative) multivariable minimization algorithm (FMINS) to iterate the parameter estimate. Since the bang-bang control function is highly nonlinear for small feedback errors u(t), it was found that an order of magnitude saving in computation time could be achieved by decreasing the absolute integration tolerance from the default values of 10^{-6} to 0.1^o and 0.01^0/sec on the angle and angular rate, respectively. This decrease in tolerances did not decrease the solution accuracy in any noticeable way. It is also worth noting that the integration almost grinds to a halt if the deadband is set to zero, this is apparently because of the very small time scale needed to resolve the limit cycle that results from zero deadband.

The resulting “optimal” parameter estimate was determined as:

$$\mathbf{X} \equiv \begin{bmatrix} K_p & K_{vm} & \tau_m \end{bmatrix} = \begin{bmatrix} 59.7/(deg) & 37.1^o/s & 0.0304s \end{bmatrix} \tag{3.3.6}$$

The speed constant K_{vm} was determined using the assumption of a constant saturation voltage of $V_a = \pm 6V$. The linear control signal u(t) is assumed dimensionless.

The “optimal” solution to the two steps are plotted below, along with the measured step responses and the residual errors for the two cases:

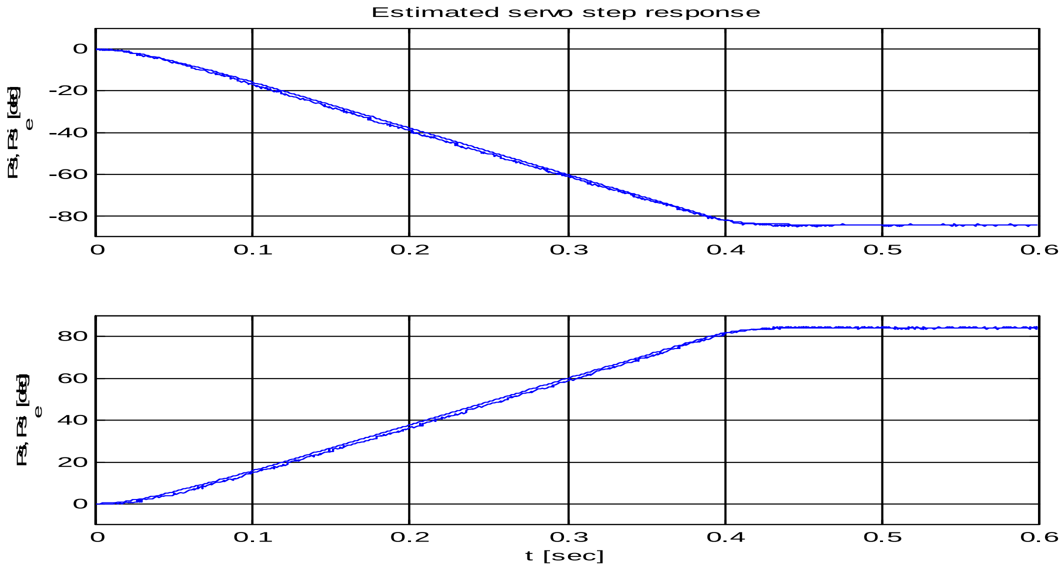

FIGURE 3.4 Measured and estimated step responses.

It is apparent that the model agrees quit well with the measured response, it can be seen that the “negative” response is a bit faster then the “positive” response.

Residuals between measured and estimated step responses:

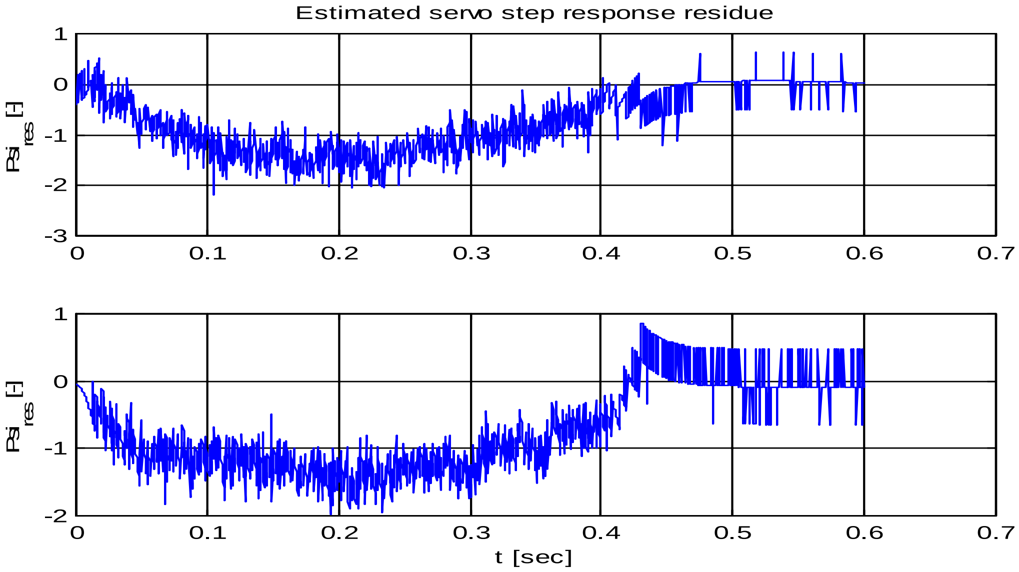

FIGURE 3.5 Residuals between measured and estimated step responses.

The residuals show that the maximum deviation between the measured and estimated response is below 4% of the step size, which must be classified as quit a good agreement.

3.3.6 Validation of bang-bang controller model:

In order to determine the validity of the bang-bang controller model with the parameters determined above, the model is compared to the measured response to steps of smaller magnitude. The smallest steps that have been measured is around $\pm 9^o$. Using the obtained parameters from above, the comparison between measured response and estimated response is shown below:

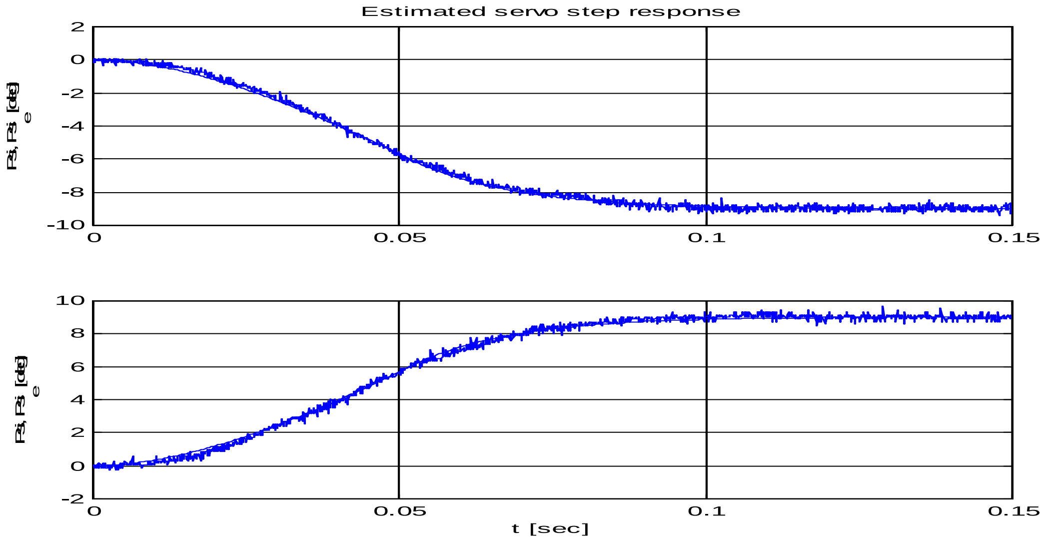

FIGURE 3.6 Measured and estimated step responses.

Residuals between measured and estimated step responses:

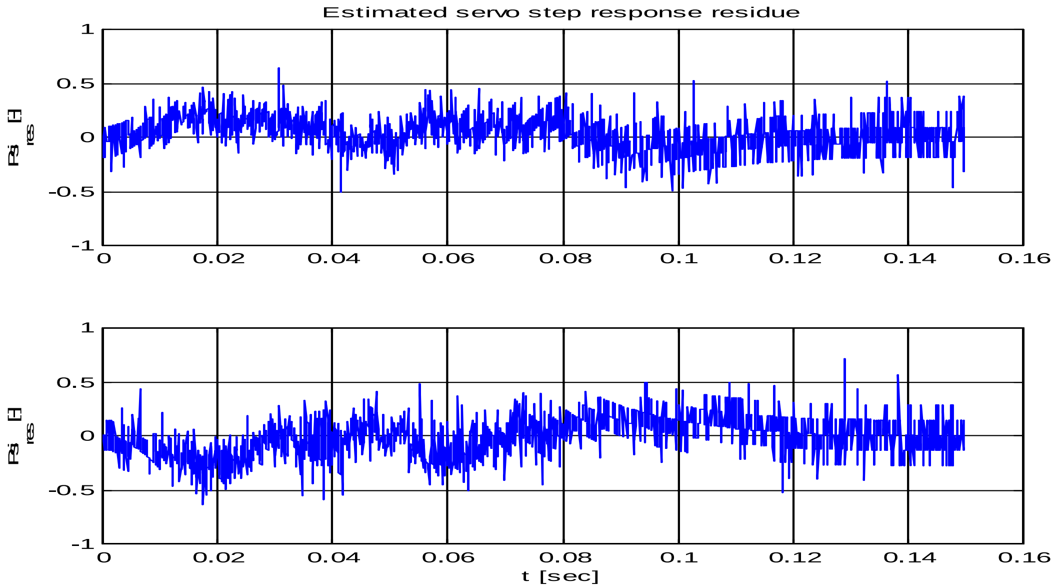

FIGURE 3.7 Residuals between measured and estimated step responses.

The residuals show that the maximum deviation between the measured and estimated response is below about 5% of the step size, thus the model fits the response very well even for a step size of almost one magnitude less then that used for parameter estimation. Indeed the measurement and quantization noise is almost of the same order of magnitude as the model error, for these small step sizes.

Experimental data for stepsizes of approximately $\pm 19^o$ and $\pm 42^o$ have also been obtained. For reasons of brevity, the residuals for these stepsizes are not shown in this thesis. However a listing of the RMS values of the residuals for the different step sizes are given below:

Positive going steps:

$\Delta\theta$	$\theta_{res,RMS}$	$\frac{\theta_{res,RMS}}{\lVert\Delta\theta\rVert}$	t_1
8.9^o	0.19^o	2.1%	0.15s
18.0^o	0.28^o	1.5%	0.20s
41.4^o	0.50^o	1.2%	0.30s
84.2^o	0.97^o	1.2%	0.60s

Tabel 3.3

Negative going steps:

$\Delta\theta$	$\theta_{res,RMS}$	$\frac{\theta_{res,RMS}}{\lVert\Delta\theta\rVert}$	t_1
-8.9^o	0.17^o	1.9%	0.15s
-19.8^o	0.22^o	1.1%	0.20s
-42.1^o	0.49^o	1.2%	0.30s
-84.2^o	0.95^o	1.1%	0.60s

Tabel 3.4

It is apparent that the relative RMS error for all step sizes in both directions, is very small. Given the above data it seems that the bang-bang controller servo model is a good model of the actual servo dynamics.

3.3.7 Describing function approximation:

The nonlinear bang-bang controller model given above has been shown to be a good model of the servo dynamics. However since it is very nonlinear even for small responses, it is not feasible to perform a normal “operating point” linearization. This poses a problem as most methods for controller and estimator design and analysis require a linear model.

One way around this problem is to use describing function analysis (Ref. 23, chapter 8). The basic idea behind describing function analysis is to obtain the input - output relationship between a sinusiod input to a nonlinearity and the fundamental frequency of the output response. Since the fundamental frequency of the output of a stable nonlinear element is equal to the input frequency, the describing function contains information about the amplitude ratio and phase difference between the input and output. Generally the describing function for a given nonlinearity will be both a function of the input amplitude and frequency. However if the nonlinearity does not contain any dynamics, the describing function will only be a function of the input amplitude. Since the bang-bang nonlinearity (also called an on-off nonlinearity) is skew symmetric, the output phase will be identical to the input phase. The describing function *N* for a on-off nonlinearity with deadband is given by (Ref. 23, p. 653):

$$N = \begin{cases} \dfrac{4M}{\pi X}\sqrt{1-\left(\dfrac{\Delta}{X}\right)^2} & X \geq \Delta \\ 0 & X < \Delta \end{cases} \tag{3.3.7}$$

Where M is the output saturation amplitude, Δ is the dead band and X is the input amplitude.

For our bang-bang servo controller, the output saturation amplitude will be taken equal to the battery supply voltage V_s:

$$N_{servo} = \begin{cases} \dfrac{4V_s}{\pi U}\sqrt{1-\left(\dfrac{\Delta u_0}{U}\right)^2} & U \geq \Delta u_0 \\ 0 & U < \Delta u_0 \end{cases} \tag{3.3.8}$$

Where N_{servo} is the servo bang-bang nonlinearity describing function, Δu_0 is the controller deadband and U is the amplitude of the input signal u(t) to the bang-bang nonlinearity. Notice that the describing function in this case can be regarded as an amplitude dependent gain.

The whole idea of introducing the describing function approximation, is that the resultant linear system approximation can be used to determine the stability and approximate response of a dynamic system which contains the original nonlinear element. For this to be the case, it is important that the higher harmonics of the output from the nonlinear element is sufficiently filtered by the dynamics of the linear parts of the system (Ref. 23, p. 652). For our system, this is probably adequately satisfied by the motor dynamics and the position integration from motor speed to output angle.

The resulting quasi linear model of the servo can then be obtained by substituting the describing function N_{servo}, for the bang-bang nonlinearity in the model (Figure 3.3):

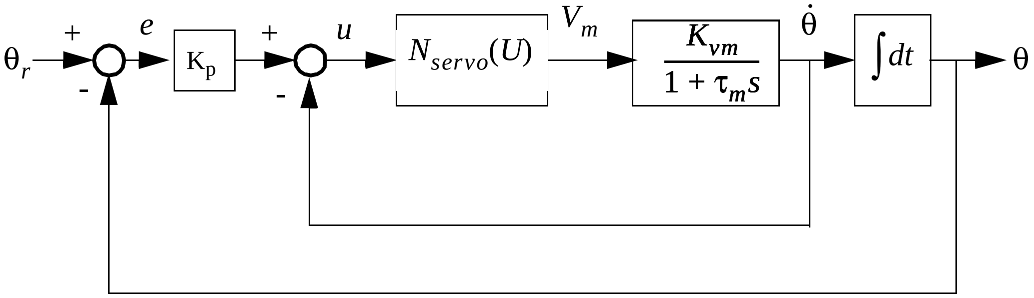

FIGURE 3.8 Semi empirical large signal servo model with describing function.

Where $N_{servo}(U)$ is used to indicate that the gain N_{servo} is a function of the amplitude U of the control signal u(t).

One problem with the describing function model is that the describing function depends on the control signal u(t) and not the reference signal θ_r. This is rather unfortunate since we do not know the amplitude of u(t) in advance. What we really want is to use the describing function model to determine a quasi linear system model that depends on the amplitude of the reference θ_r, rather then that of the control signal u(t).

For a constant value of N_{servo}, the transfer function from $\theta_r(s)$ to $\theta(s)$ can be determined as:

$$\frac{\theta(s)}{\theta_r(s)} = \frac{K_p N_{servo} K_{vm}}{\tau_m s^2 + (N_{servo} K_{vm} + 1)s + K_p N_{servo} K_{vm}} \tag{3.3.9}$$

The frequency characteristics with a constant value of N_{servo}, from $\theta_r(j\omega)$ to $\theta(j\omega)$ can then be determined as:

$$\frac{\theta(j\omega)}{\theta_r(j\omega)} = \frac{K_p N_{servo} K_{vm}}{(N_{servo} K_{vm} + 1)j\omega + K_p N_{servo} K_{vm} - \tau_m \omega^2} \tag{3.3.10}$$

The transfer function from $\theta_r(s)$ to $u(s)$ can similarly be expressed as:

$$\frac{u(s)}{\theta_r(s)} = \frac{K_p(1 + \tau_m s)s}{\tau_m s^2 + (N_{servo} K_{vm} + 1)s + K_p N_{servo} K_{vm}} \tag{3.3.11}$$

The amplitude ratio between $\theta_r(j\omega)$ and $u(j\omega)$ can then be determined as:

$$G_s(j\omega, \|u\|) = \frac{u(j\omega)}{\theta_r(j\omega)} = \frac{K_p(1 + \tau_m j\omega)j\omega}{(N_{servo} K_{vm} + 1)j\omega + K_p N_{servo} K_{vm} - \tau_m \omega^2} \tag{3.3.12}$$

In order to determine the value of the describing function N_{servo} for fixed values of reference amplitude $\|\theta_r(j\omega)\|$ and frequency ω, we can use the following method:

1. Guess the magnitude of the linear control signal $\|u(j\omega)\|$.
2. Calculate the corresponding value of the describing function N_{servo}, using Eq. 3.3.8.
3. Calculate the estimated magnitude of the corresponding reference signal $\|\theta_r(j\omega)\|_e$, using Eq. 3.3.12.
4. Calculate the error function $e = \|\theta_r(j\omega)\| - \|\theta_r(j\omega)\|_e$.
5. Adjust the guessed control signal magnitude $\|u(j\omega)\|$, based on the value of e.
6. Repeat from step #1, until $|e| \le \varepsilon \ll 1$.
7. Calculate the describing function estimate of the frequency characteristic using Eq. 3.3.10.

Describing function approximation algorithm.

This procedure has been implemented in Matlab using the “fzero” function to determine $\|u(j\omega)\|$, for a fixed input amplitude $\|\theta_r(j\omega)\|$ and a range of frequencies ω. The result is a describing function estimate of the amplitude dependent frequency characteristics of the servo.

The resulting frequency responses for three different reference amplitude values; $1°$, $5°$ and $20°$, are shown below:

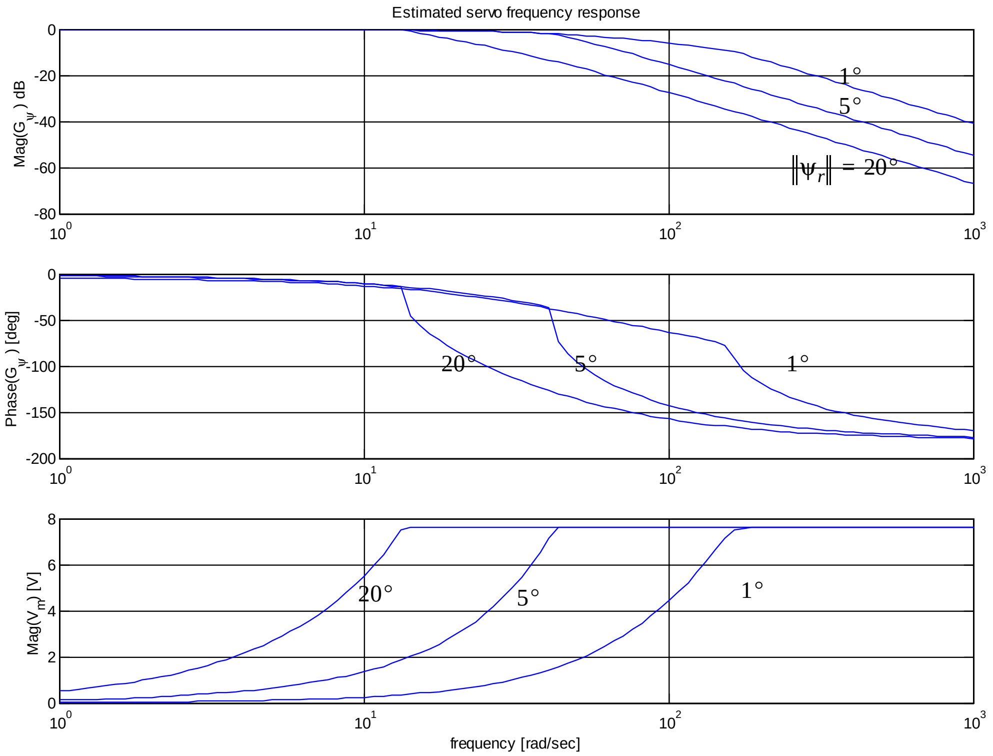

FIGURE 3.9 Frequency response of describing function approximations for different reference amplitudes (the angle annotations indicate the reference angle amplitudes).

It is apparent that the response becomes very nonlinear, particularly with respect to the phase, when the motor voltage amplitude (V_m) saturates. The resulting large phase lag without a corresponding decrease in gain can easily lead to instability if the servo is part of a closed loop control system.

It is also apparent that even for a fixed reference amplitude, there is no simple quasi linear system approximation to the frequency characteristics. It is thus doubtful that a linear controller design can be based directly on the describing function approximations.

It seems that there are three obvious ways of dealing with this nonlinearity with respect to linear control design:

1. Assume that the rest of the subsystems in the final closed loop system, have a much lower bandwidth then the servo. This enables the servo to be modelled as a unity gain transfer function.
2. Add a prefilter with a lower bandwidth then the smallest possible bandwidth of the servo, at the input to the servo. This reduces the amplitude of the high frequency reference signals to the servo, thus preventing high frequency saturation of the servo.
3. Add a parallel reference system to the servo and use the reference system to compensate for the servo nonlinearities using a local feedback loop.

The first method above, is conceptually the simplest, however there are two related disadvantages; when synthesizing the controller we do not necessarily know the resulting loop bandwidth before the design is complete. Secondly we may obtain a slow system, because of the requirement that the loop bandwidth is much lower then the servo bandwidth. The second method places no strict requirements on the final design, however it will lead to an excessive phase lag at high frequencies, because we effectively place two second order systems in series.

The third method can be described by the following state space block diagram:

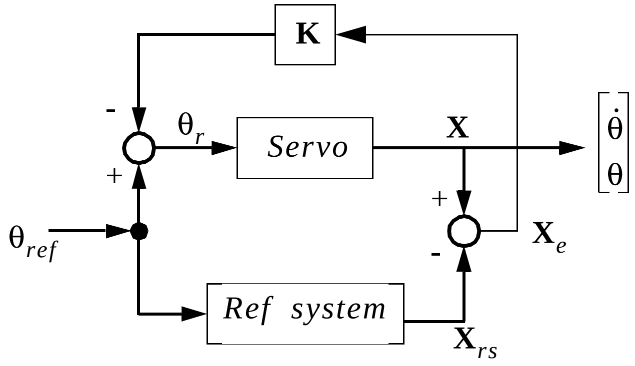

FIGURE 3.10 Reference system linearisation.

Where $\mathbf{X} = \begin{bmatrix}\dot\theta & \theta\end{bmatrix}^T$ is the nonlinear servo state space vector, $\mathbf{X}_{rs} = \begin{bmatrix}\dot\theta & \theta\end{bmatrix}_{rs}^T$ is the linear *reference system* state space vector and $\mathbf{X}_e = \mathbf{X} - \mathbf{X}_{rs}$ is the reference tracking error. The state space feedback gain is defined as $\mathbf{K} = \begin{bmatrix}K_1 & K_2\end{bmatrix}$. Notice that the reference system has been defined as a second order linear system, this is motivated by the fact that the nonlinear servo model is a second order system. It is apparent by inspection of Figure 3.10, that the effect of the feedback gain is to force the nonlinear servo to follow the reference system. Since the reference error feedback is only effective if the motor voltage amplitude $\|V_m\|$ is not saturated, it is important to choose the reference system in such way that this condition is satisfied.

Since the goal of using reference system linearisation is to force the nonlinear servo response to follow the response of the servo system, we should choose a desirable reference system response. Normally a good compromise between speed, step overshoot, stability and robustness is given by a critically damped second order system:

$$G_{rs}(s) = \frac{\theta_{rs}(s)}{\theta_r(s)} = \frac{\omega_n^2}{s^2 + 2\zeta\omega_n s + \omega_n^2} \qquad \zeta = \sqrt{2} \tag{3.3.13}$$

This makes it apparent that there is only one design parameter, the undamped natural frequency ω_n, left to determine. This can be determined by computing the frequency domain response for the maximum reference amplitude $\|\theta_{ref}\|$ using the describing function approximation for the nonlinear servo, in the configuration shown in Figure 3.10. With the proper choose of ω_n, the motor amplitude $\|V_m\|$ will not saturate for any frequency.

Before we can compute the frequency response, we have to determine the feedback gain matrix $\mathbf{K}$. Since the nonlinear servo system is inside the feedback loop, while the reference system is outside the loop, the stability of the feedback linearized system depends to a large extent on the dynamics of the nonlinear servo. Fortunately the nonlinear servo system has a total phase lag of less then $180°$ (see Figure 3.9), thus the nonlinear system will be stable for any proportional/derivative feedback gain.

The feedback linearized system can be approximately expressed in the frequency domain by using the describing function approximation. This gives the following frequency domain block diagram:

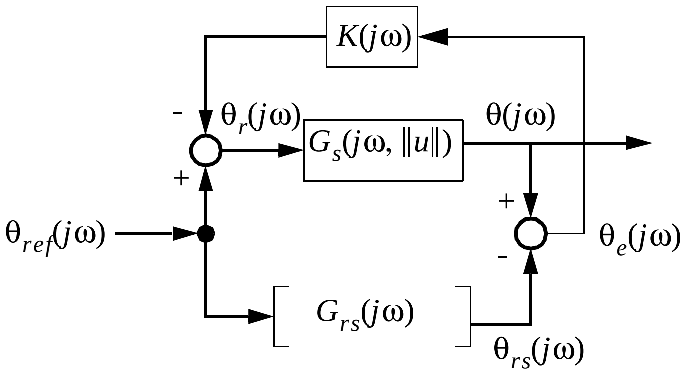

FIGURE 3.11 Reference system linearisation in frequency domain.

From the definition of the servo states and the feedback gain $\mathbf{K} = \begin{bmatrix} K_1 & K_2 \end{bmatrix}$, it is apparent that the feedback controller $K(j\omega)$ is a PD controller given by:

$$K(j\omega) = j\omega K_1 + K_2 = K_2(1 + j\tau_d\omega) \tag{3.3.14}$$

It is now apparent that the reference linearized servo system will be stable for any positive combinations of feedback gains $\mathbf{K} = \begin{bmatrix} K_1 & K_2 \end{bmatrix}$. Due to the small number of total parameters, it is feasible to obtain suitable values for the parameters using “hand optimization” on the system shown in Figure 3.11.

In order to compute the frequency domain transfer function between the input $\theta_{ref}(j\omega)$ and the output $\theta(j\omega)$, we have to determine the value of the control signal amplitude $\|u(j\omega)\|$. This can be done in a similar manner as that used to determine the describing function approximation of the frequency response of the original nonlinear servo, to constant reference amplitude signals.

Lets define the *loop gain* $L(j\omega)$ of the reference system linearized system, as the open loop gain around the feedback loop:

$$L(j\omega) \equiv K(j\omega)G_s(j\omega, \|u\|) \tag{3.3.15}$$

The frequency domain transfer function from $\theta_{ref}(j\omega)$ to $\theta_e(j\omega)$ is then obtained as:

$$\frac{\theta_e(j\omega)}{\theta_{ref}(j\omega)} = \frac{G_s(j\omega, \|u\|) - G_{rs}(j\omega)}{1 + L(j\omega)} \tag{3.3.16}$$

The transfer function from $\theta_{ref}(j\omega)$ to the servo output $\theta(j\omega)$ is given by:

$$G_{lin}(j\omega, \|u\|) = \frac{\theta(j\omega)}{\theta_{ref}(j\omega)} = \frac{(1 + K(j\omega)G_{rs}(j\omega))G_s(j\omega, \|u\|)}{1 + L(j\omega)} \tag{3.3.17}$$

From which we can see that as the feedback gain $K(j\omega)$ increases, the closed loop response approaches the reference system:

$$\frac{\theta(j\omega)}{\theta_{ref}(j\omega)} = \frac{(1 + K(j\omega)G_{rs}(j\omega))G_s(j\omega, \|u\|)}{1 + K(j\omega)G_s(j\omega, \|u\|)} \to G_{rs}(j\omega) \quad \text{as} \quad K(j\omega) \to \infty \tag{3.3.18}$$

The transfer function from the control (internal) signal $u(j\omega)$ to the servo output $\theta(j\omega)$ is given by:

$$\frac{\theta(j\omega)}{u(j\omega)} = \frac{K_{vm}N_{servo}(\|u(j\omega)\|)}{j\omega(1 + j\tau_m\omega)} \tag{3.3.19}$$

We can now determine the transfer function from the (internal) control signal $u(j\omega)$ to the servo reference input $\theta_{ref}(j\omega)$, using the transfer functions obtained above:

$$\begin{aligned} \frac{\theta_{ref}(j\omega)}{u(j\omega)} &= \left(\frac{u(j\omega)}{\theta_{ref}(j\omega)}\right)^{-1} = \frac{\theta(j\omega)}{u(j\omega)}\left(\frac{\theta(j\omega)}{\theta_{ref}(j\omega)}\right)^{-1} \quad \Leftrightarrow \\ \frac{\theta_{ref}(j\omega)}{u(j\omega)} &= \frac{K_{vm}N_{servo}(\|u(j\omega)\|)}{j\omega(1 + j\tau_m\omega)} \frac{1 + L(j\omega)}{(1 + K(j\omega)G_{rs}(j\omega))G_s(j\omega, \|u\|)} \end{aligned} \tag{3.3.20}$$

Where $N_{servo}(\|u(j\omega)\|)$ is given by Eq. 3.3.7, $G_s(j\omega, \|u\|)$ is given by Eq. 3.3.12 and $G_{rs}(j\omega)$ is given by Eq. 3.3.13.

We can now use the following algorithm to compute the approximate describing function frequency response of the feedback linearized system, with different input reference amplitudes $\|\theta_{ref}(j\omega)\|$:

1. Guess the magnitude of the linear control signal $\|u(j\omega)\|$ at a given frequency ω.
2. Calculate the corresponding value of the describing function N_{servo} using Eq. 3.3.8.
3. Calculate the estimated magnitude of the corresponding reference signal $\|\theta_{ref}(j\omega)\|_e$ using Eq. 3.3.20.
4. Calculate the error function $e = \|\theta_{ref}(j\omega)\| - \|\theta_{ref}(j\omega)\|_e$.
5. Adjust the guessed control signal magnitude $\|u(j\omega)\|$, based on the value of e.
6. Repeat from step #1, until $e \le \varepsilon \ll 1$.
7. Calculate the describing function estimate of the feedback linearized frequency characteristic $G_{lin}(j\omega, \|\theta_{ref}\|)$ using Eq. 3.3.17.

Feedback linearization approximation algorithm.

This procedure has been implemented in Matlab using the “fzero” function to determine $\|u(j\omega)\|$, for a fixed input amplitude $\|\theta_{ref}(j\omega)\|$ and a range of frequencies ω. The resulting frequency responses for three different reference amplitude values; $1°$, $5°$ and $20°$, are shown below:

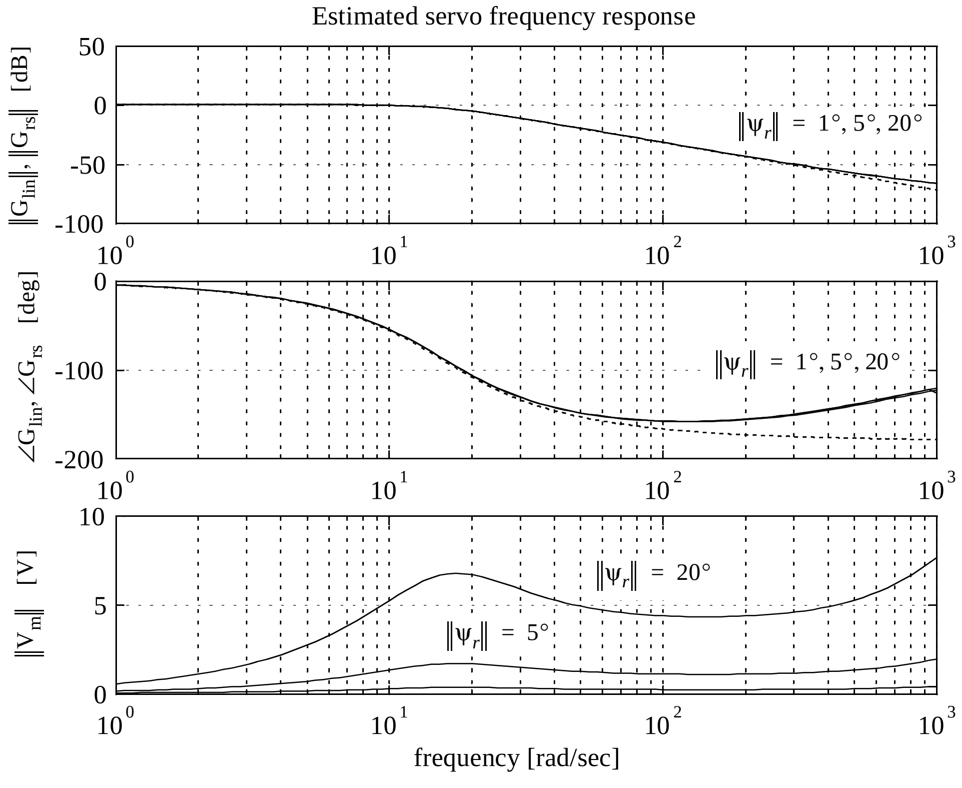

FIGURE 3.12 Approximate describing function frequency response of feedback linearized system for different reference amplitudes (the dotted line is the reference system response).

As shown in Figure 3.12, the frequency response of the feedback linearized system can be made quite close to the reference system, as long as the motor voltage amplitude $\|V_m\|$ is not saturated.

The reference system used in Figure 3.12 is defined by:

$$G_{rs}(s) = \frac{\omega_n^2}{s^2 + 2\zeta\omega_n s + \omega_n^2} \qquad \zeta = \sqrt{2} \qquad \omega_n = 2.5 \cdot (2\pi) \cong 15.7 \ [\text{rad/s}] \tag{3.3.21}$$

The feedback gain used in Figure 3.12 was defined by:

$$\mathbf{K} = \begin{bmatrix} K_1 & K_2 \end{bmatrix} = \begin{bmatrix} 25 & 0.1 \end{bmatrix} \tag{3.3.22}$$

3.4 Actuator model conclusion:

It is shown that the model airplane servos used for the UAV employ an internal bang-bang controller with proportional-derivative action. It is possible to linearize the servo response by using an outer loop which forces the servo to follow the response of a second order critically damped reference system.

3.5 References:

22.Multiplex servo datasheet.

23.Katsuhiko Ogata:”Modern Control Engineering”, second edition, Prentice Hall, Inc 1990.

Chapter 4

Lateral Guidance

4.1 Simple lateral model of UAV

The lateral guidance problem consists in controlling an UAV such that a preprogrammed path (in 2 dimensions) is followed. Due to the physical characteristics and limitations of a flying vehicle, certain restrictions are imposed on the actual trajectory of the UAV. To obtain a satisfactory and safe system, both the flight path and control strategy must reflect these restrictions.

In order to investigate the guidance problem without undue complications, a simple lateral model of a UAV will be used. In order to derive such a model we may consider the following:

An UAV flying in a straight and level flight path at a certain speed U greater then the stall speed (in level flight) U_s has the ability to “instantaneously” generate a maximum lift $F_{L,max}$ of:

$$F_{L,\,max} = mg\left(\frac{U}{U_s}\right)^2 \tag{4.1.1}$$

Where m is the mass of the UAV and g is the acceleration of gravity. In addition it is assumed that the lift is normal to the instantaneous plane of the wings.

Assuming that the lift to drag ratio is “high”, the generation of additional lift within the limit given by $F_{L,max}$ will result in an acceleration of the UAV which is essentially normal to the instantaneous velocity vector **U**. The maximum apparent gravity $g_{eff,max}$ in a reference system moving with the UAV center of gravity (CG) can then be determined as:

$$g_{eff,\,max} = g\left(\frac{U}{U_s}\right)^2 \tag{4.1.2}$$

In a lateral model we must further assume that the vertical component of the lift is always equal to the weight of the UAV. Using Pythagoras, the relation between the lateral normal acceleration a_N and the effective acceleration g_{eff} can be expressed as:

$$g_{eff}^2 = g^2 + a_N^2 \tag{4.1.3}$$

Combining the above two equations, gives the maximum lateral normal acceleration $a_{N,max}$ as a function of the flight speed U and the stall speed U_s:

$$a_{N,\,max} = g\sqrt{\left(\frac{U}{U_s}\right)^4 - 1} \tag{4.1.4}$$

Since it is assumed that all the lift is generated normal to the plane of the wings, the UAV must make “coordinated” turns to generate lateral normal acceleration. Thus the UAV must roll around its longitudinal axis in order to orientate the wings properly for the desired lateral normal acceleration. Obviously this motion can take quite a long time especially when transitioning from a turn in one direction, to the opposite direction. In the context of a simple model for the dynamic effects of the *bank to turn* control strategy, we may model the lateral dynamics as a first order system with a fixed time constant:

$$\tau \dot{a}_N + a_N = u \tag{4.1.5}$$

Where τ is the roll/bank time constant and u(t) is the control input for normal lateral acceleration. For simplicity u(t) is equal to the “steady state” value of a_N.

The lateral kinematic state of the UAV can be described by the lateral position **P**(t) = (x(t),y(t)) and the compass direction $\psi(t)$ of the velocity vector, as shown in the figure below:

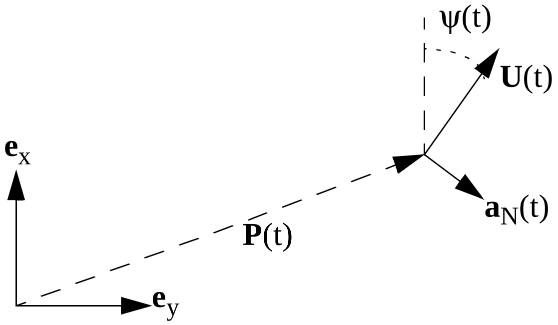

FIGURE 4.1 Lateral kinematics.

For simplicity we will assume that $\mathbf{e}_y$ points towards the geographical north and $\mathbf{e}_x$ points towards the geographical west. Thus the coordinate system defined by ($\mathbf{e}_x$,$\mathbf{e}_y$) is not a true planar system but rather the surface of a sphere (the earth). Locally however, the coordinate system is an ortogonal coordinate system. The compass direction of the flight path is defined as clockwise from the direction of north. The positive direction of the normal acceleration scalar a_N(t), is defined as $\psi(t) + 90°$.

It is apparent that there are more states defined above then necessary to describe the kinematics and dynamics of the UAV. To eliminate the redundancy, the following states will be used to describe the kinematics of the UAV; x, y and ψ. In addition the first order approximation in Eq. 4.1.5, requires an additional state. In this model we will use the scalar normal acceleration a_N as the final state. Notice that the scalar speed U(t) is not considered a state since it is by definition not changed by a normal acceleration. Instead U(t) must be considered as a parameter in the following.

The state vector **X** is then defined as:

$$\mathbf{X}(t) = \begin{bmatrix} x(t) & y(t) & \psi(t) & a_N(t) \end{bmatrix}^T \tag{4.1.6}$$

Given the above kinematic and dynamic equations, the state space equation for lateral motion becomes:

$$\begin{bmatrix} \dot{x} \\ \dot{y} \\ \dot{\psi} \\ \dot{a}_N \end{bmatrix} = \begin{bmatrix} \sin(\psi)U \\ \cos(\psi)U \\ \dfrac{a_N}{U} \\ -\dfrac{1}{\tau}a_N \end{bmatrix} + \begin{bmatrix} 0 \\ 0 \\ 0 \\ \dfrac{1}{\tau}u \end{bmatrix} \qquad |a_N| \le g\sqrt{\left(\frac{U}{U_s}\right)^4 - 1} \tag{4.1.7}$$

For simplicity, we will refer the constraint on a_N to the control input u:

$$|u| \le g\sqrt{\left(\frac{U}{U_s}\right)^4 - 1} \tag{4.1.8}$$

Indeed assuming $|a_N| \le a_{N,\,max}$ for $t < t_0$ and $|u| \le a_{N,\,max}$, guarantees $|a_N| \le a_{N,\,max}$ for all $t \in R$, since $a_N(t)$ is modelled as a first order system with unity gain.

From Eq. 4.1.7, it is apparent that the state space equation is nonlinear in ψ, in addition to the limits on u given by Eq. 4.1.8.

4.2 Guidance strategies

Before we can control the UAV, we must define in what way we want the UAV to fly through 3 dimensional airspace. There are several ways to do this. But the four most obvious strategies are (in the following we describe the 2 dimensional problem):

1. Trajectory following: The UAV should follow a space/time reference trajectory $(x(t),y(t))_{ref}$.
2. Fixed waypoint guidance: The UAV should fly towards a fixed waypoint, turning at each waypoint to proceed towards the next waypoint. This method could also be described as fixed point navigation.
3. Path following: The UAV should follow a reference path $(x(s),y(s))_{ref}$, but in contrast to trajectory following, the “distance” s along the path is not a predetermined function of time, but just a parameter used to describe the path.
4. Moving point guidance: The UAV should fly towards a moving point, which is “sliding” along the path at a (fixed) distance in “front” of the UAV.

4.3 A general approach to linearization

Most modern control system design techniques (LQR, pole placement, H_{inf}, etc.) require that the dynamics of the control object (the “plant”) be linear. The nonlinear lateral UAV dynamics given in Eq. 4.1.7 thus need to be linearized before any of these design techniques can be used. This however presents a general problem, because of the trigonometric terms relating the direction of flight ψ to the position derivative $(\dot{x}, \dot{y})$. If we a priori knew that the UAV would always fly close to a certain direction ψ_0, this could be used to linearize Eq. 4.1.7 around this direction. In practise this would however be very restrictive, since the we would need a new linearization and in turn a new control system for every direction. In addition, there could be problems associated with switching between the different controllers (bump(less) transfer etc.)

A more general approach is to first define or choose a control strategy as discussed above. Having defined a control strategy, it is relatively easy to derive a control error measure e(t), which has the property that when the control objective of the control strategy is met, the error measure (or function) is zero. In addition e(t) must be monotone in the region of zero error and preferably also in a global sense.

We can now rewrite the equations of motion in terms of the deviation between the ideal flight path/trajectory corresponding to e(t) = 0, and the actual one corresponding to the state **X**(t).

4.4 Fixed waypoint guidance

In fixed waypoint guidance, it is desired that the UAV flight path points towards the next waypoint:

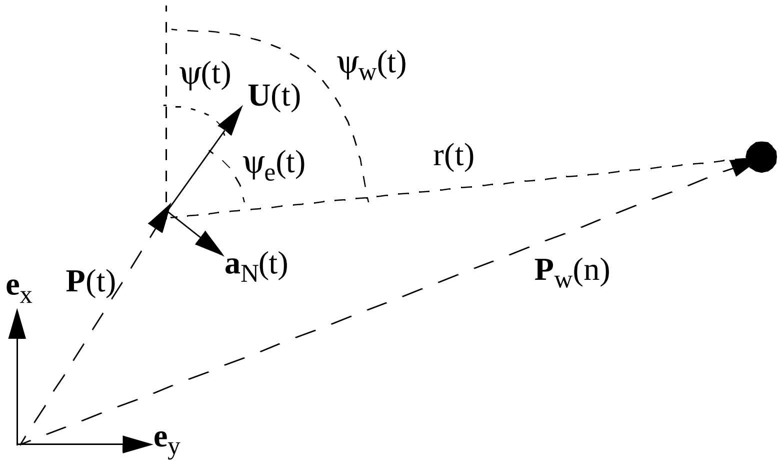

FIGURE 4.2 Fixed waypoint guidance.

Where $\mathbf{P}_w(n)$ is the position of the next waypoint (number “n”), r(t) is the range (distance) to the next waypoint, $\psi_w(t)$ is the instantaneous course to the next waypoint and $\psi_e(t)$ is the direction error, defined as:

$$\psi_e(t) \equiv \psi_w(t) - \psi(t) \tag{4.4.1}$$

Taking the derivative gives:

$$\dot{\psi}_e(t) = \dot{\psi}_w(t) - \dot{\psi}(t) \tag{4.4.2}$$

Where the derivative of $\psi(t)$ is given by Eq. 4.1.7. The derivative of $\psi_w(t)$ can be determined from geometrical considerations using Figure 4.2:

$$\dot{\psi}_w(t) = \sin(\psi_e)\frac{U}{r} \tag{4.4.3}$$

Giving the dynamics of the error direction $\psi_e(t)$ as:

$$\dot{\psi}_e(t) = \sin(\psi_e)\frac{U}{r} - \frac{a_N}{U} \tag{4.4.4}$$

The way point range rate $\dot{r}(t)$ is similarly given as:

$$\dot{r}(t) = -\cos(\psi_e)U \tag{4.4.5}$$

We are now able to write down the nonlinear equations of motion corresponding to fixed waypoint navigation:

$$\begin{bmatrix} \dot{r} \\ \dot{\psi}_e \\ \dot{a}_N \end{bmatrix} = \begin{bmatrix} -\cos(\psi_e)U \\ \sin(\psi_e)\frac{U}{r} - \frac{a_N}{U} \\ -\frac{1}{\tau}a_N \end{bmatrix} + \begin{bmatrix} 0 \\ 0 \\ \frac{1}{\tau}u \end{bmatrix} \tag{4.4.6}$$

This can then be linearized around a particular operating point $(r,U,\psi_e) = (r_0,U_0,0)$:

$$\begin{bmatrix} \dot{\psi}_e \\ \dot{a}_N \end{bmatrix} = \begin{bmatrix} \frac{U_0}{r_0} & -\frac{1}{U_0} \\ 0 & -\frac{1}{\tau} \end{bmatrix} \begin{bmatrix} \psi_e \\ a_N \end{bmatrix} + \begin{bmatrix} 0 \\ \frac{1}{\tau} \end{bmatrix} \begin{bmatrix} u \end{bmatrix} \tag{4.4.7}$$

Where the range r(t) has been eliminated because it has a purely nonlinear influence on the direction error ψ_e. Unfortunately the nonlinear influence of r(t) is such that as the waypoint is approached $r(t) \to 0$, the system matrix becomes singular due to the term U_0/r_0.

4.5 Path following

In path following, it is desired that the UAV follows a prescribed reference path $\mathbf{P}_r(s) = (x_r(s), y_r(s))$, where s is a parameter (the "distance" along the path):

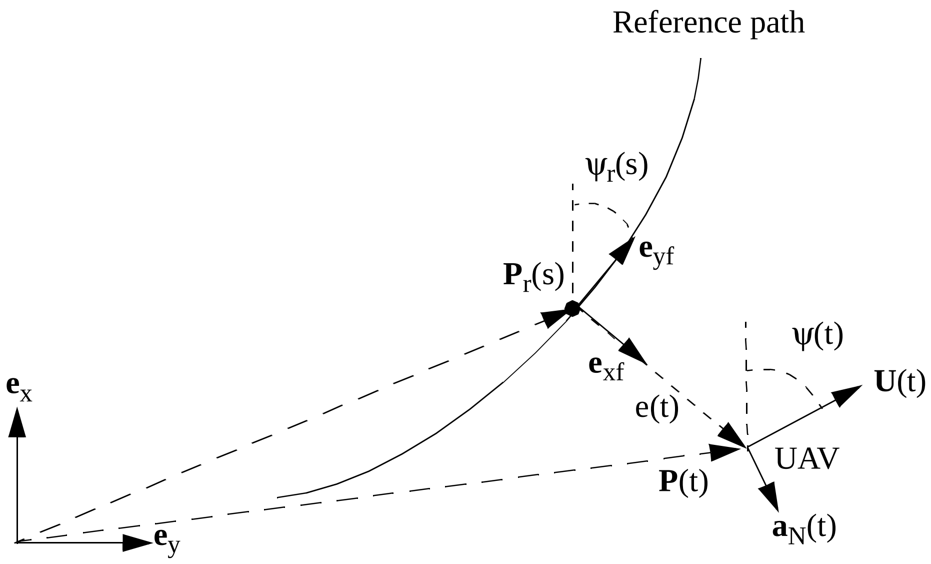

FIGURE 4.3 Path following guidance.

Where $\psi_r(s)$ is the reference path direction at "path distance" s and e(t) is the instantaneous "cross track" error. In order to define the sign of the cross track error, we have assumed that the "flight path" coordinate system $(\mathbf{e}_{xf}, \mathbf{e}_{yf})$ is obtained by translating the earth coordinate system $(\mathbf{e}_x, \mathbf{e}_y)$ to the position $\mathbf{P}_r(s)$ and rotating it the angle $\psi_r(s)$ clock wise. Furthermore we assume that the vector $\mathbf{P}(t)$-$\mathbf{P}_r(s)$ is equal to $e(t)\mathbf{e}_{xf}$. Thus the instantaneous "path distance" s(t) must be chosen so that the magnitude of e(t) has a local minimum for a fixed UAV position $\mathbf{P}(t)$.

As an aid in solving this problem, let us define the "error" direction $\psi_e(t)$, as:

$$\psi_e(t) \equiv \psi(t) - \psi_r(t) \tag{4.5.1}$$

From this and Figure 4.3, it is easy to see that the derivative of the error e(t) can be expressed as:

$$\dot{e}(t) = \sin(\psi_e(t))U(t) = \sin(\psi(t) - \psi_r(t))U(t) \tag{4.5.2}$$

The nonlinear equations of motion for the path following error system, can then be expressed as:

$$\begin{bmatrix} \dot{e} \\ \dot{\psi} \\ \dot{a}_N \end{bmatrix} = \begin{bmatrix} \sin(\psi - \psi_r)U \\ \dfrac{a_N}{U} \\ -\dfrac{1}{\tau}a_N \end{bmatrix} + \begin{bmatrix} 0 \\ 0 \\ \dfrac{1}{\tau}u \end{bmatrix} \tag{4.5.3}$$

Where we have assumed that ψ_r is determined as the path direction at the path distance s corresponding to the point where the $\|P(t) - P_r(s)\|$ has a (local) minima with respect to s.

Linearizing around the operating point $(e, U, \psi - \psi_r) = (0, U_0, 0)$ gives:

$$\begin{bmatrix} \dot{e} \\ \dot{\psi} \\ \dot{a}_N \end{bmatrix} = \begin{bmatrix} 0 & U_0 & 0 \\ 0 & 0 & \frac{1}{U_0} \\ 0 & 0 & -\frac{1}{\tau} \end{bmatrix} \begin{bmatrix} e \\ \psi \\ a_N \end{bmatrix} + \begin{bmatrix} 0 & -U_0 \\ 0 & 0 \\ \frac{1}{\tau} & 0 \end{bmatrix} \begin{bmatrix} u \\ \psi_r \end{bmatrix} \tag{4.5.4}$$

Where we have treated ψ_r as an input.

Since the derivative of e(t) is independent of e(t) and the derivative of $\psi(t)$ is likewise independent of $\psi(t)$, this system describes a double integrator driven by a first order system with a time constant of τ. Notice that in contrast to the “fixed waypoint guidance” scheme, this system is only nonlinear in the speed U.

After some arithmetic, the laplace transform of Eq. 4.5.4 is obtained as (taking the path error “e” as the output):

$$e(s) = \frac{1}{s^2(s\tau + 1)} u(s) - \frac{U_0}{s^2} \psi_r(s) \tag{4.5.5}$$

Where “s” describes the Laplace operator, not to be confused with the path distance also denoted by “s”.

One interesting thing about the transfer function from the input “u” to the path error “e” is, that it is independent of the speed U. Considering that “u” is a reference acceleration and “e” is a distance, this is not surprising.

4.6 Moving point guidance

In moving point guidance, it is desired that the UAV flies towards a moving point some distance in front of the UAV:

Where $\mathbf{P}_r(s)$ is the reference path, $\psi_r(s)$ is the reference path direction, $\psi_R(t)$ is the direction from the UAV to the instantaneous “target” point on the reference path, $\mathbf{U}_r(t)$ is the velocity vector of the instantaneous “target” point, $\psi_e(t)$ is instantaneous direction “error” and “r” is the distance between the UAV and the “target” point.

The equations of motion for the direction error, can be determined by adding the contributions due to UAV motion with the contributions due to motion of the “target” point:

$$\dot{\psi}_e = \frac{\partial \psi_e}{\partial \psi} \dot{\psi} + \frac{\partial \psi_e}{\partial \mathbf{P}} \dot{\mathbf{P}} + \frac{\partial \psi_e}{\partial \mathbf{P}_r} \dot{\mathbf{P}}_r \tag{4.6.1}$$

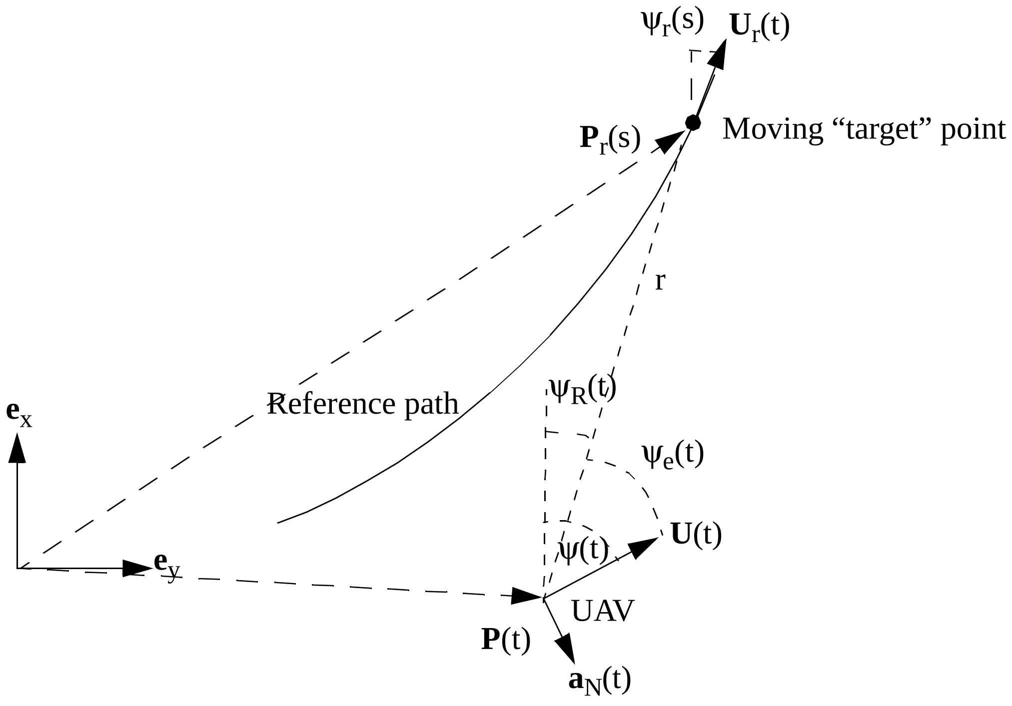

FIGURE 4.4 Moving point guidance.

Where the first two terms are due to UAV rotation and translation, while the last term is due to motion of the moving "target" point.

The first term is straight forward:

$$\frac{\partial\psi_e}{\partial\psi} = 1 \tag{4.6.2}$$

The translation term is due to the tangential motion of the UAV with respect to the "target" point:

$$\frac{\partial\psi_e}{\partial\mathbf{P}}\dot{\mathbf{P}} = \frac{\partial\psi_e}{\partial\mathbf{P}}\mathbf{U} = \sin(\psi_e)\frac{U}{r} \tag{4.6.3}$$

The last term is due to tangential motion of the "target" point with respect to the UAV:

$$\frac{\partial\psi_e}{\partial\mathbf{P}_r}\dot{\mathbf{P}}_r = \frac{\partial\psi_e}{\partial\mathbf{P}_r}\mathbf{U}_r = -\sin(\psi_r - \psi_R)\frac{U_r}{r} \tag{4.6.4}$$

This gives the following equation for the derivative of the direction error:

$$\dot{\psi}_e = \dot{\psi} + \sin(\psi_e)\frac{U}{r} - \sin(\psi_r - \psi_R)\frac{U_r}{r} \tag{4.6.5}$$

It is apparent from Figure 4.4 that ψ_R is not an independent state, but can be expressed as:

$$\psi_R = \psi - \psi_e \tag{4.6.6}$$

This gives the following derivative for direction error:

$$\dot{\psi}_e = \dot{\psi} + \sin(\psi_e)\frac{U}{r} - \sin(\psi_r + \psi_e - \psi)\frac{U_r}{r} \tag{4.6.7}$$

The equations of motion for moving point guidance can then be expressed using Eq. 4.1.7:

$$\begin{bmatrix} \dot{\psi}_e \\ \dot{\psi} \\ \dot{a}_N \end{bmatrix} = \begin{bmatrix} \frac{a_N}{U} + \sin(\psi_e)\frac{U}{r} - \sin(\psi_r + \psi_e - \psi)\frac{U_r}{r} \\ \frac{a_N}{U} \\ -\frac{1}{\tau}a_N \end{bmatrix} + \begin{bmatrix} 0 \\ 0 \\ \frac{1}{\tau} \end{bmatrix} u \tag{4.6.8}$$

The “course error” ψ_{re} can be defined as the difference between the UAV course ψ and the path course ψ_r:

$$\psi_{re} = \psi - \psi_r \tag{4.6.9}$$

Substituting into Eq. 4.6.8 gives:

$$\begin{bmatrix} \dot{\psi}_e \\ \dot{\psi}_{re} \\ \dot{a}_N \end{bmatrix} = \begin{bmatrix} \frac{a_N}{U} + \sin(\psi_e)\frac{U}{r} - \sin(\psi_e - \psi_{re})\frac{U_r}{r} \\ \frac{a_N}{U} \\ -\frac{1}{\tau}a_N \end{bmatrix} + \begin{bmatrix} 0 & 0 \\ 0 & -1 \\ \frac{1}{\tau} & 0 \end{bmatrix} \begin{bmatrix} u \\ \dot{\psi}_r \end{bmatrix} \tag{4.6.10}$$

Where the “target” point speed $U_r(t)$ is related to the UAV speed U(t) and the distance “r”. If the distance “r” is assumed continues in time, we may from geometrical considerations express $U_r(t)$ as:

$$U_r(t) = \cos(\psi_e)U(t) + \cos(\psi_r - \psi_R)\dot{r}(t) = \cos(\psi_e)U(t) + \cos(\psi_r - \psi + \psi_e)\dot{r}(t)$$

(4.6.11)

In the special case that “r” is constant, we may express $U_r(t)$ as:

$$U_r(t) = \cos(\psi_e)U(t) \tag{4.6.12}$$

The error dynamics Eq. 4.6.8, can be linearized around zero error by making the following assumptions:

$$\|\psi_e\| \ll 1 \qquad \|\psi_r - \psi_R\| \ll 1 \qquad U_r \approx U = U_0 \qquad r = r_0 \tag{4.6.13}$$

This gives the linearized error dynamics:

$$\begin{bmatrix} \dot{\psi}_e \\ \dot{\psi} \\ \dot{a}_N \end{bmatrix} = \begin{bmatrix} 0 & \frac{U_0}{r_0} & \frac{1}{U_0} \\ 0 & 0 & \frac{1}{U_0} \\ 0 & 0 & -\frac{1}{\tau} \end{bmatrix} \begin{bmatrix} \psi_e \\ \psi \\ a_N \end{bmatrix} + \begin{bmatrix} 0 & \frac{U_0}{r_0} \\ 0 & 0 \\ \frac{1}{\tau} & 0 \end{bmatrix} \begin{bmatrix} u \\ \psi_r \end{bmatrix} = \mathbf{AX} + \begin{bmatrix} \mathbf{B}_1 & \mathbf{B}_2 \end{bmatrix} \mathbf{U} \tag{4.6.14}$$

Where **B1** is associated with the controlled input “u” and **B2** with the path angle input $\psi_r(t)$.

If full state knowledge is available, a good choice of closed loop controller, is a Linear Quadratic Regulator (LQR). Such a controller can be synthesized in both the continues and discrete time domains. Since the actual physical controller will be implemented in a micro processor setting, the best performance can be expected to be achieved if the controller is synthesized in the discrete domain. This requires that the equations of motion are discretized using a suitable sampling time T_s.

With state vector $\mathbf{X}_n$ the discrete representation of Eq. 4.6.14 can be expressed as:

$$\mathbf{X}_n = \mathbf{A}_d \mathbf{X}_{n-1} + \begin{bmatrix} \mathbf{B}_{1d} & \mathbf{B}_{2d} \end{bmatrix} \mathbf{U}_n \tag{4.6.15}$$

Where the subscript “d” denotes “discrete”.

4.6.1 Simulation of moving point guidance scheme:

Using the discretized linearized equations of motion for moving point guidance, a discrete LQR controller has been designed in Matlab. The results for a simulation are shown below in Figure 4.5:

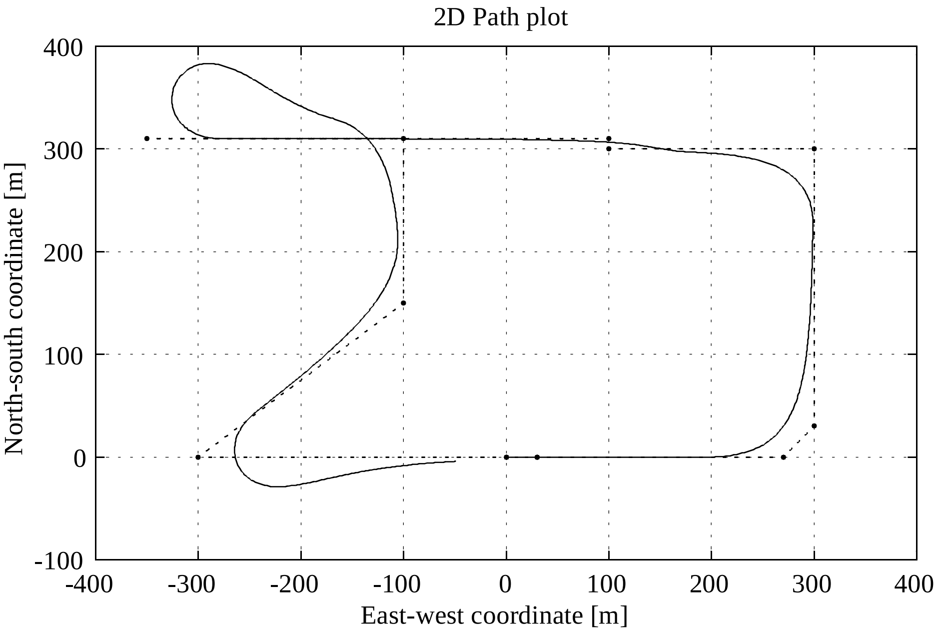

FIGURE 4.5 Moving point guidance simulation.

Figure 4.5 shows that the moving point guidance scheme works quite good even for very abrupt changes in reference path direction (the waypoints in Figure 4.5 are shown as solid dots). The scheme used in Figure 4.5 includes two nonlinear features that improves the performance for large changes in reference direction. First the moving "target" point is itself controlled to maintain a "fixed" distance in front of the vehicle using proportional control of the moving point speed based on the distance from the vehicle to the moving point. Secondly the maximum turning rate of the vehicle is limited by Eq. 4.1.4.

4.7 Lateral guidance conclusion:

A number of lateral guidance schemes have been discussed. As a result of this discussion, the moving point guidance scheme is selected as the most promising. A simulation of this scheme shows promising results for a realistic UAV mission.

Chapter 5

DGPS Instrument: Theory and Performance

5.1 Overview of GPS system

GPS is an acronym for Global Positioning System. The system is used to determine the position of a GPS receiver by measuring the distance to a number of satellites in earth orbit, using radio signals. Using a special receiver it is possible to measure the relative distance from each satellite to the receiver, by determining the time of flight of the signal from the satellite to the receiver. Multiplying the time of flight by the speed of light then gives the distance from a particular satellite to the receiver. The position of the GPS receiver can then be determined by a number of simultaneous time of flight measurements to different satellites. The space and associated control segments of the system are operated by the US Department Of Defence (DOD), while the individual civilian users of the system are responsible for receiving and processing the signals from the satellites using commercially available GPS receivers. Since all signals used in the GPS are transmitted from the satellites to the users GPS receiver, the users position can not be determined by the space segment. This also means that there is no practical limit to the number of users of the system. An in depth description of GPS, with particular emphasis on surveying applications, can be found in (Ref. 24). The following treatment is extensively based on this reference, but with special emphasis on real time position control using the GPS position as a feedback signal. In this context, the dynamic and reliability properties of the GPS position measurements are particularly important.

5.2 GPS signals

Each GPS satellite (abbreviated *SV*, which denotes Space Vehicle) contains a very accurate oscillator operating at a frequency of $f_0 = 10.23\text{MHz}$. This oscillator is used to control the carrier frequency of two radio transmitters, which operate at the frequencies $f_1 = 1575.42\text{MHz}$ and $f_2 = 1227.60\text{MHz}$, these are denoted the L1 and L2 carriers respectively. These carrier frequencies are the same for all SV's. In addition to controlling the carrier frequencies, the oscillator is also used to generate three digital modulation codes, the C/A code (Course/Acquisition), the P code (Precision) and the W code. All of these codes are so called Pseudo Random Noise (PRN) codes, which are unique for each SV. These codes consist of a sequence of ones and zeros which appear random, but are in fact periodic signals which can be used to uniquely identify and track each SV. While the C/A, P and W codes are periodic functions of time which contain no data, the so called "navigation message" contains the data necessary to compute the position and internal time of the each SV. The frequencies of the various codes are given below (Ref. 24, p. 76):

$$\begin{array}{ll} \text{C/A-code} & f_0/10 = 1.023\text{MHz} \\ \text{P-code} & f_0 = 10.23\text{MHz} \\ \text{W-code} & f_0/20 = 0.5115\text{MHz} \\ \text{Data} & f_0/204600 = 50\text{Hz} \end{array} \qquad (5.2.1)$$

Where “Data” denotes the navigation message, which is the only code that contains data.

The L1 carrier is modulated with the C/A code and the product of the P and W codes, while the L2 carrier is only modulated with the product of the P and W codes. In addition, all the codes are modulated with the Data. The W code is a very long secret code, which is only available to military users which are authorized by the DOD. Since the W code is not available to the civilian users, it is difficult to receive and process the P code. For this reason, most commercial GPS receivers only use the C/A code on the L1 carrier. These receivers are called “single frequency receivers”.

Since the receiver used in this project is of the single frequency type, we will confine the analysis to the C/A-code on the L1 carrier. According to (Ref. 24, p. 76), the modulated L1 carrier can then be expressed as:

$$\mathrm{L1}(t) = a_1 \mathrm{C/A}(t)\mathrm{D}(t)\cos(f_1 t) \qquad (5.2.2)$$

Where a_1 is the carrier amplitude, $\mathrm{C/A}(t)$ is the C/A code and $\mathrm{D}(t)$ is the navigation message data stream.

Each bit in the C/A code is called a “chip” since it carries no data. The C/A code is composed of 1023 chips, giving a repetition period of 1 ms. Since the speed of light is approximately $3\times10^8\,\mathrm{m/s}$, the chip length is approximately 300m, while the C/A code length is approximately 300km. Using a correlator the receiver is able to determine the relative code phase between different SV’s, with an ambiguity of 300km. This makes it possible to determine the 3 dimensional position without any ambiguity (Ref. 26).

5.3 SuperStar GPS receiver

Two SuperStar GPS receivers are used in this project. The SuperStar GPS receiver is produced by CMC in Canada. As standard they are able to calculate the stand alone position and velocity at a rate of 1Hz. The worst case deviation of the SuperStar stand alone position estimate has been determined as approximately 12 m in the horizontal plane and slightly more in the vertical direction. This is clearly inadequate for precision landing of an Unmanned Aerial Vehicle. For this reason, the measurements from two SuperStar receivers are used to establish a Differential GPS (DGPS) system.

The particular SuperStar receivers used for the project are supplied with “option 2”. This means that the receivers can be enabled to output both Pseudo Range (PR) and Carrier Range (CR) data at a 1Hz rate. The PR is the range measured from a particular satellite to the receiver, using a correlation with the C/A-code of the L1 carrier. The PR is not the true (geometric) range, because the local clock in the receiver is used to measure the time of arrival of the signal. Since the local clock is not perfectly synchronized to the SV clocks (so called GPS time) there will be a common bias on the PR to all SV’s. This must be eliminated when performing the position solution. For this reason it is necessary to use a minimum of 4 SV’s to obtain a 3D position solution.

The CR is the measured using the L1 carrier, so that it is in principle the number of L1 carrier wavelengths from each SV to the receiver, multiplied by the L1 wavelength. This enables a precision that is several orders of magnitude better then using PR’s. Since the RF front end of the SuperStar receiver uses a Local Oscillator (LO) to measure the CR, any errors in the LO frequency will result in a common frequency error for all CR’s. Since a frequency error is interpreted as a doppler shift in the CR, this results in a CR rate error (i.e. a velocity error). Thus just as with the PR’s, it is necessary to use at least 4 SV’s to determine a 3D position solution.

The SuperStar receiver uses two different internal clocks for determining the PR and CR, thus there is no direct correlation between the PR clock error and the CR frequency error.

There is one important problem with the CR’s, this is the fact it is impossible to directly determine the integer number of wavelengths between the SV and the receiver. This property is called *integer ambiguity.* If a SV is tracked continuously for several seconds, it is however easy to determine the change of CR with time. For this reason, it is far simpler to use the Carrier Range Rate (CRR) in the position calculation, then the CR itself. The Carrier Range Rate (CRR) is actually the change in CR between epoch times and not the true derivative of the CR, but because the SuperStar receiver uses a sampling rate of 1Hz, the CRR can be interpreted as a velocity. The SuperStar receiver automatically determines if a so called *cycle slip* has occurred since the last sample. This makes it possible to eliminate that particular CRR from the position calculation, so as to avoid erroneous CRR measurements. A *cycle slip* is the term used to describe a (temporary) loss of carrier lock for a particular SV, which introduces an integer ambiguity in the CRR.

5.4 Principles of point positioning

The most basic application of GPS measurements, is to determine a 3D position for each sample time, for a single receiver in stand alone mode. This is called “point positioning” (Ref. 24). Since only the PR’s provide an unambiguous range measurement, a point position estimate must at least incorporate 4 PR’s.

Lets assume that PR’s to at least 4 SV’s are available at a given “epoch” (the term used to define a GPS sample time, which is usually synchronized to GPS time within $1\mu\text{sec}$). If we knew the position $\mathbf{P}_{\mathrm{RX}}$ of the receiver and the position $\mathbf{P}_{\mathrm{SV,i}}$ of SV number “i”, at the epoch time, the pseudo range $\mathrm{PR_i}$ for that SV should obey the geometric relationship:

$$\|\mathbf{P}_{\mathrm{SV,i}} - \mathbf{P}_{\mathrm{RX}}\| = \mathrm{PR_i} + \Delta c \tag{5.4.1}$$

Where Δc is the receiver clock error, expressed as a distance (in meters). This equation defines the sign of the receiver clock error.

In reality of course we do not know the exact receiver position (otherwise we would not need the GPS). However we may have a position guess (or estimate) $\hat{\mathbf{P}}_{RX}$. We would then need to determine a position correction or update $\Delta\mathbf{P}_{RX}$, that gives the correct position:

$$\mathbf{P}_{RX} = \hat{\mathbf{P}}_{RX} + \Delta\mathbf{P}_{RX} \tag{5.4.2}$$

Using this expression in Eq. 5.4.1, gives:

$$\left\|\mathbf{P}_{SV,i} - (\hat{\mathbf{P}}_{RX} + \Delta\mathbf{P}_{RX})\right\| = PR_i + \Delta c \tag{5.4.3}$$

Linearizing the left hand side around $\|\Delta\mathbf{P}_{RX}\| = 0$ gives the following symbolic expression:

$$\left\|\mathbf{P}_{SV,i} - (\hat{\mathbf{P}}_{RX} + \Delta\mathbf{P}_{RX})\right\| \cong \hat{R}_i + \left.\frac{\partial R_i}{\partial \Delta\mathbf{P}_{RX}}\right|_{\|\Delta\mathbf{P}_{RX}\| = 0} \bullet \Delta\mathbf{P}_{RX} \tag{5.4.4}$$

Where $\hat{R}_i$ is defined as the distance from SV number “i” to the guessed receiver position, and R_i is the true distance from the SV to the receiver:

$$\hat{R}_i \equiv \left\|\mathbf{P}_{SV,i} - \hat{\mathbf{P}}_{RX}\right\| \tag{5.4.5}$$

$$R_i \equiv \left\|\mathbf{P}_{SV,i} - \mathbf{P}_{RX}\right\| = \left\|\mathbf{P}_{SV,i} - (\hat{\mathbf{P}}_{RX} + \Delta\mathbf{P}_{RX})\right\| \tag{5.4.6}$$

It is normal practice (Ref. 24) to use a cartesian Earth Centered Earth Fixed (ECEF) coordinate system to express the positions used in GPS calculations. Since the coordinate system is earth fixed, it rotates with the earth and is thus not a truly inertial coordinate system. The standard cartesian GPS ECEF coordinate system is denoted as “WGS-84”. It is defined in such a way that the **Z** coordinate starts at the earth center and points towards the north pole, the **X** direction points towards the mean Greenwich meridian (zero longitude) and lastly the **Y** direction points towards the mean 90^o meridian (90^o longitude).

Using the WGS-84 cartesian coordinate system, the range derivative in Eq. 5.4.4 can be expressed as:

$$\left.\frac{\partial R_i}{\partial \Delta\mathbf{P}_{RX}}\right|_{\|\Delta\mathbf{P}_{RX}\| = 0} = \frac{\partial R_i}{\partial \Delta x_{RX}}\mathbf{e}_x + \frac{\partial R_i}{\partial \Delta y_{RX}}\mathbf{e}_y + \frac{\partial R_i}{\partial \Delta z_{RX}}\mathbf{e}_z \tag{5.4.7}$$

Where $(\mathbf{e}_x, \mathbf{e}_y, \mathbf{e}_z)$ are the unit vectors defining the $(\mathbf{X}, \mathbf{Y}, \mathbf{Z})$ directions in the WGS_84 system.

Using Pythagoras relationship, the geometric range R_i from SV number “i” to the receiver can be expressed as:

$$R_i = \sqrt{(x_{SV,i} - (\hat{x}_{RX} + \Delta x_{RX}))^2 + (y_{SV,i} - (\hat{y}_{RX} + \Delta y_{RX}))^2 + (z_{SV,i} - (\hat{z}_{RX} + \Delta z_{RX}))^2}$$

(5.4.8)

The derivative with respect to Δx_{RX} is then given by:

$$\left.\frac{\partial R_i}{\partial \Delta x_{RX}}\right|_{\|\Delta \mathbf{P}_{RX}\| = 0} = \frac{1}{2}(\hat{R}_i^2)^{-\frac{1}{2}} 2(x_{SV,i} - \hat{x}_{RX})(-1) = \frac{\hat{x}_{RX} - x_{SV,i}}{\hat{R}_i} \tag{5.4.9}$$

Similarly with respect to Δy_{RX} and Δz_{RX}:

$$\left.\frac{\partial R_i}{\partial \Delta y_{RX}}\right|_{\|\Delta \mathbf{P}_{RX}\| = 0} = \frac{y_{RX} - y_{SV,i}}{\hat{R}_i} \tag{5.4.10}$$

$$\left.\frac{\partial R_i}{\partial \Delta z_{RX}}\right|_{\|\Delta \mathbf{P}_{RX}\| = 0} = \frac{z_{RX} - z_{SV,i}}{\hat{R}_i} \tag{5.4.11}$$

These derivatives can then be inserted into Eq. 5.4.4 to give a linearized expression for the SV to receiver range:

$$\|\mathbf{P}_{SV,i} - (\hat{\mathbf{P}}_{RX} + \Delta \mathbf{P}_{RX})\| \cong \hat{R}_i + \frac{x_{RX} - x_{SV,i}}{\hat{R}_i}\Delta x_{RX} + \frac{y_{RX} - y_{SV,i}}{\hat{R}_i}\Delta y_{RX} + \frac{z_{RX} - z_{SV,i}}{\hat{R}_i}\Delta z_{RX} \tag{5.4.12}$$

Using Eq. 5.4.3, gives a linearized relationship between the PR's and the correction $(\Delta x_{RX}, \Delta y_{RX}, \Delta z_{RX})$ to the guessed position:

$$\hat{R}_i + \frac{\hat{x}_{RX} - x_{SV,i}}{\hat{R}_i}\Delta x_{RX} + \frac{\hat{y}_{RX} - y_{SV,i}}{\hat{R}_i}\Delta y_{RX} + \frac{\hat{z}_{RX} - z_{SV,i}}{\hat{R}_i}\Delta z_{RX} = PR_i + \Delta c \tag{5.4.13}$$

This can be rearranged so that all the unknowns for a given epoch are placed on the left hand side of the equation:

$$\frac{\hat{x}_{RX} - x_{SV,i}}{\hat{R}_i}\Delta x_{RX} + \frac{\hat{y}_{RX} - y_{SV,i}}{\hat{R}_i}\Delta y_{RX} + \frac{\hat{z}_{RX} - z_{SV,i}}{\hat{R}_i}\Delta z_{RX} - \Delta c = PR_i - \hat{R}_i \tag{5.4.14}$$

Since we get one equation of the form Eq. 5.4.14 for each SV used in the current epoch, we can assemble the equations into a linear matrix equation:

$$\begin{bmatrix} \frac{\hat{x}_{RX} - x_{SV,1}}{\hat{R}_1} & \frac{\hat{y}_{RX} - y_{SV,1}}{\hat{R}_1} & \frac{\hat{z}_{RX} - z_{SV,1}}{\hat{R}_1} & -1 \\ \frac{\hat{x}_{RX} - x_{SV,2}}{\hat{R}_2} & \frac{\hat{y}_{RX} - y_{SV,2}}{\hat{R}_2} & \frac{\hat{z}_{RX} - z_{SV,2}}{\hat{R}_2} & -1 \\ \dots & \dots & \dots & \dots \\ \frac{\hat{x}_{RX} - x_{SV,N}}{\hat{R}_N} & \frac{\hat{y}_{RX} - y_{SV,N}}{\hat{R}_N} & \frac{\hat{z}_{RX} - z_{SV,N}}{\hat{R}_N} & -1 \end{bmatrix} \begin{bmatrix} \Delta x_{RX} \\ \Delta y_{RX} \\ \Delta z_{RX} \\ \Delta c \end{bmatrix} = \begin{bmatrix} PR_1 - \hat{R}_1 \\ PR_2 - \hat{R}_2 \\ \dots \\ PR_N - \hat{R}_N \end{bmatrix} \tag{5.4.15}$$

We can now define the “system” matrix $\mathbf{A}$ and the position correction (or update) vector $\Delta\tilde{\mathbf{P}}_{\mathrm{RX}}$ as:

$$\mathbf{A} \equiv \begin{bmatrix} \frac{\hat{x}_{\mathrm{RX}} - x_{\mathrm{SV},1}}{\hat{R}_1} & \frac{\hat{y}_{\mathrm{RX}} - y_{\mathrm{SV},1}}{\hat{R}_1} & \frac{\hat{z}_{\mathrm{RX}} - z_{\mathrm{SV},1}}{\hat{R}_1} & -1 \\ \frac{\hat{x}_{\mathrm{RX}} - x_{\mathrm{SV},2}}{\hat{R}_2} & \frac{\hat{y}_{\mathrm{RX}} - y_{\mathrm{SV},2}}{\hat{R}_2} & \frac{\hat{z}_{\mathrm{RX}} - z_{\mathrm{SV},2}}{\hat{R}_2} & -1 \\ \dots & \dots & \dots & \dots \\ \frac{\hat{x}_{\mathrm{RX}} - x_{\mathrm{SV},N}}{\hat{R}_N} & \frac{\hat{y}_{\mathrm{RX}} - y_{\mathrm{SV},N}}{\hat{R}_N} & \frac{\hat{z}_{\mathrm{RX}} - z_{\mathrm{SV},N}}{\hat{R}_N} & -1 \end{bmatrix} \qquad \Delta\tilde{\mathbf{P}}_{\mathrm{RX}} \equiv \begin{bmatrix} \Delta x_{\mathrm{RX}} \\ \Delta y_{\mathrm{RX}} \\ \Delta z_{\mathrm{RX}} \\ \Delta c \end{bmatrix} \tag{5.4.16}$$

In symbolic form, the PR point position equation (Eq. 5.4.15) can be expressed as:

$$\mathbf{A}\Delta\tilde{\mathbf{P}}_{\mathrm{RX}} = \mathbf{Y} \tag{5.4.17}$$

The first three columns of $\mathbf{A}$ can be interpreted as the direction cosines between the coordinate directions and the direction from the SV’s to the receiver.

It is apparent that if $\mathrm{N} > 4$ $(rank(\mathbf{A}) > 4)$, Eq. 5.4.17 can not in general be solved for the position correction $\Delta\tilde{\mathbf{P}}_{\mathrm{RX}}$. In this overdetermined case, the equation can instead be solved in a *least squares* sense by using the following manipulations:

$$\mathbf{A}^T\mathbf{A}\Delta\tilde{\mathbf{P}}_{\mathrm{RX}} = \mathbf{A}^T\mathbf{Y} \quad \Leftrightarrow \quad \mathbf{F}\Delta\tilde{\mathbf{P}}_{\mathrm{RX}} = \mathbf{B} \tag{5.4.18}$$

Where $\mathbf{F} \equiv \mathbf{A}^T\mathbf{A}$ is a 4×4 symmetrical matrix and $\mathbf{B} \equiv \mathbf{A}^T\mathbf{Y}$ is a 4×1 matrix.

The *least squares solution* to Eq. 5.4.17, is then given by:

$$\Delta\tilde{\mathbf{P}}_{\mathrm{RX}} = \begin{bmatrix} \Delta\mathbf{P}_{\mathrm{RX}} \\ \Delta c \end{bmatrix} = \mathbf{F}^{-1}\mathbf{B} \tag{5.4.19}$$

If there is a “big” difference between the guessed solution $\hat{\mathbf{P}}_{\mathrm{RX}}$ and the updated solution $\mathbf{P}_{\mathrm{RX}} = \hat{\mathbf{P}}_{\mathrm{RX}} + \Delta\mathbf{P}_{\mathrm{RX}}$, it may be advantageous to do a second position update using a new $\mathbf{A}$ matrix.

It should be mentioned that since radio waves propagate in a straight line at the speed of light in an inertial system, the above equations are only exact if given in an Earth Centered Inertial (ECI) system. Also the positions of the SV’s should correspond to the time of transmission, while the position of the receiver should correspond to the time of reception. Since it is usually most convenient to work in the WGS-84 ECEF coordinate system, a correction term can be applied to the guessed position $\hat{\mathbf{P}}_{\mathrm{RX}}$ to account for the earth rotation from the time of transmission to reception of the SV radio signals. More details can be found in (Ref. 25, sec. 2.5.4.2). The order of magnitude of this error can be estimated by the following considerations; the maximum peripheral speed of the surface of the earth (relative to an ECI system) is on the order 500m/s (at the equator) and the mean orbital radius of the SV’s is approximately 26000km (Ref. 24), this gives a delay of approximately 100ms between the time of transmission and the time of reception, in this interval the receiver could have moved approximately 50m due to earth rotation.

The earth rotation effects are however reasonably constant in a DGPS application with short baselines between receivers (~10km), since the transmission delay is almost the same for both receivers. For this reason, this error will be neglected in the following.

The above equations are the basis for more advanced position estimation methods using both DGPS and carrier range rate measurements.

5.5 Point position velocity estimation

As explained in Section 5.3, the SuperStar GPS receiver is able to measure the Carrier Range (CR) and the Carrier Range Rate (CRR) with much greater accuracy then the Pseudo Range (PR). Unfortunately the CR can not directly replace the PR, due to integer ambiguities. However the CRR can easily be measured, just by tracking the carrier of the SV for two consecutive epochs.

In this section we will derive the equations for estimating the velocity of a single receiver in the WGS-84 ECEF system using just the CRR. First we will derive the equations in a ECI system, with Z-axis coincident with the Z-axis of the ECEF system.

From the previous section we now that the unweighted least squares point position solution update with PR's can be expressed as:

$$\Delta\tilde{\mathbf{P}}_{\mathrm{RX}} = \mathbf{F}^{-1}\mathbf{B} = \mathbf{F}^{-1}\mathbf{A}^{T}(\mathbf{PR}-\hat{\mathbf{R}}) \tag{5.5.1}$$

If the integer ambiguity problem is ignored, the PR can be replaced by the CR:

$$\Delta\tilde{\mathbf{P}}_{\mathrm{RX}} = \mathbf{F}^{-1}\mathbf{B} = \mathbf{F}^{-1}\mathbf{A}^{T}(\mathbf{CR}-\hat{\mathbf{R}}) \tag{5.5.2}$$

The position change in WGS-84 ECEF coordinates from epoch $\mathrm{k}-1$ to epoch k is equal to the mean velocity in the same interval:

$$\mathbf{v}_{\mathrm{RX,k}} \equiv \mathbf{P}_{\mathrm{RX,k}} - \mathbf{P}_{\mathrm{RX,k\text{-}1}} = (\Delta\tilde{\mathbf{P}}_{\mathrm{RX,k}} - \hat{\mathbf{P}}_{\mathrm{RX,k}}) - (\Delta\tilde{\mathbf{P}}_{\mathrm{RX,k\text{-}1}} - \hat{\mathbf{P}}_{\mathrm{RX,k\text{-}1}}) \tag{5.5.3}$$

Where $\hat{\mathbf{P}}_{\mathrm{RX,k}}$ is the a priori RX position at epoch k.

Using Eq. 5.5.2 the difference $\Delta\tilde{\mathbf{P}}_{\mathrm{RX,k}} - \Delta\tilde{\mathbf{P}}_{\mathrm{RX,k\text{-}1}}$ can be expressed as:

$$\Delta\tilde{\mathbf{P}}_{\mathrm{RX,k}} - \Delta\tilde{\mathbf{P}}_{\mathrm{RX,k\text{-}1}} = \mathbf{F}_{\mathrm{k}}^{-1}\mathbf{A}_{\mathrm{k}}^{T}(\mathbf{CR}_{\mathrm{k}} - \hat{\mathbf{R}}_{\mathrm{k}}) - \mathbf{F}_{\mathrm{k\text{-}1}}^{-1}\mathbf{A}_{\mathrm{k\text{-}1}}^{T}(\mathbf{CR}_{\mathrm{k\text{-}1}} - \hat{\mathbf{R}}_{\mathrm{k\text{-}1}}) \tag{5.5.4}$$

Since $\mathbf{A}$ and thus $\mathbf{F}$ are functions of the direction cosines between the SV's and the RX, they only change slowly from epoch to epoch, this means that we can approximate the difference $\Delta\tilde{\mathbf{P}}_{\mathrm{RX,k}} - \Delta\tilde{\mathbf{P}}_{\mathrm{RX,k\text{-}1}}$ as:

$$\Delta\tilde{\mathbf{P}}_{\mathrm{RX,k}} - \Delta\tilde{\mathbf{P}}_{\mathrm{RX,k\text{-}1}} \cong \mathbf{F}_{\mathrm{k}}^{-1}\mathbf{A}_{\mathrm{k}}^{T}((\mathbf{CR}_{\mathrm{k}} - \mathbf{CR}_{\mathrm{k\text{-}1}}) - (\hat{\mathbf{R}}_{\mathrm{k}} - \hat{\mathbf{R}}_{\mathrm{k\text{-}1}})) = \mathbf{F}_{\mathrm{k}}^{-1}\mathbf{A}_{\mathrm{k}}^{T}(\mathbf{CRR}_{\mathrm{k}} - \hat{\mathbf{RR}}_{\mathrm{k}}) \tag{5.5.5}$$

Where the a priori range rate is defined by $\hat{\mathbf{RR}}_{\mathrm{k}} \equiv \hat{\mathbf{R}}_{\mathrm{k}} - \hat{\mathbf{R}}_{\mathrm{k\text{-}1}}$.

Combining Eq. 5.5.5 with Eq. 5.5.3 gives the desired expression for the point velocity position estimate from carrier phase measurements:

$$\mathbf{v}_{\mathrm{RX,k}} = \mathbf{F}_{\mathrm{k}}^{-1}\mathbf{A}_{\mathrm{k}}^{T}(\mathbf{CRR}_{\mathrm{k}} - \hat{\mathbf{RR}}_{\mathrm{k}}) - (\hat{\mathbf{P}}_{\mathrm{RX,k}} - \hat{\mathbf{P}}_{\mathrm{RX,k\text{-}1}}) \tag{5.5.6}$$

It is important for the correct use of this result that the a priori range rate $\hat{\mathbf{RR}}_{\mathrm{k}}$ corresponds to the a priori RX position rate $\hat{\mathbf{P}}_{\mathrm{RX,k}} - \hat{\mathbf{P}}_{\mathrm{RX,k\text{-}1}}$.

The simplest way to determine the a priori position is to use the previous calculated position as the a priori position for the next epoch. This gives the following expressions:

$$\hat{\mathbf{P}}_{\mathrm{RX,k}} = \mathbf{P}_{\mathrm{RX,k\text{-}1}} \qquad \hat{\mathbf{P}}_{\mathrm{RX,k\text{-}1}} = \mathbf{P}_{\mathrm{RX,k\text{-}2}} \qquad \hat{\mathbf{RR}}_{\mathrm{k}} = \mathbf{R}_{\mathrm{k\text{-}1}} - \mathbf{R}_{\mathrm{k\text{-}2}} \tag{5.5.7}$$

This gives the following explicit expression for the point velocity estimate:

$$\mathbf{v}_{\mathrm{RX,k}} = \mathbf{F}_{\mathrm{k}}^{-1}\mathbf{A}_{\mathrm{k}}^{T}(\mathbf{CRR}_{\mathrm{k}} - (\mathbf{R}_{\mathrm{k\text{-}1}} - \mathbf{R}_{\mathrm{k\text{-}2}})) - (\mathbf{P}_{\mathrm{RX,k\text{-}1}} - \mathbf{P}_{\mathrm{RX,k\text{-}2}}) \tag{5.5.8}$$

5.6 GPS error sources

There are several sources of error that effect the GPS receiver measurements of PR and CR (Ref. 24). These error sources can be grouped according to there physical locations:

- Errors that occur in the satellites (SV’s).
- Errors due to propagation of the radio signals through space and the atmosphere.
- Errors due to the environment surrounding the GPS receiver antenna.
- Errors due to the antenna characteristics.
- Errors in the GPS receiver.

The following is a brief discussion of the physical sources of errors in the different groups above.

5.6.1 SV related errors

As seen in the preceding section, a position error in the SV directly effects the receiver position estimate. The same is true for the SV reference frequency f_0. Any error in f_0 will effect both the L1 carrier frequency and phase and the C/A code phase. This is the reason for the extreme accuracy requirements for the SV reference frequency.

Before May 1, 2000, the DOD used so called “Selective Availability” (SA) to deny civilian users the full GPS accuracy. This was achieved by introducing two error sources, a slowly varying bias of the f_0 frequency and an intentional error in the “Ephemerides”, that the user uses to compute the SV position. The combined effects of these two errors was a receiver position error of around 100m.

Without SA, the errors in the SV positions as given in the navigation message ephemerides are on the order of a 5 to 10m or less (Ref. 24, p. 68).

The effects of SV position and timing errors are nearly perfectly eliminated by using DGPS, because the satellite geometry is nearly the same for two closely spaced receivers.

5.6.2 Propagation errors

When radio waves travel through a medium other then vacuum, the propagation velocity is slowed down. This can have a significant effect on GPS signals that travel through the atmosphere. The errors induced by the atmosphere on the GPS signal delay, is usually split into two parts, a ionospheric delay and a tropospheric delay.

The ionosphere is the upper part of the atmosphere, generally extending from around 50km height to 1000km height (Ref. 24). The ionospheric delay is generally caused by the presence of free electrons in the ionosphere. According to (Ref. 24, p. 104) the ionospheric delay may be between 0.15m and 50m. Since the signals from satellites with low elevation must pass through a greater length of the ionosphere, low elevation satellites are generally more influenced by ionospheric delay then high elevation satellites.

The other important part of the atmosphere, from a GPS point of view, is the troposphere which extends from ground level to approximately 11km height. A substantial part of the tropospheric delay is caused by atmospheric water vapour and is thus dependent on the weather conditions. The tropospheric delay also depends on the satellite elevation and is on the order of a few meters (Ref. 24, p.116).

Since the atmospheric delay is the correlated for two nearby receivers, the use of DGPS reduces these errors substantially, especially for short distances between receivers.

5.6.3 Multipath

The most important antenna environment error is multipath. Multipath is the technical term for the situation that occurs when the radio signal from a transmitter reaches the receiver along several paths. Since the GPS receiver works by measuring the path distance from the SV to the receiver, GPS position calculations are very sensitive to multipath.

Multipath can be caused by any radio reflective surface near the receiver antenna. This includes buildings, cars, trucks, the ground, mountains and so on. Due to the signal geometry, multipath is generally worse for SV’s with low elevations.

Multipath can be reduced by using a ground plane to shield the antenna from signals with low elevation, that is reflected of surfaces below the antenna. In addition most receivers have a built in *narrow correlator,* that attempts to remove multipath by suppressing interference from signals that arrive after the main signal. This is based on the fact that reflected signals (multipath signals) must travel a longer distance then the direct signal from the satellite. The narrow correlator usually successfully removes multipath with delays of more then 40 meters. Multipath is generally much smaller for carrier ranges then for pseudo ranges, except for severe multipath, which may cause carrier cycle slips.

Since multipath is very site dependent, it is not removed by DGPS. In fact the multipath errors of the reference and mobile station, may combine to produce even larger errors then for stand alone GPS.

If more then 4 SV's are available for a particular epoch, it is possible to determine which SV's are affected by multipath, by analysing the residuals. These SV's can then be eliminated from the position solution.

5.6.4 Antenna errors

Ideally, the receiver antenna should sample signals from all SV's at exactly the same geometric point. However the so called "phase center" of the antenna is not constant for signals coming from any direction.

Even though it can not be characterized as an "antenna error", the effects of multipath are greatly influenced by the antenna characteristics. Since the GPS radio signals are circularly polarized, any reflected GPS radio signal will have the opposite polarization sense. Thus an ideal circular polarised GPS antenna can be used to eliminate unwanted multipath caused be an odd number of signal reflections.

Another important method of reducing the effects of multipath is to use a ground plane for the antenna. This will greatly attenuate any signals reflected from objects below the ground plane. Unfortunately the ground plane must be quite large compared to the wavelength to be effective. However it should be possible to achieve the same effect by using an antenna with a high inherent *front to back ratio*.

5.6.5 Receiver errors

The receiver and antenna cable introduces a propagation delay for the received radio signals. It is readily appreciated that a common propagation delay results in a solution time error, but **not** in a position error. Since all contemporary GPS receivers use a separate correlator for each tracked satellite, any correlator error that is not common for all correlators will result in pseudorange and carrier phase errors that directly influence the computed position.

Using two receivers it is possible to determine the receiver errors by using a "zero" baseline test setup. This is done by connecting the two receivers to the same antenna using a signal splitter. Since antenna and multipath errors for both receivers are the same in this setup, the resulting measured double difference errors [see Section 5.8.1] are the result of receiver related errors.

5.7 Principles of differential positioning

Differential positioning is based on the simple principle of determining the relative position of two nearby receivers, by comparing the pseudo range and carrier range measurements of the same SV's measured by the two receivers. The promise of DGPS is that it can practically eliminate all SV related errors and almost all atmospheric delay errors.

5.7.1 Differential positioning using the pseudo ranges

Two receivers, denoted RX1 and RX2, are used to measure PR’s to the same SV’s at the same epoch. This gives two equations similar to Eq. 5.4.1:

$$\begin{aligned} \lVert \mathbf{P}_{\mathrm{SV,i}} - \mathbf{P}_{\mathrm{RX1}} \rVert &= \mathrm{PR}_{1\mathrm{i}} + \Delta c_1 \\ \lVert \mathbf{P}_{\mathrm{SV,i}} - \mathbf{P}_{\mathrm{RX2}} \rVert &= \mathrm{PR}_{2\mathrm{i}} + \Delta c_2 \end{aligned} \tag{5.7.1}$$

Where $\mathbf{P}_{\mathrm{SV,i}}$ again denotes the position of SV number “i”, $\mathbf{P}_{\mathrm{RX1}}$ and $\mathbf{P}_{\mathrm{RX2}}$ are the positions of the two receivers (more correctly the antenna phase centers), $\mathrm{PR}_{1\mathrm{i}}$ and $\mathrm{PR}_{2\mathrm{i}}$ are the pseudo ranges measured by the two receivers while Δc_1 and Δc_2 are the receiver clock errors.

The objective of differential positioning is to obtain the baseline (vector) between the two receivers, in other words $\mathbf{P}_{\mathrm{RX12}} \equiv \mathbf{P}_{\mathrm{RX2}} - \mathbf{P}_{\mathrm{RX1}}$. It is assumed that the position $\mathbf{P}_{\mathrm{RX1}}$ of receiver number one is approximately known.

There are several principle methods for determining the differential position. The most universal method uses the known or assumed position of RX1 to determine the pseudo range errors. These errors are then transmitted to RX2 using a radio data link. RX2 can then correct its measured pseudoranges with the received pseudo range errors. This method is universal, in that it can be used for arbitrary baseline lengths. The pseudo range error $\Delta\mathrm{PR}_\mathrm{i}$ for SV number “i” is defined by:

$$\Delta\mathrm{PR}_\mathrm{i} \equiv \lVert \mathbf{P}_{\mathrm{SV,i}} - \mathbf{P}_{\mathrm{RX,ref}} \rVert - \mathrm{PR}_\mathrm{i} \tag{5.7.2}$$

Where $\mathbf{P}_{\mathrm{RX,ref}}$ is the known or assumed position of the reference receiver antenna and PR_i is the pseudorange measured by the reference receiver. Notice that a positive pseudorange error implies that the measured pseudorange is to “short”, this means that the “true” pseudorange is obtained by *adding* the pseudorange error to the measured pseudorange.

The same principle can be used to implement a differential velocity system using measured carrier phase rates by defining the *carrier phase rate* error $\Delta\mathrm{CPR}_\mathrm{i}$ for SV number “i” as:

$$\Delta\mathrm{CPR}_\mathrm{i} \equiv \frac{\mathrm{R}_{\mathrm{i,k}} - \mathrm{R}_{\mathrm{i,k\text{-}1}}}{\lambda} - \mathrm{CPR}_\mathrm{i} \tag{5.7.3}$$

Where $\mathrm{R}_{\mathrm{i,k}}$ is the calculated range from SV number “i” to the reference receiver at epoch number “k”.

The only practical limit to this method is the gradual decorrelation of the atmospheric pseudorange errors, as the baseline distance between the mobile and reference receiver is increased.

5.8 GPS measurements

In this section the statistical properties of the PR and CRR noise will be analysed. This analysis will be based on data measured with the two SuperStar GPS receivers. The primary aim of this analysis is to be able to predict the statistical accuracy of a DGPS implementation using these receivers.

The experimental setup used for these measurements, consists of two GPS antennas mounted approximately 5 m apart on the roof of the department. The antennas are connected to the two receivers in our office, using 10 meters of cable. Since the antennas are stationary (relative to the earth), their differential position is constant and their differential velocity is zero. This makes it possible to determine the differential errors in the PR and CRR. Even though the antennas are mounted above the building roof and equipped with groundplanes, there are higher buildings to the north and south of the department. These buildings have a blocking effect and the potential to produce large multipaths for especially low elevation satellites.

5.8.1 Double difference analysis

Since we have two receivers with two independent antennas, we can use Eq. 5.7.1 to obtain the ideal relationship between the measured pseudo ranges and the geometric range to the satellites:

$$\begin{aligned} \|\mathbf{P}_{\mathrm{SV,i}} - \mathbf{P}_{\mathrm{RX1}}\| &= \mathrm{PR}_{1\mathrm{i}} + \Delta c_1 \\ \|\mathbf{P}_{\mathrm{SV,i}} - \mathbf{P}_{\mathrm{RX2}}\| &= \mathrm{PR}_{2\mathrm{i}} + \Delta c_2 \end{aligned} \qquad (5.8.1)$$

Where $\mathbf{P}_{\mathrm{SV,i}}$ again denotes the position of SV number “i”, $\mathbf{P}_{\mathrm{RX1}}$ and $\mathbf{P}_{\mathrm{RX2}}$ are the positions of the two receivers (more correctly the antenna phase centers), $\mathrm{PR}_{1\mathrm{i}}$ and $\mathrm{PR}_{2\mathrm{i}}$ are the pseudo ranges measured by the two receivers while Δc_1 and Δc_2 are the receiver clock errors.

In the test case, we have an independent accurate means of determining the true distance $\mathbf{P}_{\mathrm{RX12}} = \mathbf{P}_{\mathrm{RX12,test}} \equiv \mathbf{P}_{\mathrm{RX2}} - \mathbf{P}_{\mathrm{RX1}}$. Using this knowledge we can try to rearrange Eq. 5.8.1, so as to determine the pseudorange measurement errors.

Subtracting the first part of Eq. 5.8.1 from the second part gives:

$$\|\mathbf{P}_{\mathrm{SV,i}} - \mathbf{P}_{\mathrm{RX2}}\| - \|\mathbf{P}_{\mathrm{SV,i}} - \mathbf{P}_{\mathrm{RX1}}\| = \mathrm{PR}_{2\mathrm{i}} + \Delta c_2 - (\mathrm{PR}_{1\mathrm{i}} + \Delta c_1) \qquad (5.8.2)$$

The left hand side of this equation is the geometric range difference between the SV and the phase centers of the two antennas. The right hand side is the difference between the measured pseudo ranges and receiver clock errors.

Since the test baseline $\mathbf{P}_{\mathrm{RX12,test}}$ is accurately known, the equation can rewritten as:

$$\|\mathbf{P}_{\mathrm{SV,i}} - (\mathbf{P}_{\mathrm{RX1}} + \mathbf{P}_{\mathrm{RX12,test}})\| - \|\mathbf{P}_{\mathrm{SV,i}} - \mathbf{P}_{\mathrm{RX1}}\| = \mathrm{PR}_{2\mathrm{i}} + \Delta c_2 - (\mathrm{PR}_{1\mathrm{i}} + \Delta c_1) \qquad (5.8.3)$$

If the test baseline is short, the first distance may be expressed in terms of a linear expansion around the RX1 position. In analogy with Eq. 5.4.12, this gives:

$$\|\mathbf{P}_{\mathrm{SV,i}} - (\mathbf{P}_{\mathrm{RX1}} + \mathbf{P}_{\mathrm{RX12,test}})\| \cong \mathrm{R}_{1\mathrm{i}} + \frac{x_{\mathrm{RX1}} - x_{\mathrm{SV,i}}}{\mathrm{R}_{1\mathrm{i}}} x_{\mathrm{RX12}} + \frac{y_{\mathrm{RX1}} - y_{\mathrm{SV,i}}}{\mathrm{R}_{1\mathrm{i}}} y_{\mathrm{RX12}} + \frac{z_{\mathrm{RX1}} - z_{\mathrm{SV,i}}}{\mathrm{R}_{1\mathrm{i}}} z_{\mathrm{RX12}} \qquad (5.8.4)$$

Where the cartesian components of the test baseline in XYZ coordinates are given as $\mathbf{P}_{\mathrm{RX12,test}} = (x_{\mathrm{RX12}}, y_{\mathrm{RX12}}, z_{\mathrm{RX12}})$. The range R_{1i} is equal to the range between SV number “i” and RX1.

Combining Eq. 5.8.3 and Eq. 5.8.4 gives:

$$\frac{x_{\mathrm{RX1}} - x_{\mathrm{SV,i}}}{R_{1i}} x_{\mathrm{RX12}} + \frac{y_{\mathrm{RX1}} - y_{\mathrm{SV,i}}}{R_{1i}} y_{\mathrm{RX12}} + \frac{z_{\mathrm{RX1}} - z_{\mathrm{SV,i}}}{R_{1i}} z_{\mathrm{RX12}} = \mathrm{PR}_{2i} + \Delta c_2 - (\mathrm{PR}_{1i} + \Delta c_1) \qquad (5.8.5)$$

Since the ranges to the SV’s are more then $20\times10^3\mathrm{km}$, a combined SV and RX1 position error of around $100\mathrm{m}$ will only give a relative error on the left hand side of 0.0005% of the baseline. In other words for a baseline of $5\mathrm{m}$ length, the error on the left hand side has a magnitude of $25\mu\mathrm{m}$, which is clearly negligible compared to the pseudorange errors, as will be shown below.

What we really want to do is to determine the pseudo range measurement errors for both receivers. However since we only have one equation for both receivers for each SV, we can only determine the pseudo range difference error dPR_{ei} as defined below:

$$\mathrm{dPR}_{ei} = \mathrm{PR}_{2i} + \Delta c_2 - (\mathrm{PR}_{1i} + \Delta c_1) - \left(\frac{x_{\mathrm{RX1}} - x_{\mathrm{SV,i}}}{R_{1i}} x_{\mathrm{RX12}} + \frac{y_{\mathrm{RX1}} - y_{\mathrm{SV,i}}}{R_{1i}} y_{\mathrm{RX12}} + \frac{z_{\mathrm{RX1}} - z_{\mathrm{SV,i}}}{R_{1i}} z_{\mathrm{RX12}}\right) \qquad (5.8.6)$$

It is apparent that the pseudo range difference error is a function of the a priori unknown clock error $\Delta c_{12} \equiv \Delta c_2 - \Delta c_1$.

There are several ways to overcome this problem. The simplest solution is to choice a SV with a high elevation and hopefully low measurement error, as a reference SV. The clock error Δc_{12} can then be determined by assuming that the pseudo range difference error is zero for the reference SV:

$$\Delta c_{12} \equiv \mathrm{PR}_{1i} - \mathrm{PR}_{2i} + \left(\frac{x_{\mathrm{RX1}} - x_{\mathrm{SV,i}}}{R_{1i}} x_{\mathrm{RX12}} + \frac{y_{\mathrm{RX1}} - y_{\mathrm{SV,i}}}{R_{1i}} y_{\mathrm{RX12}} + \frac{z_{\mathrm{RX1}} - z_{\mathrm{SV,i}}}{R_{1i}} z_{\mathrm{RX12}}\right) \qquad i = i_{\mathrm{ref}} \qquad (5.8.7)$$

Where i_{ref} is the index of the reference SV.

One problem with this approach is that the reference SV after some time will cease to be the best SV. This happens because the reference SV elevation will sooner or later decrease below the acceptable limit. Another problem is that any noise on the reference SV pseudo range measurement will affect the other pseudo range errors directly without any attenuation.

One partial solution to these problems is to use more then one SV to determine the differential clock error. The simplest way to implement this is to average Eq. 5.8.7 over several reference SV’s:

$$\Delta c_{12} \equiv \frac{1}{N_{\mathrm{ref}}} \sum_{i \in i_{\mathrm{ref}}} \left\{\mathrm{PR}_{1i} - \mathrm{PR}_{2i} + \left(\frac{x_{\mathrm{RX1}} - x_{\mathrm{SV,i}}}{R_{1i}} x_{\mathrm{RX12}} + \frac{y_{\mathrm{RX1}} - y_{\mathrm{SV,i}}}{R_{1i}} y_{\mathrm{RX12}} + \frac{z_{\mathrm{RX1}} - z_{\mathrm{SV,i}}}{R_{1i}} z_{\mathrm{RX12}}\right)\right\} \qquad (5.8.8)$$

Where i_{ref} is the set of reference SV indexes.

The reference SV's may be simply chosen as the SV's with an elevation greater then some threshold. The elevation threshold should be determined so that the risk of multipath on the reference SV's is small. Depending on the antenna environment, this should probably be around 30° to 45°. The higher value is suitable for environments with tall buildings and suboptimal antenna ground planes. Since the differential clock error is now determined using several SV's, the resulting discontinueties when changing reference SV's will be smaller. It can also be expected that the differential clock error will be more accurately determined since the pseudorange errors are probably uncorrelated between the different SV's.

An experimental investigation of the differential pseudo range errors dPR_{ei} has been performed using 6 hours of continous measurements with the fixed baseline system described above. The "true" test baseline has been determined first with an accuracy of the order of 2 cm (Table E.2) using a simple ambiguity resolution method on the carrier phase measurements. The true test baseline in UTM coordinates is given in Eq. E.50.

A "skyplot" of the trajectories of the SV's in relation to the receivers is shown below:

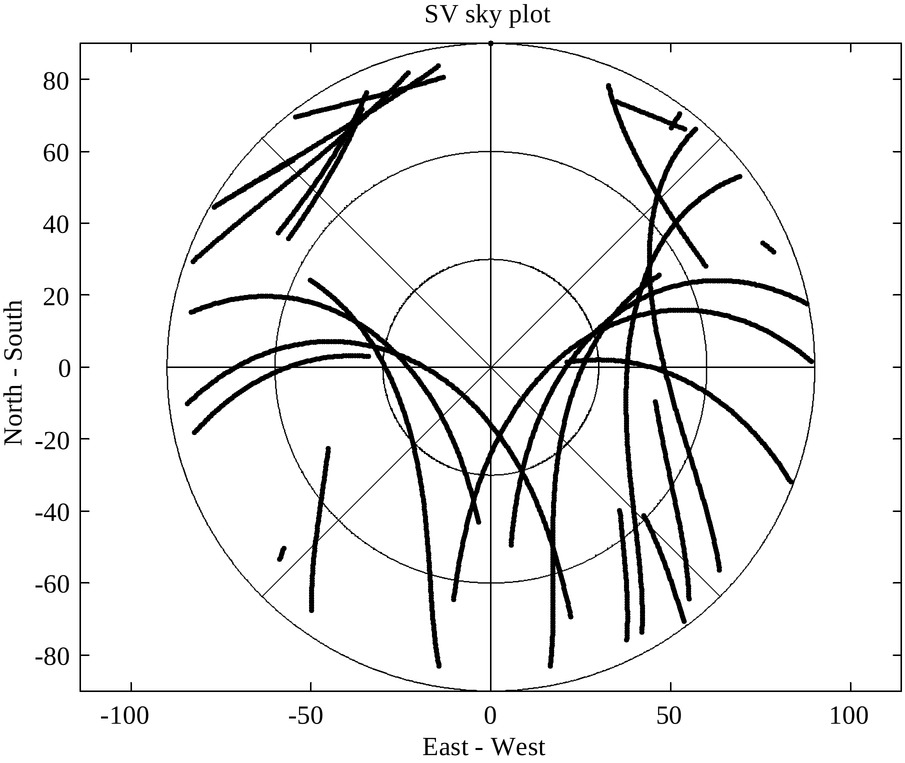

FIGURE 5.1 Skyplot of SV trajectories.

Since the SV's orbit the earth twice in 24 hours, the SV's appear to be "overtaking" the earth from west to east. Each SV will be visible for less then 6 hours at a time from any fixed position at or near the surface of the earth.

A “raw” time series plot of the pseudorange errors for all SV’s as a function of time is shown below:

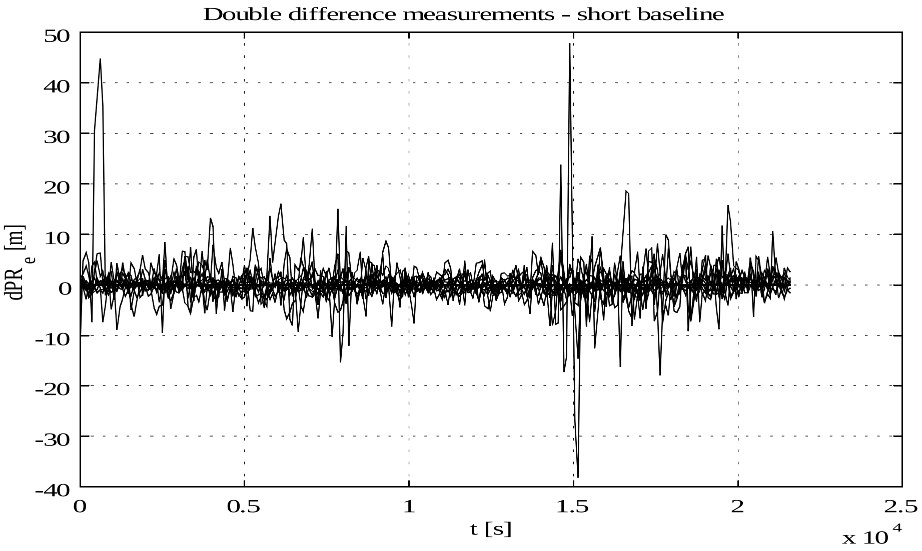

FIGURE 5.2 Time series plot of all PR errors.

Even though it is impossible to distinguish the individual PR errors in this plot, it is apparent that there are several places where the error for one or more SV’s becomes very large compared to the “background” noise.

If the large errors seen in Figure 5.2 are caused by multipath, there should be a strong correlation between the pseudo range errors and the elevation of the SV as seen from the antenna positions. This has been tested by plotting the standard deviation of the PR errors as a function of elevation for the entire dataset, as shown below:

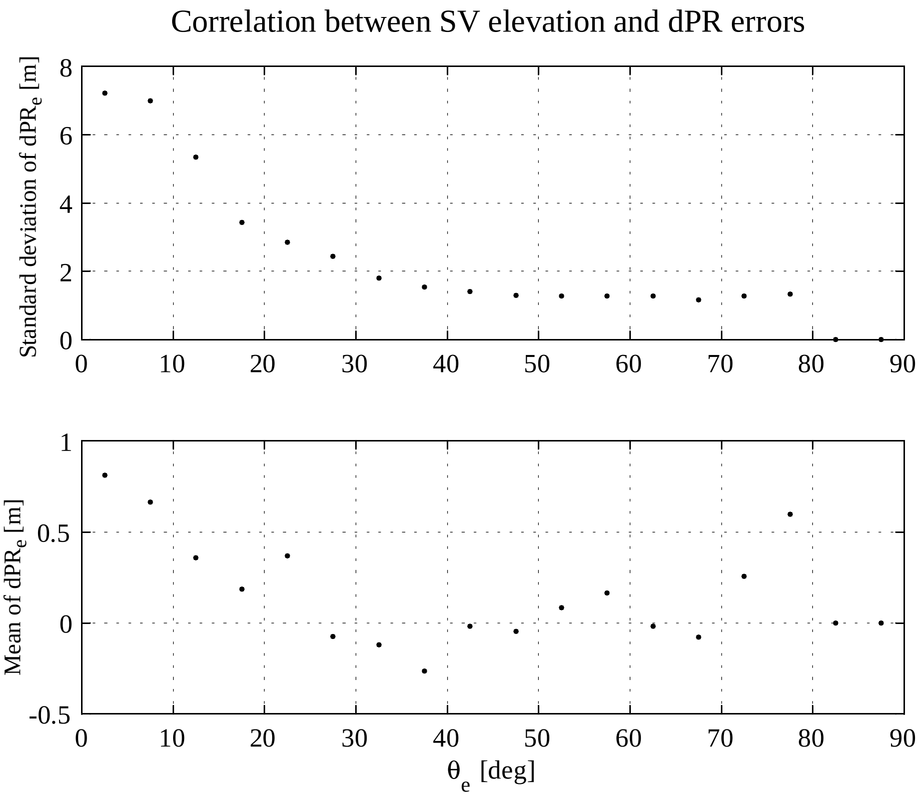

FIGURE 5.3 Standard deviation and mean of PR errors as function of SV elevation.

In order to get a significant number of datapoints for each elevation, the PR errors are grouped into $5°$ elevation intervals, centered at the points shown in the plot. There are no data available for elevations above $80°$, which is also apparent from the skyplot in Figure 5.1.

It is apparent that the proposed strong correlation between the PR errors and the SV elevation does indeed exist. This is a clear indication that the large PR errors seen in Figure 5.2 are caused by multipath. It is apparent that the standard deviation of the PR errors is almost constant above an elevation angle above $40°$. Below $40°$ the errors seem to follow an inverse relationship with elevation, until it reaches a maximum value in the $0°$ to $5°$ interval. The standard deviation of the PR errors are approximately 5.5 times larger for low elevations compared to high elevations. On all accounts this is a significant difference. The mean PR errors show a strong bias for low elevations, this indicates that the PR errors have a very low frequency component consistent with multipath. The bias at elevations above $70°$ is probably caused by the relative few datasets from this elevation range, as seen in Figure 5.1.

Having determined that the PR errors are much larger for SV's with low elevations then for SV's with high elevations, it is interesting to investigate if the shape of the Probability Density Function (pdf) and Power Spectral Density (psd) also depend on SV elevation.

The pdf's for both elevations less then 5° and more then 45° have been computed as shown in Figure 5.4 (notice the different error scales):

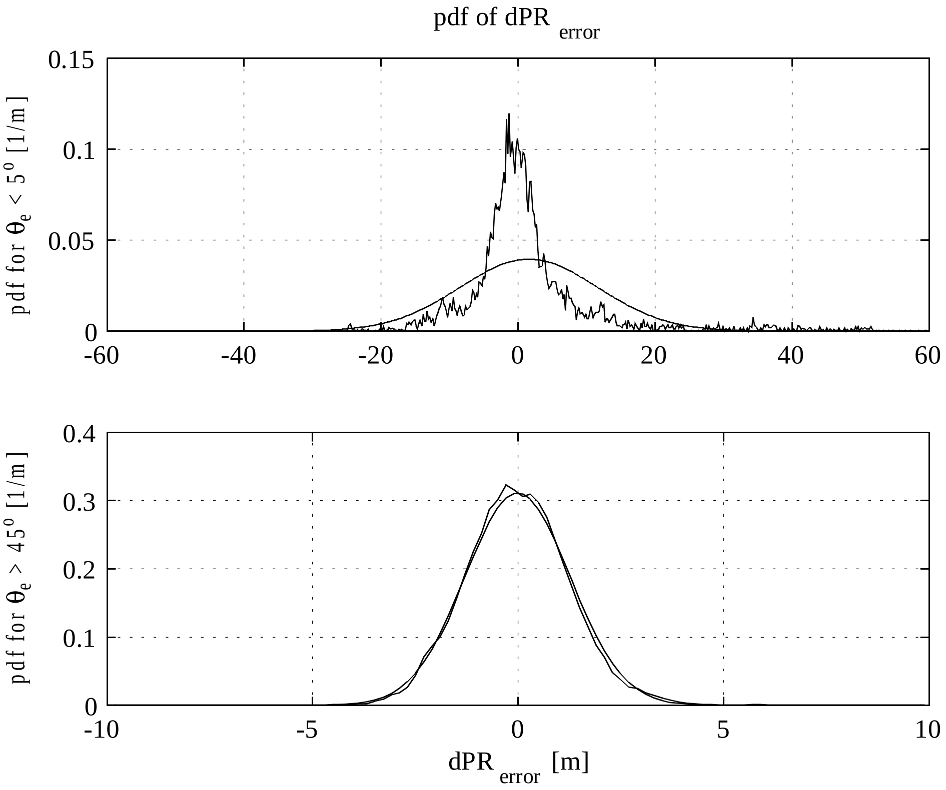

FIGURE 5.4 Probability density function of PR errors SV's with low and high elevations.

In addition to the measured pdf's, the equivalent gaussian pdf's with identical means and standard deviations are also shown in Figure 5.4. It is apparent that the pdf of the low elevation SV's has a large deviation from a gaussian distribution, which seems to be due to "outliers" with large errors. The pdf of the high elevation SV's follow the gaussian distribution closely. The mean and standard deviation for the two cases are listed in Table 5.1 below:

	Mean	Standard deviation
$\theta_e < 5^o$	1.508 m	10.095 m
$\theta_e > 45^o$	-0.015 m	1.282 m

Tabel 5.1 Statistics of differential PR errors for SV's with high and low elevations.

The conclusion is that the PR errors for SV's with low elevation is both large and significantly nongaussian.

The frequency distribution of the PR errors can be characterized by the Power Spectral Density (PSD). The PSD is defined as the fourier transform of the autocorrelation function. Since the autocorrelation function is a symmetrical real valued function, the PSD is also a symmetrical real valued function. The PSD is only defined mathematically for stationary gaussian stochastic processes. Since it has been showed above that the PR errors depend on the SV elevation, this gives somewhat of a problem if the PSD of the PR error for a specific SV is determined from the moment it rises above the horizon to the moment it sets. One approximate solution to this problem is to compute the PSD for elevation intervals that are small enough to justify the assumption of stochastic stationarity. From Figure 5.3 it is apparent that the standard deviation of the PR errors seem to have a plateau for elevations below approximately $10°$ and above approximately $45°$. This information has been used to determine the PSD in the two elevation intervals $0° < \theta_e < 10°$ and $\theta_e > 45°$, the PSD has been determined using a 512 point FFT (equivalent to 512 sec.). The resulting PSD's are then determined as the mean value of all PSD's at each frequency for every 512 seconds of data in the appropriate elevation intervals. Incomplete intervals of less then 512 continues epochs are ignored in the analysis. The results are shown in Figure 5.5 below:

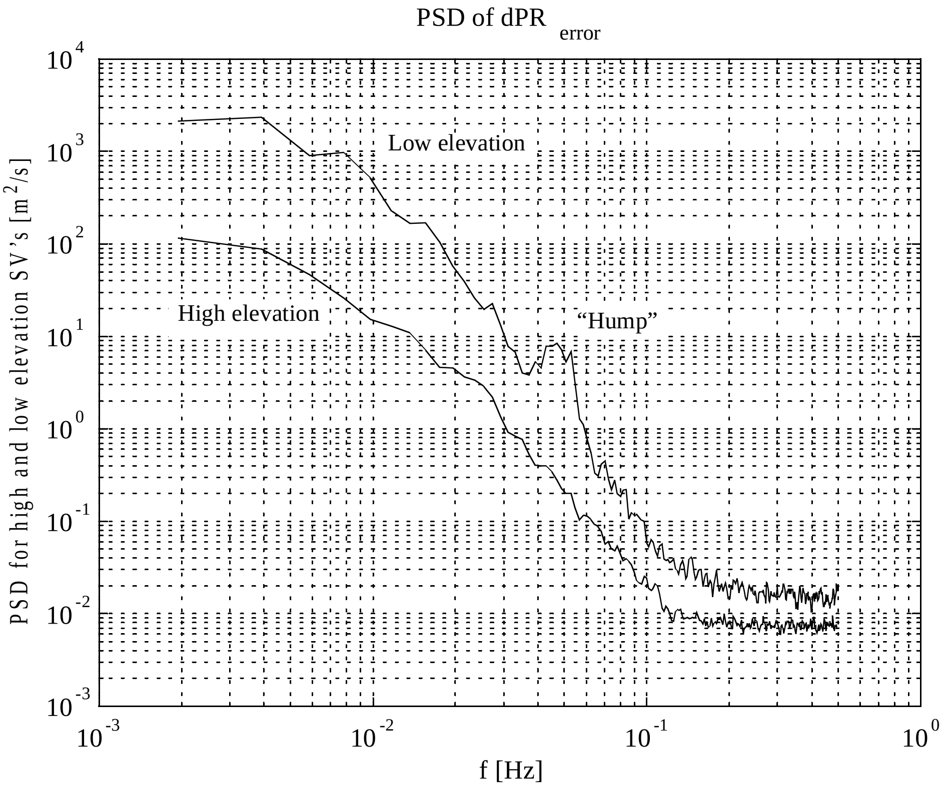

FIGURE 5.5 PSD of dPR error for high and low elevation satellites.

It is clear from Figure 5.5 that the PSD has a substantial variation with frequency. The low frequency content of the PR error is much larger then the high frequency content for both high and low elevations. The general shape of the PSD is similar for both high and low elevation SV's, however the relative difference between the PSD's is much greater for low then for high frequencies. In addition the low elevation PSD has a significant "hump" at a frequency of around $0.05\mathrm{Hz}$. It can be speculated that these differences are due to multipath, which is probably slowly varying due to the fact that the antennas and surrounding buildings are stationary. If one of the antennas where located on a moving vehicle, the shape of the low elevation PSD could conceivably differ substantially from the one shown above.

In the preceding treatment, the focus was on correlating the multipath noise with the elevation of the satellite as seen from the receiver(s). This gives a statistical correlation based on the fact that multipath is much more likely for low elevation satellites due to the signal propagation geometry. It must however be remembered that this correlation is only statistical, since a low satellite elevation does not necessarily imply that there will be any multipath. On the other hand a high satellite elevation does not guarantee a multipath free signal propagation. In other words this means that using only the elevation of the satellite is not an optimal way to determine the multipath noise on a given satellite.

The Superstar receiver has the option to output the Signal to Noise Ratio (SNR) of the measured satellite signal. The exact definition of the SNR used by the receiver is not documented in the Superstar manual. Nevertheless the statistical relationship between the SNR and the differential pseudo range errors have been estimated based on the measured PR data. It appears that a correlation does exist between the SNR and the PR errors. This correlation is shown in Figure 5.6 below:

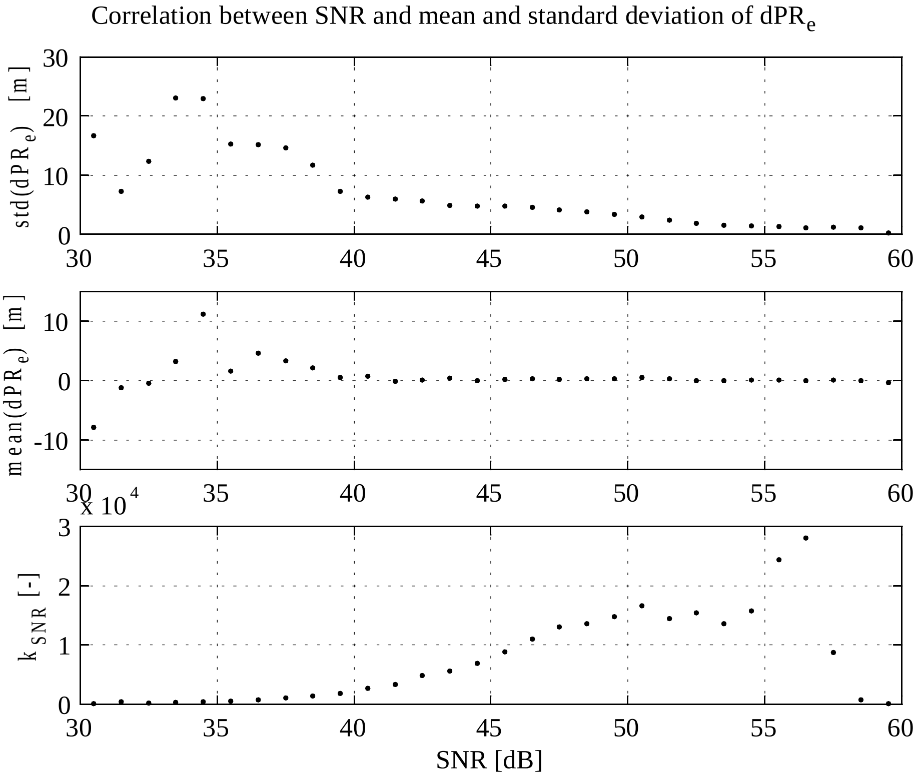
Correlation between SNR and mean and standard deviation of dPR_e

FIGURE 5.6 Correlation between SNR and dPR error.

The function $k_{SNR}(SNR)$ is the total number of differential PR measurements in each 1dB measurement interval. It is apparent that the proportion of measurements with low SNR values and high differential measurement errors, is small. This indicates that using the SNR is a very selective method to discriminate between good and bad PR measurements. Thus a weighing function based on the SNR, minimizes the proportion of PR measurements that are wrongly given a bad weight in the baseline solution. This should improve the total baseline solution, compared to using a weighting function based on the SV elevation.

In the next section, we will use the correlation between the differential PR errors and the maximum SNR of each PR measurement pair to increase the accuracy of the differential position solution. In order to simplify this, a simple analytical expression for the correlation is useful. Using the standard deviation measurements in Figure 5.6, the following piecewise linear analytical approximation has been determined:

$$\sigma_{dPR}(SNR) = \begin{cases} 1.5\text{m} & SNR > 55\text{dB} \\ 19.815\text{m} - 0.333\text{m/dB} \cdot SNR & 55\text{dB} \geq SNR > 40\text{dB} \\ 146.5\text{m} - 3.5\text{m/dB} \cdot SNR & 40\text{dB} \geq SNR \end{cases} \tag{5.8.9}$$

The function $\sigma_{dPR}(SNR)$ is super imposed on the measurements in Figure 5.6.

In some cases one or more differential PR measurements will be way off. This can be due to extreme multipath caused by complete blockage of the direct signal or by signal processing errors in the GPS receiver. When solving the linearized baseline equation with more then 4 SV's, this can be detected as extreme differential PR residuals.

It is possible to compute the residuals after each baseline solution, this can be used to eliminate SV's from the solution. This is done by detecting if one or more residuals exceed their expected error by a certain margin. Since the expected error range of a SV is proportional to the a priori standard deviation corresponding to the particular SNR, an error limit proportional to the a priori standard deviation of the differential PR measurement should be used.

5.8.2 Double difference analysis of Carrier Phase measurements

The carrier phase measurements can be used to estimate the velocity of the receiver (antenna) according to Section 5.5. In practice this will be accomplished in a differential system consisting of a stationary reference receiver and a moving vehicle mounted receiver. In such a system, the "measurements" are the double difference carrier phases. As described previously, the actual carrier phases are can only be measured exactly in terms of fractional cycles, whereas the integer number of cycle differences between two receivers can not be directly measured. Thus instead of using the ambiguous carrier phase differences, the unambiguous carrier phase rate differences will be used to estimate the velocity difference between the receivers.

The carrier phase rate differences can be directly translated into a pseudo Carrier Range Rate (CRR) difference by multiplying with the L1 wavelength. The (code) pseudo ranges where called just that because of the local receiver time errors. The same principle applies to the measured phase rates, in this case because of the Local Oscillator (LO) frequency errors. For this reason a number of reference SV's with high elevations will be used in the following when computing the differential carrier phase rate errors, completely analogous to the methods used in Section 5.8.1 for the differential pseudo range measurements.

For the sake of brevity, only the important results of the carrier range rate analysis will be discussed in the following.

Just as with the differential pseudo range errors, it has been determined that there is a strong correlation between the measured errors and the measured maximum Signal to

Noise Ratio (SNR) of the particular differential carrier range rate. This relationship is shown below in Figure 5.7:

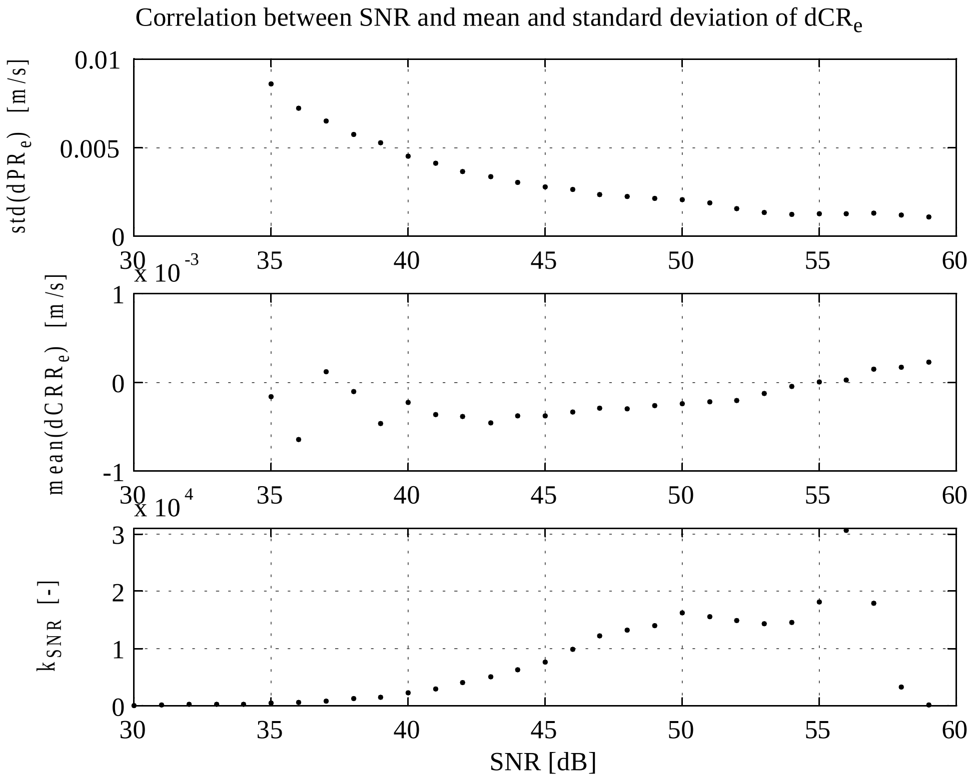

FIGURE 5.7 Correlation between SNR and dCRR error.

The function $k_{SNR}(SNR)$ is the total number of differential carrier range rate measurements in each 1dB measurement interval. It is apparent that the proportion of measurements with low SNR values and high differential measurement errors, is small. This indicates that using the SNR is a very selective method to discriminate between good and bad CRR measurements. This is exactly the same conclusion as for the PR errors.

Comparing the dPR errors in figure Figure 5.6 with the dCRR errors in Figure 5.7, it is apparent that we can roughly relate the predicted measurement errors of the two quantities by a constant:

$$\sigma_{dCRR} \approx c_{CRR}\sigma_{dPR} \qquad c_{CRR} \cong 9\times10^{-4}s^{-1} \tag{5.8.10}$$

Where σ_{dCRR} is the predicted dCRR standard deviation and σ_{dPR} is the corresponding predicted dPR standard deviation.

The physical explanation of this large difference in the measurement errors, is that moderate multipath as well as receiver noise generates errors that are fractions of the signal wavelength. This means that since the signal wavelength of the PR is equal to the C/A chip length of 300m, while the carrier wavelength is equal to approximately 20cm, the difference in errors will all other things equal be of a similar magnitude.

The Power Spectral Density (PSD) of the differential CRR errors can not be expected to be similar to that of the dPR errors because the CRR is a velocity while the PR is a distance. In addition the carrier phase multipath will generally vary much faster because of the much shorter wavelength of the carrier compared to the C/A signal. For these reasons, the PSD's of the CRR errors is much "flatter" and more like white noise then the differential PR errors. This is confirmed by Figure 5.8 below:

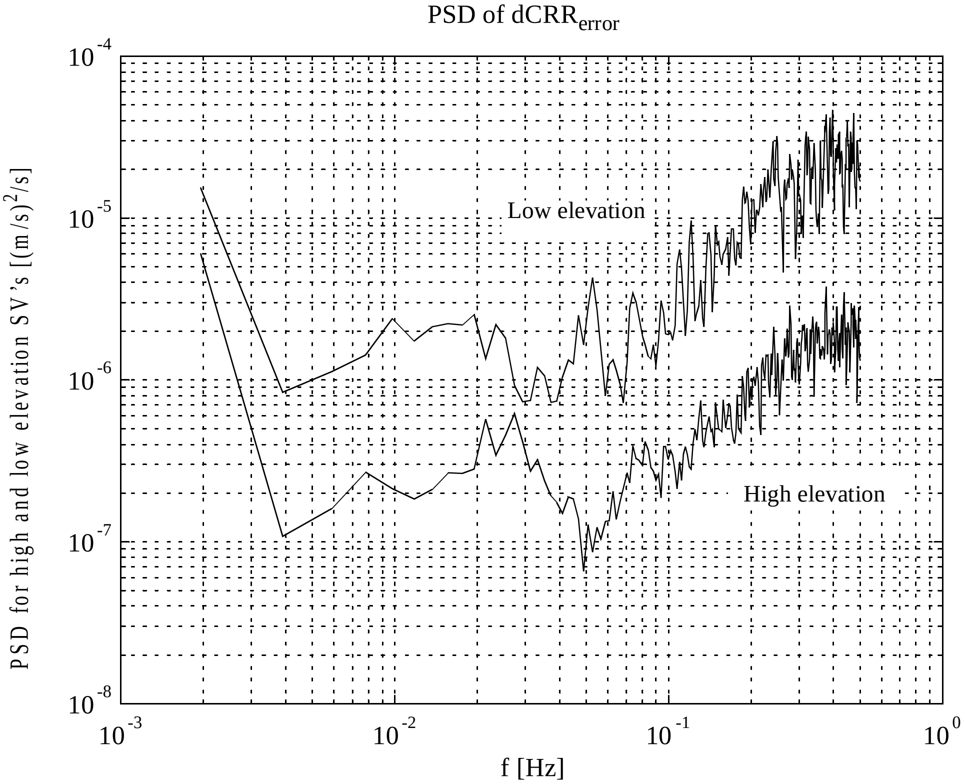

FIGURE 5.8 PSD of dCRR error for high and low elevation satellites.

In the following we will crudely assume that the dCRR errors are sampled white noise signals, with expected standard deviations according to Eq. 5.8.10.

5.9 Equations for differential positioning

5.9.1 Differential PR baseline solution

Given an overdetermined set of differential pseudo range measurements with known a priori standard deviations, the stochastic optimal baseline solution can be determined by solving a weighted linearized problem. The unweighted point position solution $\mathbf{P}_{RX} = \hat{\mathbf{P}}_{RX} + \Delta\mathbf{P}_{RX}$ can be determined by solving the 4×4 linear equation system (Eq. 5.4.18):

$$\mathbf{F}\Delta\tilde{\mathbf{P}}_{RX} = \mathbf{B} \qquad \Delta\tilde{\mathbf{P}}_{RX} = \begin{bmatrix} \Delta\mathbf{P}_{RX} \\ \Delta c \end{bmatrix} \tag{5.9.1}$$

Where $\mathbf{F} \equiv \mathbf{A}^T\mathbf{A}$ is a 4×4 symmetrical matrix and $\mathbf{B} \equiv \mathbf{A}^T\mathbf{Y}$ is a 4×1 vector. The receiver time error expressed as a distance, is given by Δc.

The matrix $\mathbf{A}$ is a function of the relative geometry between the SV's and the guessed receiver position, as given by Eq. 5.4.15. Each row in $\mathbf{A}$ corresponds to one SV:

$$\mathbf{A} \equiv \begin{bmatrix} \frac{\hat{x}_{RX} - x_{SV,1}}{\hat{R}_1} & \frac{\hat{y}_{RX} - y_{SV,1}}{\hat{R}_1} & \frac{\hat{z}_{RX} - z_{SV,1}}{\hat{R}_1} & -1 \\ \frac{\hat{x}_{RX} - x_{SV,2}}{\hat{R}_2} & \frac{\hat{y}_{RX} - y_{SV,2}}{\hat{R}_2} & \frac{\hat{z}_{RX} - z_{SV,2}}{\hat{R}_2} & -1 \\ \dots & \dots & \dots & \dots \\ \frac{\hat{x}_{RX} - x_{SV,N}}{\hat{R}_N} & \frac{\hat{y}_{RX} - y_{SV,N}}{\hat{R}_N} & \frac{\hat{z}_{RX} - z_{SV,N}}{\hat{R}_N} & -1 \end{bmatrix} \qquad (5.9.2)$$

Each row in the vector $\mathbf{Y}$ contains the difference between the measured pseudorange and the range from the SV to the guessed receiver position:

$$\mathbf{Y} \equiv \begin{bmatrix} PR_1 - \hat{R}_1 \\ PR_2 - \hat{R}_2 \\ \dots \\ PR_N - \hat{R}_N \end{bmatrix} \qquad (5.9.3)$$

If the PR measurements have different measurement noise levels, it can be shown that the stochastic best (most likely) solution estimate can be found by solving the weighted problem:

$$\mathbf{F}_w \Delta\tilde{\mathbf{P}}_{RX} = \mathbf{B}_w \qquad \mathbf{F}_w \equiv \mathbf{A}^T \mathbf{W}^2 \mathbf{A} \qquad \mathbf{B}_w \equiv \mathbf{A}^T \mathbf{W}^2 \mathbf{Y} \qquad (5.9.4)$$

Where $\mathbf{W} \equiv diag(w_1, w_2, \dots, w_N)$ is a diagonal matrix of weights on each PR measurement.

It can be shown (Ref. 30, p. 35) that the stochastic optimal weights should be proportional to the inverse of the measurement standard deviations:

$$w_i \propto \frac{1}{\sigma_{dPR,i}} \qquad (5.9.5)$$

Where $\sigma_{dPR,i}$ is the standard deviation of the differential PR measurement of SV number i. The constant of proportionality in Eq. 5.9.5 does not influence the solution, thus it can be set equal to unity.

In reality the a priori (predicted) value of the standard deviations must be used in Eq. 5.9.5, since the actual value is practically impossible to measure.

As outlined in Section 5.7, the objective of differential positioning is to obtain the baseline (vector) between the two receivers, in other words $\mathbf{P}_{RX12} \equiv \mathbf{P}_{RX2} - \mathbf{P}_{RX1}$. It is assumed that the position $\mathbf{P}_{RX1}$ of receiver number one is approximately known.

In the general case this may be done by using Eq. 5.9.4 separately for both receivers:

$$\mathbf{F}_{w1} \Delta\tilde{\mathbf{P}}_{RX1} = \mathbf{B}_{w1} \qquad \mathbf{F}_{w2} \Delta\tilde{\mathbf{P}}_{RX2} = \mathbf{B}_{w2} \qquad (5.9.6)$$

Where $\mathbf{F}_{w1}$ and $\mathbf{B}_{w1}$ are based on the guessed position and the PR measurements of RX1, while $\mathbf{F}_{w2}$ and $\mathbf{B}_{w2}$ are based on the guessed position and the PR measurements of RX2.

For short baselines the differential position calculation may be linearized around the assumed position of RX1, as shown in Section 5.8.1. In this case the guessed position RX2 is set equal to the assumed position of RX1. This gives identical values of the "**A**" matrix (Eq. 5.9.2):

$$\mathbf{A}_2 = \mathbf{A}_1 = \mathbf{A} \tag{5.9.7}$$

Since the weighting matrix $\mathbf{W}$ is based on the a priori assumed differential PR errors, correlated with the maximum SNR of each SV, we must for consistency use the same weighting matrix for both receivers. This gives the same weighted "$\mathbf{F}_w$" matrices:

$$\mathbf{F}_{w1} = \mathbf{F}_{w2} = \mathbf{F}_w = \mathbf{A}^T\mathbf{W}^2\mathbf{A} \tag{5.9.8}$$

We can now determine the linearized differential position solution be algebraically subtracting the position solution equation of RX1 from that of RX2 (Eq. 5.9.6):

$$\mathbf{F}_w(\Delta\tilde{\mathbf{P}}_{\mathrm{RX2}} - \Delta\tilde{\mathbf{P}}_{\mathrm{RX1}}) = \mathbf{B}_{w2} - \mathbf{B}_{w1} \tag{5.9.9}$$

Since the position update (or correction) is given by $\mathbf{P}_{\mathrm{RX}} = \hat{\mathbf{P}}_{\mathrm{RX}} + \Delta\mathbf{P}_{\mathrm{RX}}$ and $\hat{\mathbf{P}}_{\mathrm{RX2}} = \hat{\mathbf{P}}_{\mathrm{RX1}} = \hat{\mathbf{P}}_{\mathrm{RX}}$, the difference $\Delta\tilde{\mathbf{P}}_{\mathrm{RX2}} - \Delta\tilde{\mathbf{P}}_{\mathrm{RX1}}$ can be expressed as:

$$\Delta\tilde{\mathbf{P}}_{\mathrm{RX2}} - \Delta\tilde{\mathbf{P}}_{\mathrm{RX1}} = (\mathbf{P}_{\mathrm{RX2}} - \hat{\mathbf{P}}_{\mathrm{RX}}) - (\mathbf{P}_{\mathrm{RX1}} - \hat{\mathbf{P}}_{\mathrm{RX}}) = \mathbf{P}_{\mathrm{RX2}} - \mathbf{P}_{\mathrm{RX1}} \equiv \mathbf{P}_{\mathrm{RX12}} \tag{5.9.10}$$

The "**Y**" matrices (Eq. 5.9.3) only differ in the PR measurements, since the guessed RX2 position is taken equal to the assumed RX1 position. Thus the difference $\mathbf{B}_{w2} - \mathbf{B}_{w1}$ can be expressed as:

$$\mathbf{B}_{w2} - \mathbf{B}_{w1} = \mathbf{B}_{w12} = \mathbf{A}^T\mathbf{W}^2\mathbf{Y}_2 - \mathbf{A}^T\mathbf{W}^2\mathbf{Y}_1 = \mathbf{A}^T\mathbf{W}^2(\mathbf{Y}_2 - \mathbf{Y}_1) = \mathbf{A}^T\mathbf{W}^2\mathbf{Y}_{12} \tag{5.9.11}$$

Where PR_{1i} are the PR's measured by RX1 and PR_{2i} are the PR's measured by RX2. The PR differential measurement matrix is given by:

$$\mathbf{Y}_{12} = \begin{bmatrix} \mathrm{PR}_{11} - \mathrm{PR}_{21} \\ \mathrm{PR}_{12} - \mathrm{PR}_{22} \\ \dots \\ \mathrm{PR}_{1N} - \mathrm{PR}_{2N} \end{bmatrix} \tag{5.9.12}$$

This shows that the right hand side of Eq. 5.9.9 is a linear function of the measured PR differences.

This shows that Eq. 5.9.9 can be used directly to determine the differential position (baseline) by solving one 4×4 linear equation system:

$$\mathbf{F}_w\mathbf{P}_{\mathrm{RX12}} = \mathbf{B}_{w12} \tag{5.9.13}$$

In some cases one or more differential PR measurements will be way off. This can be due to extreme multipath caused by complete blockage of the direct signal or by signal processing errors in the GPS receiver. When solving the linearized baseline equation with more then 4 SV's, this can be detected as extreme differential PR residuals.

It is possible to compute the residuals after each baseline solution, this can be used to eliminate SV's from the solution. This is done by detecting if one or more residuals exceed their expected error by a certain margin. Since the expected error range of a SV is proportional to the a priori standard deviation corresponding to the particular SNR, an error limit proportional to the a priori standard deviation of the differential PR measurement should be used.

The pseudorange residuals corresponding to a particular baseline $\mathbf{P}_{\mathrm{RX12}}$ and differential pseudo range measurements $\mathbf{Y}_{12}$ can be defined as:

$$\mathbf{dPR}_{\mathrm{res}} = \mathbf{A}\mathbf{P}_{\mathrm{RX12}} - \mathbf{Y}_{12} \tag{5.9.14}$$

From this definition it follows that the residuals have the same dimension as the measured pseudoranges.

Since the a priori standard deviations are given by $\sigma_{\mathrm{dPR,i}} = \sigma_{\mathrm{dPR}}(\mathrm{SNR_i})$, the rejection criterion for PR measurements can be expressed as:

$$\begin{array}{ll} \|\mathrm{dPR}_{\mathrm{res,i}}\| \le \alpha\sigma_{\mathrm{dPR,i}} & \text{Include PR in solution} \\ \|\mathrm{dPR}_{\mathrm{res,i}}\| > \alpha\sigma_{\mathrm{dPR,i}} & \text{Reject PR from solution} \end{array} \tag{5.9.15}$$

Where α is a positive constant, it is customary to use $\alpha = 3$.

Since determination of the residuals require a baseline solution $\mathbf{P}_{\mathrm{RX12}}$, it is apparent that if any PR's are rejected by Eq. 5.9.15 a new solution has to be computed using Eq. 5.9.13 without the rejected PR measurement. It is only wise to remove one PR measurement at a time, even if several PR measurements fail Eq. 5.9.15. This is because one bad PR measurement will pull the baseline solution away from the correct solution and thus produce large residuals for the remaining PR measurements. The choice of which PR measurement to remove (first) should thus be based on which PR has the largest nondimensional residue $\mathrm{d\tilde{P}R}_{\mathrm{res,i}} = \mathrm{dPR}_{\mathrm{res,i}}/\sigma_{\mathrm{dPR,i}}$.

Using the above equations it is possible to implement a PR differential positioning system for short baselines. With the same 6 hour set of measurements as used above, the following results have been achieved:

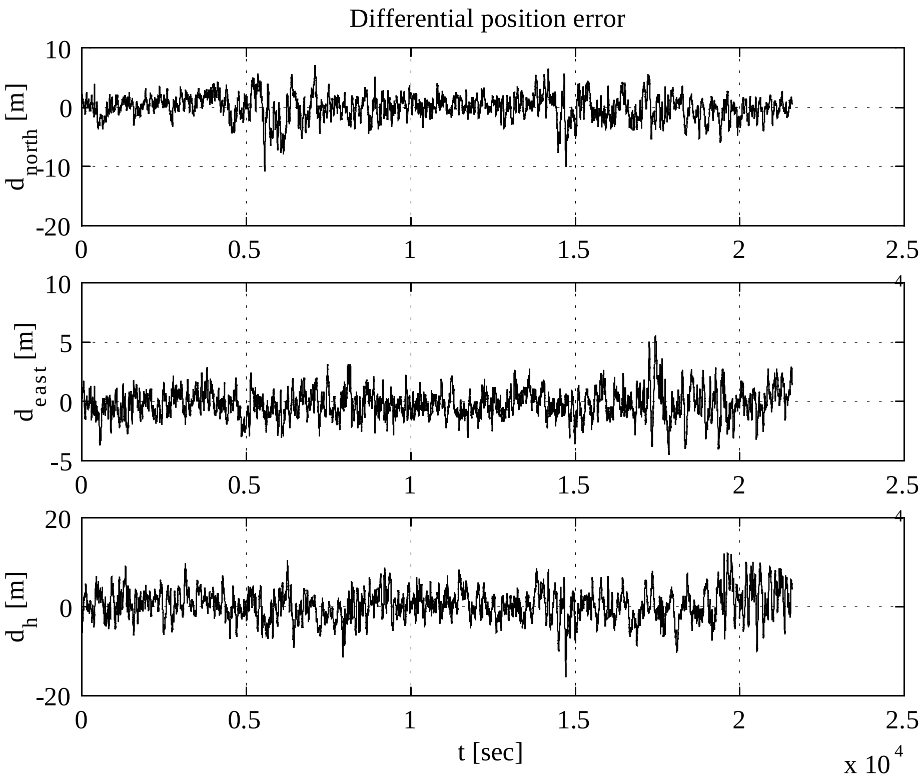

FIGURE 5.9 PR DGPS errors with SNR weigthed PR's.

The standard deviations of the North-South, East-West and vertical errors are given below in Table 5.2:

	North-South	East-West	Vertical
σ_{DGPS}	2.06m	1.17m	3.34m
$\bar{\mathbf{P}}_{RX12,error}$	0.02m	-0.17m	0.44m

Tabel 5.2 Standard deviation and mean of PR DGPS errors in local coordinates.

The corresponding probability density functions (pdf's) of the baseline error components are shown below in Figure 5.10:

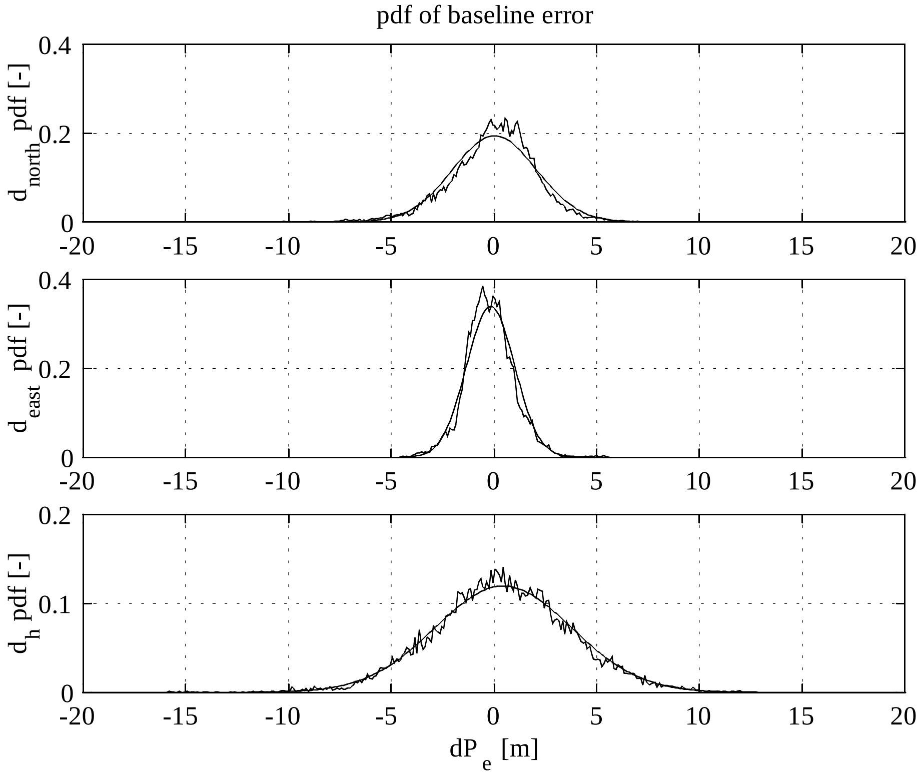

FIGURE 5.10 Probability density functions of PR DGPS errors.

It is apparent that the pdf's of the baseline errors are quite close to gaussian distributions (shown by the smooth curves). In order to better appreciate the probabilities of extreme baseline errors, Figure 5.11 shows the probabilities of exceeding a certain horizontal error R_{hor} and a certain vertical error H_{abs}:

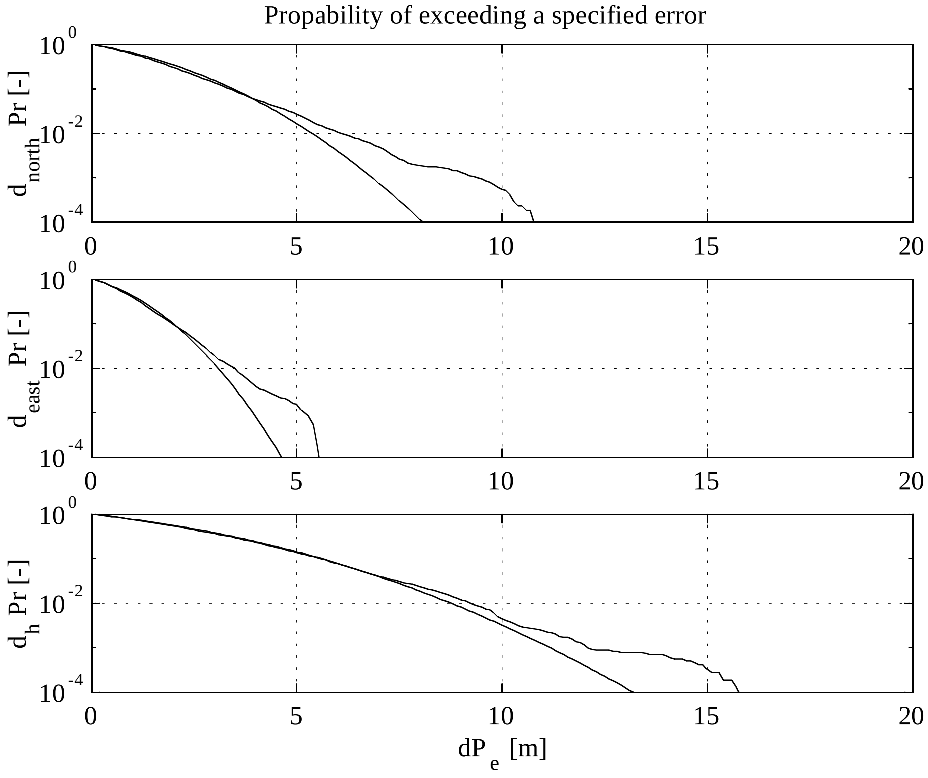

FIGURE 5.11 Exceedens propabilities on a logarithmic scale.

It is possible to predict the DGPS baseline errors by using the a priori known correlation between the SNR and the differential PR errors. From Eq. 5.9.13 we have that the weighted baseline estimate can be determined as:

$$\mathbf{P}_{\mathrm{RX12}} = \mathbf{F}_w^{-1}\mathbf{B}_{w12} = \mathbf{F}_w^{-1}(\mathbf{A}^T\mathbf{W}^2\mathbf{Y}_{12}) \tag{5.9.16}$$

In general it can be shown (Ref. 31, p. 43) that if one has a linear relationship $\mathbf{Y} = \mathbf{AX}$ between two stochastic vector quantities $\mathbf{X}$ and $\mathbf{Y}$, with the covariance of the vector $\mathbf{X}$ given by $\mathbf{Q_X}$, then the covariance $\mathbf{Q_Y}$ of $\mathbf{Y}$ is obtained as:

$$\mathbf{Q_Y} = \mathbf{AQ_XA}^T \tag{5.9.17}$$

Using this relationship on Eq. 5.9.16 gives the following expression for the a priori covariance $\mathbf{Q}_{\mathrm{RX12}}$ on the baseline solution $\mathbf{P}_{\mathrm{RX12}}$:

$$\mathbf{Q}_{\mathrm{RX12}} = (\mathbf{F}_w^{-1}\mathbf{A}^T\mathbf{W}^2)\mathbf{Q}_{\mathrm{dPR}}(\mathbf{F}_w^{-1}\mathbf{A}^T\mathbf{W}^2)^T \tag{5.9.18}$$

Where $\mathbf{Q}_{\mathrm{dPR}}$ is the differential pseudorange covariance. Since we have tacitly assumed that the differential pseudorange errors are uncorrelated, $\mathbf{Q}_{\mathrm{dPR}}$ can be expressed as a diagonal matrix:

$$\mathbf{Q}_{\mathrm{dPR}} = diag(\sigma^2_{\mathrm{dPR,1}}, \sigma^2_{\mathrm{dPR,2}}, \ldots, \sigma^2_{\mathrm{dPR,N}}) \tag{5.9.19}$$

It is important to realize that even though the differential pseudorange errors are independent, this is in general not the case for the components of the resulting computed baseline.

Using Eq. 5.9.18 with the 6 hour set of data, gives the predicted standard deviations of the differential position in local coordinates. The results are shown below in Figure 5.12:

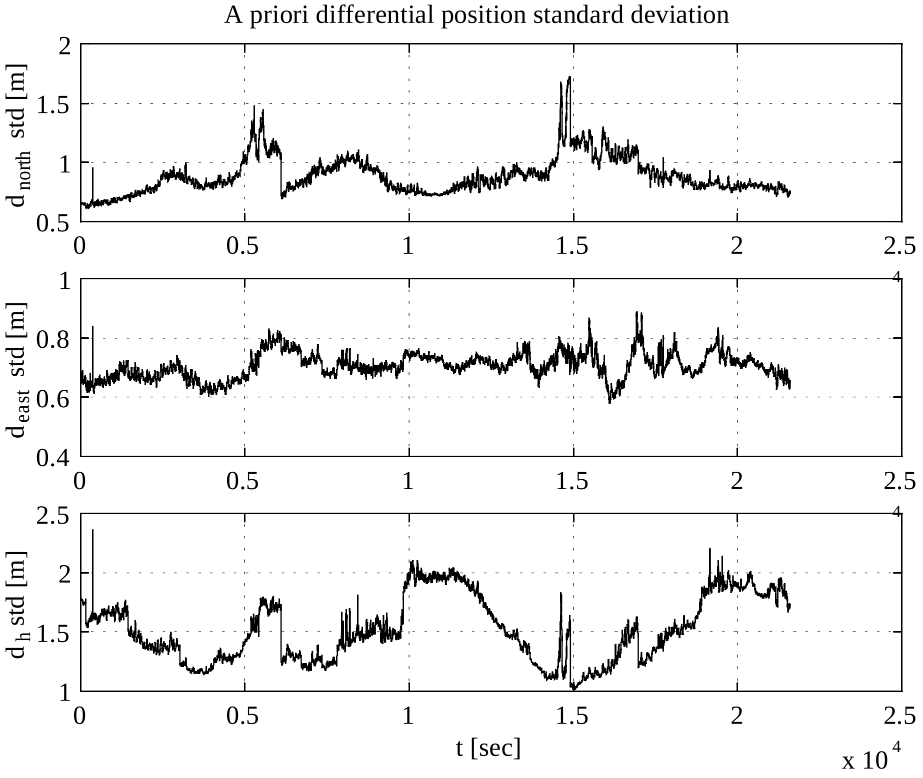

FIGURE 5.12 A priori differential position standard deviations.

It is apparent by comparing the measured standard deviations from Table 5.2 with the predicted ones from Figure 5.12, that the measured and predicted standard deviations are correlated, although the predicted and measured standard deviations are not identical. In order to investigate this further, the correlation between the measured standard deviations and the predicted standard deviations for all components of the baseline error vector have been computed. The results of this analysis is shown below in Figure 5.13:

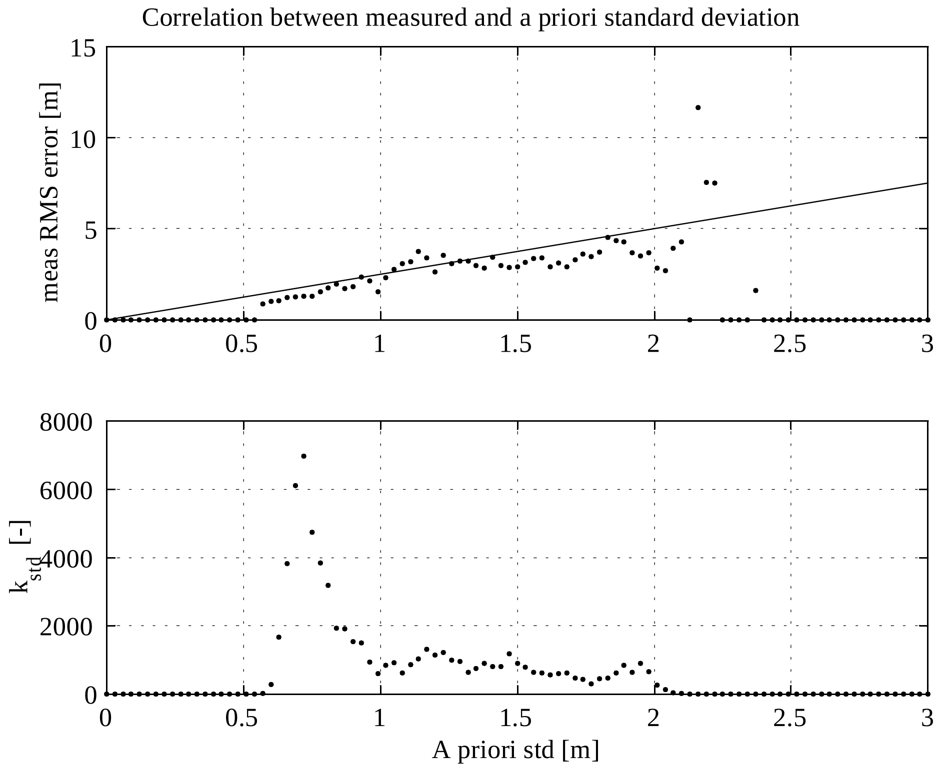

FIGURE 5.13 Correlation between predicted a priori and measured standard deviations.

It can be seen that there is an approximate linear correlation between the predicted a priori standard deviations and the measured RMS deviations (which equals the standard deviation for zero mean). This correlation can be seen in the interval $0.6 < \sigma_{apriori} < 2$, where the number of measurements pr. $\sigma_{apriori}$ interval (denoted by k_{std}) is significant. The linear “eyeballed” straight fit line approximation shown in Figure 5.13 is given by the equation:

$$\sigma_{DGPS} \approx c_{DGPS}\sigma_{DGPS,apriori} \qquad c_{DGPS} = 2.5 \tag{5.9.20}$$

The importance of Eq. 5.9.20 is that in connection with Eq. 5.9.18 it can be used to give a reasonably accurate prediction of the current PR DGPS accuracy in any direction, without the need for separate empirical correlations for each direction.

Just as the frequency distributions of the double difference pseudo range errors where computed as PSD’s in Section 5.8.1, the frequency distribution of the resulting DGPS position errors can be determined using a separate PSD for each direction. This is shown below Figure 5.14:

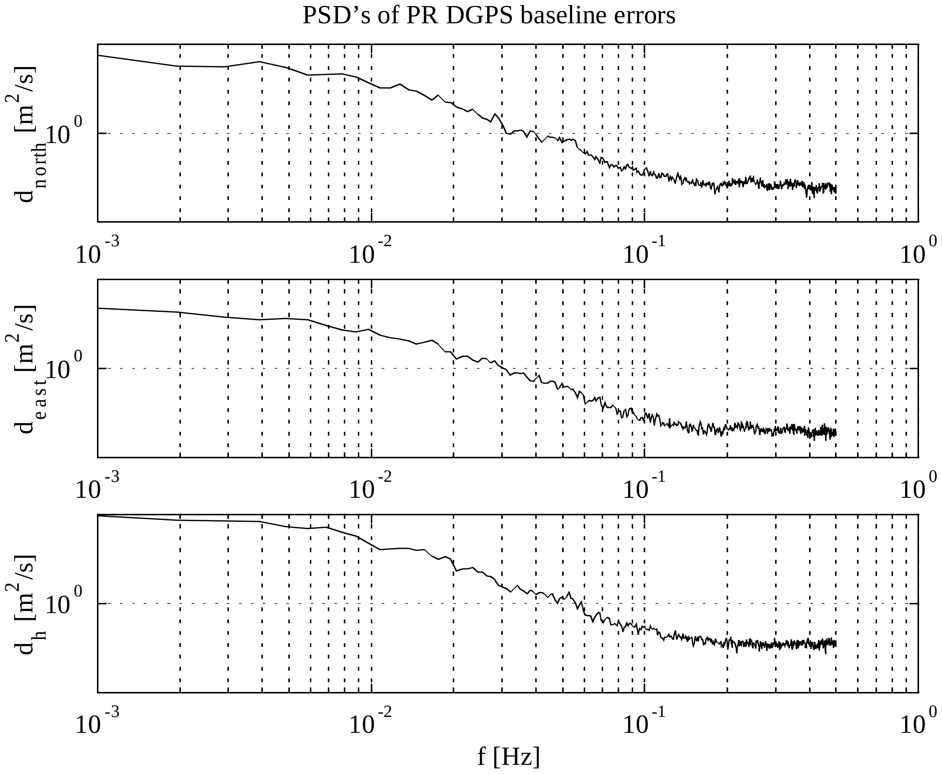

FIGURE 5.14 PSD's of SNR weighted pseudo range DGPS position errors.

For comparison with the weighted solution method given above, the standard deviations of the North-South, East-West and vertical errors without SNR based weighting are shown below in Table 5.3:

	North-South	East-West	Vertical
σ_{DGPS}	3.04m	1.81m	4.34m
$\bar{\mathbf{P}}_{RX12,error}$	0.06m	-0.15m	0.64m

Tabel 5.3 Standard deviation and mean of PR DGPS errors without SNR weighting.

5.9.2 Differential CRR velocity solution

Given an overdetermined set of differential carrier range rate measurements with known a priori standard deviations, the stochastic optimal baseline velocity solution can be determined by solving a weighted linearized problem. The unweighted point velocity solution $\mathbf{v}_{RX,k}$ can be determined by solving the $N \times 4$ linear equation system given by Eq. 5.5.8:

$$\mathbf{v}_{RX,k} = \mathbf{F}_k^{-1}\mathbf{A}_k^T(\mathbf{CRR}_k - (\mathbf{R}_{k-1} - \mathbf{R}_{k-2})) - (\mathbf{P}_{RX,k-1} - \mathbf{P}_{RX,k-2}) \tag{5.9.21}$$

If different weights are desired on the different carrier range rate measurements, the weighted point velocity solution can be determined in analogy with Eq. 5.9.16:

$$\mathbf{v}_{\mathrm{RX,k}} = \mathbf{F}_w^{-1}\mathbf{A}^T\mathbf{W}^2(\mathbf{CRR}_{\mathrm{k}} - (\mathbf{R}_{\mathrm{k-1}} - \mathbf{R}_{\mathrm{k-2}})) - (\mathbf{P}_{\mathrm{RX,k-1}} - \mathbf{P}_{\mathrm{RX,k-2}}) \tag{5.9.22}$$

Where the epoch subscripts on $\mathbf{F}_w$ and $\mathbf{A}$ have been omitted for simplicity.

The weigthed least square solution system matrix $\mathbf{F}_w$ is given by Eq. 5.9.8:

$$\mathbf{F}_w = \mathbf{A}^T\mathbf{W}^2\mathbf{A} \tag{5.9.23}$$

The differential CRR velocity solution $\mathbf{v}_{\mathrm{RX12,k}}$ is defined by:

$$\mathbf{v}_{\mathrm{RX12,k}} = \mathbf{v}_{\mathrm{RX2,k}} - \mathbf{v}_{\mathrm{RX1,k}} \tag{5.9.24}$$

The short baseline differential CRR velocity solution can then be determined as:

$$\begin{aligned}\mathbf{v}_{\mathrm{RX12,k}} = \mathbf{F}_w^{-1}\mathbf{A}^T\mathbf{W}^2((\mathbf{CRR}_{\mathrm{RX2,\,k}} - \mathbf{CRR}_{\mathrm{RX1,\,k}}) - ((\mathbf{R}_{\mathrm{k-1}} - \mathbf{R}_{\mathrm{k-2}})_{\mathrm{RX2}} - (\mathbf{R}_{\mathrm{k-1}} - \mathbf{R}_{\mathrm{k-2}})_{\mathrm{RX1}}))\\ - (\mathbf{P}_{\mathrm{RX12,k-1}} - \mathbf{P}_{\mathrm{RX12,k-2}})\end{aligned} \tag{5.9.25}$$

Where $\mathbf{CRR}_{\mathrm{RX1,\,k}}$ are the carrier range rates measured by receiver #1, $\mathbf{CRR}_{\mathrm{RX2,\,k}}$ are the carrier range rates measured by receiver #2, $(\mathbf{R}_{\mathrm{k-1}} - \mathbf{R}_{\mathrm{k-2}})_{\mathrm{RX1}}$ are the range rates of the SV's as viewed from receiver #1 while $(\mathbf{R}_{\mathrm{k-1}} - \mathbf{R}_{\mathrm{k-2}})_{\mathrm{RX2}}$ are the range rates of the SV's as viewed from receiver #2.

5.10 Code and phase DGPS

In the preceding section, a SNR weighted DGPS solution has been designed and analysed, based on only the measured pseudoranges. As shown in Appendix E, the carrier phase (or range) measurement noise is much smaller then the PR measurement noise. Since both the carrier phase and PR are measured at the same time by the receiver, an improvement in the DGPS accuracy should be achievable by combining the accurate but ambiguous carrier phases with the noisy but unambiguous pseudo ranges.

There are of course several ways to do this:

- The carrier phase can be used to smooth each pseudorange using a fixed weighting schedule.
- The carrier phase and pseudorange can be used in a Kalman filter for each SV.
- The carrier phases can be used to compute a DGPS velocity, which is combined in a DGPS position Kalman filter with the pseudo range DGPS position solution.

The first method above is exemplified by the pseudorange smoothing algorithm given by Lachapelle (Ref. 24, p. 97):

$$\mathrm{PR}_{\mathrm{sm,k}} = w\mathrm{PR}_{\mathrm{k}} + (1-w)(\mathrm{PR}_{\mathrm{sm,k-1}} + \lambda(\mathrm{CP}_{\mathrm{k}} - \mathrm{CP}_{\mathrm{k-1}})) \qquad (5.10.1)$$

Where “k” is the epoch counter and w is the measured PR weight. $\mathrm{PR}_{\mathrm{sm,k}}$ is the smoothed pseudorange and PR_{k} is the measured pseudorange.

The idea is that the weight is started at $w = 1$ for the first measurement with each SV. For subsequent measurements, the weight is reduced by a fixed amount, typically 0.01 from epoch to epoch. Thus after 100 measurements, the weight reaches a minimum value of $w = 0$. At this time, only the phase rate $\mathrm{CP}_{\mathrm{k}} - \mathrm{CP}_{\mathrm{k-1}}$ affects the smoothed pseudorange update.

The primary advantage of the simple smoothing algorithm is simplicity and ease of implementation. Unfortunately this also means that no information about the actual noise statistics of the pseudorange and carrier phase measurements are incorporated into the smoothing algorithm.

Assuming that a kalman filter on the DGPS position is used, the following procedure can be followed to design the filter.

First we assume for sake of simplicity and execution speed that the errors of each direction component are uncorrelated with the other directions. This is justified when looking at a large set of data, however it must be remembered that the errors generated by measurements of any one satellite at any one time are generally correlated between the different direction components.

By assuming that the errors are uncorrelated with the other directions, we obtain essentially 3 small kalman filters in parallel instead of one large. The following discussion can thus be confined to a single kalman filter for a one dimensional position estimate.

If an accurate dynamic model of the vehicle is available, the kalman filter could be based on this. If however the DGPS measurements are likely to be much more accurate then the dynamic model, it is better and more simple to use a kinematic model. This is based on the idea of using measurements as inputs instead of forces and moments. In our case we know that the velocity estimates based on the measured carrier phases (CP) are very accurate compared to both the dynamic model and the other available measurements. For this reason we will use the computed velocity estimates as inputs to the kinematic model:

$$\Delta x_{RX12,k+1} = \Delta x_{RX12,k} + v_{RX12,x,k} + w_{CRR,x,k} \tag{5.10.2}$$

Where $\Delta x_{RX12,k}$ is the local “x” differential position, $v_{x,RX12,k}$ is the “measured” differential velocity and $w_{CRR,x,k}$ is “measurement” noise on $v_{RX12,x,k}$. Furthermore we assume that $w_{CRR,x,k}$ is white gaussian noise.

The measurement in the kalman filter is the PR DGPS position calculation, giving the measurement equation:

$$\Delta x_{PR,k} = \Delta x_{RX12,k} + \nu_{PR,x,k} \tag{5.10.3}$$

Where $\Delta x_{PR,k}$ is the “measured” PR DGPS position and $\nu_{PR,x,k}$ is the “measurement” noise. As we have determined above, the PR DGPS errors closely approximate a gaussian distribution. However the errors are not white noise.

One way to include nonwhite noise in the kalman filter is to use a noise shaping filter (Ref. 32, p. 125). The idea behind this is to augment the system dynamics with the dynamics of a linear filter that produces the desired noise spectrum (PSD) at the output when excited by a white noise signal.

Based on the general shapes of the SNR weighted pseudo range DGPS error PSD’s in Figure 5.14, we will assume that a second order discrete *shaping* filter is sufficient to generate the desired PSD shapes. Such a filter has an infinite number of state space implementations. One problem with the PSD based shaping filter is that the PSD is derived using the assumption of stationary statistics. This means that the covariance of the filter states are assumed time invariant. However to be useful in a time varying Kalman filter we must be able to specify appropriate initial conditions for the shaping filter states and covariance. This is much easier if the filter states have a clear physical meaning.

In the continous case a general stable second order filter can be represented as a damped oscillator, with the dynamics described in terms of the undamped natural frequency, the nondimensional damping ratio and maybe a zero. An obvious state space representation of this filter would include one state representing the “position” and another representing the “velocity”.

Inspired by this continues filter, we will propose the following discrete second order state space shaping filter:

$$\begin{aligned} \boldsymbol{\varepsilon}_{DGPS,k+1} &= \begin{bmatrix} \Delta x_e \\ \Delta v_e \end{bmatrix}_{k+1} = \begin{bmatrix} 1 & 1 \\ -\Omega_n^2 & \beta \end{bmatrix} \boldsymbol{\varepsilon}_{DGPS,k} + \begin{bmatrix} k_1 \\ k_2 \end{bmatrix} w_{PR,x,k} \\ \nu_{PR,x,k} &= \begin{bmatrix} 1 & 0 \end{bmatrix} \boldsymbol{\varepsilon}_{DGPS,k} \end{aligned} \tag{5.10.4}$$

Where Ω_n can be interpreted as an approximation to the undamped natural frequency, since the sampling rate of the filter is 1Hz to coincide with the PR DGPS position update frequency. The estimated differential position measurement error is given by Δx_e and its approximate rate (velocity) is given by Δv_e:

$$(\Delta x_e)_{k+1} = (\Delta x_e)_k + (\Delta v_e)_k + k_1 \mathrm{w}_{\mathrm{PR,x,k}} \tag{5.10.5}$$

The discrete transfer function $G(\mathrm{z})$ of the filter given by Eq. 5.10.4, can be determined as (Ref. 33, eq. 2.2.9):

$$G(\mathrm{z}) = \begin{bmatrix} 1 & 0 \end{bmatrix} \left(z\mathbf{I} - \begin{bmatrix} 1 & 1 \\ -\Omega_n^2 & \beta \end{bmatrix} \right)^{-1} \begin{bmatrix} k_1 \\ k_2 \end{bmatrix} = \begin{bmatrix} 1 & 0 \end{bmatrix} \begin{bmatrix} z-1 & -1 \\ \Omega_n^2 & z-\beta \end{bmatrix}^{-1} \begin{bmatrix} k_1 \\ k_2 \end{bmatrix} \tag{5.10.6}$$

After some algebra this can be reduced to:

$$G(\mathrm{z}) = \frac{k_1(z-\beta) + k_2}{z^2 - (1+\beta)\,z + \Omega_n^2 + \beta} = \frac{k_1 z^{-1} + (k_2 - \beta k_1)\,z^{-2}}{1 - (1+\beta)\,z^{-1} + (\Omega_n^2 + \beta)\,z^{-2}} \tag{5.10.7}$$

Notice that $G(\mathrm{z})$ contains no constant term in the numerator, when $G(\mathrm{z})$ is expressed in terms of exponents of z^{-1}.

The next task is to determine the unknown coefficients Ω_n, β, k_1 and k_2 in such a way that $v_{\mathrm{PR,x,k}}$ has a spectral distribution and magnitude that approximates the measured differential position error PSD's.

There is a relationship between the integral of the PSD of a sampled signal and the standard deviation (or variance) of the signal (Ref. 28, p. 84):

$$\sigma^2\{\Delta x_{\mathrm{e}}\} + E^2\{\Delta x_{\mathrm{e}}\} = \frac{1}{f_s}\int_{-\frac{1}{2}f_s}^{\frac{1}{2}f_s} \Phi_{\Delta x_{\mathrm{e}}}(f)\,df = \frac{2}{f_s}\int_0^{\frac{1}{2}f_s} \Phi_{\Delta x_{\mathrm{e}}}(f)\,df \tag{5.10.8}$$

Where $\sigma^2\{\Delta x_{\mathrm{e}}\}$ is the variance of the differential position error Δx_{e} and $E\{\Delta x_{\mathrm{e}}\}$ is the mean of Δx_{e}. $\Phi_{\Delta x_{\mathrm{e}}}(f)$ is the PSD of Δx_{e} sampled at $f_s = 1\mathrm{Hz}$.

Since $E^2\{\Delta x_{\mathrm{e}}\} \ll \sigma^2\{\Delta x_{\mathrm{e}}\}$ according to Table 5.2, we can simplify Eq. 5.10.8 to:

$$\sigma^2\{\Delta x_{\mathrm{e}}\} = \sigma^2_{\Delta x_{\mathrm{e}}} \cong \frac{2}{f_s}\int_0^{\frac{1}{2}f_s} \Phi_{\Delta x_{\mathrm{e}}}(f)\,df \tag{5.10.9}$$

It then follows (Ref. 28, p. 92) that $\Phi_{\Delta x_{\mathrm{e}}}(z)$ can be expressed as the square of a discrete transfer function $G(\mathrm{z})$:

$$\Phi_{\Delta x_{\mathrm{e}}}(\mathrm{z}) = G(\mathrm{z})G(-\mathrm{z})\sigma^2_{white} = |G(\mathrm{z})|^2\sigma^2_{white} \tag{5.10.10}$$

Where σ^2_{white} is the variance of a discrete time white noise signal which is applied to the stable filter $G(\mathrm{z})$ to obtain a noise signal with the PSD $\Phi_{\Delta x_{\mathrm{e}}}(\mathrm{z})$.

In addition we will assume that $G(z)$ is “normalized” so that:

$$\frac{2}{f_s}\int_0^{\frac{1}{2}f_s}|G(z)|^2 df = \frac{1}{\pi f_s}\int_0^{\pi f_s}|G(z)|^2 d\omega = 1 \qquad z = e^{j\omega T_s} = e^{j2\pi f T_s} \tag{5.10.11}$$

According to Eq. 5.10.10, this implies that:

$$\Phi_{\Delta x_e}(z) = G(z)G(-z)\sigma^2_{white} = |G(z)|^2\sigma^2_{\Delta x_e} \tag{5.10.12}$$

The coefficients of the discrete filter $G(z)$ can then be obtained by a least squares curve fit to the measured PSD’s.

In order to minimize the relative error residual with equal weight on all parts of the frequency range, the square of the logarithmic residual will be minimized on a logarithmic frequency scale:

$$F(\Omega_n, \beta, k_1, k_2) = \int_{\omega_{min}}^{\omega_{max}} \left(\log(\Phi_{\Delta x_e}(\omega)) - \log(|G(z)|^2\sigma^2_{\Delta x_e})\right)^2 d(\log(\omega)) \qquad \begin{array}{l} \omega_{min} = \dfrac{2\pi f_s}{N_{FFT}} \\ \omega_{max} = \pi f_s \end{array} \tag{5.10.13}$$

Thus Ω_n, β, k_1 and k_2 are determined in such a way that $F(\Omega_n, \beta, k_1, k_2)$ is minimized under the constraint given by Eq. 5.10.11. $\sigma^2_{\Delta x_e}$ is determined from the experimental PSD using Eq. 5.10.9. $N_{FFT} = 512$ is the number of points in the FFT used to determine the PSD. Since $\Phi_{\Delta x_e}(\omega)$ is only known at discrete frequencies, Eq. 5.10.13 is actually implemented as a sum rather then an integral.

The actual minimization is performed in Matlab using the “fmins” function. The constraint is implemented by using the ratio k_1/k_2 as an independent parameter instead of k_1 and k_2.

The resulting coefficients in the discrete noise shaping filter is shown below in Table 5.4:

	Ω_n [rad/s]	β	k_1	k_2
All directions	0.0501	0.8938	0.0943	0.0124

Tabel 5.4 Coefficients of discrete DGPS error noise shaping filter.

In order to simplify things a little, the same PSD fit is used for all error directions (i.e. only the applied white noise excitation has a different magnitude). It is evident from Figure 5.15 below that this is a reasonable approximation, since the PSD fit is good for all three error directions.

The actual “measured” PSD’s and the fitted approximations are shown below in Figure 5.15:

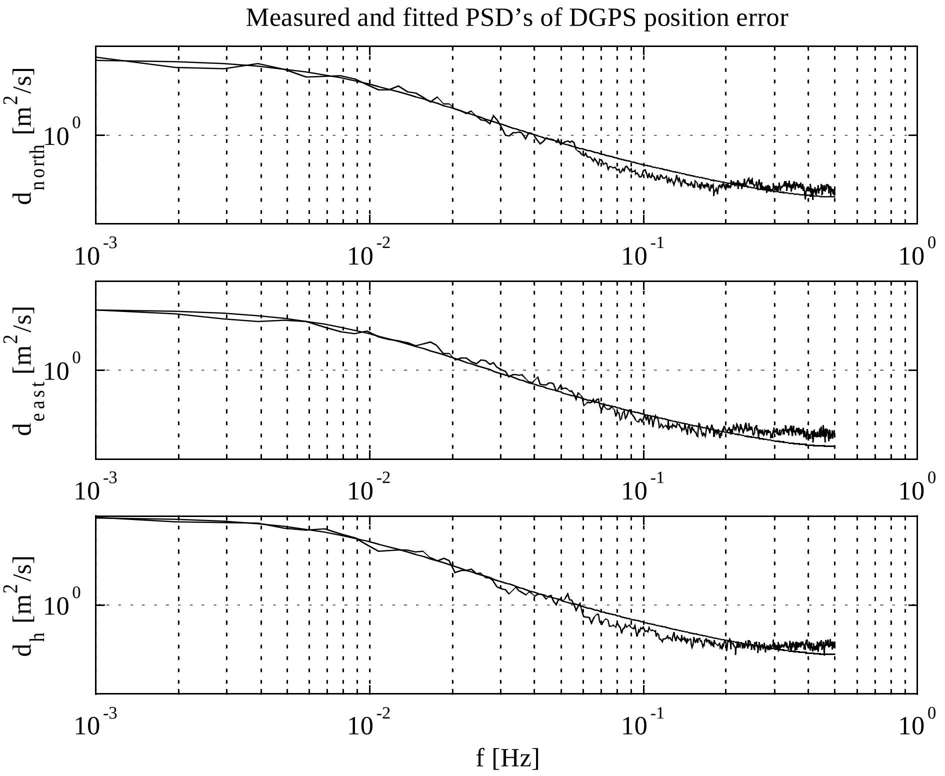

FIGURE 5.15 PSD’s of SNR weighted pseudo range DGPS position errors.

The resulting augmented kinematic system thus consists of Eq. 5.10.2 and Eq. 5.10.3 combined with Eq. 5.10.4:

$$\begin{aligned} \mathbf{x}_{k+1} &= \mathbf{A}_{DGPS}\mathbf{x}_k + \mathbf{B}_{DGPS}\mathbf{u}_k + \mathbf{G}_{DGPS}\mathbf{w}_k \\ \mathbf{z}_k &= \mathbf{C}_{DGPS}\mathbf{x}_k \\ \mathbf{w}_k &\sim (\mathbf{0}, \mathbf{Q}_{DGPS,k}) \end{aligned} \tag{5.10.14}$$

Notice that this model contains no white “measurement” noise, since the measurement noise is entirely modelled by the noise shaping filter which is part of the state vector.

With the vector signals defined by:

$$\mathbf{x}_k = \begin{bmatrix} \Delta x_{RX12,k} \\ \boldsymbol{\varepsilon}_{DGPS,k} \end{bmatrix} \qquad \mathbf{u}_k = \begin{bmatrix} v_{RX12,x,k} \end{bmatrix} \qquad \mathbf{z}_k = \begin{bmatrix} \Delta x_{PR,k} \end{bmatrix} \qquad \mathbf{w}_k = \begin{bmatrix} w_{CRR,x,k} \\ w_{PR,x,k} \end{bmatrix} \tag{5.10.15}$$

The constant matrices are defined by:

$$\mathbf{A}_{\mathrm{DGPS}} = \begin{bmatrix} 1 & 0 & 0 \\ 0 & 1 & 1 \\ 0 & -\Omega_n^2 & \beta \end{bmatrix} \qquad \mathbf{B}_{\mathrm{DGPS}} = \begin{bmatrix} 1 \\ 0 \\ 0 \end{bmatrix} \qquad \mathbf{G}_{\mathrm{DGPS}} = \begin{bmatrix} 1 & 0 \\ 0 & k_1 \\ 0 & k_2 \end{bmatrix} \qquad \mathbf{C}_{\mathrm{DGPS}} = \begin{bmatrix} 1 & 1 & 0 \end{bmatrix}$$

$$\mathbf{Q}_{\mathrm{DGPS,k}} = \begin{bmatrix} \sigma^2_{\mathrm{CRR}} & 0 \\ 0 & \sigma^2_{\mathrm{DGPS}} \end{bmatrix} \tag{5.10.16}$$

Their are many implementations of the Kalman filter (Ref. 32, chapter 2.3). In the “A Priori Recursive Formulation” (Ref. 32, Table 2.3-3) the time and measurement updates are combined. This gives a compact filter equation with only one filter state update at each sample time. It is however more flexible to use separate measurement and time updates. This is due to the fact that if some measurements are missing due to measurement problems (in this case missing PR DGPS position updates), the filter can continue to provide state estimates for some time using just the time updates. For this reason we will implement the kalman filter using separate time and measurement updates.

Time update (Ref. 32, Table 2.3-1):

$$\begin{aligned} \mathbf{P}^-_{\mathrm{k+1}} &= \mathbf{A}_{\mathrm{DGPS}}\mathbf{P}_{\mathrm{k}}\mathbf{A}^T_{\mathrm{DGPS}} + \mathbf{G}_{\mathrm{DGPS}}\mathbf{Q}_{\mathrm{DGPS,k}}\mathbf{G}^T_{\mathrm{DGPS}} \\ \hat{\mathbf{x}}^-_{\mathrm{k+1}} &= \mathbf{A}_{\mathrm{DGPS}}\hat{\mathbf{x}}_{\mathrm{k}} + \mathbf{B}_{\mathrm{DGPS}}\mathbf{u}_{\mathrm{k}} \end{aligned} \tag{5.10.17}$$

Where $\hat{\mathbf{x}}^-_{\mathrm{k+1}}$ is the a priori state estimate and $\mathbf{P}^-_{\mathrm{k+1}}$ is the calculated a priori state estimate covariance.

Kalman gain (Ref. 32, Table 2.3-2):

$$\mathbf{K}_{\mathrm{k+1}} \equiv \mathbf{P}^-_{\mathrm{k+1}}\mathbf{C}^T_{\mathrm{DGPS}}(\mathbf{C}_{\mathrm{DGPS}}\mathbf{P}^-_{\mathrm{k+1}}\mathbf{C}^T_{\mathrm{DGPS}} + \mathbf{R}_{\mathrm{DGPS,k+1}})^{-1} \tag{5.10.18}$$

Measurement update (Ref. 32, Table 2.3-2):

$$\begin{aligned} \hat{\mathbf{x}}_{\mathrm{k+1}} &= \hat{\mathbf{x}}^-_{\mathrm{k+1}} + \mathbf{K}_{\mathrm{k+1}}(\mathbf{z}_{\mathrm{k+1}} - \mathbf{C}_{\mathrm{DGPS}}\hat{\mathbf{x}}^-_{\mathrm{k+1}}) \\ \mathbf{P}_{\mathrm{k+1}} &= (\mathbf{I} - \mathbf{K}_{\mathrm{k+1}}\mathbf{C}_{\mathrm{DGPS}})\mathbf{P}^-_{\mathrm{k+1}} \end{aligned} \tag{5.10.19}$$

Where $\hat{\mathbf{x}}_{\mathrm{k+1}}$ is the a posteriori state estimate and $\mathbf{P}_{\mathrm{k+1}}$ is the calculated a posteriori state estimate covariance.

Since the Kalman filter is time varying it is important for the correct function of the filter to initialize the estimated state vector and covariance with realistic values. Before the first measurement is taken, we have no knowledge of the differential position. Thus in principle the variance of the estimated position is infinite. This is unfortunate for implementation of the filter, since the Kalman gain will become infinite as well (see Eq. 5.10.18).

This problem can be effectively resolved by using the first DGPS position measurement as the initial state estimate of the position and the corresponding SNR predicted variance as the variance of the position estimate. Since the DGPS measurement error is unknown when the filter is started, the expected error filter state vector $\boldsymbol{\varepsilon}_{\mathrm{DGPS},0}$ is zero. This gives the following expression for the initial state estimate:

$$\hat{\mathbf{x}}_0 = \begin{bmatrix} \Delta x_{\mathrm{PR},0} \\ 0 \\ 0 \end{bmatrix} \tag{5.10.20}$$

However according to Eq. 5.10.4, the first state of $\boldsymbol{\varepsilon}_{\mathrm{DGPS}} = [\Delta x_e \ \Delta v_e]^T$ is equal to the predicted DGPS measurement error, thus the variance of $(\Delta x_e)_0$ is equal to the a priori SNR weigthed DGPS measurement variance. The state Δv_e is approximately equal to the DGPS measurement error rate. From the preceding analysis we already know that the majority of the DGPS measurement error has a very low frequency distribution.

The initial covariance of the error filter states can be determined by assuming that the initial covariance is equal to the steady state covariance of the error filter without measurement updates. This steady state error filter covariance can be determined using the matrix equivalent of Eq. 5.10.9. However since we have already implemented a numerical simulation of the Kalman filter, we can use a simplified version of this to attain the steady state value of the error filter covariance without measurement updates for a unit value DGPS measurement noise $(\sigma_{\Delta x_e} = 1)$. The resulting initial value of the error filter covariance can then be determined as:

$$\left(\mathbf{P}_{\boldsymbol{\varepsilon}_{\mathrm{DGPS}}}\right)_0 = \begin{bmatrix} 1.0003 & -0.0049 \\ -0.0049 & 0.0009 \end{bmatrix} \sigma^2_{\Delta x_{\mathrm{PR},0}} \tag{5.10.21}$$

Notice that the variance of $(\Delta x_e)_0$ is not exactly equal to $\sigma^2_{\Delta x_{\mathrm{PR},0}}$ because of rounding errors in the filter coefficients from Table 5.4.

This gives the following result for the covariance $\mathbf{P}_0$ of complete initial state vector estimate $\hat{\mathbf{x}}_0$:

$$\mathbf{P}_0 = \begin{bmatrix} 1 & -0.99 & 0 \\ -0.99 & 1 & -4.9\times10^{-3} \\ 0 & -4.9\times10^{-3} & 0.9\times10^{-3} \end{bmatrix} \sigma^2_{\Delta x_{\mathrm{PR},0}} \tag{5.10.22}$$

This completes the kinematic DGPS position filter design.

5.11 Performance of the complete DGPS system

We can now determine and analyse the performance of the kinematic Kalman filter DGPS system designed above. For the purpose of guiding an UAV to an autonomous precision landing on a small runway, the most important DGPS specifications are:

- What is the risk of exceeding a specified horizontal and vertical error?
- Can we predict the risk of exceeding a specified error at any one time?
- What is the availability of the complete (kalman filtered) DGPS system?

Using the measured DGPS raw data (pseudoranges and carrier phases) and the just designed Kalman filter, we will try to answer these questions below.

In order to get a qualitative understanding of the filter performance, we will start by looking at a randomly picked short time series of the kalman filter states and covariance. The filter is initialized at the beginning of the run as described in the previous section. Notice that this is not a “simulation”, since the filter is run on actual DGPS measurements collected in the short baseline test setup described previously.

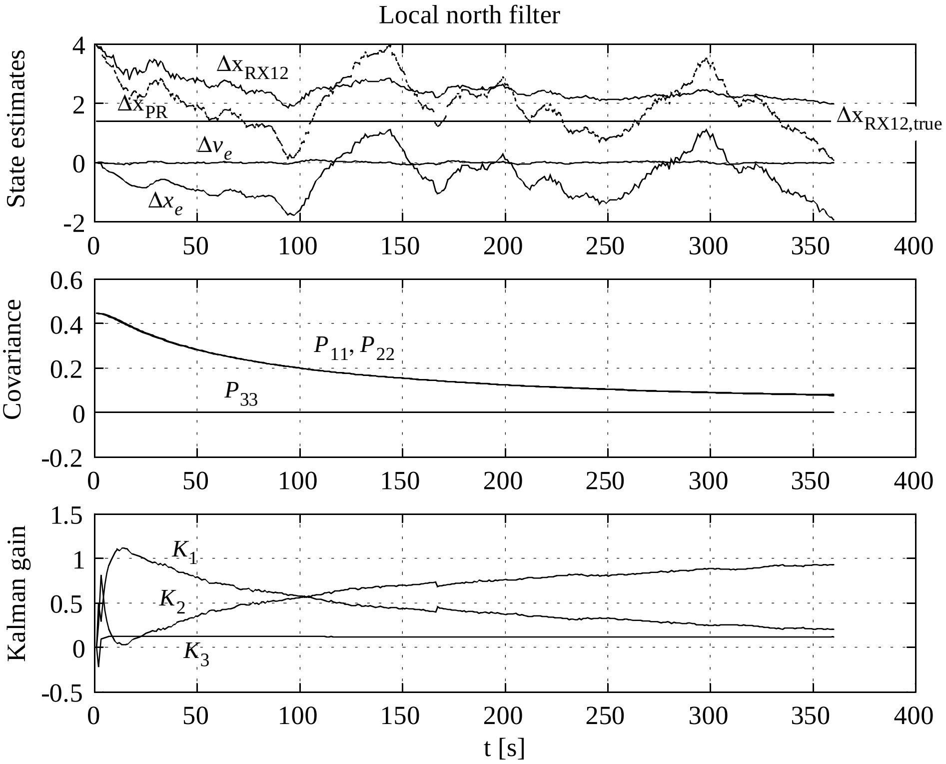

FIGURE 5.16 North-south Kalman filter run using actual measurements.

From the kalman filter state trajectory it is apparent that at the very beginning of the time series, the (differential) position estimate Δx_{RX12} follows the “measured” position Δx_{PR} quite closely. However as more measurements arrive, the position estimate quite nicely approaches the true position $\Delta x_{RX12,true}$, while the estimated measurement error Δx_e captures the noise present in Δx_{PR}. It is also apparent that the estimated (a priori) covariance P_{11} of Δx_{RX12} follows a realistic trajectory, since it has a long “time constant” which is compatible with the low frequency noise content of the DGPS measurement error shown in Figure 5.15. Similarly, the Kalman gain K_1 (feedback to Δx_{RX12}) decreases with time after a short transient, while the Kalman gain K_2 (feedback to Δx_e) increases with time. The general conclusion from Figure 5.16 is thus that the Kalman seems to be working as desired.

The state estimate and DGPS measurement errors for all directions (north-south, east-west and up-down) for this dataset are shown below:

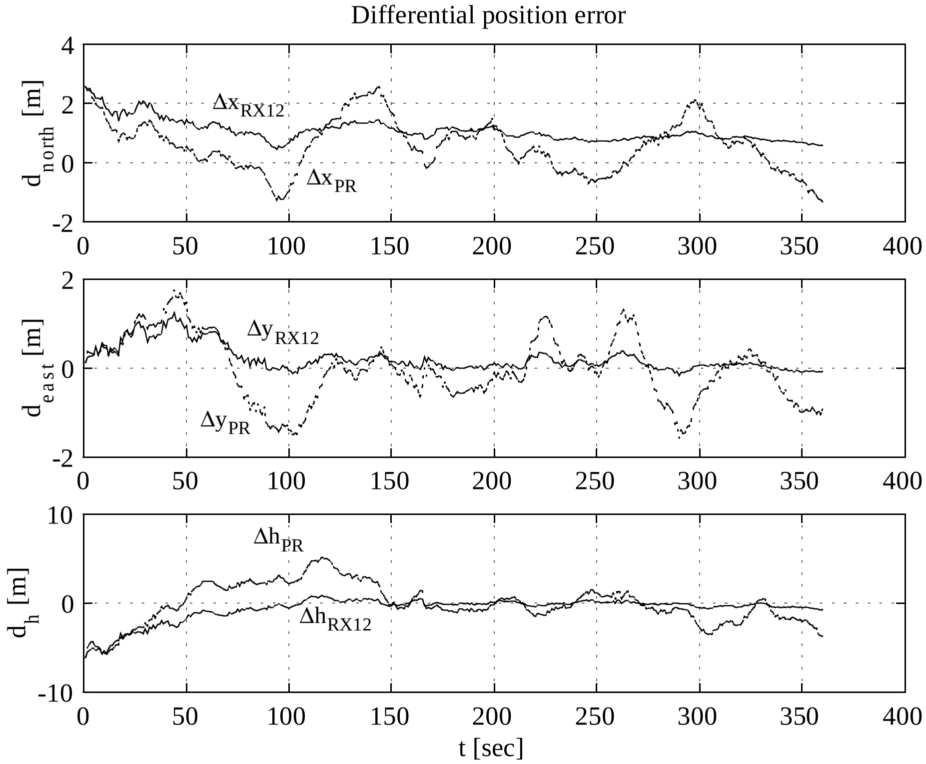

FIGURE 5.17 Kalman filter DGPS measurement input and position estimate errors.

Basically Figure 5.17 shows that the qualitatively correct behaviour of the Kalman filter is also valid for the other directions.

We will now look at a longer time span of one hour (3600 sec.) in order to see the asymptotic behaviour of the Kalman filter:

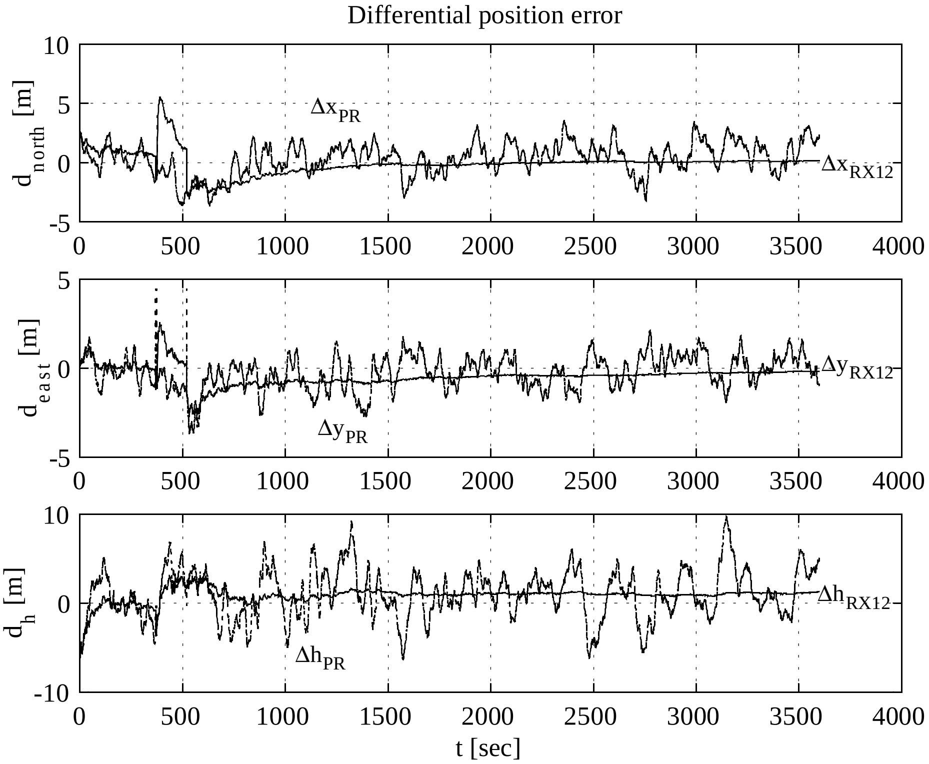

FIGURE 5.18 Kalman filter DGPS measurement input and position estimate errors.

Figure 5.18 confirms that for long time spans the Kalman filter has excellent DGPS measurement error rejection. Notice the discontinueties at around 400 sec. and again at around 500 sec. This is due to lack of a sufficient number of valid phase measurements to perform a velocity calculation. In this simple implementation of the filter this results in a reset of the Kalman filter on the next sample. However when used in conjunction with an inertial navigation system (INS), the velocity estimate of the INS can be used temporarily instead of the carrier phase measurements to update the DGPS Kalman filter during brief outages of DGPS measurements. This can prevent the temporary loss of precision caused by a Kalman filter reset.

In a practical UAV navigation and guidance application of the DGPS Kalman filter one can not in general afford to wait for several thousand seconds before using the position estimates. In practice we want to know the available precision within a few minutes time from a Kalman filter reset. Figure 5.19 below is thus a run of the same data as in

Figure 5.18, but now we have forced a Kalman filter reset for each 500 sec. time interval (not that the measured DGPS position is omitted for clarity):

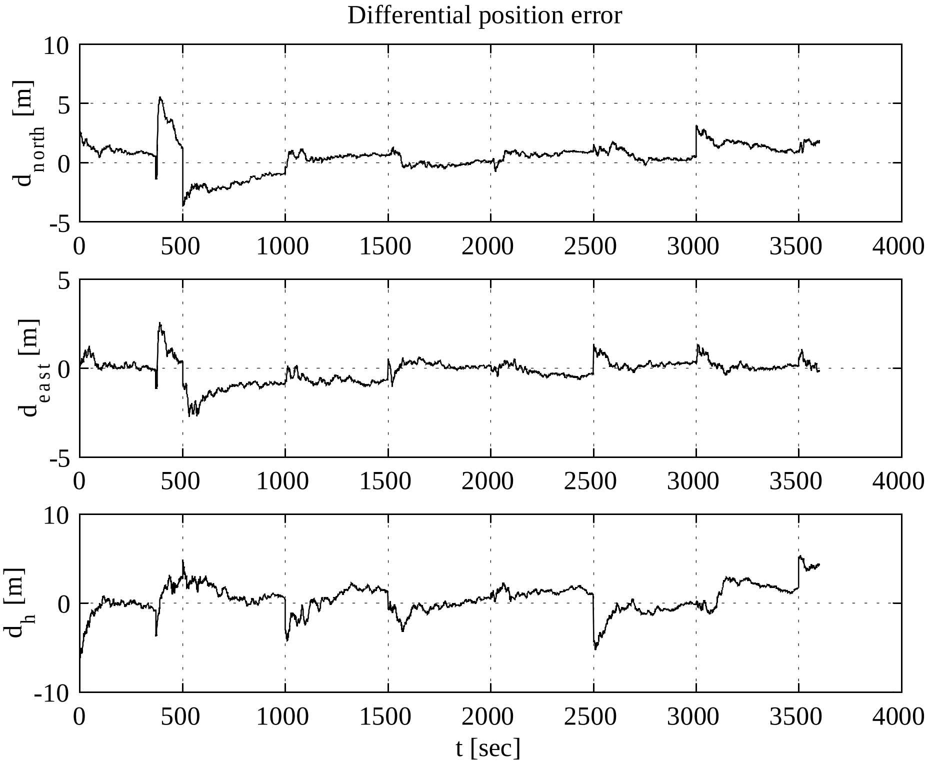

FIGURE 5.19 Kalman filter performance with reset and reinitialization for every 500 sec.

It is apparent from Figure 5.19 that the Kalman filter does indeed converge towards a small error after every reset.

In order to quantify the performance of the Kalman filter it is however necessary to perform a more stringent analysis of the results. Since the Kalman filter predicts the instantaneous position estimate variance, it is logical to try to correlate the actual measured estimate error variance with the predicted (a priori) value.

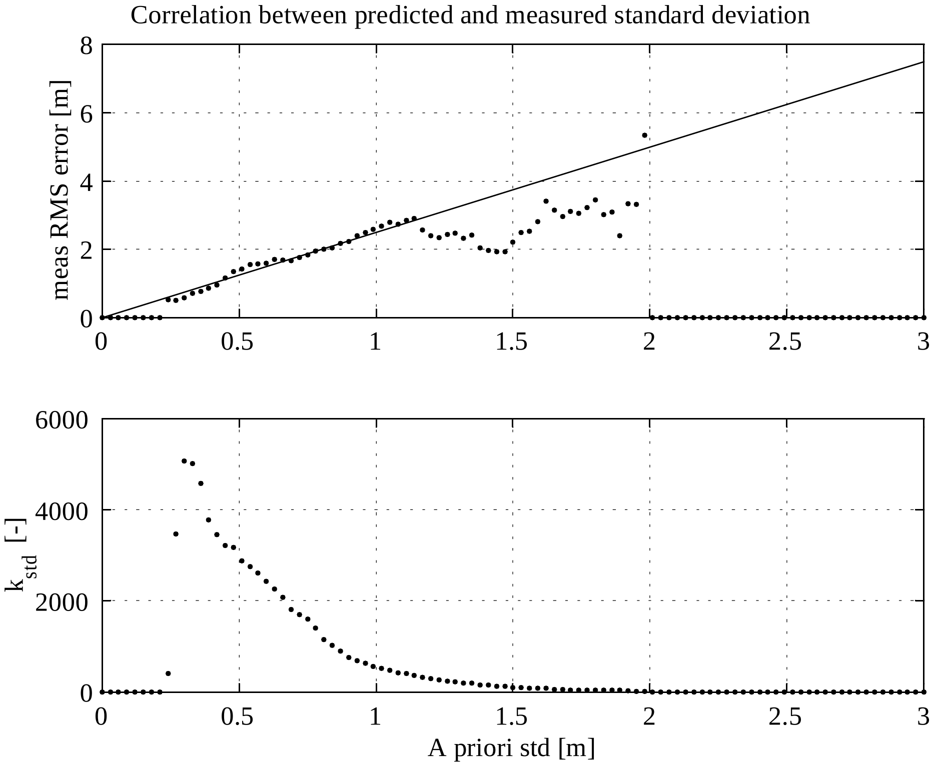

FIGURE 5.20 Correlation between predicted a priori and measured standard deviations.

Figure 5.20 is based on the same 6 hour measurement interval as in Figure 5.13 and can thus be used to show the difference between the SNR weigthed DGPS error statistics and the Kalman filtered error statistics. Notice that the Kalman filter is forced to reset every 500 sec., just as in Figure 5.19. The first observation is that the linear correlation (given by Eq. 5.9.20) between the predicted and measured standard deviations is still valid:

$$\sigma_{\text{Kalman}} \approx c_{\text{DGPS}}\sigma_{\text{Kalman,apriori}} \qquad c_{\text{DGPS}} = 2.5 \tag{5.11.1}$$

However when compared to the unfiltered case, it is apparent that the relative number of “measurements” with a priori standard deviations larger then about 1.5 m is much smaller for the Kalman filter. This is very important because it indicates that the Kalman filter is effective in reducing the occurrence of extreme errors, which could be catastrophic during autonomous landing of an UAV.

Since the error statistics of the Kalman filter is obviously very nonstationary (i.e. a decreasing error variance as function of time) there is really not any stringent statistical meaning in a time invariant error probability analysis. In spite of this fact, the user of the system still needs to know the expected error statistics of the Kalman filter estimats.

To satisfy this desire we will analyse the estimation errors as functions of time after a reset/reinitialization of the Kalman filter.

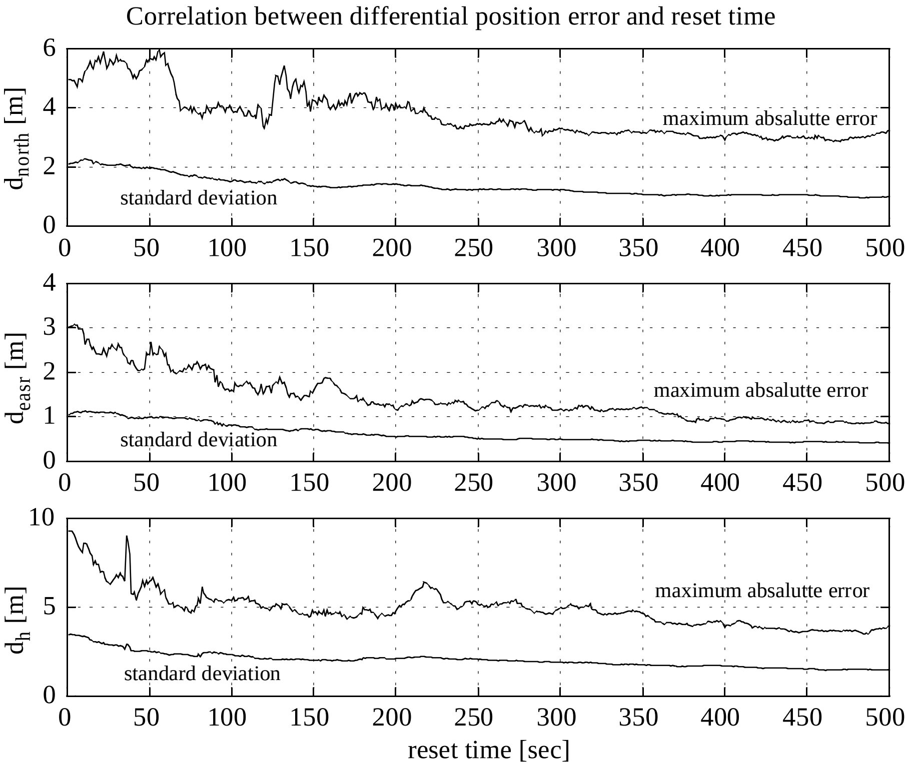

FIGURE 5.21 Correlation between differential position error and reset time.

Figure 5.21 confirms that the general differential position error trend is for decreasing error with increasing time from filter reset. It is apparent that both the standard deviation and maximum errors become more smooth as the reset time increases. This is due to the smoothing properties of the Kalman filter. If one where to choice an appropriate “warm up” time for the Kalman filter, it seems that 240 seconds (4 minutes) could be a good “round” compromise between system availability and error minimization.

What we really want is to be able to determine the probability of exceeding a certain error given the predicted differential position estimate standard deviation from the Kalman filter. Figure 5.20 provides a partial answer to this problem, however if the user wants to estimate the probability of exceeding a certain error we really need to know the shape of the probability distribution function (pdf). This however requires a much longer dataset for statistical significance due to the observed temporal correlation of the DGPS errors. Until such an analysis is performed we can use Figure 5.21 as a guideline.

5.12 DGPS conclusion:

By statistical analysis of double difference pseudorange measurement errors it has been shown that the worst errors are probably caused by multipath. It is also demonstrated that the errors are correlated to the indicated signal to noise ratio. This information is used along with knowledge of the temporal correlation of the pseudorange errors to design a kinematic Kalman filter which significantly improves the accuracy of the DGPS system.

5.13 References

24.GPS book.

25.“Global Positioning System, Standard Positioning Service, Signal Specification”, DOD, June 2, 1995.

26.“Global Positioning System, Standard Positioning Service, Performance Standard”, Assistant Secretary of Defence for Command, Control, Communications, and Intelligence, October, 2001.

27.G.Chritiansen, E.Both,P.Ø.Sørensen:”Mekanik”,Laboratoriet for Teknisk Fysik, Danmarks Tekniske Højskole, 1990.

28.S.Boel Pedersen:”Introduktion til signalanalyse - 2. Signaler med endelig effekt’, Laboratoriet for Elektronik, februar 1992.

29.Kurt Andersen:”Samplede Regulerings Systemer - Bind 1”, Servolaboratoriet, 1982.

30.Per Christian Hansen:”Hæfte 53 - kurvetilpasning”, Numerisk Institut, DTU.

31.E. Mærsk-Møller, Poul Frederiksen:”Landmåling Elementudjævning”, Institut for Landmåling og Fototgrammetri, Januar 1984.

32.F.L.Lewis:”Optimal Estimation, with an introduction to stochastic control theory”,John Wiley & Sons, 1986.

33.F.L.Lewis:”Applied Optimal Control & Estimation, Digital Design & Implementation”,Prentice Hall and Digital Signal Processing Series, Texas Instruments, 1992.

Chapter 6

Inertial Navigation System

6.1 Overview of system hardware

The Inertial Navigation System (INS) hardware consists of a self contained instrument comprising 3 independent rate gyro sensors and 2 independent 2 axis acceleration sensors. The rate gyro sensors are arranged in a nominally 3 dimensional ortogonal configuration, while the acceleration sensors are arranged in two nominally ortogonal planes. Thus there is an acceleration measurement redundancy in one direction. In addition to the primary inertial sensors, there are 3 auxiliary temperature sensors, one fixed to each rate gyro sensor, in close thermal contact with the gyro sensor.

The instrument has dedicated Analog to Digital (A/D) converters and analog signal conditioning circuits for all sensors. The analog signal conditioning characteristics for each type of sensor is given below:

Sensor	Principle	Analog interface	Electrical bandwidth[a]	Nominal Sensitivity[b]
-	-	-	f_{BW}	-
Rate gyro	Vibrating beam	Differential	72Hz	~0.7mV/(deg/s)
Temperature	PT100	Bridge	770Hz	~30mV/K
Acceleration	Mass/spring with capacitive pick-up	Single ended	1540Hz	~20mV/(m/s^2)

Tabel 6.1Analog sensor signal conditioning.

---

[a] May exceed sensor bandwidth.

[b] At output of analog signal conditioning circuit.

The A/D conversion process is performed with A/D converters with the following nominal characteristics:

Sensor	A/D range	Ideal precision	Resolution	Physical resolution
Rate gyro	4V	16 bits	0.06mV	~0.1deg/s
Temperature	4V	12 bits	1mV	~0.04K
Acceleration	4V	12 bits	1mV	~0.05m/s^2

Tabel 6.2A/D sensor signal processing.

The results of the A/D conversion is loaded serially into the onboard 16-bit Fujitsu microcontroller. This microcontroller performs all the digital signal processing to implement an inertial navigation system. This includes prefiltering, temperature compensation, orthogonalization and state estimation. In addition the microcontroller handles communication to the rest of the system using the build in Controller Area Network (CAN) interface. The rest of this document describes in general terms the mathematical models of each sensor and the digital signal processing algorithms involved in obtaining an estimate of the inertial state of the vehicle which uses this INS.

6.2 Sensor models

Below the principles and mathematical models of each type of sensor in the INS is described.

6.2.1 Rate gyro with temperature sensor

Each rate gyro sensor element is a model ENC-03JA vibrating rate gyro transducer from Murata. The principle of operation is that a beam with free-free boundary conditions is forced to vibrate at is fundamental natural transverse eigenfrequency using integral piezo elements. The plane of forced vibration is fixed to the sensor housing. Any applied rotation of the sensor housing will give rise to coriolis forces that will in turn produce an out of plane vibratory deflection. This out of plane vibration is picked up by piezo elements as a differential AC voltage that is subsequently demodulated and output as a differential DC voltage which is ideally proportional to the rate of rotation around the axis of sensitivity.

In reality there are some major error sources in the transducer. Most importantly, temperature drift in the demodulating electronics contribute to drift in sensitivity and particularly in the offset (zero rate output). Secondly the axis of sensitivity may not exactly match the ideal direction, which results in cross coupling sensitivity to off axis rotation. This is further compounded by geometrical errors with respect to the nominal sensor orientation in relation to the INS coordinate system.

The mathematical model of each rate gyro sensor element, that will be used in this thesis is given below:

$$\Delta V_{out,\,i} = \omega_i c_i(T_i) + V_i(T_i) + v_i(t) \tag{6.2.1}$$

Where ω_i is the rate of rotation around the (a priori unknown) axis of sensitivity, $c_i(T_i)$ is the temperature dependent sensitivity, $V_i(T_i)$ is the temperature dependent offset, $v_i(t)$ is the measurement noise process and T_i is the sensor temperature. The subscript “i” is used to indicate that these quantities are specific to sensor number “i”.

As can be seen, this simple sensor model does not account for nonlinearities in sensitivity or for the sensor frequency response.

As a model for the sensors temperature response to the environment, the following parallel first order thermal model will be used:

$$\begin{bmatrix} \dot{T}_i \\ \dot{T}_{mi} \end{bmatrix} = \begin{bmatrix} -\dfrac{1}{\tau_T} & \dfrac{1}{\tau_{\Delta T}} \\ \dfrac{1}{\tau_{\Delta T}} & -\dfrac{1}{\tau_{Tm}} \end{bmatrix} \begin{bmatrix} T_i \\ T_{mi} \end{bmatrix} + \begin{bmatrix} \dfrac{1}{\tau_T} \\ \dfrac{1}{\tau_{Tm}} \end{bmatrix} T_a \tag{6.2.2}$$

Where T_{mi} is the measured sensor temperature and T_a is the ambient temperature. The thermal time constants τ_T and τ_{Tm} represents the time constants for the rate gyro sensor and the temperature sensor respectively. These are with respect to ambient temperature changes. The thermal time constant $\tau_{\Delta T}$ represents the mutual time constant between the rate gyro sensor and the temperature sensor. Despite the fact that these time constants may vary from sensor to sensor, this will be neglected in this thesis, for ease of analysis.

The design and mounting of each rate gyro / temperature sensor transducer has been optimized to give a high mutual thermal coupling and low coupling to the ambient environment. This gives the following approximate relationships between the thermal time constants:

$$\tau_T \cong \tau_{Tm} \qquad \tau_T \gg \tau_{\Delta T} \tag{6.2.3}$$

So that the thermal time constants with respect to ambient temperature changes are roughly the same for both rate gyro sensor and temperature sensor, while the mutual time constant is more then an order of magnitude smaller.

The net result is that the measured temperature will track the actual rate gyro temperature closely even with large and rapid changes in ambient temperature.

When power is applied to the INS, the thermal equilibrium of both the rate gyro sensor and the temperature sensor element will change due to heat dissipation in both sensors. Since the net power dissipation and thermal mass are not exactly the same for both elements, a transient temperature error between the elements will be generated. After a certain time of the order of the mutual thermal time constant $\tau_{\Delta T}$, the two sensor elements will attain a constant temperature difference. To obtain accurate temperature compensation of the rotation rate using Eq. 6.2.1, it is advisable to wait for a certain warm-up time, after INS turn on, before using the gyro measurements. After this warm-up time we may use Eq. 6.2.1 to compensate the gyro sensor for temperature drift, by using the measured sensor temperature T_{mi} instead of the actual sensor temperature T_i. This works because we can assume from the above that the temperature difference T_i-T_{mi} is almost constant for the entire ambient temperature range of the INS.

The rate gyro sensor process noise ($v_i(t)$) statistics is not known exactly a priori due to the difficulty of measuring small analog noise signals independently of the measuring equipment. Thus this will be identified from in situ measurements using the INS A/D converter. The same system identification process is used to determine the unknown sensitivity and offset functions of Eq. 6.2.1.

6.2.2 Acceleration sensors

Each acceleration sensor element is a model ADXL210 two axis $\pm 10G$ micro machined mass/spring sensor with capacitive sensing, from Analog Devices. The principle of operation is that a small mass suspended in springs is deflected by accelerations, this deflection is then measured using a variable comb shaped capacitor between the fixed and moving parts of the sensor. The maximum bandwidth of the sensor is according to the data sheet approximately 10kHz (Ref. 35). The actual implemented bandwidth can be adjusted to the application by using suitable filtering capacitors. In the INS, filtering capacitors with a nominal value of 100nF are used, giving a nominal -3dB bandwidth of 50Hz. The measurement noise of the acceleration sensor is according to the datasheet composed of a white noise component and a thermal drift component. The white noise component is filtered by the low pass filter, thus giving a bandwidth limited white noise component. The thermal drift “noise” naturally depends on the ambient environment of the INS. Since the sensors are physically shielded from the environment by the mounting method, the thermal drift can be assumed to be a very low frequency noise component.

6.3 Instrument model

The complete instrument is composed of 3 rate gyro sensors and 2 two axis accelerometers, ideally giving three independent measurements of angular rate and acceleration. In reality the sensors are not oriented exactly along the ideal ortogonal axes of the instrument, this gives rise to cross coupling between the sensor outputs. If we assume that the instrument axes $(\mathbf{e}_x,\mathbf{e}_y,\mathbf{e}_z)_{INS}$ constitute a right hand oriented cartesian coordinate system and that each sensor has a specific direction of maximum sensitivity, we may relate the real scalar output of each sensor to the ideal vector output of the combination, by using an appropriate transformation.

For the rate gyro sensors:

$$\boldsymbol{\omega}_{INS} = \begin{bmatrix} \omega_x \\ \omega_y \\ \omega_z \end{bmatrix}_{INS} = \mathbf{M}_{gyro} \begin{bmatrix} \omega_1 \\ \omega_2 \\ \omega_3 \end{bmatrix}_{sensor} \tag{6.3.1}$$

Where ω_{INS} is the angular rate vector for the INS and $(\omega_1,\omega_2,\omega_3)$ is the scalar outputs from the individual physical sensors, corrected for temperature drift and other nonlinarieties. The 3x3 matrix $\mathbf{M}_{gyro}$ defines the linear transformation between sensor axes and INS axes.

We have implicitly assumed that a linear relationship exists between the (linearized and temperature corrected) sensor outputs and the INS angular rate vector. It is also implied that the sensor axes of sensitivity is fixed in the INS coordinate system.

Similarly we may express the transformation between measured accelerations and the INS acceleration vector as:

$$\mathbf{a}_{INS} = \begin{bmatrix} a_x \\ a_y \\ a_z \end{bmatrix}_{INS} = \mathbf{M}_{acc} \begin{bmatrix} a_1 \\ a_2 \\ a_3 \\ a_4 \end{bmatrix}_{sensor} \tag{6.3.2}$$

Where $\mathbf{a}_{INS}$ is the acceleration vector in the moving INS coordinate system and (a_1,a_2,a_3,a_4) is the scalar outputs from the individual physical sensors, corrected for temperature drift and other nonlinearities. Here the 3x4 matrix $\mathbf{M}_{acc}$ defines the transformation between the acceleration sensor outputs and the INS coordinate system. Notice that $\mathbf{a}_{\mathrm{INS}}$ includes the apparent effect of the acceleration of gravity “g”, since it is most practical to correct for the orientation of the INS with respect to earth after performing the orthogonalization.

6.4 Kinematic model of INS

Both the INS angular rate vector ω_{INS} and acceleration $\mathbf{a}_{\mathrm{INS}}$ are referenced to the moving frame of the INS coordinate system. In order to use these measurements for navigation and guidance, they must be related to an appropriate global coordinate system. In the following, the curvilinear earth coordinate system $(\mathbf{e}_x,\mathbf{e}_y,\mathbf{e}_z)_e$, will be assumed to be such a system. This coordinate system, for short the earth coordinate system, is a coordinate system that is everywhere (on the or near the surface of the earth) oriented in such a way that the x-direction points towards the geographical north, the y-direction towards the geographical east and the z-direction points straight down. In the light of the required accuracy, the following simplifying *assumptions / approximations* will be made with regards to the earth coordinate system:

1. The earth coordinate system is an inertial coordinate system.
2. The earth coordinate system is a locally cartesian coordinate system with negligible curvature.
3. No distinction between the local gravity vector direction and the direction to the center of the earth.
4. The earth coordinate system is right hand oriented.

Using some of these assumptions, we can express the transformation between the earth fixed coordinate system and the INS system as a translation and a rotation:

$$\begin{bmatrix} x \\ y \\ z \end{bmatrix}_{\mathrm{earth}} = \mathbf{M}_{\mathrm{I2V}} \begin{bmatrix} x \\ y \\ z \end{bmatrix}_{INS} + \mathbf{P}_{\mathrm{INS}} \qquad (6.4.1)$$

Where $(x,y,z)_{\mathrm{earth}}$ is any vector expressed in earth coordinates and $(x,y,z)_{\mathrm{INS}}$ is the *same* vector expressed in INS coordinates. $\mathbf{M}_{\mathrm{I2V}}$ is a 3x3 transformation matrix that accounts for the relative orientation of the two coordinate systems, while $\mathbf{P}_{\mathrm{INS}}$ is the position of the INS coordinate system origo in earth coordinates.

Since the transformation matrix $\mathbf{M}_{\mathrm{I2V}}$ defines a transformation between two cartesian right hand oriented coordinate systems, the reverse transformation $\mathbf{M}_{\mathrm{V2I}}$ is equal to the transpose of $\mathbf{M}_{\mathrm{I2V}}$ (Ref. 34, p. 11):

$$\mathbf{M}_{\mathrm{V2I}} \equiv \mathbf{M}_{\mathrm{I2V}}^{-1} = \mathbf{M}_{\mathrm{I2V}}^{T} \qquad (6.4.2)$$

6.4.1 Orientation of INS

In general a 3x3 matrix has 9 independent scalar parameters, however the orientation of the INS with respect to the earth coordinate system can be described by using only 3

Degrees Of Freedom (DOF). There are many ways to choice these degrees of freedom, but 2 properties are important for the proper choice:

- It can be shown that any 3 parameter description of the orientation, has singularities at certain orientations. It is thus an advantage if possible to place the singularities at orientations that are rarely encountered.
- It is an advantage to use parameters that are intuitively understood.

For these reasons, we will use the following 3 degrees of freedom for describing the INS orientation relative to the earth coordinate system:

- The azimuth angle θ_a, between the INS x-axis and the earth x-axis (true north), using a positive rotation around the z-axis. This corresponds to the generally used definition of the “heading”.
- The elevation angle θ_e, between the INS x-axis and the horizon, using a positive rotation around the y-axis. This is sometimes called the “pitch” angle.
- The roll angle θ_r, positive around the x-axis.

The rotations are done in the order; azimuth, elevation and lastly roll. The above mentioned singularities are located at orientations corresponding to $\theta_e = \pm 90^o$, where it is impossible to distinguish between azimuth and roll. However for the present UAV application of this INS, these orientations are really not important.

It will be assumed that the angles have the following ranges:

- $\theta_a \in [0{,}360^o]$, $\theta_e \in \pm 90^o$ and $\theta_r \in \pm 180^o$.

And similarly when expressed in radians.

For a rotation around the z-axis of a cartesian right hand oriented coordinate system, the rotation matrix for a rotation angle θ, is given by (Ref. 34):

$$\mathbf{M}_1(\theta) = \begin{bmatrix} \cos(\theta) & \sin(\theta) & 0 \\ -\sin(\theta) & \cos(\theta) & 0 \\ 0 & 0 & 1 \end{bmatrix} \tag{6.4.3}$$

For a rotation of θ, around the y-axis:

$$\mathbf{M}_2(\theta) = \begin{bmatrix} \cos(\theta) & 0 & -\sin(\theta) \\ 0 & 1 & 0 \\ \sin(\theta) & 0 & \cos(\theta) \end{bmatrix} \tag{6.4.4}$$

While for a rotation of θ, around the x-axis, the transformation is:

$$\mathbf{M}_3(\theta) = \begin{bmatrix} 1 & 0 & 0 \\ 0 & \cos(\theta) & \sin(\theta) \\ 0 & -\sin(\theta) & \cos(\theta) \end{bmatrix} \tag{6.4.5}$$

The complete transformation between vehicle coordinates and INS coordinates can then be expressed as:

$$\mathbf{M}_{\mathrm{V2I}} = \mathbf{M}_{\mathrm{V2I}}(\theta_r, \theta_e, \theta_a) = \mathbf{M}_3(\theta_r)\mathbf{M}_2(\theta_e)\mathbf{M}_1(\theta_a) \qquad (6.4.6)$$

Notice that the order of the rotation matrices are reversed compared to the order that the rotations are performed.

The inverse transformation can then be determined as:

$$\mathbf{M}_{\mathrm{I2V}} = \mathbf{M}^T_{\mathrm{V2I}} = \mathbf{M}_{\mathrm{I2V}}(\theta_r, \theta_e, \theta_a) \qquad (6.4.7)$$

For computational convenience, we may want to have explicit expressions for these transformations. These are given in Appendix G

Since θ_a, θ_e and θ_r will be used as states to describe the orientation of the INS, we need expressions relating the derivatives of these angles to the INS angular rate $\omega = (\omega_x, \omega_y, \omega_z)$, in order to construct a state space model of the INS. What we actually need is a relation of the type:

$$(\dot{\theta}_r, \dot{\theta}_e, \dot{\theta}_a) = f(\theta_r, \theta_e, \theta_a, \omega_x, \omega_y, \omega_z) \qquad (6.4.8)$$

Where “f” is an algebraic $\Re^6 \rightarrow \Re^3$ function.

In Appendix H, Eq. H.10 the relation between derivatives of the Euler angles and the INS angular rate is determined as:

$$\dot{\theta} = \begin{bmatrix} \dot{\theta}_r \\ \dot{\theta}_e \\ \dot{\theta}_a \end{bmatrix} = \begin{bmatrix} 1 & \sin(\theta_r)\tan(\theta_e) & \cos(\theta_r)\tan(\theta_e) \\ 0 & \cos(\theta_r) & -\sin(\theta_r) \\ 0 & \dfrac{\sin(\theta_r)}{\cos(\theta_e)} & \dfrac{\cos(\theta_r)}{\cos(\theta_e)} \end{bmatrix} \begin{bmatrix} \omega_x \\ \omega_y \\ \omega_z \end{bmatrix} = \mathbf{M}_{\mathrm{Euler}}(\boldsymbol{\theta})\boldsymbol{\omega} \qquad (6.4.9)$$

Where $\mathbf{M}_{\mathrm{Euler}}$ is the orientation dependent “transformation” between INS angular rates ω and euler rates $\dot{\boldsymbol{\theta}}$. The euler angle vector θ is here defined as $\boldsymbol{\theta} \equiv (\theta_r, \theta_e, \theta_a)$.

6.4.2 Velocity and position

In general the position and velocity of the INS in earth coordinates can be determined as the temporal integral of the true acceleration in earth coordinates:

$$\ddot{\mathbf{P}}_{\mathrm{INS}} = \dot{\mathbf{V}}_{\mathrm{INS,e}} = \mathbf{a}_{\mathrm{INS,e}} \qquad \mathbf{P}_{\mathrm{INS}}(t = t_0) = \mathbf{P}_0 \qquad \mathbf{V}_{\mathrm{INS,e}}(t = t_0) = \mathbf{V}_0 \quad (6.4.10)$$

Where the subscript “e” on the velocity and acceleration vectors refers to earth coordinates.

The acceleration in earth coordinates can be determined from the apparent acceleration in INS coordinates, by using the INS to vehicle transformation matrix $\mathbf{M}_{\mathrm{I2V}}$:

$$\mathbf{a}_{\mathrm{INS,e}} = \begin{bmatrix} a_x \\ a_y \\ a_z \end{bmatrix}_{INS,\,e} = \mathbf{M}_{\mathrm{I2V}}\mathbf{a}_{\mathrm{INS}} - \begin{bmatrix} 0 \\ 0 \\ 1 \end{bmatrix} g = \mathbf{M}_{\mathrm{I2V}}\mathbf{a}_{\mathrm{INS}} + \mathbf{M}_g g \qquad (6.4.11)$$

The last term containing the acceleration of gravity “g”, corrects for the measured apparent acceleration due to gravity. Where $\mathbf{M}_{\mathrm{g}}$ is defined as $\mathbf{M}_g \equiv -\begin{bmatrix} 0 & 0 & 1 \end{bmatrix}^T$.

6.4.3 Complete kinematic model of INS

The complete kinematic model of the INS can be found by combining Eq. 6.4.9, Eq. 6.4.10 and Eq. 6.4.11:

$$\begin{bmatrix} \dot{\mathbf{P}} \\ \dot{\mathbf{V}} \\ \dot{\boldsymbol{\theta}} \end{bmatrix} = \begin{bmatrix} 0 & \mathbf{I} & 0 \\ 0 & 0 & 0 \\ 0 & 0 & 0 \end{bmatrix} \begin{bmatrix} \mathbf{P} \\ \mathbf{V} \\ \boldsymbol{\theta} \end{bmatrix} + \begin{bmatrix} 0 & 0 & 0 \\ \mathbf{M}_{\mathrm{I2V}}(\boldsymbol{\theta}) & \mathbf{M}_g & 0 \\ 0 & 0 & \mathbf{M}_{\mathrm{Euler}}(\boldsymbol{\theta}) \end{bmatrix} \begin{bmatrix} \mathbf{a}_{\mathrm{INS}} \\ g \\ \boldsymbol{\omega} \end{bmatrix} = \mathbf{A}_{\mathrm{kin}} \begin{bmatrix} \mathbf{P} \\ \mathbf{V} \\ \boldsymbol{\theta} \end{bmatrix} + \mathbf{B}_{\mathrm{kin}}(\boldsymbol{\theta}) \begin{bmatrix} \mathbf{a}_{\mathrm{INS}} \\ g \\ \boldsymbol{\omega} \end{bmatrix} \qquad (6.4.12)$$

Which is a state space model with states **P**, **V** and θ and inputs $\mathbf{a}_{\mathrm{INS}}$, g and ω. This gives 9 scalar states and 7 scalar inputs.

It is apparent that in this kinematic model of the INS, the system matrix $\mathbf{A}_{\mathrm{kin}}$ is constant, while the input matrix $\mathbf{B}_{\mathrm{kin}}$ is a function of the orientation as given by the Euler angles θ. What has essentially been obtained is a kinematic state space model driven by the inertial measurements.

6.4.4 Kinematic model with noise

In an ideal case, Eq. 6.4.12 makes it possible to compute the position, velocity and orientation of the INS at any time $t \geq t_0$, given the an initial position, velocity and orientation at $t = t_0$. However in practice the measurement errors and noise inherent in the acceleration and angular rate measurements, introduces a slow drift in the kinematic states, since the kinematic model consists entirely of integrators. In fact, since the position is obtained by double integration of the acceleration, the position is an unstable state. Since the inertial measurements are inputs to the kinematic model, the physical measurement noise must be mathematically represented as process noise:

$$\begin{bmatrix} \dot{\mathbf{P}} \\ \dot{\mathbf{V}} \\ \dot{\boldsymbol{\theta}} \end{bmatrix} = \mathbf{A}_{\mathrm{kin}} \begin{bmatrix} \mathbf{P} \\ \mathbf{V} \\ \boldsymbol{\theta} \end{bmatrix} + \mathbf{B}_{\mathrm{kin}}(\boldsymbol{\theta}) \begin{bmatrix} \mathbf{a}_{\mathrm{INS}} \\ g \\ \boldsymbol{\omega} \end{bmatrix} + \mathbf{B}_{\mathrm{kin}}(\boldsymbol{\theta}) \begin{bmatrix} \mathbf{v}_{\mathrm{a,INS}} \\ 0 \\ \mathbf{v}_{\omega} \end{bmatrix} \qquad (6.4.13)$$

Where $\mathbf{v}_{\mathrm{a,INS}}$ is the stochastic acceleration measurement noise in INS coordinates and $\mathbf{v}_{\omega}$ is the stochastic angular rate measurement noise in INS coordinates. We have for simplicity assumed that the error in “g” is much smaller then in the acceleration measurements.

There are several different ways to describe the physical measurement noise processes, however for practical purposes we will have to make the following assumptions regarding the stochastic nature of the physical measurement noise (Ref. 36):

- The probability density functions (PDF’s) of the measurement noise is gaussian.
- The measurement noise is ergodic.
- The noise process is stationary.

The first two assumptions makes it possible to use available methods for estimation in stochastic systems. The third assumption means that a properties of the stochastic signal do not change with time, which simplifies the analysis and makes it possible in practice to determine the frequency characteristics of the measurement noise from experiments.

6.4.5 Dynamic model

One basic property of the kinematic model, given above, is that the model is independent of the actual dynamics of the vehicle using the INS. This is of course an advantage from a standpoint of simplicy. However neglecting any knowledge of the vehicle dynamics will inherently give a less “optimal” state estimate. This is especially apparant when considering the angular rate measurements. Since the angular rate ω in the linear case is the integral of the angular accelerations, it follows that the angular rates must be continues functions of time. If this was not the case, the vehicle would be disturbed by torque impulses, which is not realistic for an airborne vehicle.

In order to improve upon the kinematic model, an “accurate” dynamic model of the vehicle containing the INS could be used. In our case this could be an accurate linearized aerodynamic model of the UAV. Assuming that the model was not only a detailed but also an accurate model of the dynamics of the actual UAV, this would then make it possible to synthesis an “optimal” (Extended) Kalman Filter (EKF). In reality it would however be difficult and time consuming to obtain such an accurate model, even worst we may in fact jeopardize the stability and convergence of the state estimator by placing to much trust in an erroneous model (Ref. 36, Chapter 4). It is demonstrated that one way to prevent divergence is to ensure that all unstable states are affected by (fictitious) process noise (Ref. 36, Chapter 4).

Without going into mathematical detail, we can thus summarize that we want a dynamic model that captures the essential features of the true dynamics of the vehicle, but that still contains some process noise to account for modelling errors. It is obvious that there are many different ways to arrive at a model with these general features. In this thesis we will not pursue the mathematical intricacies of obtaining an “optimal” solution to this problem. Instead a simple workable solution will be proposed.

Since the desired model must be a “dynamic” model, it is obvious to start by looking at the frequency content of the UAV behaviour. Since the primary forces on the UAV are aerodynamic, we can assume that the vehicle is not subject to any impulses. This can be described mathematically by stating that for “high” frequencies the velocity and angular rates must approach zero. Since an impulse is also associated with discontinues higher order derivatives, we can equally well state that the acceleration and angular acceleration must approach zero for high frequencies:

$$\dot{\mathbf{V}} \to 0 \qquad for \qquad f \to \infty \tag{6.4.14}$$

and

$$\dot{\boldsymbol{\omega}} \to 0 \qquad for \qquad f \to \infty \tag{6.4.15}$$

For “low” frequencies, we do not have such a readily available deterministic model. The obvious choice is therefore to model the low frequency dynamics by a stochastic noise process.

6.5 System calibration

In the above sections, the sensor and instrument models have been described. For both the individual sensors and their combinations, a number of unknown parameters have been defined. These include deterministic parameters like the gain, offset, temperature dependency and frequency characteristics. Stochastic parameters like measurement noise levels and frequency content are also used. In order to use these models to improve the accuracy of the INS, these parameters have to be estimated and tabulated. The only feasible method of doing this with sufficient accuracy is by using actual measurements on the INS. Since the INS is a self contained analog and digital signal conditioning unit, such measurements will conveniently also include effects due to low level signal conditioning. The total process of using measurements to obtain the different parameters can be described as “calibration”. Calibration can in principle be performed in two ways, off-line and on-line calibration. Off-line calibration is the “traditional” form of calibration. It is basically done in a “laboratory” environment, where the instrument is subjected to different external stimuli. The response to the external stimuli are then recorded and compared to a suitable reference measurement. Using the accurate reference and the raw measurement data, the unknown parameters of the sensor and instrument models can then be determined. On-line calibration is instead performed during the actual operation of the instrument. This can thus be performed during the entire service life of the instrument. Normally off-line calibration involves some kind of interactive process, while on-line calibration is a more automated process. Below we will describe both the on-line and off-line calibration performed on the INS.

6.5.1 Off-line calibration

Off-line calibration has the following advantages:

- Accurate due to good control of the laboratory environment and external stimuli.
- Different phenomena can relatively easily be distinguished and separated.
- System models can be obtained which are essential for operational use with state estimation filters.

However there also some major disadvantages:

- Accurate reference instruments and actuators are needed.
- Time consuming measurements and analysis.
- High degree of operator work load.
- The laboratory environment does not accurately reflect the operational environment, which means that some residual errors will still exist during operation.

In view of these considerations, the following off-line calibrations of the INS will be performed:

1. Noise models and frequency contents.
2. Temperature dependent offset.
3. Sensor gain and frequency characteristics.

4. Sensor nonlinearities.
5. Orthogonalization of sensor measurements.

We will assume that the individual sensor noise models are independent of the state of the sensor. This means that the first two calibrations can be performed with the INS stationary ($\boldsymbol{\omega}_{\mathrm{INS}} \equiv 0$ and $\mathbf{a}_{\mathrm{INS}} \equiv \mathrm{constant}$). In effect the sensor noise can be measured by sampling each sensor with the operational sampling rate. A frequency analysis of the data then yields the sensor noise models. The temperature dependent offset can be measured by subjecting the complete INS to one or more slow temperature cycles, encompassing the operational range. Comparing the primary sensor output to the build in temperature sensors, then gives the temperature dependent offset.

The last three types of measurements require a suitable externally measurable motion stimulation. For the rate gyro sensors, this is provided by a suitable “spintable”. The spintable is a one degree of freedom rotational platform. Using a suitable test fixture, it is possible to rotate the entire INS around one of the principle axes at a time. Using a suitable control of the spintable, a sinusiodal angular rate excitation is used:

$$\omega_p \cong A_\omega \sin(2\pi f_{osc} t) \tag{6.5.1}$$

Where ω_p denotes one of the principal axes angular rates: ω_x, ω_y or ω_z. The desired frequency of torsional oscillation is given by f_{osc}, while the desired amplitude of oscillatory angular rate is given by A_ω.

6.6 References

34. B.F. Doolin:"The Application of Matrix Methods to Coordinate Transformations Occurring in Systems Studies Involving Large Motions of Aircraft", NACA TN 3968, Washington May 1957.
35. "ADXL202/ADXL210 datasheet", Analog Devices Inc., 1999.
36. Frank L. Lewis:"Optimal Estimation with an introduction to stochastic control theory",John Wiley & Sons, Inc. 1986.
37. David Eberly: "Quaternion Algebra and Calculus", Magic Software, 6006 Meadow Run Court, Chapel Hill, NC 27516.

Chapter 7

General Instrument Program Structure

7.1 UAV instruments

This document is intended as an overview of the general program structure for UAV instruments which are based on the MB90F598 16-bit microcontroller (MC) from Fujitsu. This document makes frequent references to the “F^2MC-16LX Family, 16-bit Microcontroller, MB90595 Series, Hardware Manual” (Ref. 38), for short HM. The program structure arrived at in this document is of course heavily dependent on the features and structure of this particular MC, this means that the applied program structure may not be applicable to other systems with similar tasks.

The Unmanned Aerial Vehicle (UAV) has a number of separate instruments for navigation, guidance and control of the system. For reasons of modularity and ease of interface and development, the individual instruments are self contained units that communicate through a Controller Area Network (CAN) bus (Ref. 39), as shown below:

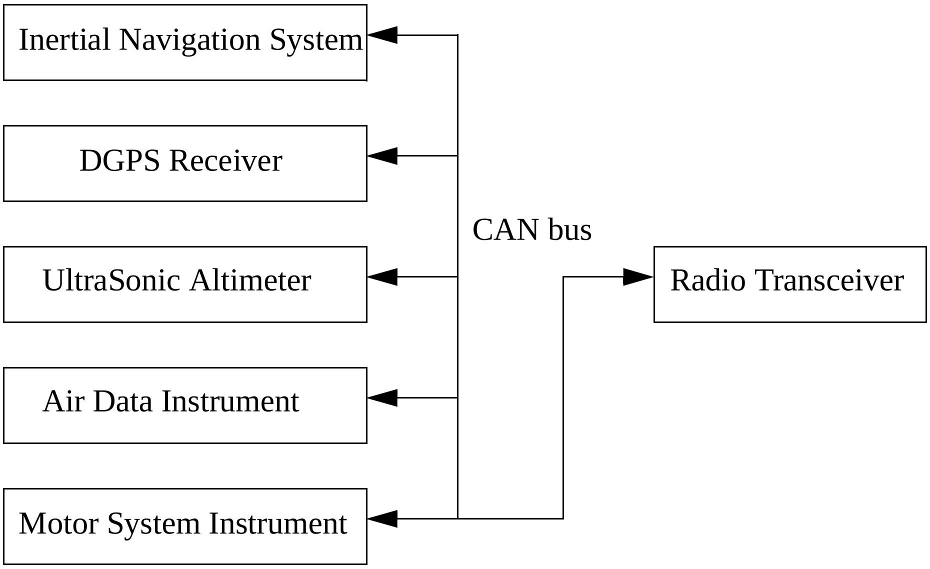

FIGURE 7.1 UAV instrument structure.

The CAN bus is a serial two wire differential bus with a highly sophisticated low level protocol. The main features are; low level error detection and automatic retransmission, message identifiers instead of addresses, medium speed (500kHz-1MHz bandwidth), non destructive arbitration of bus conflicts and all messages are received and accepted simultaneously at all nodes in the system. The bus is physically a two wire line topology (multidrop) with 120Ω termination at each end. For the user, some features that are particularly interesting are:

- Since data are identified using a message identifier (ID), an instrument does not need to know the “address” of any node that uses its data. Instead it is up to each instrument to determine if a message on the bus is relevant to its function.
- It is very important that no two messages have the same ID, as this will lead to undetectable data corruption.
- The message ID is also the priority, the lower the ID the higher the priority.
- Messages are received simultaneously (less then 1usec uncertainty) at all nodes in the system.

These features will be used extensively when designing the software for each instrument.

7.2 Overview of tasks

The “tasks” are defined as the general actions and processes that the MC must perform to complete its functions as part of UAV instrument.

7.2.1 Synchronisation

In order to use the measurements from the individual instruments to determine the state of the complete vehicle, it is very important that the precise sampling time of the individual measurements are known. This both applies to the timing within each instrument and the timing between instruments. Synchronisation is here defined as the process of synchronising the local clocks within each instrument to a common time source, internal or external to the UAV. It is apparent that synchronisation involves a “master” clock source and several “slaves” that are synchronized to the master. There are thus two kinds of tasks, one kind for the master and another kind for the slaves. Since synchronisation defines the timing for everything else, this task must have the highest priority of all the repetitive tasks. In the current system, synchronisation is performed using over the CAN-bus, using a special message and algorithm according to the method described in (Ref. 40).

7.2.2 Sampling

Sampling is the process of measuring the outputs of the particular sensors/transducers of the instrument. Normally sampling is initiated by the MC, but on some instruments the transducers periodically send data to the MC using a serial synchronous or asynchronous interface. In addition to the appropriate hardware, sampling usually involves a special piece of software called a “device driver”, that handles low level interface to onboard MC peripherals and input/output (IO) ports. It is usually desired that the sampling period is fixed and synchronised with the rest of the system. In some cases it may be acceptable that samples are taken at “random” times, but accurately time stamped. In some instruments different kinds of sensors may use different sampling times. Sampling is a high priority time critical task.

7.2.3 Data processing and local state estimation

Data processing is the process of converting the raw binary measurements into usable information for transmission to the rest of the system. According to the application and particular instrument, data processing can be everything from doing nothing with the raw data, to complex linearization, temperature compensation, filtering and state estimation. Data processing may involve using data from other instruments, received from the CAN-bus. Data processing is usually the most computationally intensive task that the MC must perform. For filtering or state estimation, some amount of memory is needed to store states between sampling times. Since data processing is a prerequisite to any control actions, it is a high priority task, but not as time critical as sampling.

7.2.4 Control signal generation

Control signal generation is the process of using data processed information from within the instrument or from other instruments, to compute control signals. Control signal generation is subjected to many of the same considerations as data processing. It usually succeeds data processing, but must be performed within a set time frame. Priority and time criticallity is much the same as for data processing. In same cases control generation can be performed before all data processing is finished. This strategy may be used to save time from sampling to control actuation. It is apparent the control signal generation is not used in most “instruments”, but is included here for completeness. In general “control signal generation” and “actuation” can also include transmission of data by the Radio Transceiver to a ground control station.

7.2.5 Actuation

Actuation is the task of outputting the computed control signals to the actual physical actuators, though appropriate ports on the MC. Actuation is a high priority time critical task because it must usually be performed at a definite moment for best results. Usually actuation is either synchronized with the next sample time or occurs a fixed time interval after the sample time. As the case for sampling, actuation involves the use of device drivers to interface to the MC ports and peripherals.

7.2.6 CAN-bus transmission

The transmission of CAN-bus messages is not extremely time critical, but since other instruments might use the message for data processing or control it must be completed in a fixed time frame (which may vary from message to message). Thus CAN-bus transmission has a relatively high priority. Since the priority of the CAN-bus messages are determined by their ID’s, it is important to assign appropriate ID’s to different types of messages in the system design phase.

7.2.7 CAN-bus message decoding

The decoding of CAN-bus messages is sometimes time critical, depending of course on the message type and the particular instrument. The relative priority of decoding of CAN-bus messages will is therefore instrument dependent.

7.2.8 Serial asynchronous communication (RS-232)

The universal serial asynchronous interface (UART) is used to communicate with PC's, mostly for user interface applications. Since the UART is relatively slow, it is not really suited for high speed real time control applications. Also due to the asynchronous nature of communication using the UART, synchronization can not be performed accurately using this interface. In order to prevent the process of sending a string of bytes through the UART, from locking up the system for long periods of time, a device driver using input and output buffers should be used. For the above reasons, RS-232 communication has a low priority in most applications.

7.2.9 System state estimation

Since some instruments may have simple tasks compared to their computational resources, the excess computational resources may be used to estimate global system states. Global system states are here defined as states that are important for the navigation and control of the complete system, as opposed to local states that are used in low level filtering and similar tasks. The idea behind doing global state estimation in different instruments, is to utilize all available computational resources, thus freeing up hard pressed instruments and controllers from excessive computational burdens. Also such a scheme can relatively easily introduce redundancy into the system, without additional hardware. System state estimation should be performed after the primary instrument tasks.

7.2.10 System state synchronization

If the global system states are estimated in different instruments, it must also be possible to perform global system synchronisation of the system states. This can be performed if each instrument periodically transmits its global state estimates using the CAN-bus, instruments can then compare there global state estimates with that of other instruments and act accordingly. Notice that global state estimates (of the same states) from different instruments, must have different CAN-bus ID's in order to avoid data corruption.

7.2.11 Initialization

After power up or reset of each instrument, variables, states and tasks much be initialized. This may also include receiving initial values of global states from the CAN-bus.

7.2.12 Error handling

There several types of possible errors that can occur. Some errors may be detectable and perhaps recoverable without resetting the MC. Others may require resetting of the MC, followed by initialization.

Program detectable errors:

- Failure of sensors: detectable by out of range measurements or excessive measurement residuals in state estimators.

- CAN-bus overload: detectable by inability to transmit message in allowable time frame.
- RS-232 errors: detectable by error bits in UART.
- Excessive global state residuals: detectable by comparing with estimates of states from other instruments.

Non program detectable errors:

- Program lock up (“infinite loop”): Detectable by activation of “Watch-Dog Timer” / (WDT) reset after a predefined interval.
- Exceptions:

After a reset, the initialization routine can read the “Watch-Dog Timer Control Register“(WDTC) to determine if the reset was caused by the WDT reset or power on reset.

7.2.13 Signal flow

Before describing the program structure in detail, it is an advantage to determine the desired signal flow for each sample interval:

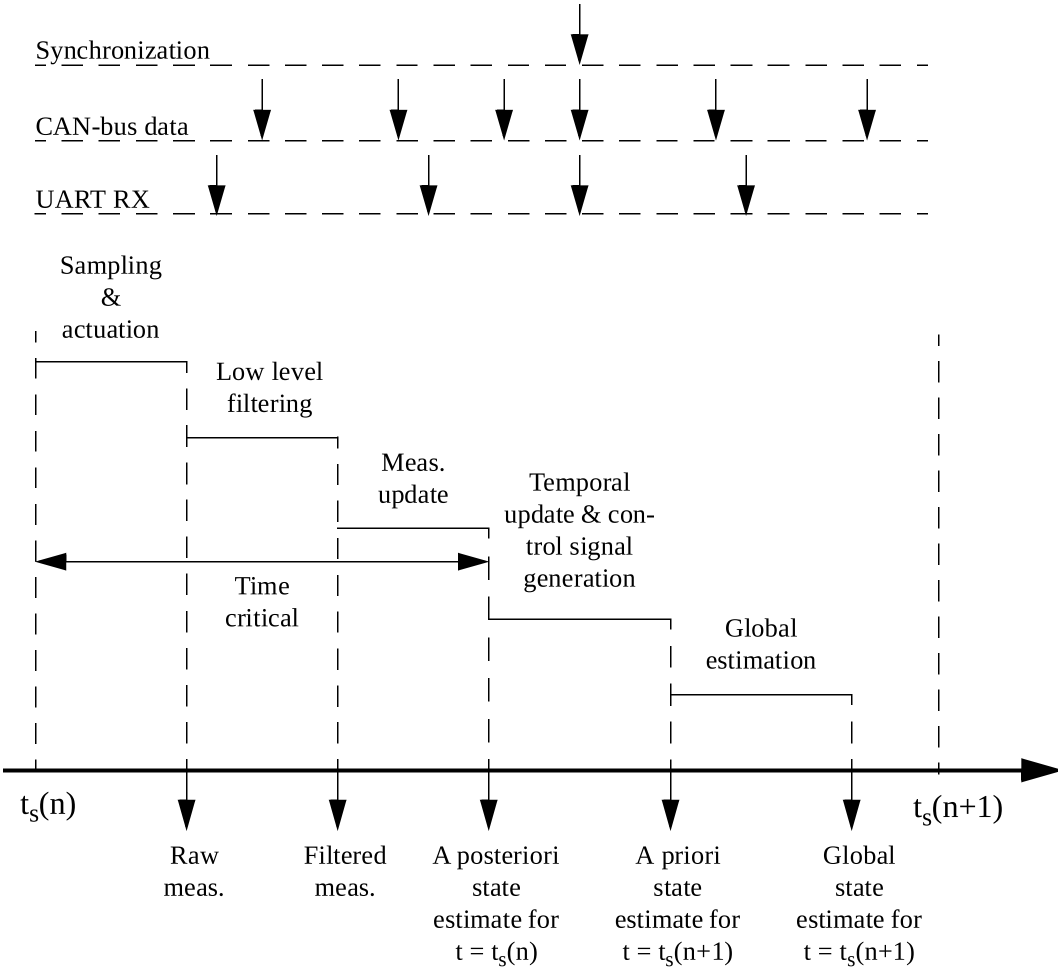

FIGURE 7.2 Instrument signal flow graph.

The “global” estimation process is only performed in instruments with “spare” computational resources, for the purpose of increasing the system fault tolerance. The main idea is that sampling and control actuation is performed at the start of the each sample interval. This is possible because the control signals for the next sample time is determined from the predicted state estimate at the next sample time. This method simplifies controller design because actuation and measurement is performed virtually simultaneously, at the beginning of each sample time interval.

7.3 General program structure

The general program structure consists of several high priority interrupt driven loops and a low priority main loop.

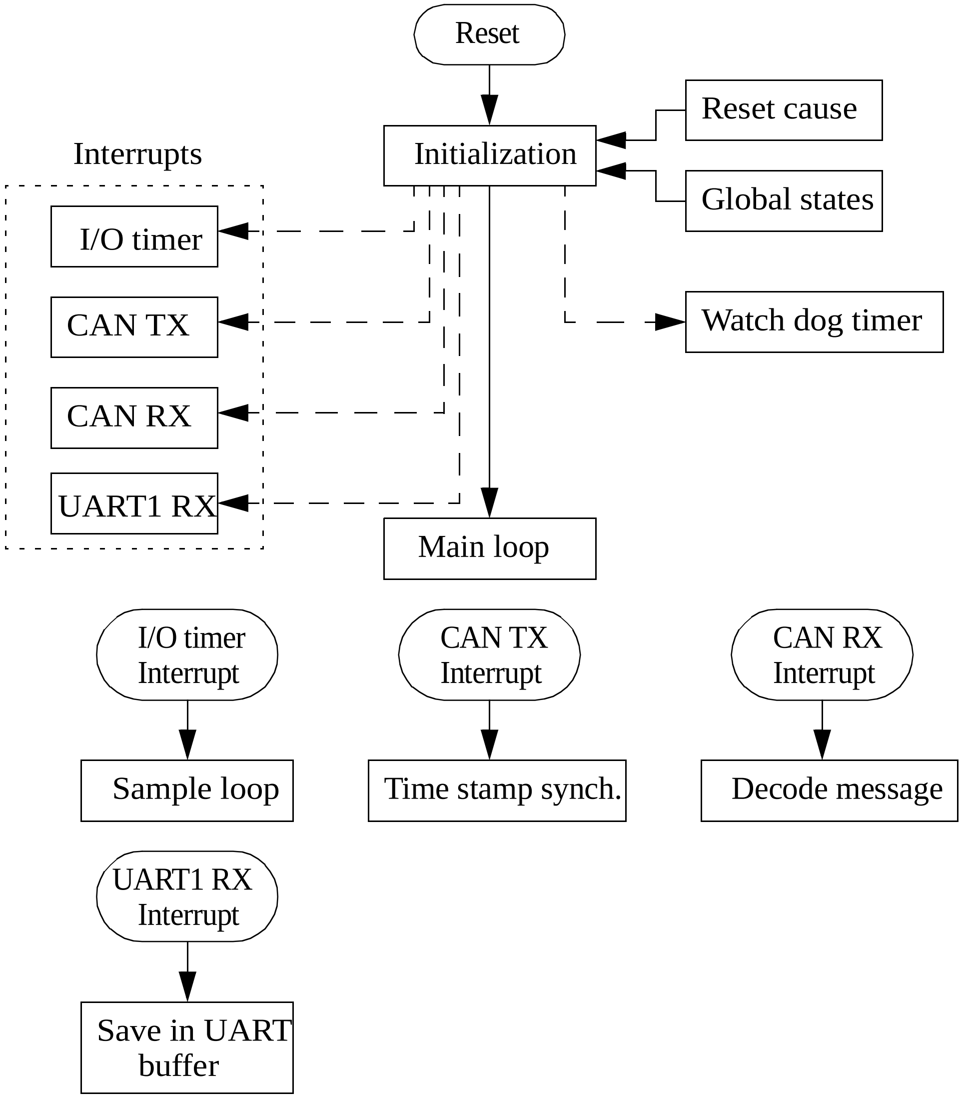

FIGURE 7.3 General instrument program structure.

The priorities of the different interrupts are given below:

Interrupt	Task	Priority
CAN TX	Time stamp transmission of synchronization	6
CAN RX	Time stamp reception of synchronization Decode messages to internal variables.	6[a]
I/O timer	Main sample and control loop.	5
UART1 RX	Save received char from UART1 in RX-buffer.	4

Tabel 7.1 Interrupt priorities.

---

a. Defaults to same priority as CAN TX interrupt.

7.3.1 Main loop

The main loop handles asynchronous events and low priority tasks. This includes detection and time stamping of asynchronous general purpose digital inputs and transmission of data using the UARTS (RS-232).

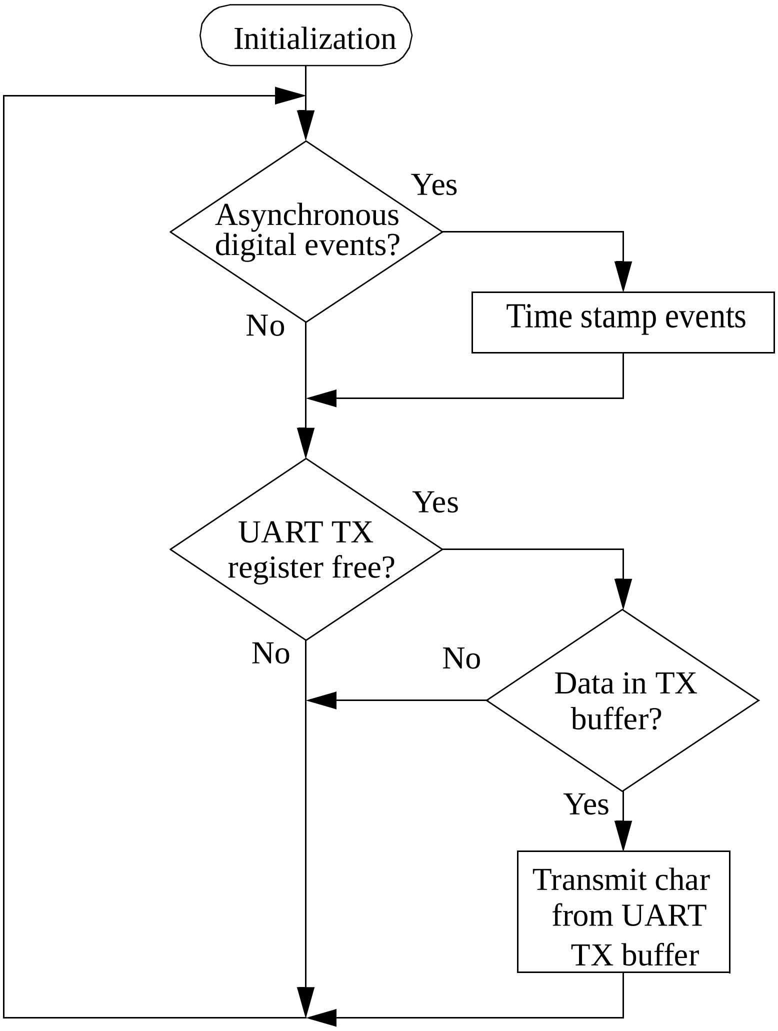

FIGURE 7.4 Main loop.

7.3.2 Sample loop

The sample loop includes all the tasks that are related to the sampling process: Sampling, data processing, control signal generation and actuation. The algorithme assummes that a predictor-corrector type state estimator is for data processing of measurements.

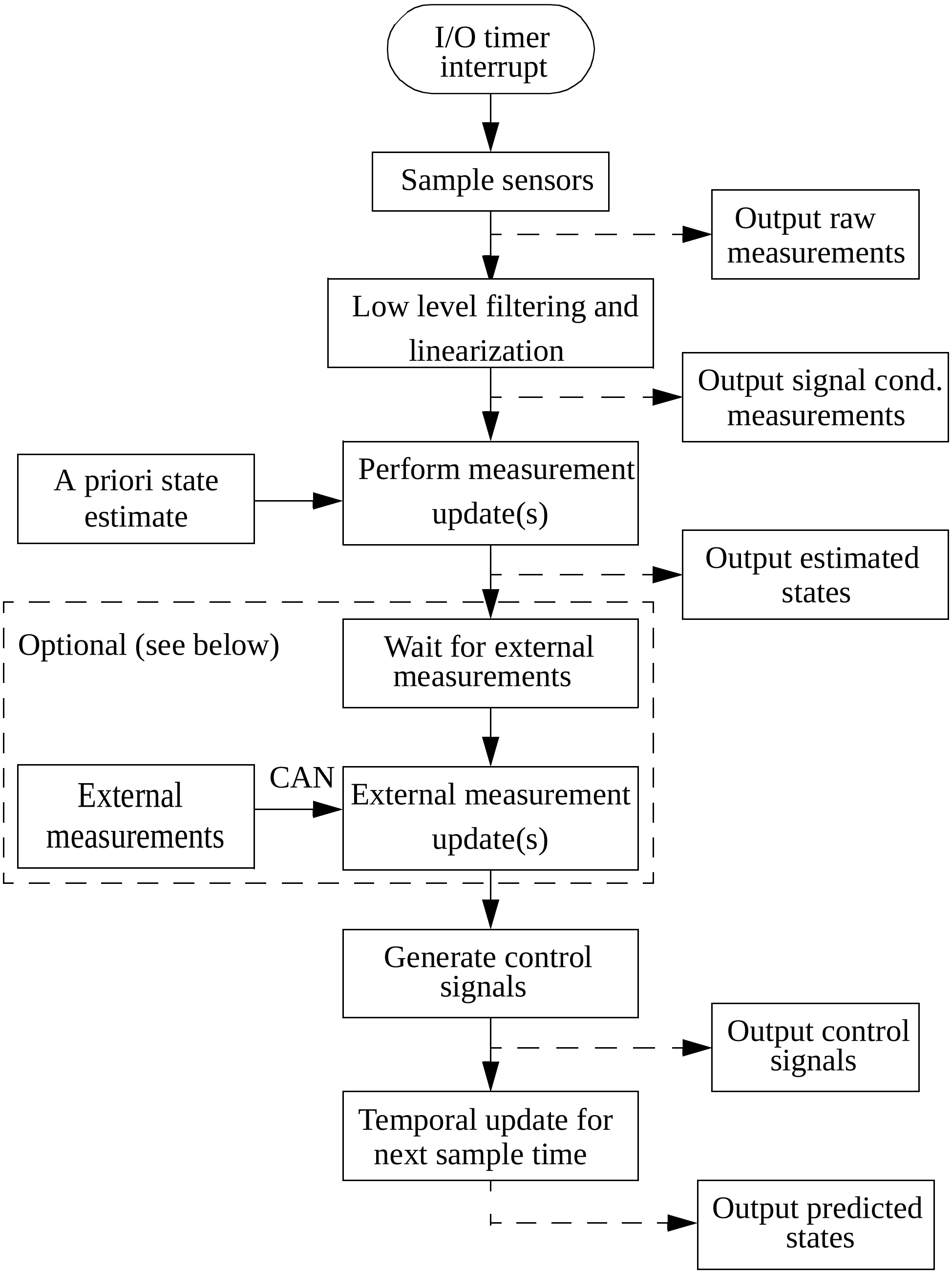

FIGURE 7.5 Sample loop.

The main idea behind the order of computations, is that the prediction step is performed immediately after low level signal conditioning. While the temporal update (integration) for the next sample epoch is performed after the new state estimate and any control signals have been computed and output to the CAN-bus, UART or to the actuation loop. The incorporation of external measurements from the CAN in the state estimate may be performed before control signal generation as shown above. However there are certain disadvantages with this approach: It is necessary to wait for the CAN-message to arrive, thus delaying any control actions. Also it must be resolved how to handle the absence of external data, without causing a lock up of the program. Therefore it may be simpler and more robust to simply generate the control signal based on the estimated state after including just the internally measured estimate updates. The extreme consequence of this is that the control signals are generated based on just the predicted state at the present sampling time. This allows the control signal to be generated before the present sampling time, thus enabling control actuation just after sampling (if any).

The external state estimates can then be included as soon as they are received from the CAN-bus, as described below.

7.3.3 Synchronization protocol

Synchronization involves two kinds of processes, one kind for the “master” and one kind for the “slaves”. The synchronization algorithm described below is based on the synchronization protocol from (Ref. 40). The main idea behind the protocol is to use the fact that CAN-bus messages are received (accepted) at all nodes in the CAN-bus network simultaneously (less then 1 usec uncertainty). The protocol uses this property to determine the errors between the local clocks in each slave instrument and the reference clock in the master instrument. This error can then be adjusted to zero in a continues or discontinues manner using a feedback loop in each slave instrument. The protocol only needs one type of CAN-bus message to accomplish this, as shown below:

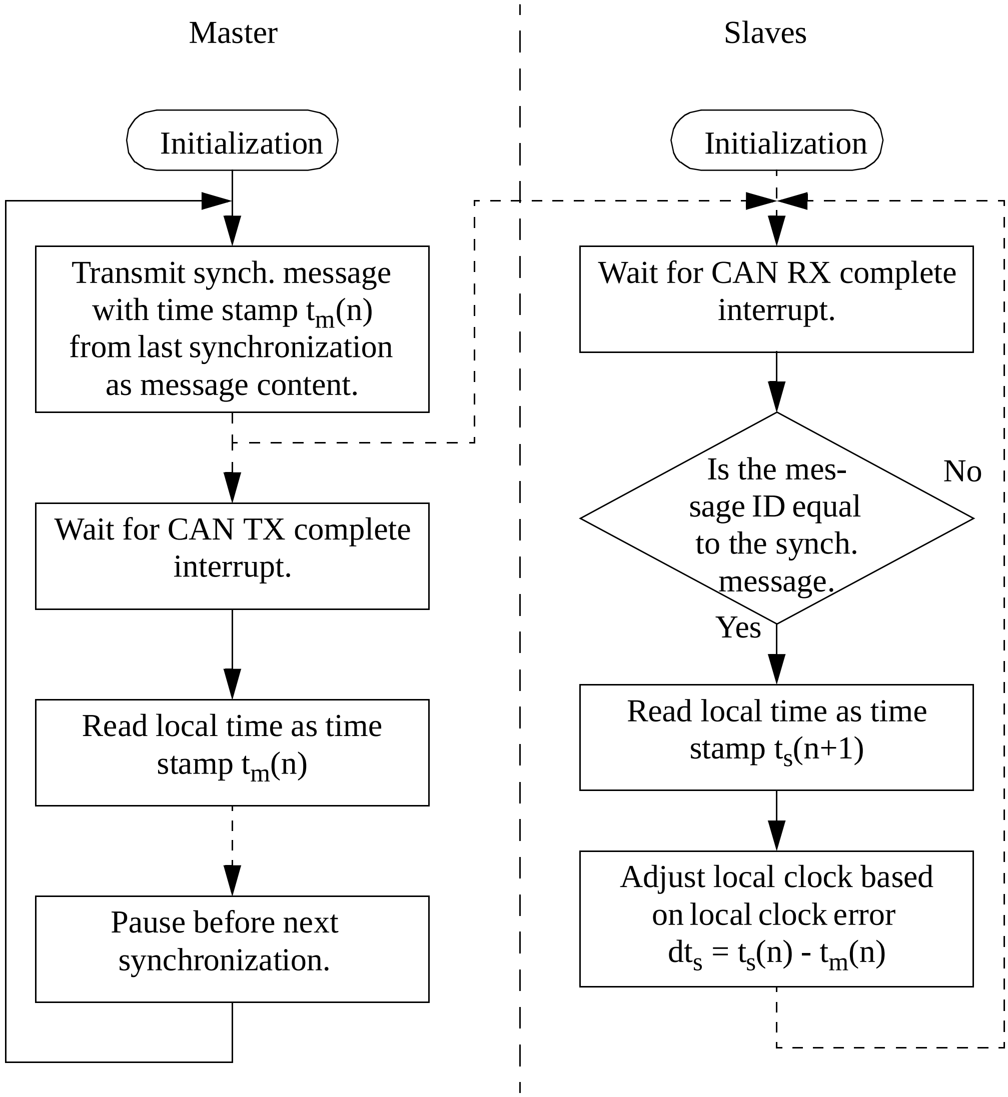

FIGURE 7.6 Basic CAN-bus synchronization protocol.

In the figure above, TX is an abbreviation for Transmit and RX an abbreviation for Receive. The dashed lines indicate flow paths that are triggered by internal or external interrupts. Due to the fact that the TX complete interrupt and RX interrupts are flagged at the same time, the main limitation on the accuracy of the above algorithm is due to uncertainty in interrupt processing times. Large errors can result if the CAN TX and RX interrupts are postponed due to higher priority interrupts or temporary “masking” of the interrupt flags. It is for this reason that the CAN RX and TX interrupts are assigned the highest priority of all regular interrupts.

There are several possible improvements to the above synchronization protocol:

- Estimation of uncertainty of slave and master time stamps due to interrupt delays.
- Indication of uncertainty of master time stamp t_m in CAN message data block.
- Weighting of indicated time errors $dt_s = t_s - t_m$ in clock adjustment procedure, according to measurement uncertainty in dt_s and uncertainty in t_s.
- Rapid resynchronization after a node reset, followed by smooth adjustments for jump less tracking of the master clock.
- Possibility for smooth transition to redundant reserve master clocks.

7.3.4 CAN-bus reception

In Figure 7.6, above, the signal flow and program structure for synchronization of slave nodes are shown. Since the synchronization of the slave nodes is performed using the CAN-bus, all CAN messages must initially be treated as shown above in order to obtain a time stamp for the synchronization messages. Thus the CAN RX interrupt routine is obtained as an extension of Figure 7.6:

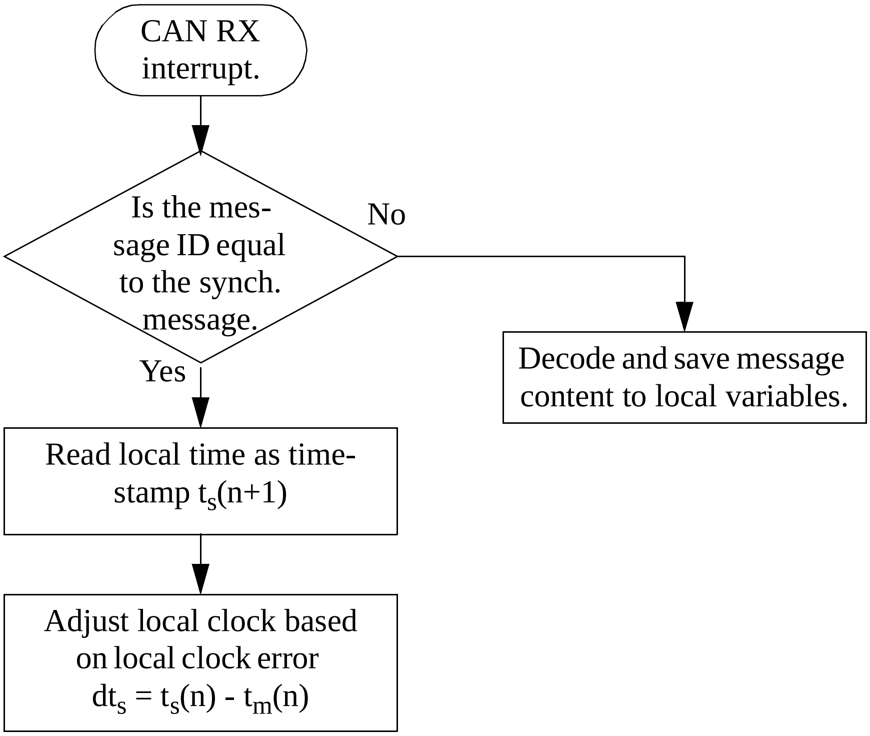

FIGURE 7.7 CAN-bus RX interrupt routine.

7.3.5 UART RX interrupt

The UART receive (RX) interrupt is activated by the reception of a valid byte (char) by the UART1 (default) or UART0 (optional) onboard UART's. The purpose of the interrupt is to save the received byte in the instrument UART RX buffer. This must be done before the UART has finished receiving the next byte, to prevent loss of data. The required interrupt delay constraints are given below:

UART baud rate	Maximum delay for processing	Machine cycles at 16MHz
9615bits/s	936 us	14976
19230bits/s	468 us	7488
38460bits/s	234 us	3744
62500bits/s	144 us	2304

Tabel 7.2UART RX allowable interrupt latencies.

The last column indicates the allowable number of machine cycles from the time of the UART RX interrupt request until the received byte is read from the UART, without danger of UART over run. The table assumes an internal machine clock frequency of 16MHz. The UART RX interrupt routine is shown below:

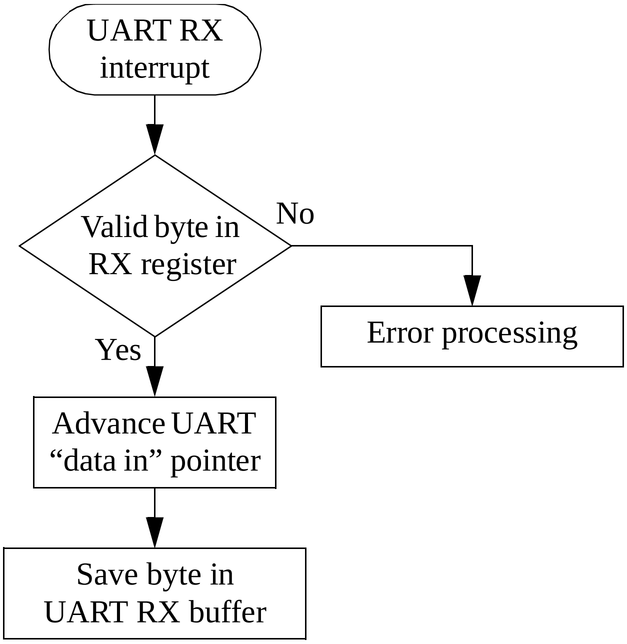

FIGURE 7.8 UART RX interrupt routine.

The UART RX buffer is organised as a ring buffer. This means that a certain fixed amount of RAM (Random Access Memory) in the MC is allocated for the buffer. Each time a byte is received it is stored in the next available position in the buffer, as indicated by a "data in" pointer. When the data in the buffer is read by another program application, a "data out" pointer is advanced to indicate the position to which data has been processed. When the "data in" or "data out" pointer arrives at the "end" of the buffer area it wraps around to the beginning of the buffer area, thus creating an "infinite" ring buffer. If the "data in" pointer over takes the "data out" pointer, old data in the buffer will be overridden. For this reason it is important that the “end user” program application regularly processes the data from the buffer.

A similar ring buffer is used for transmitting through the UART, as outlined in Section 7.3.1.

7.4 References

38.“F^{2}MC-16LX FAMILY, 16-BIT MICROCONTROLLER, MB90595 SERIES, HARDWARE MANUAL”, 1998, Fujitsu Limited, Germany.

39.Bosch:”CAN Specification 2.0B”, www.can.bosch.com/content/Literature.html.

40.M. Gergeleit, H. Streich: “Implementing a Distributed High-Resolution Real-Time Clock using the CAN-Bus”, 1st international CAN-Conference 94, Mainz, 13.-14. 09, Can in Automation e.V., Erlangen, 1994

Appendix A: Electric propeller propulsion system

A.1: DC-motor and gearing

A DC motor runs on direct current, using mechanical commutation to control the current in the field windings. The stator of the motor consists of a permanent magnet. Since the motor is intended to run at a relatively high speed, the nonlinearities associated with nonideal commutation and a finite number of field windings can be ignored. The only important nonlinearity for our application, is coulomb friction (i.e. “sliding” friction), which primarily affects the maximum efficiency of the motor. A model of the available motor torque τ_m and the motor current I_m is given by (Ref. 18):

$$\tau_m = k_m I_m - \tau_c = k_m \frac{V_m - k_e \omega_m}{R_m} - \tau_c \qquad I_m = \frac{V_m - k_e \omega_m}{R_m} \tag{A.1}$$

Where V_m is the voltage at the motor terminals, ω_m is the angular velocity of the motor shaft, R_m is the combined resistance of the motor windings and commutators, k_m is the motor “torque” constant, k_e is the motor “induced voltage” constant and τ_c is the constant motor coulomb friction torque. It can be shown that if a consistent set of units are used, the numerical value (but not the dimension) of k_m and k_e will be the same.The net result is that the static (constant speed) and dynamic (variable speed) characteristics of the DC motor can be described by three parameters: k_m, R_m and τ_c. In reality the values of R_m and τ_c may be highly variable near zero speed due to commutation and sticktion. For this reason, the motor parameters are best estimated when the motor is not at standstill.

It is apparent that for a *constant* motor voltage V_m, both the motor torque and the motor current I_m are linear functions of the motor angular velocity (or “speed”) ω_m. This linear relationship can be described by two extremes, the motor “stall” or zero speed condition and the motor zero torque (or no load) condition. The stall torque τ_{ms} and the stall current I_{ms} can be determined from Eq. A.1 as:

$$\tau_{ms} = k_m \frac{V_m}{R_m} - \tau_c \qquad I_{ms} = \frac{V_m}{R_m} \tag{A.2}$$

The motor no load speed (also called the “idle” speed) ω_{mi} and current I_{mi} can be determined from Eq. A.1 as:

$$\omega_{mi} = \frac{V_m}{k_e} - \frac{R_m \tau_c}{k_e k_m} \qquad I_{mi} = \frac{V_m - k_e \omega_{mi}}{R_m} = \frac{V_m - k_e\left(\frac{V_m}{k_e} - \frac{R_m \tau_c}{k_e k_m}\right)}{R_m} = \frac{\tau_c}{k_m} \tag{A.3}$$

It is apparent that the no load current is strongly dependent on the coulomb friction, since a friction of zero would imply zero no load current.

The power delivered to the motor shaft W_m is given by the product of the torque and the angular velocity:

$$W_m = \tau_m \omega_m = \left(k_m \frac{V_m - k_e \omega_m}{R_m} - \tau_c\right)\omega_m \tag{A.4}$$

The electric power W_e delivered to the motor terminals is given by the product of the terminal voltage and the field current:

$$W_e = V_m I_m = V_m\left(\frac{V_m - k_e\omega_m}{R_m}\right) \tag{A.5}$$

The efficiency η_m of the motor is by definition the ratio of the mechanical power delivered to the motor shaft and the electrical power delivered to the motor terminals:

$$\eta_m \equiv \frac{W_m}{W_e} = \frac{\tau_m\omega_m}{V_m I_m} \tag{A.6}$$

From Eq. A.3, it is apparent that zero coulomb friction would imply that the no load speed is equal to V_m/k_e, thus given that k_e is equal to k_m, the efficiency of the motor is only limited by the coulomb friction τ_c. It is readily apparent from Eq. A.6, that the efficiency of the motor goes to zero as the speed approaches zero.

A practical problem encountered when trying to extract as much power as possible from a given motor, by increasing the motor terminal voltage, is that the difference between the applied electric power W_m and the obtained mechanical power W_e is absorbed as heat power W_{th} (sometimes called thermal power) in the motor field windings:

$$W_{th} = W_e - W_m = (1 - \eta_m)W_e \tag{A.7}$$

For most practical purposes the power absorbed by coulomb friction does not influence the thermal behaviour of the motor, since the coulomb friction is small and not directly related to the temperature of the field windings. The heat power can thus be approximated by the electric power dissipated in the commutator and field windings:

$$W_{th} \cong R_m I_m^2 \tag{A.8}$$

Thus the thermal power is directly related to the field current. Since the motor torque is proportional to the current when the coulomb friction is neglected (Eq. A.1), we can express the thermal power as a function of the motor torque:

$$W_{th} \cong R_m I_m^2 \cong R_m\left(\frac{\tau_m}{k_m}\right)^2 = \frac{R_m\tau_m^2}{k_m^2} \tag{A.9}$$

This means that the maximum continues torque is limited by the allowable thermal power in a given installation. The allowable continues thermal power is usually limited by the allowable field winding temperature and the total thermal resistance from the field windings to the ambient atmosphere. The allowable transient thermal power is in addition affected by the heat capacity of the field windings.

In some instances we may have to choose and model a DC-motor based on very scarce data. Typically the following data is available from the manufacturer:

- The “nominal” motor voltage V_{nom} and the following characteristics at that voltage: The idle speed ω_{mi} and current I_{mi}, the maximum efficiency $(\eta_m)_{max}$ and the current at maximum efficiency $I|_{\eta_m = (\eta_m)_{max}}$ and finally the stalled current I_{ms}.
- The “maximum” voltage V_{max}.

Using the equations given above, it is possible to derive the “real” motor parameters k_m, R_m and τ_c from just this information.

Eq. A.2 gives the rotor resistance as:

$$R_m = \left.\frac{V_m}{I_{ms}}\right|_{V_m = V_{nom}} \tag{A.10}$$

Eq. A.3 combined with $k_e = k_m$ gives the torque constant as:

$$\begin{gathered} \omega_{mi} = \frac{V_m}{k_e} - \frac{R_m\tau_c}{k_e k_m} \qquad I_{mi} = \frac{\tau_c}{k_m} \\ \omega_{mi} = \frac{V_m}{k_m} - \frac{R_m I_{mi}}{k_m} \quad \Leftrightarrow \quad k_m = \left.\left(\frac{V_m - R_m I_{mi}}{\omega_{mi}}\right)\right|_{V_m = V_{nom}} \end{gathered} \tag{A.11}$$

Finally using Eq. A.3 again, gives the coulomb friction as:

$$\tau_c = k_m I_{mi} \tag{A.12}$$

Unfortunately the maximum allowable power dissipation is not normally specified. However we can probably assume on the safe side that the motor can run continuously at the maximum voltage at the point of maximum efficiency.

Using the above relationships, the torque, current, efficiency and thermal power of a typical small electric motor has been computed at a fixed voltage, as shown in Figure A.1 below:

A mechanical gear is usually used to match the usually high output speed of the motor to the desired low output speed of the propeller, so that a large relatively slowly turning propeller with a high aerodynamic efficiency can be used.

An ideal gear is characterized by zero mechanical energy loss. This means that even though the angular velocity of the output shaft is lower then that of the input shaft, the output power is equal to the input power:

$$\tau_{out}\omega_{out} = \tau_{in}\omega_{in} \qquad \text{, ideal gear} \tag{A.13}$$

The gear ratio N_{gear} is usually defined as the ratio between the output angular velocity and the input angular velocity:

$$\omega_{out} = N_{gear}\omega_{in} \tag{A.14}$$

In most practical gears, the gear ratio is constant and is independent of the angular velocity or the torque.

In practical gears, some mechanical energy is dissipated as friction torque inside the gear. This means that the output torque is lower then the ideal value, since the gear ratio is not effected by the efficiency of the gear:

$$\tau_{out} = \eta_g \frac{\omega_{in}}{\omega_{out}} \tau_{in} = \eta_g \frac{\tau_{in}}{N_{gear}} \tag{A.15}$$

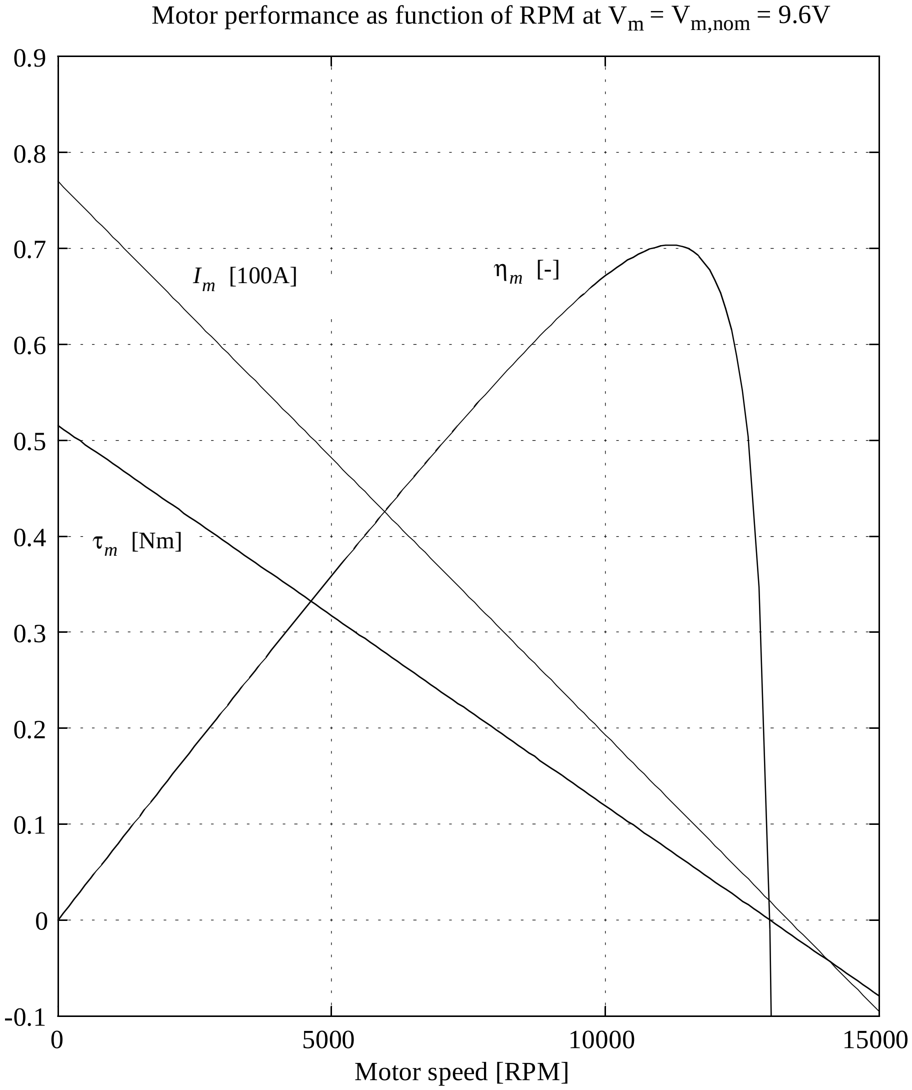

FIGURE A.1 Plot of Graupner Speed 700 BB/9.6V characteristics at nominal voltage

This equation defines the gear efficiency η_g.

It is important to realize that the gear efficiency is not a constant. In most small gears, the torque is transmitted between gear wheels using partly rolling and partly sliding motion. For power transmission applications, the gear wheels are typically not preloaded (see (Ref. 18, p. TBD) for details). This means that most of the friction torque is coulomb friction (sliding friction) between the gear wheels proportional to the input torque in accordance with the definition of the gear efficiency η_g in Eq. A.15. However it most be remembered that some minimum torque is needed just to overcome the sliding friction in the internal bearings in the gear. This means that the efficiency decreases for low torque levels. In electric propulsion applications with reasonable sized gears, it is probably safe to assume a constant gear efficiency.

A.2:Propeller

The propeller is used to transform the mechanical energy from the output shaft of the gear/motor into translational motion of the vehicle through the atmosphere. A propeller usually consists of two or more identical propeller blades that rotate at a quasi constant rate of rotation around a common shaft which is nominally aligned with the relative flow direction of the atmosphere with respect to the vehicle.

The thrust is the propulsive aerodynamic force generated by the relative motion of the propeller with respect to the atmosphere. The aim of propeller design is usually to achieve as much propulsive power as possible for a given amount of mechanical power applied to the propeller shaft.

In general the propulsive efficiency of a propeller at given operational conditions can be defined by:

$$\eta_p = \frac{F_{th} V}{\omega_p \tau_p} \tag{A.16}$$

Where F_{th} is the thrust of the propeller and V is the airspeed of the vehicle relative to the atmosphere. The above equation follows directly from the definition of mechanical power as speed times force. It is important to realize that the efficiency of a propeller of a given geometry is not constant but depends on both the airspeed and the angular velocity of the propeller.

The so called *actuator disc theory* (Ref. 19, chap. 9) is a simple approximation of a propeller. The actuator disc can be visualised as an imaginary flat disc lying in the rotational plane of the propeller as shown below in Figure A.2:

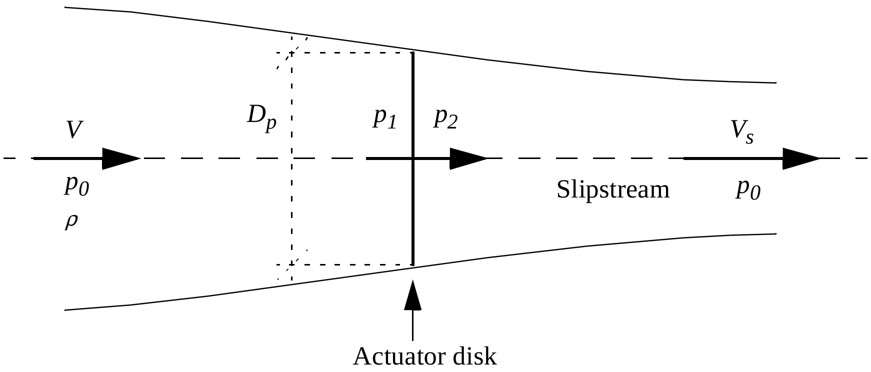

FIGURE A.2 Crossection through circular actuator disc.

The actuator disc raises the pressure from p_1 to p_2, when the air passes through its plane. Due to continuity and the assumption of incompressible flow, the velocity is unchanged by the actuator disc. Thus the velocity at the actuator disc is denoted by V_0. The atmospheric pressure far ahead of the actuator disc is given by p_0 and the atmospheric density by ρ. Far behind the disc the air pressure in the slipstream from the actuator disc reaches equilibrium with the atmospheric pressure p_0 again. At this point the slipstream velocity reaches its maximum value of V_s.

A description of actuator disc theory is given in (Ref. 19, p. 460-466). Here we will describe some of the important results of practical significance. It can be shown that the velocity V_0 at the disc is the mean of the initial velocity V and the slipstream velocity V_s:

$$V_0 = \frac{V + V_s}{2} \tag{A.17}$$

The thrust of the actuator disc can be expressed both in terms of the pressure difference across the disc and the momentum increase in the slipstream:

$$F_{th} = A_d(p_2 - p_1) = \rho A_d V_0 (V_s - V) \tag{A.18}$$

Where A_d is the “surface” area of the actuator disc.

Since the thrust acts at the actuator disc with local velocity V_0, the power delivered to the air at the actuator disc is given by:

$$W_d = F_{th} V_0 = A_d(p_2 - p_1) V_0 = \rho A_d V_0^2 (V_s - V) \tag{A.19}$$

Combining Eq. A.17 and Eq. A.18 gives a relationship between the slipstream velocity and the thrust:

$$F_{th} = \rho A_d V_0 (V_s - V) = \frac{1}{2}\rho A_d (V + V_s)(V_s - V) = \frac{1}{2}\rho A_d (V_s^2 - V^2) \tag{A.20}$$

This can be rearranged to give the slipstream velocity as a function of the thrust:

$$V_s^2 = \frac{2F_{th}}{\rho A_d} + V^2 \tag{A.21}$$

Since the power delivered to the actuator disc is given by $P_d = F_{th} V_0$, the efficiency η_d of the actuator disc can be determined as:

$$\eta_d = \frac{F_{th} V}{W_d} = \frac{F_{th} V}{F_{th} V_0} = \frac{V}{V_0} = \frac{2V}{V + V_s} \tag{A.22}$$

Combining Eq. A.21 and Eq. A.22 gives the efficiency as a function of the thrust, area of the actuator disc, air density and airspeed:

$$\eta_d = \frac{2V}{V + V_s} = \frac{2V}{V + \sqrt{\frac{2F_{th}}{\rho A_d} + V^2}} \tag{A.23}$$

The required power to obtain this thrust can then be determined from Eq. A.22:

$$W_d = \frac{F_{th} V}{\eta_d} = \frac{F_{th}}{2}\left(V + \sqrt{\frac{2F_{th}}{\rho A_d} + V^2}\right) \tag{A.24}$$

Not surprisingly the necessary shaft power increases with increasing velocity and increasing *disc loading* F_{th}/A_d.

It can be shown (Ref. 19, p. 463) that any real propeller of the same diameter as the actuator disc, will have an efficiency which is less then that of the equivalent actuator disc at the same operating conditions. This is mainly due to two phenomenon; the flow around the real propeller blades results in aerodynamic loses due two friction and separation and secondly the slipstream velocity is not uniform due to 3 dimensional flow around the propeller. Thus actuator disc theory can be used to compute the highest attainable efficiency and lowest attainable shaft power of a propeller of a given size and thrust.

A more detailed analysis which explicitly accounts for the geometry of the propeller blades and the speed of rotation can be obtained using “blade element theory” (Ref. 19, section 9.4). In this theory, the propeller is subdivided into independent blade elements in the radial direction. The thrust and torque increments for each blade element is then determined using 2 dimensional airfoil theory. The thrust and torque of the entire propeller can then be obtained by integration over all radial blade elements multiplied by the number of blades.

The objective of any detailed aerodynamic analysis of a propeller is to obtain a set of nondimensionalized coefficients describing the propeller characteristics, such as thrust, torque and efficiency. It can be shown that neglecting Reynolds number and mach number effects (Ref. 19, p. 466-467), the nondimensional propeller characteristics are a function of the *advance ratio* J defined by (Ref. 19, p. 467):

$$J \equiv \frac{V}{f_p D_p} = \frac{V}{2\pi\omega_p D_p} \tag{A.25}$$

Where f_p is the number of revolutions pr. second of the propeller and ω_p is the corresponding propeller angular velocity. As above, the free airspeed is given by V and the propeller diameter by D_p.

The primary propeller coefficients are the thrust coefficient k_T and the torque coefficient k_Q, defined by (Ref. 19, p. 467):

$$\begin{aligned} F_{th} &= k_T \rho f_p^2 D_p^4 \\ Q &= k_Q \rho f_p^2 D_p^5 \end{aligned} \tag{A.26}$$

Where Q is the torque which must be applied to the propeller hub to achieve constant propeller speed of revolution. It is important to note the extreme dependence on the propeller diameter for geometrically similar propellers under similar operating conditions.

Instead of the torque, we can determine the power W_p as:

$$W_p = Q\omega_p = \frac{k_Q \rho f_p^3 D_p^5}{2\pi} = k_P \rho f_p^3 D_p^5 \qquad k_P = 2\pi k_Q \tag{A.27}$$

Where k_P is the power coefficient.

The propeller efficiency η_p can be determined from k_T and k_Q or k_P as (Ref. 19, p. 467):

$$\eta_p = \frac{1}{2\pi}\frac{k_T}{k_Q}J = \frac{k_T}{k_P}J \tag{A.28}$$

From which the intuitive conclusion can be drawn that the efficiency is maximized by increasing the ratio between the thrust and torque, at a given operating point.

The objective of the present analysis is thus to obtain adequate approximations of $k_T(J)$ and $k_Q(J)$ or $k_P(J)$ for a given propeller geometry.

The relative air velocity and aerodynamic forces on a propeller blade element is shown schematically below in Figure A.3:

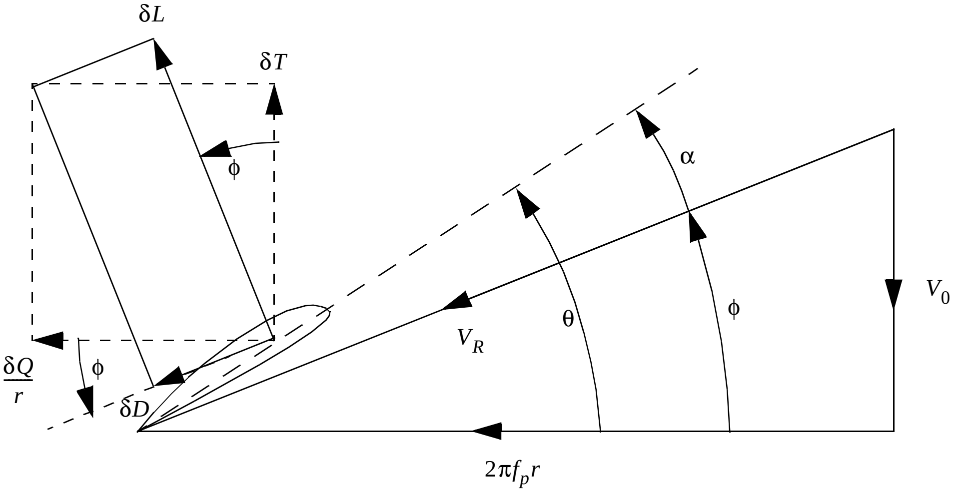

FIGURE A.3 Relative air velocity and aerodynamic forces on blade element.

Figure A.3 corresponds closely to Fig. 9.9 of (Ref. 19), except that the inflow velocity V_0 is used instead of the inflow factor. This is because the inflow factor is not defined for zero far field velocity V. The following equations thus corresponds to those given in (Ref. 19, p. 476-479).

The relative air velocity V_R is given by pythagoras from Figure A.3:

$$V_R^2 = (2\pi f_p r)^2 + V_0^2 \quad (A.29)$$

The local blade aerodynamic angle of attack can be determined from Figure A.3 as:

$$\alpha = \theta - \phi = \theta - \operatorname{atan}\left(\frac{V_0}{2\pi f_p r}\right) \quad (A.30)$$

The lift increment δL pr. unit blade radius is given by:

$$\delta L = \frac{1}{2} c(r) \delta r \rho V_R^2 C_L(r, \alpha) \quad (A.31)$$

The drag increment δD pr. unit blade radius is similarly given by:

$$\delta D = \frac{1}{2} c(r) \delta r \rho V_R^2 C_D(r, \alpha) \quad (A.32)$$

The local blade chord at radius r is denoted by $c(r)$, the local blade lift coefficient at radius r and aerodynamic angle of attack α is denoted by $C_L(r, \alpha)$, while the local blade drag coefficient is denoted by $C_D(r, \alpha)$.

From a propulsive viewpoint, the important “forces” are the thrust and the (propeller shaft) torque increment pr. unit blade radius, denoted by $\delta T / \delta r$ and $\delta Q / \delta r$ respectively.

From Figure A.3 the following trigonometric relationships between the lift and drag and the thrust and “torque force” on a blade element can be obtained:

$$\delta T = \cos(\phi)\delta L - \sin(\phi)\delta D \tag{A.33}$$

$$\delta Q = (\sin(\phi)\delta L + \cos(\phi)\delta D)r \tag{A.34}$$

Where r is the local blade element radius (distance to propeller shaft axis).

The shaft power δP required to drive the blade element at constant speed can then be determined as:

$$\delta P = 2\pi f_p \delta Q \tag{A.35}$$

The blade element efficiency η_e can then be determined as the ratio of effective power to shaft power of the blade element:

$$\eta_e \equiv V\frac{\delta T}{\delta P} = \frac{V}{2\pi f_p}\frac{\delta T}{\delta Q} \tag{A.36}$$

Notice that the far field air velocity V and not the local velocity V_0 is used in this definition, just as in Eq. A.22.

If the complete propeller geometry and aerodynamic properties of every blade element is specified, blade element theory as given above can in principle used to determine the complete characteristics of a particular propeller at a particular advance ratio. This is conceptually done in an iterative fashion by assuming that the inflow velocity V_0 is equal to the far field velocity V. Then the forces on a particular blade element can be determined using the above equations. Eq. A.21 from actuator disc theory can then be used to determine the slipstream velocity for that particular blade element, by taking the local thrust as the thrust of one blade element multiplied by the number of propeller blades and the actuator disc area as the swept area of the blade element. Eq. A.17 can then be used to find a new value for the inflow velocity V_0. Using this new V_0 value, new forces on the blade element can be found using blade element theory. After some iterations, convergence of the forces and inflow velocity will (hopefully) be achieved. By repeating this procedure for a number of radial blade elements, it is finally possible to integrate the thrust and torque contributions from the blade elements to get the characteristics of the complete propeller.

The above procedure will in theory give a reasonably accurate prediction of the characteristics of a particular propeller. However it is not really well suited for the purpose of choosing a suitable propeller and predicting the performance of a particular propeller for aircraft design purposes. This is mainly because of the shear effort involved in determining the complete geometry of the propeller (i.e. $c(r)$ and $\theta(r)$) and the aerodynamic properties of each blade element (i.e. $C_L(r, \alpha)$ and $C_D(r, \alpha)$). This basically means that blade element theory is best suited for propeller design and not for aircraft design.

A.3: Correlation to measured propeller characteristics

We can however use a simplified version of blade element theory to obtain a semiempirical propeller model which is useful for choosing a suitable propeller from a list of ready made propellers and for making engineering estimates of the performance of ready made propellers which lack adequate published performance data. This last point is particularly important when using model aircraft propellers, which are notorious for their almost complete lack of performance specifications.

Instead of analysing a large number of radial positions of the propeller using blade element theory with arbitrary $C_L(r, \alpha)$ and $C_D(r, \alpha)$ polars, we will correlate our propeller with a propeller of known characteristics by comparing the blade incidences θ_{75R} at a radius of $r = 0.75R$, where $R = 0.5D$ is the propeller radius. This choice of "characteristic" radius is inspired by (Ref. 20).

We will develop a correlation based on (Ref. 20, Fig. 5):

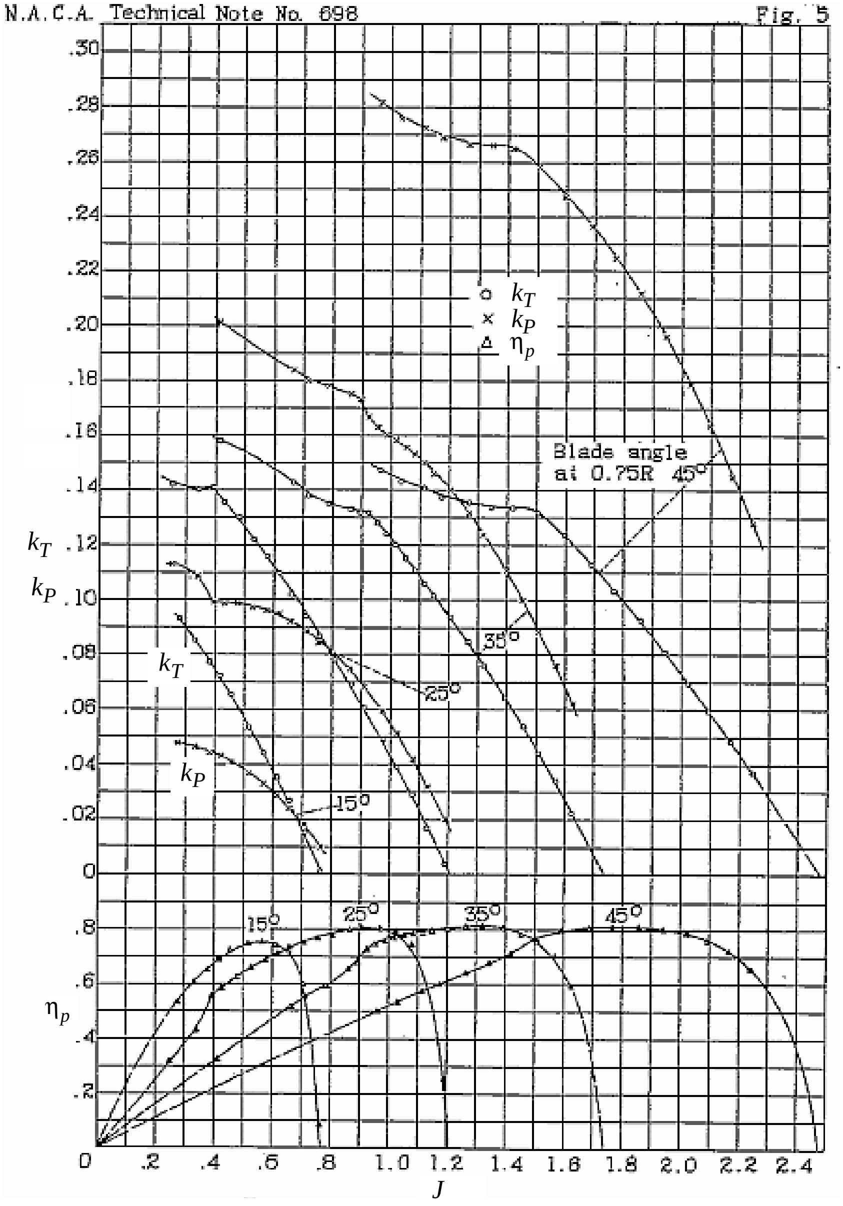

FIGURE A.4 Measured characteristics of a family of 2 bladed propellers (Ref. 20, Fig. 5).

In practice most propellers (including model airplane propellers) are characterised by the diameter D_p and the pitch P. The pitch is ideally the theoretical distance that the propeller advances in one revolution. However unlike the threads of a screw, the propeller moves through a fluid and not a solid. In practice the pitch of a propeller is defined using one of the following definitions:

- The distance that the propeller advances in one revolution at zero thrust.
- The distance that the propeller advances in one revolution at zero thrust from the blade section at $r = 0.75R$.
- The distance the propeller advances in one revolution as if the blade section at $r = 0.75R$ was cutting through a solid at an angle given by the local incidence $\theta_{75\mathrm{R}}$.

Only the first two definitions are unambiguous. The last definition has the problem that the difference between the zero lift angle and incidence depends on both the camber of the blade section and on the definition of the airfoil chord line. Unfortunately the pitch definition is rarely specified. However in most cases it appears that the last definition is used, even though it is the least precise.

Using the last pitch definition, we can obtain the following relationship between the incidence $\theta_{75\mathrm{R}}$ and the pitch with the aid of Figure A.3:

$$P = 0.75\pi D_p \tan(\theta_{75\mathrm{R}}) \tag{A.37}$$

This shows that the pitch is proportional to $\theta_{75\mathrm{R}}$ for small values of $\theta_{75\mathrm{R}}$.

This can be rewritten in terms of the nondimensional pitch P':

$$P' \equiv \frac{P}{D_p} = 0.75\pi \tan(\theta_{75\mathrm{R}}) \tag{A.38}$$

Referring to Figure A.4 we can make the following observations:

- The thrust $k_T(J)$ and power $k_P(J)$ coefficient curves are shifted to the right proportional to the nondimensional geometric pitch.
- In addition the power coefficient $k_P(J)$ is scaled approximately proportionally to the nondimensional geometric pitch.
- The maximum efficiency $\eta_{p,\max}$ is almost independent of the nondimensional geometric pitch.

Lets denote the nondimensional pitch of the reference propeller as P'_{ref} and the nondimensional pitch of the actual propeller as P'.

On the basis of these observations, we will propose the following scaling rules:

Scaling rule for the thrust coefficient:

$$k_T(J) \cong k_{T,\mathrm{ref}}(J - (P' - P'_{\mathrm{ref}})) \tag{A.39}$$

Where $k_{T,\mathrm{ref}}(J)$ is the thrust coefficient of the reference propeller.

The power coefficient is obtained as:

$$k_P(J) \cong k_{P,\mathrm{ref}}(J - (P' - P'_{\mathrm{ref}}))\frac{P'}{P'_{ref}} \tag{A.40}$$

Where $k_{P,\mathrm{ref}}(J)$ is the power coefficient of the reference propeller.

All we have to do now is choose the right reference curve to use for the correlation with our propeller. It turns out that non of the readily available model aircraft propellers for electric propulsion has a nondimensional pitch greater then one. The stated nondimensional pitch (Ref. 20, Fig. 3) of the propellers in Figure A.4 is shown below:

$\theta_{75R,\mathrm{ref}}$	P'_{ref}
15^o	0.64
25^o	1.10
35^o	1.65
45^o	2.36

Tabel A.1 Nondimensional pitch of propellers in Figure A.4.

This leads to the conclusion that the $\theta_{75R,\mathrm{ref}} = 15°$ curve should be used to obtain the characteristics of our propellers, with the help of Eq. A.39 and Eq. A.40.

As shown in Figure A.4, (Ref. 20) does not contain measurements for $J \le 0$ or for advance ratios giving negative thrust ($k_{T,\mathrm{ref}}(J) < 0$). The lack of measurements for $J \le 0$ and $k_{T,\mathrm{ref}}(J) < 0$ has been circumvented by extrapolation from known values, using some reasoning about the physics of the problem.

Having propeller characteristics for large advance ratios (where $k_{T,\mathrm{ref}}(J) < 0$), has the advantage that we can model the behaviour of a propeller that is “windmilling” (i.e. driven by the wind). This feature can be used as an airbrake to enable steep landing approaches and reduce the landing roll after touchdown.

A.4: Battery and motor “speed” regulator

The electric power for the propulsion system is stored in rechargable batteries. Control of the applied motor voltage is achieved using a “speed” regulator. The regulator will be approximated as a controlled voltage source. Since the regulator is implemented as a pulse width modulated (PWM) voltage source, the efficiency is close to unity. This means that the actual battery voltage is not important as long as it exceeds the desired motor voltage. Thus for preliminary analysis we can specify the battery entirely in terms of the available energy.

Appendix B: Spectral factorization of continues gust PSD’s

The PSD for “vertical” gusts are given by the Dryden approximation (Ref. 1, section III.13):

$$\Phi_w(\omega) = \frac{\sigma_w^2 L_w}{\pi U_w} \frac{1 + 3\left(\frac{L_w \omega}{U_w}\right)^2}{\left(1 + \left(\frac{L_w \omega}{U_w}\right)^2\right)^2} \tag{B.1}$$

Where $\Phi_w(\omega)$ is the temporal gust PSD for vertical gusts with respect to the angular frequency ω, L_w is the vertical turbulence length scale, σ_w is the vertical gaussian turbulence intensity and U_w is the flight speed through the quasisteady atmosphere. The flight speed U_w is defined as the speed relative to the atmosphere *without* wind gusts, but *including* steady wind. $\bar{w}(h)$.

The PSD can be factorized as:

$$\Phi_w(\omega) = G_w(j\omega)G_w(-j\omega)\sigma_w^2 \tag{B.2}$$

Where $G_w(s)$ is the transfer function of a linear continues filter which produces a stochastic signal with PSD given by $\Phi_w(\omega)$, when excited by a continues white noise signal with power density σ_w^2.

It is thus apparent that we should be able to realize $G_w(s)$ as a second order filter. A general continues second order filter can be expressed as:

$$G_w(s) = \frac{b_1 s + b_2}{s^2 + 2\alpha s + \omega_n^2} \tag{B.3}$$

Where ω_n is the undamped natural frequency of the filter.

Thus we have to determine the coefficients of $G_w(s)$ in such way that Eq. B.2 is satisfied. Computing the right hand side of Eq. B.2 gives:

$$\begin{aligned}
\Phi_w(\omega) &= \left(\frac{jb_1\omega + b_2}{-\omega^2 + j2\alpha\omega + \omega_n^2}\right)\left(\frac{-jb_1\omega + b_2}{-\omega^2 - j2\alpha\omega + \omega_n^2}\right)\sigma_w^2 \\
\Phi_w(\omega) &= \frac{b_1^2\omega^2 + b_2^2}{(-\omega^2 + \omega_n^2)^2 + 4\alpha^2\omega^2}\sigma_w^2 \\
\Phi_w(\omega) &= \frac{b_1^2\omega^2 + b_2^2}{\omega^4 + \omega_n^4 - 2\omega^2\omega_n^2 + 4\alpha^2\omega^2}\sigma_w^2 \\
\Phi_w(\omega) &= \frac{\left(\frac{1}{\omega_n}\right)^4 (b_1^2\omega^2 + b_2^2)}{1 + \left(\frac{\omega}{\omega_n}\right)^4 + \frac{4\alpha^2\omega^2 - 2\omega^2\omega_n^2}{\omega_n^4}}\sigma_w^2
\end{aligned} \tag{B.4}$$

We can then determine the value of the coefficients by comparing to Eq. B.2.

The denominator coefficients can be determined as:

$$\left(1+\left(\frac{L_w\omega}{U_w}\right)^2\right)^2 = 1+\left(\frac{L_w\omega}{U_w}\right)^4+2\left(\frac{L_w\omega}{U_w}\right)^2 = 1+\left(\frac{\omega}{\omega_n}\right)^4+\frac{4\alpha^2\omega^2-2\omega^2\omega_n^2}{\omega_n^4} \tag{B.5}$$

The coefficient ω_n can easily be determined by comparing the contributions with quadratic coefficients of ω:

$$\omega_n = \frac{U_w}{L_w} \tag{B.6}$$

The coefficient α can be determined by comparing the contributions with ω^2:

$$\begin{gathered}\frac{4\alpha^2-2\omega_n^2}{\omega_n^4} = 2\left(\frac{L_w}{U_w}\right)^2 \Leftrightarrow \frac{4\alpha^2-2\left(\frac{U_w}{L_w}\right)^2}{\left(\frac{U_w}{L_w}\right)^4} = 2\left(\frac{L_w}{U_w}\right)^2 \Leftrightarrow \frac{4\alpha^2-2\left(\frac{U_w}{L_w}\right)^2}{\left(\frac{U_w}{L_w}\right)^2} = 2\\ \frac{4L_w^2\alpha^2-2U_w{}^2}{U_w{}^2} = 2 \Leftrightarrow 4L_w^2\alpha^2-2U_w{}^2 = 2U_w{}^2 \Leftrightarrow 4L_w^2\alpha^2 = 4U_w{}^2\\ \alpha = \frac{U_w}{L_w} = \omega_n\end{gathered} \tag{B.7}$$

The coefficients in the numerator can be determined by comparing the numerator of Eq. B.1 with the numerator of Eq. B.4:

$$\frac{L_w}{\pi U_w}\left(1+3\left(\frac{L_w\omega}{U_w}\right)^2\right) = \left(\frac{1}{\omega_n}\right)^4(b_1^2\omega^2+b_2^2) = \left(\frac{L_w}{U_w}\right)^4(b_1^2\omega^2+b_2^2) \tag{B.8}$$

Comparing the coefficients of ω^2 gives:

$$3\frac{L_w}{\pi U_w}\left(\frac{L_w}{U_w}\right)^2 = \left(\frac{L_w}{U_w}\right)^4 b_1^2 \Leftrightarrow \frac{3}{\pi} = \frac{L_w}{U_w}b_1^2 \Leftrightarrow b_1 = \sqrt{\frac{3U_w}{\pi L_w}} \tag{B.9}$$

Comparing the constant terms gives:

$$\frac{L_w}{\pi U_w} = \left(\frac{L_w}{U_w}\right)^4 b_2^2 \Leftrightarrow \frac{U_w^3}{\pi L_w^3} = b_2^2 \Leftrightarrow b_2 = \sqrt{\frac{U_w^3}{\pi L_w^3}} \tag{B.10}$$

In summary we have determined the coefficients of $G_w(s)$ as:

$$\omega_n = \frac{U_w}{L_w} \qquad \alpha = \frac{U_w}{L_w} = \omega_n \qquad b_1 = \sqrt{\frac{3U_w}{\pi L_w}} \qquad b_2 = \sqrt{\frac{U_w^3}{\pi L_w^3}} \tag{B.11}$$

If we want to be able to produce a time domain gust signal using the filter $G_w(s)$, we can determine a state space implementation of $G_w(s)$ directly from Eq. B.4 using the reachable canonical form (Ref. 10, p. 67):

$$\begin{aligned} \dot{\mathbf{x}}_w &= \mathbf{A}_w\mathbf{x}_w + \mathbf{B}_w\mathbf{u}_w = \begin{bmatrix} 0 & 1 \\ -\omega_n^2 & -2\alpha \end{bmatrix}\mathbf{x}_w + \begin{bmatrix} 0 \\ 1 \end{bmatrix}u_w \\ y_w &= \mathbf{C}_w\mathbf{x}_w = \begin{bmatrix} b_2 & b_1 \end{bmatrix}\mathbf{x}_w \end{aligned} \tag{B.12}$$

This implements the filter $G_w(s) = \frac{Y(s)}{U(s)}$, where $Y(s)$ is the Laplace transform of the filter output $y_w(t)$ and $U(s)$ is the Laplace transform of the filter input $u_w(t)$.

For horizontal gusts in the axial flight path direction, the following PSD approximation due to Dryden is used:

$$\Phi_u(\omega) = \frac{2\sigma_u^2 L_u}{\pi U_w}\frac{1}{1 + \left(\frac{L_u\omega}{U_w}\right)^2} \tag{B.13}$$

Where $\Phi_u(\omega)$ is the temporal gust PSD for longitudinal gusts, L_u is the longitudinal turbulence length scale and σ_u is the longitudinal gaussian turbulence intensity.

This can be factorized as:

$$\Phi_u(\omega) = G_u(j\omega)G_u(-j\omega)\sigma_u^2 \tag{B.14}$$

Where $G_u(s)$ is the transfer function of a linear continues filter which produces a stochastic signal with PSD given by $\Phi_u(\omega)$, when excited by a continues white noise signal with power density σ_u^2.

It is then apparent that we should be able to realize $G_u(s)$ as a first order filter. A general continues first order filter can be expressed as:

$$G_u(s) = \frac{b_1}{s + a_1} \tag{B.15}$$

Where a_1 can be interpreted as the inverse of the filter time constant.

The right hand side of Eq. B.14 can then be expressed as:

$$\Phi_u(\omega) = \left(\frac{b_1}{j\omega + a_1}\right)\left(\frac{b_1}{-j\omega + a_1}\right)\sigma_u^2 = \frac{b_1^2}{\omega^2 + a_1^2}\sigma_u^2 = \frac{\left(\frac{1}{a_1}\right)^2 b_1^2}{\left(\frac{\omega}{a_1}\right)^2 + 1}\sigma_u^2 \tag{B.16}$$

Comparing the denominator of Eq. B.13 with that of Eq. B.16 gives:

$$1 + \left(\frac{L_u\omega}{U_w}\right)^2 = \left(\frac{\omega}{a_1}\right)^2 + 1 \quad \Leftrightarrow \quad a_1 = \frac{U_w}{L_u} \tag{B.17}$$

Comparing the numerator of Eq. B.13 with that of Eq. B.16 gives:

$$\frac{2\sigma_u^2 L_u}{\pi U_w} = \left(\frac{1}{a_1}\right)^2 b_1^2 \sigma_u^2 \quad\Leftrightarrow\quad \frac{2L_u}{\pi U_w} = \left(\frac{L_u}{U_w}\right)^2 b_1^2 \quad\Leftrightarrow\quad b_1 = \sqrt{\frac{2U_w}{\pi L_u}} \tag{B.18}$$

The reachable canonical state space form of $G_u(s)$ can then be determined as:

$$\begin{aligned} \dot{\mathbf{x}}_u &= \mathbf{A}_u \mathbf{x}_u + \mathbf{B}_u \mathbf{u}_u = \left[-a_1\right] \mathbf{x}_u + \left[1\right] u_u \\ y_u &= \mathbf{C}_u \mathbf{x}_u = \left[b_1\right] \mathbf{x}_u \end{aligned} \tag{B.19}$$

Appendix C: Conversion between stability and flight axis

One common way to include the aerodynamic effect of the lateral curvature of the flight path, in the lateral aerodynamic model, is to include a coefficient that depends on the yaw rate "r". The yaw rate is here defined as the derivative of the azimuth angle (compass course) of the longitudinal axis of the vehicle. This is done in the commonly used "stability" axis system, this system is defined in such a way that initially the $\mathbf{e}_x$ axis points in the same direction as $\mathbf{e}_{xf}$, for zero sideslip. However, the "stability" axis system moves with the body from this "trim" condition. For this reason it is unsuitable for simulations involving large lateral and longitudinal motions.

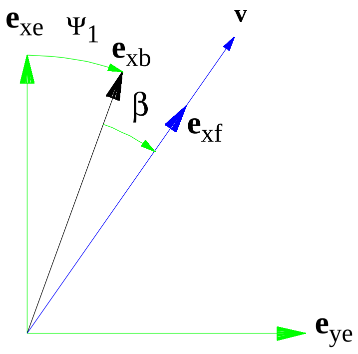

FIGURE C.1 Stability axis.

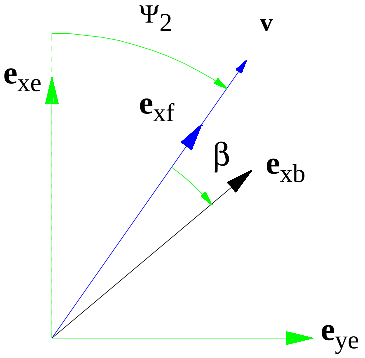

FIGURE C.2 Flight axis.

Where Ψ_1 is yaw angle of the UAV body, while Ψ_2 is the yaw angle of the flight path. It is apparent that the sense of the sideslip angle β is different for the two systems, while the absolute value is the same. Supposing that the $\mathbf{e}_{ze}$, the $\mathbf{e}_{zb}$ and the $\mathbf{e}_{zf}$ axis all point in the same direction (vertical down), the lateral curvature κ_b can be determined as:

$$\kappa_b = \frac{\dot{\Psi}_2}{U} \tag{C.1}$$

Comparing Figure C.1 and Figure C.2, we can write the down the following geometrical relationship:

$$\Psi_2 = \Psi_1 - \beta\big|_{flight} \tag{C.2}$$

The derivative of this is:

$$\dot{\Psi}_2 = \kappa_b U = \dot{\Psi}_1 - \dot{\beta}\Big|_{flight} \tag{C.3}$$

Conversion between aerodynamic derivatives in stability axis and flight axis:

In general we can write the lateral aerodynamic coefficients (C_Y, C_l and C_n) as:

Stability axis:

$$C_x = C_{x_\beta}(\alpha)\beta + C_{x_{\dot{\beta}}}(\alpha)\frac{\dot{\beta} s_w}{2U} + C_{xr}(\alpha)\frac{r s_w}{2U} + C_{x_p}(\alpha)\frac{\omega_{rf} s_w}{2U} + C_{x\eta}(\alpha)\eta_{\beta j}$$

(C.4)

Flight axis:

$$C_x = C_{x_\beta}(\alpha)\beta + C_{x_{\dot{\beta}}}(\alpha)\frac{\dot{\beta} s_w}{2U} + C_{x\kappa_b}(\alpha)\frac{\kappa_\beta s_w}{2} + C_{x_p}(\alpha)\frac{\omega_{rf} s_w}{2U} + C_{x\eta}(\alpha)\eta_{\beta j}$$

(C.5)

Where “x” can be “Y”, “l” or “n”. In the stability axis system, the subscript “r” denotes the yaw rate $\dot{\Psi}_1$.

The derivatives (of the aerodynamic coefficients) on the right hand side can *loosely* be defined as:

$$C_{x_y} \equiv \frac{\partial C_x}{\partial_y} \tag{C.6}$$

Where “y” is an aerodynamic variable such as β, $\dot{\beta}$, r, p e.t.c.

The aerodynamic derivatives with respect to β, p or $\eta_{\beta j}$ do not change by going from one system to another. We can also see from Eq. C.3, that when β is constant we have $\dot{\Psi}_2 = \dot{\Psi}_1$. Thus the aerodynamic derivative of κ_b is equal to that of “r”:

$$C_{x\kappa_b}(\alpha) = C_{xr}(\alpha) \tag{C.7}$$

When we however have a constant flight path yaw angle in the flight axis system ($\kappa_b = 0$), it is apparent from Eq. C.3, that we will have a yaw rate of $\dot{\Psi}_1 = \dot{\beta}|_{flight}$ in the stability axis system. The following relationship can then be established:

$$C_{x_{\dot{\beta}}}(\alpha)\Big|_{flight} = -C_{x_{\dot{\beta}}}(\alpha)\Big|_{stability} + C_{xr}(\alpha)|_{stability} \tag{C.8}$$

The definition of the roll angle rate about the longitudinal flight path axis, can be considered equal for both axis systems:

$$p \cong \omega_{rf} \tag{C.9}$$

Aerodynamic forces and moments:

For small lateral perturbations from zero sideslip, the stability system has the same orientation as the flight system. This means that the forces and moments found from the aerodynamic coefficients (C_L, C_D, C_Y, M_{yy}, M_{xx} and M_{zz}), are essentially the same for both systems.

Using the above relations, we can write the transformations between aerodynamic derivatives in the stability axis system and the flight axis system:

	Flight axis		Stability axis
Side force:	$C_{Y\beta}$	=	$-C_{Y\beta}$
	$C_{Y_{\dot{\beta}}}$	=	$-C_{Y_{\dot{\beta}}} + C_{Y_r}$
	$C_{Y\kappa_b}$	=	C_{Y_r}
	C_{Y_p}	=	C_{Y_p}
	C_{Y_η}	=	C_{Y_η}
Rolling moment:	$C_{l\beta}$	=	$-C_{l\beta}$
	$C_{l_{\dot{\beta}}}$	=	$-C_{l_{\dot{\beta}}} + C_{l_r}$
	$C_{l\kappa_b}$	=	C_{l_r}
	C_{l_p}	=	C_{l_p}
	C_{l_η}	=	C_{l_η}
Yawing moment:	$C_{n\beta}$	=	$-C_{n\beta}$
	$C_{n_{\dot{\beta}}}$	=	$-C_{n_{\dot{\beta}}} + C_{n_r}$
	$C_{n\kappa_b}$	=	C_{n_r}
	C_{n_p}	=	C_{n_p}
	C_{n_η}	=	C_{n_η}

Tabel C.1 Conversion between stability and flight axis.

Appendix D: Determination of approximate transfer function of servo

For a constant value of N_{servo}, the transfer function from $\theta_r(s)$ to $\theta(s)$ can be determined as:

$$\frac{\theta(s)}{\theta_r(s)} = \frac{K_p N_{servo} K_{vm}}{\tau_m s^2 + (N_{servo} K_{vm} + 1)s + K_p N_{servo} K_{vm}} \tag{D.1}$$

The transfer function from $\theta_r(s)$ to $u(s)$ can similarly be expressed as:

$$\frac{u(s)}{\theta_r(s)} = \frac{K_p(1 + \tau_m s)s}{\tau_m s^2 + (N_{servo} K_{vm} + 1)s + K_p N_{servo} K_{vm}} \tag{D.2}$$

Substituting $j\omega$ for s gives:

$$\frac{u(j\omega)}{\theta_r(j\omega)} = \frac{K_p(1 + \tau_m j\omega)j\omega}{(N_{servo} K_{vm} + 1)j\omega + K_p N_{servo} K_{vm} - \tau_m \omega^2} \tag{D.3}$$

The amplitude ratio between $\theta_r(j\omega)$ and $u(j\omega)$ can then be determined as:

$$\frac{\|u(j\omega)\|}{\|\theta_r(j\omega)\|} = \frac{\left\|K_p(j\omega + \tau_m \omega^2)(K_p N_{servo} K_{vm} - \tau_m \omega^2 - j\omega(N_{servo} K_{vm} + 1))\right\|}{(N_{servo} K_{vm} + 1)^2 + (K_p N_{servo} K_{vm} - \tau_m \omega^2)^2} \tag{D.4}$$

$$\frac{\|u(j\omega)\|}{\|\theta_r(j\omega)\|} = \frac{K_p \sqrt{\omega^2(\tau_m(K_p N_{servo} K_{vm} - \tau_m \omega^2) + (N_{servo} K_{vm} + 1))^2 + (\omega(K_p N_{servo} K_{vm} - \tau_m \omega^2) + \tau_m \omega^2 (N_{servo} K_{vm} + 1))^2}}{(N_{servo} K_{vm} + 1)^2 + (K_p N_{servo} K_{vm} - \tau_m \omega^2)^2}$$

From Eq. 3.3.8, we know that the amplitude of $N_{servo}(j\omega)$ can be determined as:

$$\|N(j\omega)\| = \frac{4V_s}{\pi\|u(j\omega)\|} \tag{D.5}$$

Appendix E: Static baseline between two GPS receivers using carrier phases

In order to quantify the pseudo range errors including the biases, it is necessary to determine the position difference between two static receivers to a relatively high accuracy. This could be done by directly measuring the distance vector between the receivers using a tape measure and compass. However this may prove cumbersome and inaccurate. There is however another way to accomplish this. Since the carrier phase measurements are several orders of magnitude more accurate then the pseudo ranges, they may be used to determine the distance vector (baseline) between two receivers. Unfortunately this is somewhat complicated by the fact that it is only possible to measure the carrier phases with an integer ambiguity of wavelengths. In order words we can easily measure the “millimeters” but not the “meters”. The following is a description of a simple “ambiguity resolution” method, based on the “Least Squares Ambiguity Search Technique” proposed by Hatch (Ref. 24, p. 232).

Assume that we have two receivers; RX1 and RX2. The two receivers are set up in such a way that their antennas are static and track a common number of satellites N_{SV}. For a single epoch, we may similarly to Eq. 5.4.1, express the range R_{i1} from RX1 to SV number “i” as:

$$\|\mathbf{P}_{SV,i} - \mathbf{P}_{RX1}\| = R_{i1} = \lambda CP_{i1} + \lambda N_{i1} + \lambda\Delta c_1 \tag{E.1}$$

Where Δc_1 is the RX1 LO phase error ($0 \le \Delta c_1 < 1$). $\lambda \equiv c/f_1 \cong 20\mathrm{cm}$ is the L1 carrier wavelength, CP_{i1} is the carrier phase ($0 \le CP_{i1} < 1$) and lastly N_{i1} is the integer ambiguity ($N_{i1} \in \aleph$).

A similar expression can be determined for RX2:

$$\|\mathbf{P}_{SV,i} - \mathbf{P}_{RX2}\| = R_{i2} = \lambda CP_{i2} + \lambda N_{i2} + \lambda\Delta c_2 \tag{E.2}$$

It is now possible to form the (single) difference between these two equations:

$$\begin{aligned} \Delta R_i \equiv R_{i2} - R_{i1} &= \lambda(CP_{i2} - CP_{i1}) + \lambda(N_{i2} - N_{i1}) + \lambda(\Delta c_2 - \Delta c_1) \\ \Delta R_i &= \lambda(CP_{i2} - CP_{i1}) + \lambda N_{i12} + \lambda\Delta c_{12} \end{aligned} \tag{E.3}$$

Where ΔR_i is the unknown range difference between the receivers, in the “direction” of SV number “i”, $CP_{i2} - CP_{i1}$ is the measured carrier phase difference, N_{i12} is the unknown integer ambiguity difference and Δc_{12} is the LO phase error difference.

From Section 5.4, we can expand the true range R_{i1} around the guessed position $\hat{\mathbf{P}}_{RX1}$ with the associated guessed range $\hat{R}_{i1}$:

$$\begin{aligned} R_{i1} &\cong \hat{R}_{i1} + \frac{x_{RX1} - x_{SV,i}}{\hat{R}_{i1}}\Delta x_{RX1} + \frac{y_{RX1} - y_{SV,i}}{\hat{R}_{i1}}\Delta y_{RX1} + \frac{z_{RX1} - z_{SV,i}}{\hat{R}_{i1}}\Delta z_{RX1} \\ R_{i1} &\cong \hat{R}_{i1} + \frac{(\hat{\mathbf{P}}_{RX1} - \mathbf{P}_{SV,i})}{\hat{R}_{i1}} \bullet \Delta\mathbf{P}_{RX1} \end{aligned} \tag{E.4}$$

Where $\Delta\mathbf{P}_{RX1} = (\Delta x_{RX1}, \Delta y_{RX1}, \Delta z_{RX1})$ is the vector from the guessed position to the true position. A similar expression of course holds for RX2.

Combining Eq. E.3 and Eq. E.4, gives a linearized relationship between the measured single difference phases and the SV ranges:

$$\hat{R}_{i2} + \frac{(\hat{\mathbf{P}}_{RX2} - \mathbf{P}_{SV,i})}{\hat{R}_{i2}} \bullet \Delta\mathbf{P}_{RX2} - \left(\hat{R}_{i1} + \frac{(\hat{\mathbf{P}}_{RX1} - \mathbf{P}_{SV,i})}{\hat{R}_{i1}} \bullet \Delta\mathbf{P}_{RX1}\right) \cong \lambda(CP_{i2} - CP_{i1}) + \lambda N_{i12} + \lambda\Delta c_{12} \qquad (E.5)$$

Assuming that the phase difference $(CP_{i2} - CP_{i1})$ is measured and that N_{i12} is known, while the relative LO phase error Δc_{12} is unknown, the equation can be rearranged with the unknowns on the left hand side:

$$\frac{(\hat{\mathbf{P}}_{RX2} - \mathbf{P}_{SV,i})}{\hat{R}_{i2}} \bullet \Delta\mathbf{P}_{RX2} - \frac{(\hat{\mathbf{P}}_{RX1} - \mathbf{P}_{SV,i})}{\hat{R}_{i1}} \bullet \Delta\mathbf{P}_{RX1} - \lambda\Delta c_{12} \cong \lambda(CP_{i2} - CP_{i1}) + \lambda N_{i12} - \Delta\hat{R}_i \qquad (E.6)$$

Where $\Delta\hat{R}_i \equiv \hat{R}_{i2} - \hat{R}_{i1}$ is the difference between the range from the guessed RX2 position to the SV and the range from guessed RX1 position to the SV.

Since we are interested in the differential position $\mathbf{P}_{RX12} \equiv \mathbf{P}_{RX2} - \mathbf{P}_{RX1}$, with the position of the reference station RX1 known, it follows that the position correction $\Delta\mathbf{P}_{RX1}$ of the RX1 position can be taken equal to zero:

$$\frac{(\hat{\mathbf{P}}_{RX2} - \mathbf{P}_{SV,i})}{\hat{R}_{i2}} \bullet \Delta\mathbf{P}_{RX12} - \lambda\Delta c_{12} \cong \lambda(CP_{i2} - CP_{i1}) + \lambda N_{i12} - \Delta\hat{R}_i \qquad (E.7)$$

Where $\Delta\mathbf{P}_{RX12}$ is the relative RX1 to RX2 position correction, of the guessed RX1 to RX2 position difference $\hat{\mathbf{P}}_{RX12}$.

In analogy with the point position solution given in Section 5.4 the equations for all N satellites, which are common to RX1 and RX2, can be expressed as a linear matrix equation:

$$\begin{bmatrix} \frac{\hat{x}_{RX2} - x_{SV,1}}{\hat{R}_{12}} & \frac{\hat{y}_{RX2} - y_{SV,1}}{\hat{R}_{12}} & \frac{\hat{z}_{RX2} - z_{SV,1}}{\hat{R}_{12}} & -\lambda \\ \frac{\hat{x}_{RX2} - x_{SV,2}}{\hat{R}_{22}} & \frac{\hat{y}_{RX2} - y_{SV,2}}{\hat{R}_{22}} & \frac{\hat{z}_{RX2} - z_{SV,2}}{\hat{R}_{22}} & -\lambda \\ \dots & \dots & \dots & \dots \\ \frac{\hat{x}_{RX2} - x_{SV,N}}{\hat{R}_{N2}} & \frac{\hat{y}_{RX2} - y_{SV,N}}{\hat{R}_{N2}} & \frac{\hat{z}_{RX2} - z_{SV,N}}{\hat{R}_{N2}} & -\lambda \end{bmatrix} \begin{bmatrix} \Delta x_{RX12} \\ \Delta y_{RX12} \\ \Delta z_{RX12} \\ \Delta c_{12} \end{bmatrix} \cong \begin{bmatrix} \lambda(CP_{12} - CP_{11}) + \lambda N_{1,12} - \Delta\hat{R}_1 \\ \lambda(CP_{22} - CP_{21}) + \lambda N_{2,12} - \Delta\hat{R}_2 \\ \dots \\ \lambda(CP_{N2} - CP_{N1}) + \lambda N_{N,12} - \Delta\hat{R}_N \end{bmatrix} \qquad (E.8)$$

This naturally leads to the introduction of two matrices $\mathbf{A}_{CP}$ and $\mathbf{Y}_{CP}$:

$$\mathbf{A}_{CP} \equiv \begin{bmatrix} \frac{\hat{x}_{RX2} - x_{SV,1}}{\hat{R}_{12}} & \frac{\hat{y}_{RX2} - y_{SV,1}}{\hat{R}_{12}} & \frac{\hat{z}_{RX2} - z_{SV,1}}{\hat{R}_{12}} & -\lambda \\ \frac{\hat{x}_{RX2} - x_{SV,2}}{\hat{R}_{22}} & \frac{\hat{y}_{RX2} - y_{SV,2}}{\hat{R}_{22}} & \frac{\hat{z}_{RX2} - z_{SV,2}}{\hat{R}_{22}} & -\lambda \\ \dots & \dots & \dots & \dots \\ \frac{\hat{x}_{RX2} - x_{SV,N}}{\hat{R}_{N2}} & \frac{\hat{y}_{RX2} - y_{SV,N}}{\hat{R}_{N2}} & \frac{\hat{z}_{RX2} - z_{SV,N}}{\hat{R}_{N2}} & -\lambda \end{bmatrix} \qquad \mathbf{Y}_{CP} \equiv \begin{bmatrix} \lambda(CP_{12} - CP_{11}) + \lambda N_{1,12} - \Delta\hat{R}_1 \\ \lambda(CP_{22} - CP_{21}) + \lambda N_{2,12} - \Delta\hat{R}_2 \\ \dots \\ \lambda(CP_{N2} - CP_{N1}) + \lambda N_{N,12} - \Delta\hat{R}_N \end{bmatrix} \qquad (E.9)$$

In theory, the solution to Eq. E.8 can be expressed as:

$$\Delta\tilde{\mathbf{P}}_{\mathrm{RX12}} = \begin{bmatrix} \Delta x_{\mathrm{RX12}} \\ \Delta y_{\mathrm{RX12}} \\ \Delta z_{\mathrm{RX12}} \\ \Delta c_{12} \end{bmatrix} = (\mathbf{A}_{\mathrm{CP}})^{-1}\mathbf{Y}_{\mathrm{CP}} \tag{E.10}$$

This equation can of course only be solved if $(\mathbf{A}_{\mathrm{CP}})^{-1}$ exists, i.e. the rank of $\mathbf{A}_{\mathrm{CP}}$ must be 4.

Since we have just *assumed* that the integer ambiguities $\mathrm{N}_{\mathrm{i12}}$ are known, which they are not in general, $\mathbf{Y}_{\mathrm{CP}}$ and thus the solution $\Delta\tilde{\mathbf{P}}_{\mathrm{RX12}}$ in Eq. E.10 corresponds to a certain *choice* of integer ambiguities given 4 SV's.

The key to the "Least Squares Ambiguity Search Technique" proposed by Hatch (Ref. 24, p. 232) is to assume that the carrier phases to more then 4 common SV's are available. This implies that the system of equations (Eq. E.8) are overdetermined for a given choice of integer ambiguities. This extra information can then be used to select the most likely set of integer ambiguities that satisfies the system of equations in a stochastic (least squares) sense.

E.5: Ambiguity search

The first step in solving the system of equations (Eq. E.8), with the a priori unknown ambiguities, is to determine the statistical "best" ambiguities.

First the ambiguity search range must be determined. This is the set of integer ambiguities, which is known to contain the true ambiguities. This set of integer ambiguities can be expressed as:

$$\mathrm{N}_{\mathrm{i12,min}} \le \mathrm{N}_{\mathrm{i12}} \le \mathrm{N}_{\mathrm{i12,max}} \tag{E.11}$$

The ambiguity search range can be determined from the pseudo range differential position estimate.

In order to start the search, 4 SV's with a good DOP and reasonable elevations are selected (more then about $20°$). Using these 4 *primary* SV's and their associated integer ambiguity ranges as given by Eq. E.11, a number of candidate solutions to Eq. E.10 are determined. This gives a number of candidate position solutions. The candidate positions can then be expressed as:

$$\mathbf{P}_{\mathrm{RX12C}} \cong \hat{\mathbf{P}}_{\mathrm{RX12}} + \Delta\tilde{\mathbf{P}}_{\mathrm{RX12C}} = \hat{\mathbf{P}}_{\mathrm{RX12}} + (\mathbf{A}_{\mathrm{CPC}})^{-1}\mathbf{Y}_{\mathrm{CPC}} \tag{E.12}$$

Where $\hat{\mathbf{P}}_{\mathrm{RX12}}$ is the a priori estimated baseline vector, $\mathbf{A}_{\mathrm{CPC}}$ is the Carrier Phase Candidate system matrix, $\mathbf{Y}_{\mathrm{CPC}}$ is the Carrier Phase Candidate measurement matrix and $\mathbf{P}_{\mathrm{RX12C}}$ is the candidate baseline vector.

It follows that $\mathbf{A}_{CPC}$ is a 4x4 matrix and $\mathbf{Y}_{CPC}$ is a 4x1 matrix, defined as subsets of $\mathbf{A}_{CP}$ and $\mathbf{Y}_{CP}$ respectively:

$$\mathbf{A}_{CPC} \equiv \begin{bmatrix} \frac{\hat{x}_{RX2} - x_{SV,1}}{\hat{R}_{12}} & \frac{\hat{y}_{RX2} - y_{SV,1}}{\hat{R}_{12}} & \frac{\hat{z}_{RX2} - z_{SV,1}}{\hat{R}_{12}} & -\lambda \\ \frac{\hat{x}_{RX2} - x_{SV,2}}{\hat{R}_{22}} & \frac{\hat{y}_{RX2} - y_{SV,2}}{\hat{R}_{22}} & \frac{\hat{z}_{RX2} - z_{SV,2}}{\hat{R}_{22}} & -\lambda \\ \frac{\hat{x}_{RX2} - x_{SV,3}}{\hat{R}_{32}} & \frac{\hat{y}_{RX2} - y_{SV,3}}{\hat{R}_{32}} & \frac{\hat{z}_{RX2} - z_{SV,3}}{\hat{R}_{32}} & -\lambda \\ \frac{\hat{x}_{RX2} - x_{SV,4}}{\hat{R}_{42}} & \frac{\hat{y}_{RX2} - y_{SV,4}}{\hat{R}_{42}} & \frac{\hat{z}_{RX2} - z_{SV,4}}{\hat{R}_{42}} & -\lambda \end{bmatrix} \qquad \mathbf{Y}_{CPC} \equiv \begin{bmatrix} \lambda(CP_{12} - CP_{11}) + \lambda N_{1,12} - \Delta\hat{R}_1 \\ \lambda(CP_{22} - CP_{21}) + \lambda N_{2,12} - \Delta\hat{R}_2 \\ \lambda(CP_{32} - CP_{31}) + \lambda N_{3,12} - \Delta\hat{R}_3 \\ \lambda(CP_{42} - CP_{41}) + \lambda N_{4,12} - \Delta\hat{R}_4 \end{bmatrix} \qquad \text{(E.13)}$$

Inspection of $\mathbf{Y}_{CPC}$ reveals that it is in fact the sum of 3 components; the unambiguous phase measurements $\lambda(CP_{i2} - CP_{i1})$, the integer ambiguities λN_{i12} and the a priori estimated range difference $-\Delta R_1$. This means that $\mathbf{Y}_{CPC}$ can be expressed as:

$$\mathbf{Y}_{CPC} = \mathbf{Y}_{CPC1}(CP_{i2} - CP_{i1}) + \mathbf{Y}_{CPC2}(N_{i12}) + \mathbf{Y}_{CPC3}(\Delta\hat{R}_1) = \lambda \begin{bmatrix} CP_{12} - CP_{11} \\ CP_{22} - CP_{21} \\ CP_{32} - CP_{31} \\ CP_{42} - CP_{41} \end{bmatrix} + \lambda \begin{bmatrix} N_{1,12} \\ N_{2,12} \\ N_{3,12} \\ N_{4,12} \end{bmatrix} - \begin{bmatrix} \Delta\hat{R}_1 \\ \Delta\hat{R}_2 \\ \Delta\hat{R}_3 \\ \Delta\hat{R}_4 \end{bmatrix} \qquad \text{(E.14)}$$

The candidate baseline vectors (the solutions to Eq. E.12) can then be expressed as:

$$\mathbf{P}_{RX12C} \cong \hat{\mathbf{P}}_{RX12} + (\mathbf{A}_{CPC})^{-1}\mathbf{Y}_{CPC1}(CP_{i2} - CP_{i1}) + (\mathbf{A}_{CPC})^{-1}\mathbf{Y}_{CPC2}(N_{i12}) + (\mathbf{A}_{CPC})^{-1}\mathbf{Y}_{CPC3}(\Delta\hat{R}_i) \qquad \text{(E.15)}$$

It is possible to rearrange this equation, so that it contains a "constant" part and a part that is linear with respect to the ambiguities $\mathbf{N}_{12} \equiv \begin{bmatrix} N_{1,12} & N_{2,12} & N_{3,12} & N_{4,12} \end{bmatrix}^T$:

$$\mathbf{P}_{RX12C} \cong \hat{\mathbf{P}}_{RX12,0} + \mathbf{M}_{CPC2}\mathbf{N}_{12} \qquad \text{(E.16)}$$

Where $\hat{\mathbf{P}}_{RX12,0}$ and $\mathbf{M}_{CPC2}$ are independent of $\mathbf{N}_{12}$:

$$\hat{\mathbf{P}}_{RX12,0} \equiv \hat{\mathbf{P}}_{RX12} + \lambda(\mathbf{A}_{CPC})^{-1}\mathbf{CP}_{12} - (\mathbf{A}_{CPC})^{-1}\Delta\hat{\mathbf{R}}_{12} \qquad \text{(E.17)}$$

$$\mathbf{M}_{CPC2} \equiv \lambda(\mathbf{A}_{CPC})^{-1} \qquad \text{(E.18)}$$

Eq. E.16 is of course valid for several consecutive epochs, with constant ambiguities $\mathbf{N}_{12(t)} = \mathbf{N}_{12}$. However, neither $\mathbf{CP}_{12}$, $\Delta\mathbf{R}_{12} \equiv \begin{bmatrix} \Delta\hat{R}_{1,12} & \Delta\hat{R}_{2,12} & \Delta\hat{R}_{3,12} & \Delta\hat{R}_{4,12} \end{bmatrix}^T$ or $\mathbf{A}_{CPC}$ are independent of time. This implies that $\mathbf{P}_{RX12,0}$ and $\mathbf{M}_{CPC2}$ are functions of time.

As will become apparent later, $\hat{\mathbf{P}}_{RX12,0(t)}$ has a constant deterministic derivative superimposed with a relatively high frequency noise component. On the basis of these observations, we will assume that for a 300 sec. time span (5 min.), a linear model of the deterministic time dependency of Eq. E.16 can be used:

$$\mathbf{P}_{RX12C} \cong (\mathbf{C}_{RX12,0} + \mathbf{C}_{RX12,1}t) + (\mathbf{M}_{CPC2,0} + \mathbf{M}_{CPC2,1}t)\mathbf{N}_{12} \qquad \text{(E.19)}$$

Where the constants $\mathbf{C}_{RX12,0}$, $\mathbf{C}_{RX12,1}$, $\mathbf{M}_{CPC2,0}$ and $\mathbf{M}_{CPC2,1}$ are given by:

$$\begin{aligned} &\mathbf{C}_{RX12,0} \cong \hat{\mathbf{P}}_{RX12,0}(t = 0) \qquad \mathbf{C}_{RX12,1} \cong \frac{\partial}{\partial t}(\hat{\mathbf{P}}_{RX12,0}) \\ &\mathbf{M}_{CPC2,0} \equiv \mathbf{M}_{CPC2}(t = 0) \qquad \mathbf{M}_{CPC2,1} = \frac{\mathbf{M}_{CPC2}(\Delta t_{epoch}) - \mathbf{M}_{CPC2}(0)}{\Delta t_{epoch}} \cong \dot{\mathbf{M}}_{CPC2} \end{aligned} \tag{E.20}$$

The actual values of $\mathbf{C}_{RX12,0}$ and $\mathbf{C}_{RX12,1}$ are determined by a least squares curve fit over the appropriate epoch range, since $\hat{\mathbf{P}}_{RX12,0}$ is corrupted by phase measurement noise, which is not a problem with $\mathbf{M}_{CPC2}$. The origin of the integer time “t” is assumed to be at the start of the epoch range, the total epoch range is given by Δt_{epoch}. Since several consecutive epochs are now considered when determining $\hat{\mathbf{P}}_{RX12,0}$ and thus $\mathbf{C}_{RX12,0}$, we can not in general require that $0 \le CP_{i1} < 1$ and $0 \le CP_{i2} < 1$ for every epoch. Instead we will require that the phases are in these ranges for the first epoch, for subsequent epochs the phases are allowed to decrease or increase continuously without jumps.

The result is that these “measurement” constants can be seen as “mean” values and “mean” derivatives of $\hat{\mathbf{P}}_{RX12,0}$. Eq. E.19 thus has a better signal to noise ratio then the original single epoch equation given by Eq. E.16, because of the smoothing effect of the least squares curve fit. This reduces the effects of broadband phase measurement noise (i.e. white noise). This leads to the important practical conclusion that each candidate position can be determined by one matrix multiplication and one vector addition. This makes computation of all the candidate positions relatively fast.

We can now return to the problem of determining the ambiguity search ranges for the primary SV’s. Since equation Eq. E.19 is used to determine a candidate position, given a specific integer ambiguity, this relationship can be rearranged to determine a “float” integer ambiguity given a position guess:

$$\mathbf{Y}_{CPC2} = \mathbf{M}_{CPC2}^{-1}(\mathbf{P}_{RX12C} - \hat{\mathbf{P}}_{RX12,0}) \tag{E.21}$$

Using the definition of $\mathbf{Y}_{CPC2}$ gives:

$$\begin{bmatrix} N_{1,12} \\ N_{2,12} \\ N_{3,12} \\ N_{4,12} \end{bmatrix} = \frac{\mathbf{M}_{CPC2}^{-1}(\mathbf{P}_{RX12C} - \hat{\mathbf{P}}_{RX12,0})}{\lambda} \tag{E.22}$$

This equation can be used to determine the ambiguity search limits, given the geometric limits on the candidate positions as determined using the pseudorange baseline uncertainty.

Another method of determining the most likely float ambiguity is based on the time varying part of Eq. E.19. Since Eq. E.19 must be valid for any epoch in the epoch range, it follows that $\dot{\mathbf{P}}_{RX12C}$ must be zero for the most likely float ambiguity. This can be formulated as:

$$\dot{\mathbf{P}}_{RX12C} \cong \mathbf{C}_{RX12,1} + \mathbf{M}_{CPC2,1}\mathbf{N}_{12} = 0 \tag{E.23}$$

The most likely float ambiguity $\mathbf{N}_{12F}$ can then be determined as:

$$\mathbf{N}_{12F} = -\mathbf{M}_{CPC2,1}^{-1}\mathbf{C}_{RX12,1} \tag{E.24}$$

The corresponding float baseline solution $\mathbf{P}_{RX12F}$ is given by:

$$\mathbf{P}_{RX12F} = \mathbf{C}_{RX12,0} + \mathbf{M}_{CPC2,0}\mathbf{N}_{12F} \tag{E.25}$$

The key to the ambiguity resolution method is then to test the compatibility of each of these candidate solutions, to the carrier phase measurements for the rest of the SV's. This compatibility can be quantified by the residual. The residual is zero when the measured phase difference exactly corresponds to the baseline estimate. The residual can then be defined from Eq. E.7 as:

$$\mathrm{CP}_{res,i} \equiv \frac{1}{\lambda}\left\{\frac{(\hat{\mathbf{P}}_{RX2} - \mathbf{P}_{SV,i})}{\hat{\mathrm{R}}_{i2}} \bullet \Delta\mathbf{P}_{RX12C} + \Delta\hat{\mathrm{R}}_{i}\right\} - \{(\mathrm{CP}_{i2} - \mathrm{CP}_{i1}) + \mathrm{N}_{i12} + \Delta c_{12c}\} \tag{E.26}$$

Where the phase residual for SV number "i" is denoted by $\mathrm{CP}_{res,i}$. The candidate baseline update $\Delta\mathbf{P}_{RX12C}$ and LO phase error Δc_{12C}
are determined from Eq. E.12 as:

$$\begin{bmatrix}\Delta\mathbf{P}_{RX12C}\\ \Delta c_{12C}\end{bmatrix} = \Delta\tilde{\mathbf{P}}_{RX12C} = \mathbf{P}_{RX12C} - \hat{\mathbf{P}}_{RX12} = \hat{\mathbf{P}}_{RX12,0} + \mathbf{M}_{CPC2}\mathbf{N}_{12} - \hat{\mathbf{P}}_{RX12} \tag{E.27}$$

Using Eq. E.26 and Eq. E.27 for a secondary SV, gives a carrier phase residual for each of the candidate baselines. The true baseline must then belong to the candidate baselines which exhibit a numerical small residual to the secondary SV's.

For computational ease we can define an auxiliary function which is equal to the residual for $\mathrm{N}_{i12} = 0$:

$$\tilde{\mathrm{C}}\mathrm{P}_{res,i} \equiv \frac{1}{\lambda}\left\{\frac{(\hat{\mathbf{P}}_{RX2} - \mathbf{P}_{SV,i})}{\hat{\mathrm{R}}_{i2}} \bullet \Delta\mathbf{P}_{RX12C} + \Delta\hat{\mathrm{R}}_{i}\right\} - \{(\mathrm{CP}_{i2} - \mathrm{CP}_{i1}) + \Delta c_{12C}\} \tag{E.28}$$

This can be expressed in matrix form for all secondary SV's as:

$$\tilde{\mathbf{C}}\mathbf{P}_{res} = \tilde{\mathbf{C}}\mathbf{P}_{res,0} + \mathbf{M}_{res}\Delta\tilde{\mathbf{P}}_{RX12C} \tag{E.29}$$

Where $\tilde{\mathbf{C}}\mathbf{P}_{res,0}$ and $\mathbf{M}_{res}$ are constants with respect to both epoch count and candidate position, defined by:

$$\tilde{\mathbf{C}}\mathbf{P}_{res,0} \equiv \frac{1}{\lambda}\Delta\hat{\mathbf{R}}_{12} - \mathbf{CP}_{12} \tag{E.30}$$

$$\mathbf{M}_{res,i} \equiv \begin{bmatrix}\frac{1}{\lambda}\frac{(\hat{\mathbf{P}}_{RX2} - \mathbf{P}_{SV,i})}{\hat{\mathrm{R}}_{i2}} & -1\end{bmatrix} \tag{E.31}$$

Where $(\hat{\mathbf{P}}_{RX2} - \mathbf{P}_{SV,i})$ is used as a row matrix (i.e. with dimensions 1×3) and $\mathbf{M}_{res,i}$ is the i'th row of $\mathbf{M}_{res}$.

Using $\tilde{CP}_{res,i}$, we can determine the (smallest) residual and corresponding integer ambiguity for the each secondary SV, with respect to a candidate solution $\Delta\mathbf{P}_{RX12C}$:

$$CP_{res,i} = \tilde{CP}_{res,i} - round(\tilde{CP}_{res,i}) \tag{E.32}$$

And:

$$N_{i12} = \tilde{CP}_{res,i} - CP_{res,i} = round(\tilde{CP}_{res,i}) \tag{E.33}$$

Where the operator "$round(x)$" is x rounded to the nearest integer.

It then follows that the phase residuals will belong to the range $-0.5 < CP_{res,i} \le 0.5$, with a value of zero if the secondary SV phase measurements are perfectly matched to the candidate position. As a convenient measure of the "size" of the phase residual vector $\mathbf{CP}_{res}$, we may use the Root Mean Square (RMS) residue:

$$RMS_{res} = \frac{\|\mathbf{CP}_{res}\|}{\sqrt{N_{sec}}} \tag{E.34}$$

Where N_{sec} is the number of secondary SV's and $\|\mathbf{x}\|$ is the 2 norm of the vector "$\mathbf{x}$".

Since $|CP_{res,i}| \le 0.5$, the maximum value of RMS_{res} is equal to 0.5, independent of the number of secondary SV's.

As given above, the residual is determined for a single epoch. Just as with the candidate positions, we can reduce the effects of broadband measurement noise by fitting a straight line to the data. This will not only provide a more accurate residual estimate but also an idea of the measurement noise for a particular SV:

$$\tilde{\mathbf{CP}}_{res} \cong (\mathbf{C}_{res,0} + \mathbf{C}_{res,1}t) + (\mathbf{M}_{res,0} + \mathbf{M}_{res,1}t)\Delta\tilde{\mathbf{P}}_{RX12C} \tag{E.35}$$

Where the constants $\mathbf{C}_{res,0}$, $\mathbf{C}_{res,1}$, $\mathbf{M}_{res,0}$ and $\mathbf{M}_{res,1}$ are given by:

$$\begin{gathered} \mathbf{C}_{res,0} \cong \tilde{\mathbf{CP}}_{res,0}(t=0) \qquad \mathbf{C}_{res,1} \cong \frac{\partial}{\partial t}(\tilde{\mathbf{CP}}_{res,0}) \\ \mathbf{M}_{res,0} \equiv \mathbf{M}_{res}(t=0) \qquad \mathbf{M}_{res,1} = \frac{\mathbf{M}_{res}(\Delta t_{epoch}) - \mathbf{M}_{res}(0)}{\Delta t_{epoch}} \cong \dot{\mathbf{M}}_{res} \end{gathered} \tag{E.36}$$

The actual values of $\mathbf{C}_{res,0}$ and $\mathbf{C}_{res,1}$ are determined by a least squares curve fit over the appropriate epoch range, since $\mathbf{CP}_{res,0}$ is corrupted by phase measurement noise. The procedure is otherwise similar to the one used to determine the primary SV measurement constants.

This enables the carrier phase residual vector $\mathbf{CP}_{res}$ for any candidate position, to be computed using only one matrix product, one vector addition and one round operation.

Before proceeding further, there is one slight correction which is worth making to the above expressions, at least for consistency. When $\hat{\mathbf{P}}_{RX12,0}$ is determined for each epoch, it will be noticed that the last element, the Local Oscillator (LO) phase difference Δc_{12} varies erratically from epoch to epoch. This implies that the curve fit used to obtain $\mathbf{C}_{RX12,0}$ and $\mathbf{C}_{RX12,1}$ in Eq. E.19, will be meaningless for the phase difference terms. Since the phase difference directly influences the phase difference measurements

$\mathbf{CP}_{12}$, it will directly influence $\widetilde{\mathbf{CP}}_{\mathrm{res},0}$ as defined in Eq. E.30. It would thus be desirable if the influence of the phase difference could be removed before determining the "measurement constants". This can be accomplished by noting that at each epoch, the phase difference for the candidate position with $\mathbf{N}_{12} = \mathbf{0}$ is determined as the last element of $\hat{\mathbf{P}}_{\mathrm{RX12},0}$ using Eq. E.17. Furthermore the term $\mathbf{M}_{\mathrm{CPC2}}\mathbf{N}_{12}$ contains the contribution to the phase difference, caused by a candidate baseline different from $\hat{\mathbf{P}}_{\mathrm{RX12},0}$. The trick is then to first determine the phase difference using Eq. E.17:

$$\Delta c_{12,0} = \begin{bmatrix} 0 & 0 & 0 & 1 \end{bmatrix} \hat{\mathbf{P}}_{\mathrm{RX12},0} \tag{E.37}$$

This contribution is added to Eq. E.30, to obtain an expression for $\widetilde{\mathbf{CP}}_{\mathrm{res},0}$ corrected for the phase difference for $\mathbf{N}_{12} = \mathbf{0}$ (the sign of this term is given by Eq. E.28):

$$\widetilde{\mathbf{CP}}_{\mathrm{res},0} \equiv \frac{1}{\lambda}\Delta\hat{\mathbf{R}}_{12} - \mathbf{CP}_{12} - \Delta c_{12,0} \tag{E.38}$$

Now the term $\Delta c_{12,0}$ can be removed from $\hat{\mathbf{P}}_{\mathrm{RX12},0}$:

$$\hat{\mathbf{P}}_{\mathrm{RX12},0} = \begin{bmatrix} \mathrm{x}_{\mathrm{RX12},0} \\ \mathrm{y}_{\mathrm{RX12},0} \\ \mathrm{z}_{\mathrm{RX12},0} \\ \Delta c_{12,0} \end{bmatrix} = \begin{bmatrix} \mathrm{x}_{\mathrm{RX12},0} \\ \mathrm{y}_{\mathrm{RX12},0} \\ \mathrm{z}_{\mathrm{RX12},0} \\ 0 \end{bmatrix} \tag{E.39}$$

This will produce the correct result when calculating the residuals using Eq. E.29, because the 4'th element of $\Delta\tilde{\mathbf{P}}_{\mathrm{RX12C}}$ is zero when $\mathbf{N}_{12} = \mathbf{0}$. In other words the term $\mathbf{M}_{\mathrm{res}}\Delta\tilde{\mathbf{P}}_{\mathrm{RX12C}}$ corrects the residual for phase differences caused by $\mathbf{N}_{12} \neq \mathbf{0}$.

The rest of the above equations are used as described, including the curve fits of $\mathbf{C}_{\mathrm{RX12},0}$, $\mathbf{C}_{\mathrm{RX12},1}$, $\mathbf{C}_{\mathrm{res},0}$ and $\mathbf{C}_{\mathrm{res},1}$.

Figure E.1 shows a 300 sec. sample of $\hat{\mathbf{P}}_{\mathrm{RX12},0}$:

Figure E.2 shows a 300 sec. sample of $\widetilde{\mathbf{CP}}_{\mathrm{res},0}$:

As noted above these plots clearly shows the linear time variation of the measured phase quantities, superimposed with broadband measurement noise.

We are able to compute both the candidate positions and residuals for any epoch using Eq. E.19 and Eq. E.36. In order to use the information contained in both the constant and time varying parts of these equations, we can compute the residuals for two different epochs in the measurement range. Without further analysis, we have chosen to use the start and end epoch times.

The appropriate equation for the start epoch time ($t = 0$) are given by:

$$\mathbf{P}_{\mathrm{RX12C,S}} \cong \mathbf{C}_{\mathrm{RX12},0} + \mathbf{M}_{\mathrm{CPC2},0}\mathbf{N}_{12} \tag{E.40}$$

$$\widetilde{\mathbf{CP}}_{\mathrm{res,S}} \cong \mathbf{C}_{\mathrm{res},0} + \mathbf{M}_{\mathrm{res},0}\Delta\tilde{\mathbf{P}}_{\mathrm{RX12C,S}} \tag{E.41}$$

$$\mathrm{RMS}_{\mathrm{res,S}} = \frac{\left\|\mathbf{CP}_{\mathrm{res,S}}\right\|}{\sqrt{\mathrm{N}_{\mathrm{sec}}}} \tag{E.42}$$

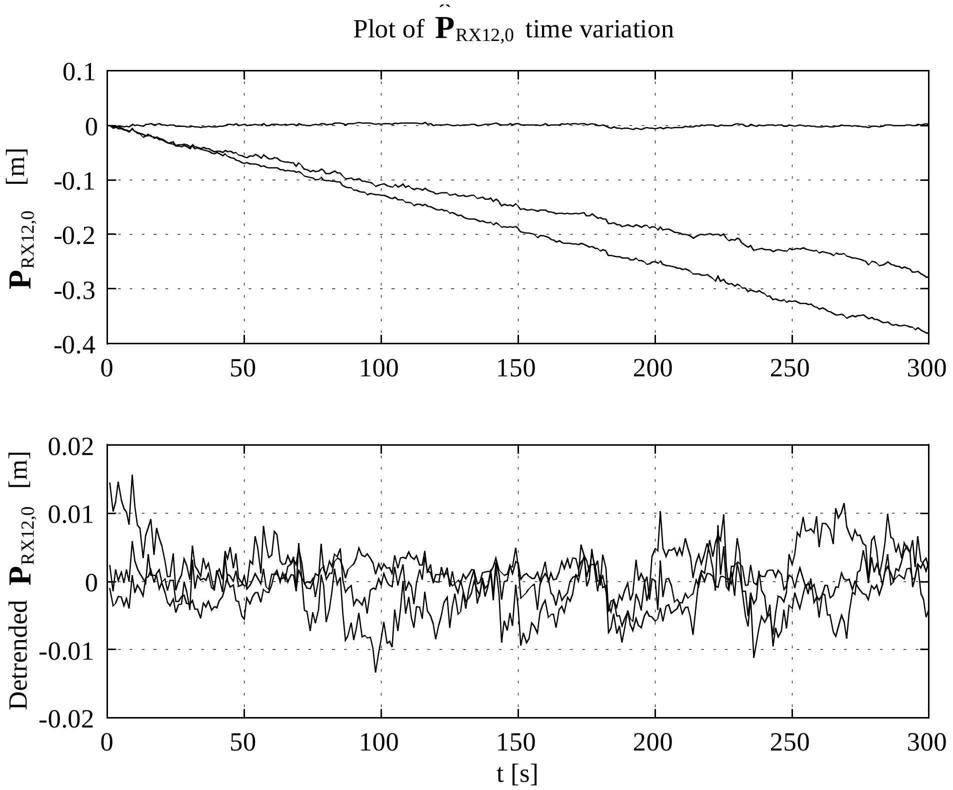

FIGURE E.1 $\hat{\mathbf{P}}_{RX12,0}$ sample (initial value set to zero for clarity).

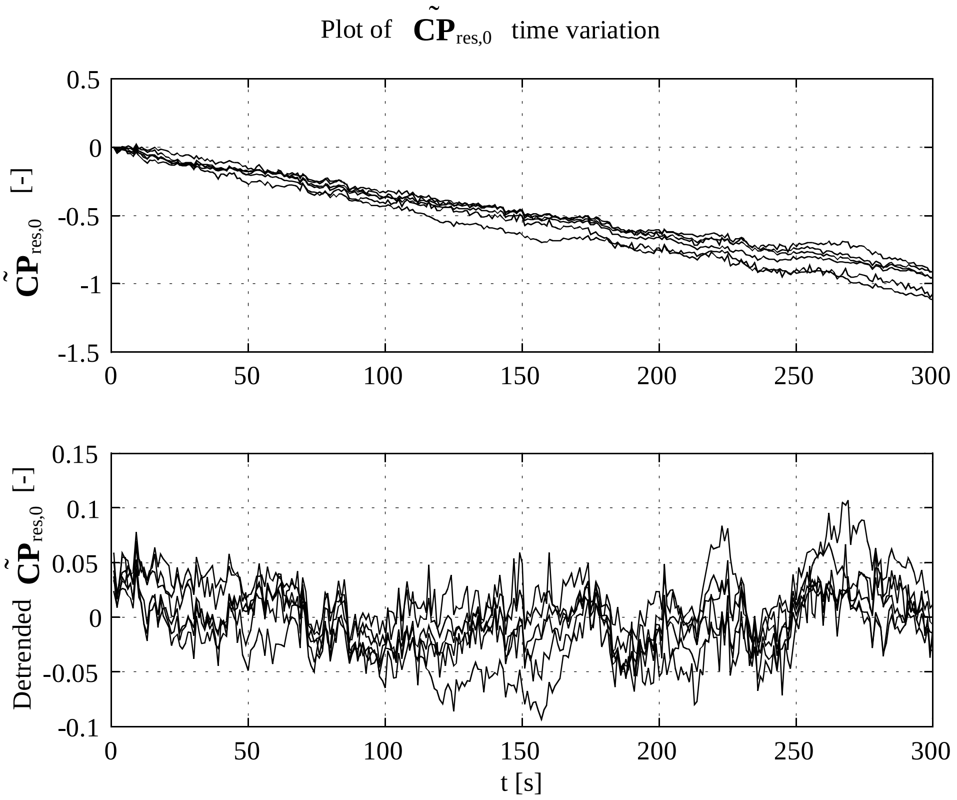

FIGURE E.2 $\tilde{\mathbf{CP}}_{res,0}$ sample (initial value set to zero for clarity).

For the end epoch ($t = \Delta t_{epoch}$):

$$\mathbf{P}_{RX12C,E} \cong (\mathbf{C}_{RX12,0} + \mathbf{C}_{RX12,1}\Delta t_{epoch}) + (\mathbf{M}_{CPC2,0} + \mathbf{M}_{CPC2,1}\Delta t_{epoch})\mathbf{N}_{12} \tag{E.43}$$

$$\tilde{\mathbf{CP}}_{res,E} \cong (\mathbf{C}_{res,0} + \mathbf{C}_{res,1}t) + (\mathbf{M}_{res,0} + \mathbf{M}_{res,1}t)\Delta\tilde{\mathbf{P}}_{RX12C,E} \tag{E.44}$$

$$\mathrm{RMS}_{res,E} = \frac{\|\mathbf{CP}_{res,E}\|}{\sqrt{N_{sec}}} \tag{E.45}$$

Notice that the ambiguity $\mathbf{N}_{12}$ is of course the same for both the start and end epochs.

This gives three error measures:

$$\mathrm{RMS}_{res,S} \tag{E.46}$$

$$\mathrm{RMS}_{res,E} \tag{E.47}$$

$$\Delta_{RX12C} = \|\mathbf{P}_{RX12C,E} - \mathbf{P}_{RX12C,S}\| \tag{E.48}$$

The question then arises of how to combine these error measures to obtain a single error measure for each candidate baseline. Since $\mathrm{RMS}_{res,S}$ and $\mathrm{RMS}_{res,E}$ can be assumed to have identical statistics due their “symmetrical” definitions, these error measures can be combined with equal weights. Unfortunately Δ_{RX12C} has different units and error statistics then the RMS residuals. Thus a sensible combination of all 3 error measures requires knowledge of statistics of both the RMS residuals and Δ_{RX12C}.

For the present application, it has not been considered justified to determine these statistics accurately. For this reason only the RMS residuals are used to construct a “worse case” total error measure defined by:

$$error \equiv max(\mathrm{RMS}_{res,S}, \mathrm{RMS}_{res,E}) \tag{E.49}$$

Where “$max(x, y)$ “is the maximum value of the real numbers x and y.

Since carrier phase data for a number of epochs are analysed, it is possible to obtain an estimate of the carrier phase measurement noise by assuming that the noise is ergodic. The carrier phase RMS noise can be determined by removing the linear trend from $\tilde{\mathbf{CP}}_{res,0}$, and calculating the RMS value of the remaining signal. The RMS noise value can be used as part of a “confidence” check on the obtained “true” ambiguity solution.

It then “only” remains to choose suitable sets of primary and secondary SV’s, calculate the candidate baselines from the primary SV’s, test each candidate position using the residual for the secondary SV’s and finally choose the best candidate baseline with the smallest root mean square residual. This will then determine the “true” integer ambiguities for both the primary and secondary set of SV’s.

It is now possible to formulate the following ambiguity search algorithm, which avoids storage of all the candidate positions, thus minimizing memory usage and at the same time eliminating indexing of large arrays. The algorithm is divided into the following sequential steps:

1. Compute a best guess baseline $\hat{\mathbf{P}}_{RX12}$ based on the pseudorange measurements.

2. Choose a consecutive set of measurements containing on the order of 300 epochs. The set should contain at least 7 SV’s, with no cycle slips.
3. Partition the SV’s into a primary and secondary set, based upon the SV elevation and the primary SV DOP. The DOP of the 4 primary SV’s should be less then 5.
4. Using carrier phase data from the selected epoch range, compute the appropriate measurement constants for the primary and secondary SV’s, as given by Eq. E.20 and Eq. E.36.
5. Select an ambiguity search range defined by $N_{i12,min}$ and $N_{i12,max}$ based on the pseudorange noise and multipath environment, using $\hat{\mathbf{P}}_{RX12,0}$ and $\mathbf{M}_{CPC2}$.
6. Search through all the candidate baselines using Eq. E.19. Compute the residuals $CP_{res,i}$ to the secondary SV’s, at each candidate baseline. Store the candidate point and associated ambiguities if the square sum of the residuals are in the lowest 100 range of the previously tested candidate points.
7. Test the “best” baseline against the next “best” and against the carrier phase RMS noise, to determine the confidence level of the baseline estimate.

This procedure has been implemented in Matlab. The primary SV’s have been chosen from the SV’s with elevation angles above $15°$, to reduce the effects of multipath. For the short baseline established between two antennas on the roof of the department, the following results have been obtained for 13 measurement sessions of 300 sec. duration:

Float ambiguity solution using Eq. E.24 and Eq. E.25:

GPS time of first measurement epoch	ΔNorthing	ΔEasting	ΔH	SEP
[sec]	[m]	[m]	[m]	[m]
499576	1.296	-4.549	0.165	11.377
500176	1.478	-4.414	0.442	4.570
500476	1.506	-4.505	0.465	5.653
500776	1.133	-4.415	0.864	5.237
501076	1.394	-4.499	0.368	21.994
501376	1.024	-5.021	0.761	2.085
501676	0.916	-4.863	0.912	2.788
501976	1.282	-4.725	0.634	7.204
502276	1.331	-4.581	0.508	3.707
502576	1.452	-4.256	0.334	6.067
502876	1.412	-4.451	0.443	0.802
503176	1.413	-4.055	0.088	7.761
503476	1.252	-4.858	0.555	17.430

Tabel E.1 Float ambiguity solution.

GPS time of first measurement epoch	ΔNorthing	ΔEasting	ΔH	SEP
[sec]	[m]	[m]	[m]	[m]
Mean value	1.299	-4.553	0.503	-
RMS deviation	0.180	0.263	0.246	-

Tabel E.1 Float ambiguity solution.

GPS time is from the beginning of week epoch. “Northing” and “Easting” are the cartesian coordinates defined using the UTM (Universal Transversal Mercator) projection. H is the local vertical coordinate (positive up). “SEP” is a crude worst case approximation to the Spherical Error Probable (Ref. 24, p. 280), which is the radius of the sphere that contains 50% of the stochastic measurements.

Fixed integer ambiguity solution using the above algorithm with residual minimization:

GPS time of first measurement epoch	ΔNorthing	ΔEasting	ΔH	*error* $(\mathrm{RMS}_{\mathrm{res}})$	*error ratio*
[sec]	[m]	[m]	[m]	[-]	[-]
499576	1.402	-4.466	0.317	0.092	0.621
500176	1.403	-4.467	0.324	0.041	0.257
500476	1.407	-4.469	0.319	0.056	0.308
500776	1.412	-4.471	0.320	0.141	0.836
501076	1.413	-4.475	0.318	0.156	0.821
501376	1.407	-4.469	0.341	0.121	0.775
501676	1.414	-4.476	0.350	0.137	0.867
501976	1.412	-4.474	0.346	0.129	0.878
502276	1.409	-4.473	0.348	0.099	0.644
502576	1.399	-4.468	0.343	0.082	0.661
502876	1.395	-4.467	0.346	0.068	0.487
503176	1.393	-4.469	0.355	0.061	0.429
503476	1.391	-4.468	0.352	0.055	0.373
Mean value	1.404	-4.470	0.337	-	-
RMS deviation	0.008	0.003	0.015	-	-

Tabel E.2 Fixed Ambiguity solution.

It is apparent that the RMS deviation for the fixed ambiguity solutions is at least 15 times smaller then for the float solution. Since no method is available to the author for determining the test baseline with greater accuracy then the fixed ambiguity solution, we will use the fixed ambiguity solution as the “ground truth” for all other measurements related to the test baseline, in this thesis.

The true baseline is thus given by:

$$\mathbf{P}_{\mathrm{RX12,test}} \equiv \left[1.404 \;\; -4.470 \;\; 0.337\right]\mathrm{m} \qquad \text{In UTM coordinates} \tag{E.50}$$

Appendix F: Simplified Kalman Filter Expressions

This Appendix contains the derivations of the presimplified kinematic Kalman filter in Section 5.10.

The modified Kalman gain from (Ref. 32, p. 123):

$$\mathbf{K}_{\mathrm{k}} \equiv (\mathbf{A}_{\mathrm{DGPS}}\mathbf{P}_{\mathrm{k}}^{-}\mathbf{C}_{\mathrm{DGPS}}^{T} + \mathbf{G}_{\mathrm{DGPS}}\mathbf{S}_{\mathrm{DGPS}}^{T})(\mathbf{C}_{\mathrm{DGPS}}\mathbf{P}_{\mathrm{k}}^{-}\mathbf{C}_{\mathrm{DGPS}}^{T} + \mathbf{R}_{\mathrm{DGPS,k}})^{-1} \tag{F.1}$$

With the definitions:

$$\mathbf{A}_{\mathrm{DGPS}} = \begin{bmatrix} 1 & 0 & 0 \\ 0 & 0 & 1 \\ 0 & -a_2 & -a_1 \end{bmatrix} \qquad \mathbf{B}_{\mathrm{DGPS}} = \begin{bmatrix} 1 \\ 0 \\ 0 \end{bmatrix} \qquad \mathbf{G}_{\mathrm{DGPS}} = \begin{bmatrix} 1 & 0 \\ 0 & 0 \\ 0 & b_1 \end{bmatrix}$$

$$\mathbf{C}_{\mathrm{DGPS}} = \begin{bmatrix} 1 & 1 & 0 \end{bmatrix} \qquad \mathbf{D}_{\mathrm{DGPS}} = \begin{bmatrix} b_0 \end{bmatrix} \tag{F.2}$$

$$\mathbf{Q}_{\mathrm{DGPS,k}} = \begin{bmatrix} \sigma_{\mathrm{CRR}}^2 & 0 \\ 0 & \sigma_{\mathrm{DGPS}}^2 \end{bmatrix} \qquad \mathbf{R}_{\mathrm{DGPS,k}} = \begin{bmatrix} b_0^2\sigma_{\mathrm{DGPS}}^2 \end{bmatrix}$$

The cross covariance $\mathbf{S}_{\mathrm{DGPS}}$ between the measurement and process noise is given by Eq. 5.10.9:

$$\mathbf{S}_{\mathrm{DGPS}} = \begin{bmatrix} \mathbf{0} & \mathbf{D}_{\mathrm{DGPS}} \end{bmatrix}\sigma_{\mathrm{DGPS}}^2 = \begin{bmatrix} 0 & b_0 \end{bmatrix}\sigma_{\mathrm{DGPS}}^2 \tag{F.3}$$

Let the elements of the a priori covariance $\mathbf{P}_{\mathrm{k}}^{-}$ (of the state estimate) be defined by:

$$\mathbf{P}_{\mathrm{k}}^{-} \equiv \begin{bmatrix} P_{11} & P_{12} & P_{13} \\ P_{21} & P_{22} & P_{23} \\ P_{31} & P_{32} & P_{33} \end{bmatrix} = \begin{bmatrix} P_{11} & P_{12} & P_{13} \\ P_{12} & P_{22} & P_{23} \\ P_{13} & P_{23} & P_{33} \end{bmatrix} \tag{F.4}$$

The last equality follows from the fact that the covariance is symmetrical by definition.

The term $\mathbf{C}_{\mathrm{DGPS}}\mathbf{P}_{\mathrm{k}}^{-}\mathbf{C}_{\mathrm{DGPS}}^{T} + \mathbf{R}_{\mathrm{DGPS,k}}$ can be expressed as:

$$\mathbf{C}_{\mathrm{DGPS}}\mathbf{P}_{\mathrm{k}}^{-}\mathbf{C}_{\mathrm{DGPS}}^{T} + \mathbf{R}_{\mathrm{DGPS,k}} = \begin{bmatrix} 1 & 1 & 0 \end{bmatrix}\begin{bmatrix} P_{11} & P_{12} & P_{13} \\ P_{12} & P_{22} & P_{23} \\ P_{13} & P_{23} & P_{33} \end{bmatrix}\begin{bmatrix} 1 \\ 1 \\ 0 \end{bmatrix} + b_0^2\sigma_{\mathrm{DGPS}}^2 = P_{11} + 2P_{12} + P_{22} + b_0^2\sigma_{\mathrm{DGPS}}^2 \tag{F.5}$$

The term $\mathbf{A}_{\mathrm{DGPS}}\mathbf{P}_{\mathrm{k}}^{-}\mathbf{C}_{\mathrm{DGPS}}^{T}$ can be expressed as:

$$\mathbf{A}_{\mathrm{DGPS}}\mathbf{P}_{\mathrm{k}}^{-}\mathbf{C}_{\mathrm{DGPS}}^{T} = \begin{bmatrix} 1 & 0 & 0 \\ 0 & 0 & 1 \\ 0 & -a_2 & -a_1 \end{bmatrix}\begin{bmatrix} P_{11} & P_{12} & P_{13} \\ P_{12} & P_{22} & P_{23} \\ P_{13} & P_{23} & P_{33} \end{bmatrix}\begin{bmatrix} 1 \\ 1 \\ 0 \end{bmatrix} = \begin{bmatrix} 1 & 0 & 0 \\ 0 & 0 & 1 \\ 0 & -a_2 & -a_1 \end{bmatrix}\begin{bmatrix} P_{11} + P_{12} \\ P_{12} + P_{22} \\ P_{13} + P_{23} \end{bmatrix}$$

$$\mathbf{A}_{\mathrm{DGPS}}\mathbf{P}_{\mathrm{k}}^{-}\mathbf{C}_{\mathrm{DGPS}}^{T} = \begin{bmatrix} P_{11} + P_{12} \\ P_{13} + P_{23} \\ -a_2(P_{12} + P_{22}) - a_1(P_{13} + P_{23}) \end{bmatrix} \tag{F.6}$$

The term $\mathbf{G}_{\text{DGPS}}\mathbf{S}_{\text{DGPS}}^{T}$ can be expressed as:

$$\mathbf{G}_{\text{DGPS}}\mathbf{S}_{\text{DGPS}}^{T} = \begin{bmatrix} 1 & 0 \\ 0 & 0 \\ 0 & b_1 \end{bmatrix} \begin{bmatrix} 0 \\ b_0 \end{bmatrix} \sigma_{\text{DGPS}}^{2} = \sigma_{\text{DGPS}}^{2} \begin{bmatrix} 0 \\ 0 \\ b_1 b_0 \end{bmatrix} \qquad \text{(F.7)}$$

This leads to the following expression for the modified Kalman gain:

$$\mathbf{K}_{\text{k}} = \frac{1}{P_{11} + 2P_{12} + P_{22} + b_0^2\sigma_{\text{DGPS}}^2} \begin{bmatrix} P_{11} + P_{12} \\ P_{13} + P_{23} \\ -a_2(P_{12} + P_{22}) - a_1(P_{13} + P_{23}) + b_1 b_0 \sigma_{\text{DGPS}}^2 \end{bmatrix} \qquad \text{(F.8)}$$

Appendix G: Transformation Matrices

Using Eq. 6.4.3 to Eq. 6.4.6, the following explicit expression for the vehicle to INS coordinate system transformation can be determined:

$$\mathbf{M}_{\mathrm{V2I}} = \mathbf{M}_{\mathrm{V2I}}(\theta_a, \theta_e, \theta_r) = \mathbf{M}_3(\theta_r)\mathbf{M}_2(\theta_e)\mathbf{M}_1(\theta_a)$$

$$\mathbf{M}_{\mathrm{V2I}} = \begin{bmatrix} \cos(\theta_e)\cos(\theta_a) & \cos(\theta_e)\sin(\theta_a) & -\sin(\theta_e) \\ \sin(\theta_r)\sin(\theta_e)\cos(\theta_a) - \cos(\theta_r)\sin(\theta_a) & \sin(\theta_r)\sin(\theta_e)\sin(\theta_a) + \cos(\theta_r)\cos(\theta_a) & \sin(\theta_r)\cos(\theta_e) \\ \cos(\theta_r)\sin(\theta_e)\cos(\theta_a) + \sin(\theta_r)\sin(\theta_a) & \cos(\theta_r)\sin(\theta_e)\sin(\theta_a) - \sin(\theta_r)\cos(\theta_a) & \cos(\theta_r)\cos(\theta_e) \end{bmatrix}$$

(G.1)

The INS to vehicle system transformation can then be determined using Eq. 6.4.7:

$$\mathbf{M}_{\mathrm{I2V}} = \mathbf{M}_{\mathrm{V2I}}^T = \mathbf{M}_{\mathrm{I2V}}(\theta_a, \theta_e, \theta_r)$$

$$\mathbf{M}_{\mathrm{I2V}} = \begin{bmatrix} \cos(\theta_e)\cos(\theta_a) & \sin(\theta_r)\sin(\theta_e)\cos(\theta_a) - \cos(\theta_r)\sin(\theta_a) & \cos(\theta_r)\sin(\theta_e)\cos(\theta_a) + \sin(\theta_r)\sin(\theta_a) \\ \cos(\theta_e)\sin(\theta_a) & \sin(\theta_r)\sin(\theta_e)\sin(\theta_a) + \cos(\theta_r)\cos(\theta_a) & \cos(\theta_r)\sin(\theta_e)\sin(\theta_a) - \sin(\theta_r)\cos(\theta_a) \\ -\sin(\theta_e) & \sin(\theta_r)\cos(\theta_e) & \cos(\theta_r)\cos(\theta_e) \end{bmatrix}$$

(G.2)

In some cases the it may be appropriate to obtain simplified expressions for the transformation matrices, corresponding to typical operating areas for the INS.

Operation at small elevation angles $\theta_e \approx 0$ and small roll angles $\theta_r \approx 0$:

$$\sin(\theta_e) \cong \theta_e \qquad \cos(\theta_e) \cong 1 \qquad \sin(\theta_r) \cong \theta_r \qquad \cos(\theta_r) \cong 1 \qquad \sin(\theta_r)\sin(\theta_e) \cong 0 \tag{G.3}$$

Vehicle to INS transformation:

$$\mathbf{M}_{\mathrm{V2I}} \cong \begin{bmatrix} \cos(\theta_a) & \sin(\theta_a) & -\theta_e \\ -\sin(\theta_a) & \cos(\theta_a) & \theta_r \\ \theta_e\cos(\theta_a) + \theta_r\sin(\theta_a) & \theta_e\sin(\theta_a) - \theta_r\cos(\theta_a) & 1 \end{bmatrix} \tag{G.4}$$

INS to vehicle transformation:

$$\mathbf{M}_{\mathrm{I2V}} \cong \begin{bmatrix} \cos(\theta_a) & -\sin(\theta_a) & \theta_e\cos(\theta_a) + \theta_r\sin(\theta_a) \\ \sin(\theta_a) & \cos(\theta_a) & \theta_e\sin(\theta_a) - \theta_r\cos(\theta_a) \\ -\theta_e & \theta_r & 1 \end{bmatrix} \tag{G.5}$$

Appendix H: Euler rates

We are seeking a function linking the Euler rates $(\dot{\theta}_a, \dot{\theta}_e, \dot{\theta}_r)$, to the angular rates in INS coordinates $(\omega_x, \omega_y, \omega_z)_{INS}$:

$$(\dot{\theta}_a, \dot{\theta}_e, \dot{\theta}_r) = f(\theta_a, \theta_e, \theta_r, \omega_x, \omega_y, \omega_z) \tag{H.1}$$

The INS orientation as given by the Euler angles $(\theta_a, \theta_e, \theta_r)$ can be expected to be parameters for this function.

Since the transformation from INS to vehicle coordinates, can be written as:

$$\mathbf{M}_{\mathrm{I2V}} = \begin{bmatrix}\mathbf{e}_{xiv} & \mathbf{e}_{yiv} & \mathbf{e}_{ziv}\end{bmatrix} \tag{H.2}$$

Where $\mathbf{e}_{xiv}$, $\mathbf{e}_{yiv}$ and $\mathbf{e}_{ziv}$ are column unit vectors of the INS coordinate system, expressed in vehicle coordinates.

Since $(\omega_x, \omega_y, \omega_z)_{INS}$ represents the rates of rotation of the INS axes, we can express the derivatives of the INS axes in vehicle coordinates as:

$$\dot{\mathbf{e}}_{xiv} = \mathbf{e}_{yiv}\omega_z - \mathbf{e}_{ziv}\omega_y \tag{H.3}$$

$$\dot{\mathbf{e}}_{yiv} = \mathbf{e}_{ziv}\omega_x - \mathbf{e}_{xiv}\omega_z \tag{H.4}$$

$$\dot{\mathbf{e}}_{ziv} = \mathbf{e}_{xiv}\omega_y - \mathbf{e}_{yiv}\omega_x \tag{H.5}$$

Thus the derivative of the transformation matrix Eq. H.2, can be expressed as:

$$\dot{\mathbf{M}}_{\mathrm{I2V}} = \begin{bmatrix}\dot{\mathbf{e}}_{xiv} & \dot{\mathbf{e}}_{yiv} & \dot{\mathbf{e}}_{ziv}\end{bmatrix} = \mathbf{M}_{\mathrm{I2V}}\begin{bmatrix}0 & -\omega_z & \omega_y \\ \omega_z & 0 & -\omega_x \\ -\omega_y & \omega_x & 0\end{bmatrix} \tag{H.6}$$

This is one way of determining the derivative of the INS to vehicle transformation matrix. Another way is to express it in terms of the Euler angle rates:

$$\dot{\mathbf{M}}_{\mathrm{I2V}} = f(\theta_a, \theta_e, \theta_r, \dot{\theta}_a, \dot{\theta}_e, \dot{\theta}_r) \tag{H.7}$$

The derivative $\dot{\theta}_e$ can be determined by equating element (3,1) of Eq. H.7, with element (3,1) of Eq. H.6:

$$-\cos(\theta_e)\dot{\theta}_e = \sin(\theta_r)\cos(\theta_e)\omega_z - \cos(\theta_r)\cos(\theta_e)\omega_y$$

$$\underline{\dot{\theta}_e = \cos(\theta_r)\omega_y - \sin(\theta_r)\omega_z} \tag{H.8}$$

The derivative $\dot{\theta}_a$ can be determined by equating element (2,1) of Eq. H.7, with element (2,1) of Eq. H.6:

$$-\sin(\theta_e)\sin(\theta_a)\dot{\theta}_e + \cos(\theta_e)\cos(\theta_a)\dot{\theta}_a = -(\cos(\theta_r)\sin(\theta_e)\sin(\theta_a) - \sin(\theta_r)\cos(\theta_a))\omega_y \ldots$$
$$+ (\sin(\theta_r)\sin(\theta_e)\sin(\theta_a) + \cos(\theta_r)\cos(\theta_a))\omega_z$$

$$\cos(\theta_e)\cos(\theta_a)\dot{\theta}_a = \sin(\theta_e)\sin(\theta_a)(\cos(\theta_r)\omega_y - \sin(\theta_r)\omega_z) - (\cos(\theta_r)\sin(\theta_e)\sin(\theta_a) - \sin(\theta_r)\cos(\theta_a))\omega_y \ldots$$
$$+ (\sin(\theta_r)\sin(\theta_e)\sin(\theta_a) + \cos(\theta_r)\cos(\theta_a))\omega_z$$

$$\cos(\theta_e)\cos(\theta_a)\dot{\theta}_a = -(\cos(\theta_r)\sin(\theta_e)\sin(\theta_a) - \sin(\theta_r)\cos(\theta_a) - \cos(\theta_r)\sin(\theta_e)\sin(\theta_a))\omega_y \ldots$$
$$+ (\sin(\theta_r)\sin(\theta_e)\sin(\theta_a) + \cos(\theta_r)\cos(\theta_a) - \sin(\theta_r)\sin(\theta_e)\sin(\theta_a))\omega_z$$

$$\underline{\dot{\theta}_a = \frac{\sin(\theta_r)}{\cos(\theta_e)}\omega_y + \frac{\cos(\theta_r)}{\cos(\theta_e)}\omega_z} \tag{H.9}$$

The derivative $\dot{\theta}_r$ can be determined by equating element (3,2) of Eq. H.7, with element (3,2) of Eq. H.6:

$$\cos(\theta_r)\cos(\theta_e)\dot{\theta}_r - \sin(\theta_r)\sin(\theta_e)\dot{\theta}_e = \sin(\theta_e)\omega_z + \cos(\theta_r)\cos(\theta_e)\omega_x$$

$$\cos(\theta_r)\cos(\theta_e)\dot{\theta}_r = \sin(\theta_r)\sin(\theta_e)\cos(\theta_r)\omega_y + (\sin(\theta_e) - \sin(\theta_r)\sin(\theta_r)\sin(\theta_e))\omega_z$$
$$+ \cos(\theta_r)\cos(\theta_e)\omega_x$$

$$\underline{\dot{\theta}_r = \omega_x + \sin(\theta_r)\tan(\theta_e)\omega_y + \cos(\theta_r)\tan(\theta_e)\omega_z} \tag{H.10}$$

In summary we can write the derivatives of the Euler angles as:

$$\begin{bmatrix} \dot{\theta}_r \\ \dot{\theta}_e \\ \dot{\theta}_a \end{bmatrix} = \begin{bmatrix} 1 & \sin(\theta_r)\tan(\theta_e) & \cos(\theta_r)\tan(\theta_e) \\ 0 & \cos(\theta_r) & -\sin(\theta_r) \\ 0 & \dfrac{\sin(\theta_r)}{\cos(\theta_e)} & \dfrac{\cos(\theta_r)}{\cos(\theta_e)} \end{bmatrix} \begin{bmatrix} \omega_x \\ \omega_y \\ \omega_z \end{bmatrix} \tag{H.11}$$

A few interesting comments about this “transformation”:

- When $\theta_r = \theta_e = 0$, the matrix is equal to the identity matrix.
- The relation does not depend on the azimuth angle θ_a.
- Some elements are singular at $\theta_e = \pm 90^o$.

Appendix I: Quaternions

A quaternion is an extension of complex numbers. Instead of containing one imaginary part, as the usual complex numbers, the quaternions contain three different imaginary parts:

$$q = w + xi + yj + zk \tag{I.1}$$

The quaternion q contains the three imaginary elements i, j, k. w, x, y and z are real numbers. Some general properties of quaternions are given in (Ref. 37). It is possible to multiply two quaternions and obtain the conjugate, the norm and the inverse of a quaternion see (Ref. 37) for details. It should be mentioned that multiplication of quaternions are not commutative, in other words the order of multiplication is important.

It turns out that a unit quaternion can be used to represent a 3D rotation. A unit quaternion can be represented as:

$$q = \cos(\theta) + u\sin(\theta) \tag{I.2}$$

Where $u = xi + yj + zk$ is regarded as a 3D unity vector (i.e. $x^2 + y^2 + z^2 = 1$). It can then be shown (Ref. 37, p. 3-4) that Eq. I.2 represents a 3D rotation of the size 2θ around the vector $u = (x, y, z)$, using the right hand rule.

It can be shown that two or more successive rotations can be obtained by straight forward multiplication of the quaternions corresponding to the individual rotations. Lets assume as an example that we have one rotation represented by the quaternion q_1 and another by the quaternion q_2. The resulting quaternion from doing first the rotation defined by q_1 and then the rotation defined by q_2, is the rotation defined by the quaternion q:

$$q = q_2 \cdot q_1 \tag{I.3}$$

Using the above expression we are able to derive an expression relating the derivative of a quaternion to the angular body rates. Lets assume that the orientation of a rigid body at time t is given by the quaternion $q(t)$ (expressing the orientation relative to a reference orientation in an inertial reference system). The rotation of the vehicle in a small time interval Δt is denoted by the quaternion Δq. According to Eq. I.3, the orientation at time $t + \Delta t$ can be determined as:

$$q(t + \Delta t) = \Delta q \cdot q(t) \tag{I.4}$$

The rotation Δq can then be expressed in the form of Eq. I.2:

$$\Delta q = \cos(\Delta\theta) + u\sin(\Delta\theta) \tag{I.5}$$

Assuming that $\Delta\theta$ is small ($\Delta\theta \ll 1$), the familiar trigonometric relationships are obtained:

$$\cos(\Delta\theta) \cong 1 \qquad \sin(\Delta\theta) \cong \Delta\theta \qquad , \quad \Delta\theta \to 0 \tag{I.6}$$

Thus Δq can be expressed as:

$$\Delta q = 1 + u\Delta\theta \tag{I.7}$$

Since u can be interpreted as the axis of rotation and $2\Delta\theta$ as "size" of the rotation (in a right hand sense), we can express the last term of Eq. I.7 as a function of the angular body rate $\boldsymbol{\omega}$:

$$\hat{u}(2\Delta\theta) \cong \hat{\omega}\Delta t \qquad \Delta t \rightarrow 0 \tag{I.8}$$

Where $\hat{\omega} \equiv i\omega_x + j\omega_y + k\omega_z$ is $\boldsymbol{\omega} = \begin{bmatrix}\omega_x & \omega_y & \omega_z\end{bmatrix}^T$ expressed as an quaternion.

Combining Eq. I.4, Eq. I.7 and Eq. I.8 gives:

$$q(t + \Delta t) \cong \left(1 + \frac{\hat{\omega}\Delta t}{2}\right) \cdot q(t) \tag{I.9}$$

This can be manipulated to the expression:

$$\frac{q(t + \Delta t) - q(t)}{\Delta t} \cong \frac{\hat{\omega} \cdot q(t)}{2} \tag{I.10}$$

Letting Δt approach zero then gives the desired Ordinary Differential Equation (ODE) for quaternions in terms of the body rates:

$$\dot{q}(t) = \frac{1}{2}\hat{\omega} \cdot q(t) \tag{I.11}$$

Notice that since quaternions are noncummunative, the multiplication order on the right hand side is important.

The above expression is not immediately suitable for numerical solution using a standard ODE integration package, because quaternions are not usually supported. Instead we can try to reformulate this expression into one involving a vector expression of a quaternion.

An explicit expression for the right hand side of Eq. I.11 can be obtained as (Ref. 37,p. 1):

$$\begin{aligned}\dot{q}(t) &= \frac{\omega \cdot q(t)}{2} = \frac{1}{2}(0 + i\omega_x + j\omega_y + k\omega_z)(w_q + ix_q + jy_q + kz_q) \\ &= \frac{1}{2}(0 - \omega_x x_q - \omega_y y_q - \omega_z z_q) + \\ &\quad \frac{1}{2}i(0 + \omega_x w_q + \omega_y z_q - \omega_z y_q) + \\ &\quad \frac{1}{2}j(0 - \omega_x z_q + \omega_y w_q + \omega_z x_q) + \\ &\quad \frac{1}{2}k(0 + \omega_x y_q - \omega_y x_q + \omega_z w_q)\end{aligned} \tag{I.12}$$

It is now possible to express Eq. I.11 as a real valued first order ODE system by introducing the vector representation $\mathbf{q} = \begin{bmatrix}x_q & y_q & z_q & w_q\end{bmatrix}^T$ of $q = w_q + ix_q + jy_q + kz_q$:

$$\dot{\mathbf{q}} = \begin{bmatrix}\dot{x}_q \\ \dot{y}_q \\ \dot{z}_q \\ \dot{w}_q\end{bmatrix} = \frac{1}{2}\begin{bmatrix}w_q & z_q & -y_q \\ -z_q & w_q & x_q \\ y_q & -x_q & w_q \\ -x_q & -y_q & -z_q\end{bmatrix}\begin{bmatrix}\omega_x \\ \omega_y \\ \omega_z\end{bmatrix} = \mathbf{M}_{\mathrm{Quat}}(\mathbf{q})\boldsymbol{\omega} \tag{I.13}$$

It is apparent that $\mathbf{M}_{\text{Quat}}$ has a certain symmetry in the upper 3 x 3 part. More important is the fact that all elements of $\mathbf{M}_{\text{Quat}}$ are finite for any unit quaternion ($\|q\| = \|\mathbf{q}\| = \sqrt{x_q^2 + y_q^2 + z_q^2 + w_q^2} = 1$). This prevents numerical problems when solving the ODE for the vehicle attitude.

In general the vehicle attitude at the start of the simulation or the actual mission is not equal to the attitude of the local earth coordinate system. Thus it must be possible to describe the initial vehicle attitude in a user friendly way. One obvious choice for this is to use the Euler angles as described in Section 6.4.1. The advantage of using the Euler angles is that the are relatively easy to understand intuitively.

The transformation from the vehicle system (aligned with the local earth system) to the body system is accomplished by the rotations θ_a, θ_e and θ_r, denoting the azimuth, elevation and roll angles.

The rotation θ_a is positive around the z-axis. The quaternion q_a representing θ_a can thus be expressed as:

$$q_a = \cos\left(\frac{\theta_a}{2}\right) + k\sin\left(\frac{\theta_a}{2}\right) \tag{I.14}$$

Similarly the rotation θ_e around the y-axis can be represented by the quaternion q_e:

$$q_e = \cos\left(\frac{\theta_e}{2}\right) + j\sin\left(\frac{\theta_e}{2}\right) \tag{I.15}$$

And lastly the rotation θ_r around the x-axis can be represented by the quaternion q_r:

$$q_r = \cos\left(\frac{\theta_r}{2}\right) + i\sin\left(\frac{\theta_r}{2}\right) \tag{I.16}$$

According to the rotation concatenation rule given by Eq. I.3, the final vehicle orientation can then be expressed as the product of the quaternions in the reverse order of the rotations:

$$q = q_r \cdot q_e \cdot q_a \tag{I.17}$$

Using the explicit expressions for q_a, q_e and q_r gives:

$$\begin{aligned}
q &= \left(\cos\left(\frac{\theta_r}{2}\right) + i\sin\left(\frac{\theta_r}{2}\right)\right)\left(\cos\left(\frac{\theta_e}{2}\right) + j\sin\left(\frac{\theta_e}{2}\right)\right)\left(\cos\left(\frac{\theta_a}{2}\right) + k\sin\left(\frac{\theta_a}{2}\right)\right) \\
&= \left(\cos\left(\frac{\theta_r}{2}\right) + i\sin\left(\frac{\theta_r}{2}\right)\right)\left(\cos\left(\frac{\theta_e}{2}\right)\cos\left(\frac{\theta_a}{2}\right) + i\sin\left(\frac{\theta_e}{2}\right)\sin\left(\frac{\theta_a}{2}\right) + j\sin\left(\frac{\theta_e}{2}\right)\cos\left(\frac{\theta_a}{2}\right)\right) \\
&= \cos\left(\frac{\theta_r}{2}\right)\cos\left(\frac{\theta_e}{2}\right)\cos\left(\frac{\theta_a}{2}\right) - \sin\left(\frac{\theta_r}{2}\right)\sin\left(\frac{\theta_e}{2}\right)\sin\left(\frac{\theta_a}{2}\right) + \\
&\quad i\left(\cos\left(\frac{\theta_r}{2}\right)\sin\left(\frac{\theta_e}{2}\right)\sin\left(\frac{\theta_a}{2}\right) + \sin\left(\frac{\theta_r}{2}\right)\cos\left(\frac{\theta_e}{2}\right)\cos\left(\frac{\theta_a}{2}\right)\right) + \\
&\quad j\cos\left(\frac{\theta_r}{2}\right)\sin\left(\frac{\theta_e}{2}\right)\sin\left(\frac{\theta_a}{2}\right) + \\
&\quad k\sin\left(\frac{\theta_r}{2}\right)\sin\left(\frac{\theta_e}{2}\right)\cos\left(\frac{\theta_a}{2}\right)
\end{aligned} \tag{I.18}$$

This can be directly expressed in vector form as:

$$\mathbf{q} = \begin{bmatrix} \cos\left(\frac{\theta_r}{2}\right)\sin\left(\frac{\theta_e}{2}\right)\sin\left(\frac{\theta_a}{2}\right) + \sin\left(\frac{\theta_r}{2}\right)\cos\left(\frac{\theta_e}{2}\right)\cos\left(\frac{\theta_a}{2}\right) \\ \cos\left(\frac{\theta_r}{2}\right)\sin\left(\frac{\theta_e}{2}\right)\sin\left(\frac{\theta_a}{2}\right) \\ \sin\left(\frac{\theta_r}{2}\right)\sin\left(\frac{\theta_e}{2}\right)\cos\left(\frac{\theta_a}{2}\right) \\ \cos\left(\frac{\theta_r}{2}\right)\cos\left(\frac{\theta_e}{2}\right)\cos\left(\frac{\theta_a}{2}\right) - \sin\left(\frac{\theta_r}{2}\right)\sin\left(\frac{\theta_e}{2}\right)\sin\left(\frac{\theta_a}{2}\right) \end{bmatrix} \qquad \text{(I.19)}$$

ISBN 87-91184-15-0